COLLECTED PAPERS on Nanophotonics

Vol. 21

August 2005 – July 2006

Prof. Motoichi OHTSU

MEMBERS

(From April 1, 2006)

*[I] THE UNIVERSITY OF TOKYO**

Professor

Motoichi OHTSU[a-e] (Dr. Eng.)

Graduate Student (Doctor Candidate)

Wataru NOMURA
Shunsuke YAMAZAKI
Kokoro KITAMURA
Chia-Jean Wang[f]

Graduate Students (Master Course)

Hiroki YONEMITSU
Tohru NAKAMATA
Hyungsu JEONG
Shunsuke TANAKA
Takumi YAMAMOTO

Undergraduate Students

Jun Hyoung KIM
Masaaki YASUI

Secretary

Rieko TUKAMOTO
Kumiko NOZAWA
Sachiyo KOJIMA

a) Also a director, "Development of High-Capacity Optical Storage Technology" project, METI (Ministry of Economy, Trade and Industry) and NEDO (New Energy and Industrial Technology Development Organization)
b) Also a team leader, "Nanophotonics team",
SORST (Solution Oriented Research for Science and Technology), JST (Japan Science and Technology Agency)

c) Also a leader, "Optical near field lithography project",
Leading Project, MEXT (Ministry of Education, Culture, Sports, Science, and Technology)
d) Also a director, NPO-Research Institute of Nanophotonics
e) Also a director, "Nanophotonics Total Expansion: Industry-University Cooperation and Human Resource Development", METI (Ministry of Economy, Trade and Industry) and NEDO (New Energy and Industrial Technology Development Organization)
(f) Visiting PhD student supported by EAPSI (East Asia and Pacific Summer Institutes for U.S. Graduate Studensts), sponsored by NSF (National Science Foundation) and JSPS (Japan Society for the Promotion of Science) (13, June 2006- 23, August 2006). Permanent affiliation: Electrical Engineering Department, University of Washington

(*)
Department of Electronics Engineering, School of Engineering,
The University of Tokyo
(Rm 215, Bdg. Eng-9)
2-11-16 Yayoi, Bunkyo-ku, Tokyo 113-8656, Japan
Phone：+81-3-5841-1189
FAX: +81-3-5841-1140
E-mail: ohtsu@ee.t.u-tokyo.ac.jp
URL(1): http://uuu.t.u-tokyo.ac.jp
URL(2):http://www.nanophotonics.info

東京大学大学院工学系研究科電子工学専攻
〒113-8656 **東京都文京区弥生** 2-11-16 **工学部** 9 **号館** 215 **号室**
Phone: 03-5841-1189, Fax: 03-5841-1140
E-mail: ohtsu@ee.t.u-tokyo.ac.jp
URL(1): http://uuu.t.u-tokyo.ac.jp
URL(2):http://www.nanophotonics.info

*[II] NANOPHOTONICS TEAM**

Researchers

Tadashi KAWAZOE (Dr. Sci.)
Takashi YATSUI (Dr. Eng.)

Manager

Akiyoshi ORIDE

Secretary

Tomoko TOTAKE

(*)

Nanophotonics Team, SORST (Solution Oriented Research for Science and Technology), JST (Japan Science and Technology Agency)
4th Floor, Tenko Building #17
687-1 Tsuruma, Machida-shi, Tokyo 194-0004
Phone: +81-42-788-6030, Fax: +81-42-788-6031

（独）科学技術振興機構、戦略的創造研究推進事業「発展・継続」研究,
ナノフォトニクスチーム
〒194-0004 **東京都町田市鶴間** 687-1 **第** 17 **天幸ビル** 4 **階**
Phone: 042-788-6030, Fax: 042-788-6031

*[III] OPTICAL NEAR FIELD LITHOGRAPHY PROJECT**

Manager

Masatake KAWANO

Research Assistant

Hisayo ITO
Masako NISHIDA

Secretary

Akemi KATO

(*)

Optical Near Field Lithography Project, Leading Project,
MEXT (Ministry of Education, Culture, Sports, Science, and Technology)
4th Floor, Tenko Building #17
687-1 Tsuruma, Machida-shi, Tokyo 194-0004
Phone: +81-42-788-2211, Fax: +81-42-799-0886

文部科学省 リーディングプロジェクト、
近接場光リソグラフィ プロジェクト
〒194-0004 **東京都町田市鶴間** 687-1 **第** 17 **天幸ビル** 4 **階**
Phone: 042-788-2211, Fax: 042-799-0886

*[IV] RESEARCH INSTITUTE OF NANOPHOTONICS**

Director

Motoichi OHTSU

(*)

Research Insitutute of Nanophotonics,
Nonprofit Organization
1-20-10 Sekiguchi, Bunkyo-ku, Tokyo 112-0014
Phone: +81-3-5225-6432. Fax: +81-3-5225-6435
E-mail: ohtsu-rinps@nanophotonics.t.u-tokyo.ac.jp
URL: http://www.nanophotonics.info

特定非営利法人 ナノフォトニクス工学推進機構
〒112-0014 **東京都文京区関口** 1-20-10
Phone: 03-5225-6432. Fax: 03-5225-6435
E-mail: ohtsu-rinps@nanophotonics.t.u-tokyo.ac.jp
URL: http://www.nanophotonics.info

*[V] Nanophotonics Total Expansion: Industry-University Cooperation and Human Resource Development **

Associate Professor

Makoto NARUSE[g] (Dr. Eng.)

Research Associate

Kazuhiro NISHIBAYASHI (Dr. Sci.)

Manager

Yoshichika UCHIYAMA[h]

Secretaries

Rieko TUKAMOTO
Kumiko NOZAWA

(g) Permanent affiliation: National Institute of Information and Communication Technology
(h) Permanent affiliation: NEDO (New Energy and Industrial Technology Development Organization)
(*)
Department of Electronics Engineering, School of Engineering,
The University of Tokyo
(Rm 219, Bdg. Eng-9)
2-11-16 Yayoi, Bunkyo-ku, Tokyo 113-8656, Japan
Phone:+81-3-5841-1670
FAX: +81-3-5841-1140
E-mail: info@ nanophotonics.t.u-tokyo.ac.jp
URL: http://uuu.t.u-tokyo.ac.jp

東京大学大学院工学系研究科電子工学専攻
〒113-8656 **東京都文京区弥生** 2-11-16 **工学部** 9 **号館** 219 **号室**
Phone:+81-3-5841-1670
FAX: +81-3-5841-1140
E-mail: info@ nanophotonics.t.u-tokyo.ac.jp
URL: http://uuu.t.u-tokyo.ac.jp

LIST OF PAPERS

[(pp.XX-XX); pages in this issue of the COLLECTED PAPERS**]**

[I] ORIGINAL PAPERS

[6] E.-S. Jang, J. Y. Bae, J. Yoo, W. I. Park, D.-W. Kim, G.-C. Yi, T. Yatsui, and M.Ohtsu, “Quantum confinement effect in ZnO/$Mg_{0.2}Zn_{0.8}O$ multishell nanorod heterostructures,” Applied Physics Letters, Vol. 88, No. 2, January 2006, pp.023102-1–023102-3

(pp.23-25)

[7] M. Naruse, T. Kawazoe, S. Sangu, K. Kobayashi, and M. Ohtsu, "Optical interconnects based on optical far- and near-field interactions for high-density data broadcasting," Optics Express Vol.14, No. 1, January 2006, pp.306-313

(pp.27-34)

[8] T. Yatsui, W. Nomura, and M. Ohtsu, “Self-Assembly of Size- and Position-Controlled Ultralong Nanodot Chains using Near-Field Optical Desorption,” Nano Letters, Vol. 5, No. 12, December 2005, pp.2548–2551

(pp.35-38)

[9] M. Naruse, T. Yatsui, W. Nomura, N. Hirose, and M. Ohtsu, “Hierarchy in optical near-fields and its application to memory retrieval,” Optics Express, Vol. 13, No. 23, November 2005, pp.9265–9271

(pp.39-45)

[10] T. Kawazoe, S.Maruyama, K. Kobayashi, and M. Ohtsu, “Observation of Faraday Rotation and Magnetic Circular Dichroism in an Optical Near-Field Probe Coated with Fe,” IEICE Transactions on Electronics, Vol.E 88-C, No.9, September 2005, pp.1850-1852

(pp.47-49)

[11] T. Kawazoe, K. Kobayashi, and M. Ohtsu, “Anti-Parallel Dipole Coupling of Quantum Dots via an Optical Near-Field Interaction,” IEICE Transactions on Electronics , Vol.E88-C, No.9, September 2005, pp.1845-1849

(pp.51-55)

[12] J. Lim, T. Yatsui, and M. Ohtsu, "Observation of Size-Dependent Resonance of Near-Field Coupling between a Deposited Zn Dot and the Probe Apex during Near-Field Optical Chemical Vapor Deposition," IEICE Transactions on Electronics, Vol. E88-C, No. 9, September 2005, pp.1832–1835

(pp.57-60)

[13] S. Sangu, K. Kobayashi, and M. Ohtsu, "Nanophotnic Devices and Fundamental Functional Operations," IEICE Transactions on Electronics, Vol.E 88-C, No.9, September 2005, pp.1824-1831

(pp.61- 68)

[14] M. Naruse, T. Miyazaki, T. Kawazoe, S. Sangu, K. Kobayashi, F. Kubota, and M. Ohtsu, "Nanophotnic Computing Based on Optical Near-Fiele Interactions between Quantum Dots," IEICE Transactions on Electronics, Vol.E 88-C, No.9, September 2005, pp.1817-1823

(pp.69-75)

[15] T. Yatsui, W. Nomura, and M. Ohtsu, "Size-, Position-, and Separation-Controlled One-Dimensional Alignment of Nanoparticles Using an Optical Near Field," IEICE Transactions on Electronics, Vol. E 88-C, No. 9, September 2005, pp.1798–1802

(pp.77-81)

[16] K. Kobayashi, T.Kawazoe, and M. Ohtsu, "Importance of Multiple-Phonon Interactions in Molecular Dissociation and Nanofabrication Using Optical Near Fields," IEEE Transactions on Nanotechnology , Vol.4, No.5, September 2005, pp. 517-522

(pp. 83-88)

[II] PRESENTATIONS IN INTERNATIONAL CONFERENCES

[1] M. Naruse, T. Yatsui, T. Kawazoe, Y. Akao, and M. Ohtsu, "Nanophotonic traceable memory vased on energy-localization and hierarchy of optical near-fields," in Conference on IEEE nano 2006, July 17-20, 2006, Cincinnati, OH, USA (poster paper number 67)

(pp.89-92)

[2] T. Yatsui, W. Nomura, and M. Ohtsu, "Near-field fabrication of size- and position-controlled ultra-long nanodot chains," in Conference on Lasers and Electro-Optics/Quantum Electronics and Laser Science Conference and Photonic Applications Systems Technologies (Optical Society of America 2006), May 22-26, 2006, Long Beach, CA, USA (paper number QTuA7)

(pp.93-94)

[3]T. Yatsui, T. Kawazoe, S. Sangu, M. Ohtsu, S. J. An, J. Yoo, and G.-C. Yi "Direct observation of optical near-field energy transfer between ZnO nanorod double-quantum-well structures," in Conference on Lasers and Electro-Optics/Quantum Electronics and Laser Science Conference and Photonic Applications Systems Technologies (Optical Society of America 2006), May 22–26, 2006, Long Beach, CA, USA (paper number QTuK6)

(pp.95-96)

[4] T.Kawazoe M.Naruse and M. Ohtsu, "Dynamical optical near-field of energy transfers among quantum dots for a nanometric optical buffering," ABSTRACTS of in Conference on Lasers and Electro-Optics/Quantum Electronics and Laser Science Conference and Photonic Applications Systems Technologies (Optical Society of America 2006), May 22-26, Long Beach, USA (paper number CFE3)

(pp.97-98)

[5] K.Kobayashi, T.Kawazoe, M..Ohtsu, "Energy transfer in a near-field photochemical process via localized photons dressed by polarons," Abstracts of The 5th Asia-Pacific Conference on Near-Field Optics, Optical Society of Japan, November 14-17, 2005, Niigata, Japan (Session 1) p.3

(p.99)

[6] W. Nomura, T. Yatsui, M. Ohtsu, "Near-field Optical energy transfer of a nanodot coupler with resonant light scattering of Au nanoparticles," Abstracts of The 5th Asia-Pacific Conference on Near-Field Optics, Optical Society of Japan, November 14–17, 2005, Niigata, Japan (Session 5) p.20

(p.101)

[7] T. Yatsui, S. Sangu, T. Kawazoe, M. Ohtsu, J. Yoo, S. J. An, and G.-C. Yi, "Near-field measurement of spectral anisotropy and optical absorption of isolated ZnO nanorod single-quantum-well structures," Abstracts of The 5th Asia-Pacific Conference on Near-Field Optics, Optical Society of Japan, November 14–17, 2005, Niigata, Japan (paper number P-17) p.53

(p.103)

[8] K. Kitamura, T. Yatsui, and M. Ohtsu, "Fabrication of GaN Whiskers using Photochemical Etching for Realizing Nanophotonic Device," Abstracts of The 5th Asia-Pacific Conference on Near-Field Optics, Optical Society of Japan, November 14–17, 2005, Niigata, Japan (paper number P-19) p.55

(p.105)

[9] Y. Saito, S. Mononobe, I. Kato, M. Ohtsu, and H. Honma, "Electroless Nickel Plating under Ultrasonic Irradiation to Fabricate a Scanning Near-Field Optical Microscopy Probe," Abstracts of The 5th Asia-Pacific Conference on Near-Field Optics, Optical Society of Japan, November 14-17, 2005, Niigata, Japan (paper number P-52) p.88

(p.107)

[10] T. Kawazoe, H.Yonemitsu, and M. Ohtsu, "Nanofabrication using Nonadiabatic Near-field Photolithography," Abstracts of The 5th Asia-Pacific Conference on Near-Field Optics, Optical Society of Japan, November 14-17, 2005, Niigata, Japan (paper number P-72) p.108

(p.109)

[11] M. Naruse, T. Miyazaki, T. Kawazoe, T. Yatsui, S. Sangu, K. Kobayashi, and M. Ohtsu, "From optical near-field interaction to nanophotonic information systems," Nanophotonics for Communication: Materials and Devices II (Nibir K. Dhar, Achyut K. Dutta, Kiyoshi Asakawa Eds.), Proc. SPIE Vol. 6017, October , 2005, pp. 1–13, [Invited presentation]

(pp.111-123)

[12] G.-C. Yi, W. I. Park, J. Yoo, D.-W. Kim, T. Joo, T. Yatsui, J. Lim, and M. Ohtsu, "Photoluminescent characteristics of ZnO nanorods and ZnO/ZnMgO nanorod heterostructures," Proc. SPIE, Vol. 6013, October, 2005, pp.601301-1–601301-8 [Invited presentation]

(pp.125-132)

[13]]M. Ohtsu, "Nanophotonics:Devices,Fabrication and Systems," Proceeding of the International Symposium on Advanced Electronics for Future Generations -"Secure-Life Electronics"for Quality Life and Society-, October 11- 12, 2005, Tokyo, JAPAN (paper number479-486)

[Invited presentation]

(pp.133- 140)

[14] T. Kawazoe, T. Yatsui, and M. Ohtsu, "Nanophotonics using optical near fields," First Conference on Advances in Optical Materials, Delegate Manual, October 12- 15, 2005, Tucson, AZ, USA (paper number IS19)

(p.141)

[15] M. Ohtsu, W. Nomura and T. Yatsui, “Development of optical far-/near-field conversion device,” Proceeding of the International Symposium on Advanced Electronics for Future Generations —“Secure-Life Electronics” for Quality Life and Society—, October 11–12, 2005, Tokyo, Japan , pp.487-492

(pp.143-148)

[16] I.Kato, S.Mononobe, M.Ohtsu, and H.Honma,“Fabrication of a near-field optical probe by electroless nickel plating,”Books of abstracts “Electrochemistry for the Next Generation” September 25-30, 2005,Busan, Korea (paper number 4C-059-P) p.810

(p.149)

[17] T. Yatsui, W. Nomura, and M. Ohtsu, “Size- and position-controlled nano-scale fabrication for nanophotonic devices,” Proc. SPIE, Vol. 5927, July 31–August 4, 2005, San Diego, CA, USA, pp.59270Q-1–59270Q-8

[Invited presentation]

(pp.151-158)

[18] W. Nomura, T. Yatsui, and M. Ohtsu, “Efficient energy transfer of a nanodot coupler with resonant light scattering of metallic nanoparticles,” Proc. SPIE, Vol. 5927, July 31–August 4, 2005, San Diego, CA, USA, pp.59270B-1–59270B-8

(pp.159-166)

[III] REVIEW PAPERS

[1] M. Ohtsu, " Starting a new year realizing qualitative innovation by nanophotonics", OPTRONICS, Vol.25, No.1, January 2006, pp.143
【大津元一、「ナノフォトニクスによる質的改革の年がスタート」、OPTRONICS、第 25 巻、第 1 号、2006 年 1 月、pp.143】

(p.167)

[2] M. Ohtsu, " Fabrication of a Scanning Near-Field Optical Microscopy Probe Using Electroless Nip Plating Under Ultrasonic Irradiation", Journal of The Surface Finishing Society of Japan, Vol.56, No.12, December 2005, pp.200-203
【齋藤裕一、物部秀二、大津元一、本間英夫、「超音波照射を用いた無電解ニッケルめっきによる近接場光学プローブの作成」、表面技術、第 56 巻、第 12 号、2005 年 12 月、pp.200-203】

(pp.169-172)

[3] M. Ohtsu, " The View in the future of Nanophotonics", Engineering Materials, Vol.53, No127, December, 2005, pp.80-83
【大津元一、「ナノフォトニクスの将来展望」、工業材料、第 53 巻、第 12 号、2005 年 12 月、pp.80-83】

(pp.173-176)

[4] T. Yatsui and M. Ohtsu, "Nanophotonic device and their fabrication –Nanophotonic operation and their fabrication method using optical near-field–," O Plus E, Vol.27, No.12, November 2005, pp.1388-1392
【八井崇、大津元一、「ナノ光デバイスとその製作－近接場光特有の動作と加工技術」、O Plus E、第 27 巻、第 12 号、2005 年 12 月、pp.1388-1392】

(pp.177-181)

[IV] PUBLISHED BOOKS

[1] M. Ohtsu (ed.), *Progress in Nano-Electro-Optics V*, Springer Verlag, Berlin, 2006, (185 pages)

(pp.183-187)

[2] M. Ohtsu and K.Kobayashi, *Fandamentals of Nanophotonics,* Ohm-sha ,Tokyo May 2006, (269 pages)
【大津元一、小林潔　「ナノフォトニクスの基礎」、オーム社、2006 年 5 月、(269 ページ)】

(pp.189- 192)

[3] T. Kawazoe, M. Ohtsu (ed.), "Chapter 5 Nanophotonic devices", in *All about nanooptics and nanophotonics*, ed. By S.Kawada, Frontier Publishers, May *2006*, (pp.297-304)
【川添忠、大津元一　「第 5 章　ナノフォトニックデバイス」, 『ナノオプティクス・ナノフォトニクスのすべて』監修　河田聡、フロンティア出版、2006 年 5 月, (pp.297-304) 】

[4] T. Yatsui and M. Ohtsu, "Chapter 20 Nano-scale patterning using optical near-field,"in *Nano-scale patterning technology*, Science & Technology Co.,Ltd., Tokyo, February 2006, (pp.135-139)
【八井崇、大津元一　「第 20 章　近接場光を利用した微細加工パターニング」、『超微細パターン技術』、分担執筆、サイエンス＆テクノロジー社、2006 年 2 月、(pp.135-139)】

[V] AWARDS

[I] ORIGINAL PAPERS

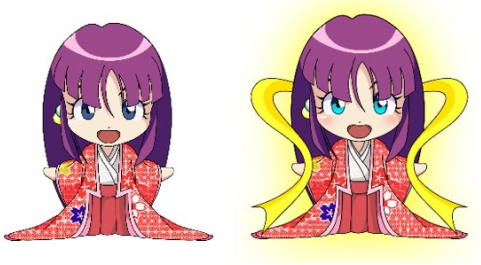

Available online at www.sciencedirect.com
SCIENCE DIRECT
Journal of Non-Crystalline Solids 352 (2006) 2492–2495
JOURNAL OF NON-CRYSTALLINE SOLIDS
www.elsevier.com/locate/jnoncrysol

Nanophotonics using optical near fields

Tadashi Kawazoe [a,*], Takashi Yatsui [a], Motoichi Ohtsu [a,b]

[a] SORST, Japan Science and Technology Agency, Tenkoh Building 17-4F, 687-1 Tsuruma, Machida, Tokyo 194-0004, Japan
[b] Department of Electronics Engineering, University of Tokyo, Bunkyo-ku, Tokyo 113-8656, Japan

Available online 18 May 2006

Abstract

This paper introduces recent successes in nanophotonics utilizing local electromagnetic interactions between a few nanometric elements (i.e., the optical near-field interaction). The sections of this paper review nanophotonic devices, nanofabrication, and systems for operating nanophotonic devices efficiently. Using CuCl quantum dots, the operations of an optical switch measuring 20-nm in size (i.e., a nanophotonic switch) and a nanometric optical condenser, which attracts optical energy into a 10-nm spot (i.e., an optical nano-fountain), were verified experimentally. The power consumption of these devices is only 1/100 000 that of conventional electronic devices. A nanodot coupler fabricated from a linear array of closely spaced metallic nanoparticles has also been introduced for transmitting an optical signal to a nanophotonic device. To increase the optical far- to near-field conversion efficiency for transmission, a surface plasmon polariton (SPP) condenser was fabricated from hemispherical metallic nanoparticles, so that it worked as a 'phased array'. The SPP can be focused with a spot size as small as 400 nm.

PACS: 42.65.Pc; 42.79.Ta; 78.70.−g; 78.67.−n; 73.20.Mf

Keywords: Optical microscopy; Nanocrystals; Quantum wells, wires and dots; Non-linear optics; Optical spectroscopy

1. Introduction

First, we present possible technical problems facing future optical technology in order to explain our motivation [1]. Optical fiber transmission systems require increased integration of photonic devices if data transmission rates are to reach 10 Tb/s by the year 2015. To support this increase, it is estimated that the size of photonic matrix switching devices should be reduced to a 100-nm scale, to integrate more than $10\,000 \times 10\,000$ input and output channels on a substrate. Since conventional photonic devices, e.g., diode lasers and optical waveguides including photonic crystals, have to confine the light wave within their cavities and core layers, respectively, their minimum sizes are limited by the diffraction of light. Therefore, they cannot meet this requirement, because the required size exceeds this diffraction limit.

Consequently, it is evident that a novel optical nanotechnology that exceeds the diffraction limit is required in order to support the optical science and technology of the 21st century. To meet this requirement, Ohtsu proposed a novel technology called nanophotonics [2]. Nanophotonics is defined as a technology that utilizes local electromagnetic interactions between a small nanometric element and an optical near field (ONF). The primary advantage of nanophotonics is the capacity to realize novel functions based on local electromagnetic interactions.

Section 2 outlines the nanophotonic devices that we have proposed. The operations of a nanophotonic switch and an optical nano-fountain are described. Section 3 reviews a surface plasmon polariton (SPP) condenser, which was fabricated from hemispherical metallic nanoparticles and works as a 'phased array'. Section 4 summarizes the main points discussed here.

* Corresponding author. Tel.: +81 42 788 6039; fax: +81 42 788 6031.
E-mail address: kawazoe@ohtsu.jst.go.jp (T. Kawazoe).

0022-3093/$ - see front matter © 2006 Elsevier B.V. All rights reserved.
doi:10.1016/j.jnoncrysol.2006.03.023

2. Nanophotonic devices

The energy transfer from smaller to larger quantum dots (QDs) has been studied in spectrally, spatially, and temporally resolved experiments. We proposed a model for the unidirectional resonant energy transfer between QDs via the ONF interaction and observed the energy transfer among randomly dispersed CuCl QDs using an ONF spectrometer [3]. The theoretical analysis and temporal evolution of the energy transfer via the ONF interaction were also discussed [4,5]. The nanophotonic devices that we proposed are realized by controlling this energy transfer [6–9].

We used cubic CuCl QDs in a NaCl matrix as the device material. For CuCl QDs, any possible energy transfer other than the ONF interaction, such as carrier tunneling and Coulomb coupling, can be neglected. To demonstrate the switching operation, we found a QD trio in the sample with effective sizes of 2.8, 3.9, and 5.6 nm, which is a size ratio close to $1:\sqrt{2}:2$, that could be used as the Input Dot, Output Dot, and Control Dot, respectively. In these cubic QDs, the quantized $(1,1,1)$ energy levels in the Input Dot, $(2,1,1)$ Output Dot, and $(2,2,2)$ Control Dot resonate with each other. Furthermore, the $(1,1,1)$ energy levels in the Output Dot and $(2,1,1)$ in the Control Dot also resonate. When the separations of the QDs are between 1 and 30 nm, resonant near-field energy transfer occurs between the QDs before the carriers recombine in the QDs [3]. For separations less than 1 nm, the quantized states in the QDs are coupled and change even before excitation, and no energy transfer between spatially individual QDs occurs, while the excitation energy relaxes among the coupled states in the coupled system. Fig. 1 shows the experimental setup and energy diagram of a QD trio and the excitation lasers. In the experiment, second harmonic generation (SHG) of Ti:sapphire lasers ($\lambda = 379.5$ nm and $\lambda = 385$ nm), which were tuned to the $(1,1,1)$ exciton energy levels in the Input Dot and Control Dot, respectively, were used as the input and control light sources. A fiber probe collected the output signal, and its intensity was measured using a cooled micro-channel plate after passing through three 1-nm bandwidth interference filters tuned to the $(1,1,1)$ exciton energy level in the Output Dot at $\lambda = 383$ nm.

Fig. 2(a) and (b) shows the spatial distribution of the output signal intensity in the OFF and ON states, using near-field spectroscopy at 15 K. The two-dimensional

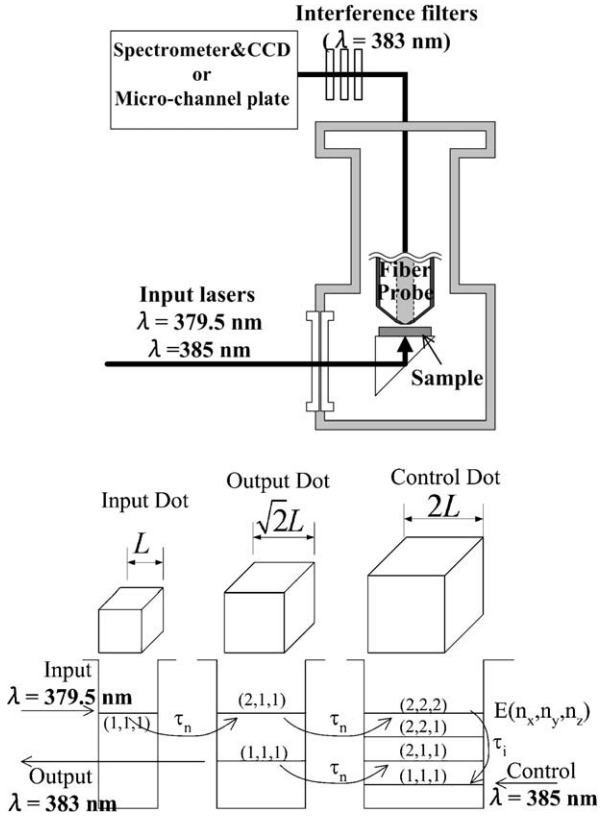

Fig. 1. The experimental setup and energy diagram of the QD trio and excitation lasers.

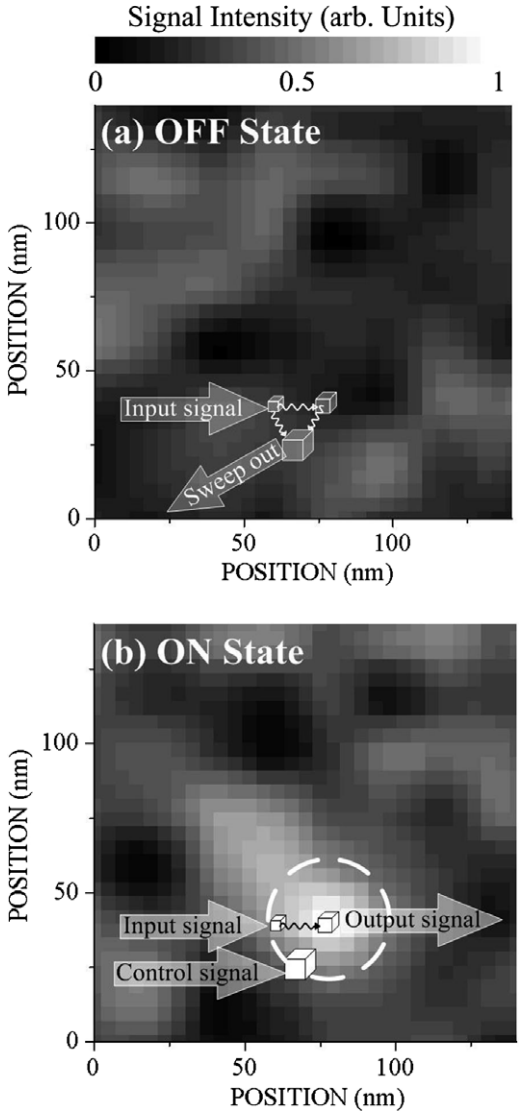

Fig. 2. The spatial distribution of the output signal from the nanophotonic switch measured using a near-field microscope in the OFF (a) and ON (b) states.

intensity distributions were obtained by scanning the fiber probe. The spatial resolution of 20-nm was estimated from the experimental results. The insets in Fig. 2 are schematic drawings of the existing QD trio used for switching, which was confirmed by the near-field luminescence spectrum. In the OFF state, no output signal was observed, because the energy of the input signal was transferred to the Control Dot and swept out as luminescence at 385 nm. In the ON state, we obtained a clear output signal in the broken circle.

The advantages of this nanophotonic switch are its small size and high-density integration capability based on the locality of the ONF. The figure of merit (FOM) of an optical switch should be more important than the switching speed. Here, we define the FOM as $F = C/(V \cdot t_{sw} \cdot P_{sw})$, where C, V, t_{sw}, and P_{sw} are the ON–OFF ratio, volume of the switch, switching time, and switching energy, respectively. The FOM of our switch is more than 10 times higher than that of a conventional photonic switch, because its volume and switching energy are 10^{-5} times and 10^{-3} times smaller, respectively. The power consumption of these devices, which generates heat, is only 1/100 000 that of conventional electronic devices, because only the sublevel transition generates heat, which is less than 30 meV/cycle at room temperature. We consider this ultra-low heat generation to be one of the most important advantages of our nanophotonic device.

As we and other research groups have reported, the principle of the energy transfer among QDs is equivalent to that of a light-harvesting photosynthetic system, which concentrates and harvests optical energy in nanometric photosynthetic systems. The optical energy concentrator 'optical nano-fountain' that we proposed operates in the same manner as a light-harvesting system.

When different sized QDs with resonant energy sublevels are distributed as shown in Fig. 3(a), energy transfer occurs via the ONF, as illustrated by the arrows. Light incident to the QD array is ultimately concentrated in the largest QD. The size of the area of light concentration corresponds to that of the QD. Therefore, this device realizes nanometric optical concentration. Since the mechanism of the optical nano-fountain is similar to that of the light-trapping system in photosynthetic bacteria, the operation of the optical nano-fountain is a biomimetic action. The device proposed here is called an 'optical nano-fountain' because light spurts from the largest QD after it has been concentrated by stepwise energy transfer from smaller neighboring QDs. In action, the device looks like a fountain in a basin.

For operation, we maintained a sample at the optimum temperature of 40 K, at which the inhomogeneous linewidth of the energy levels in the QDs exceeds 1 meV. Therefore, the resonant condition between the QDs is looser and the possibility of energy transfer increases. By contrast, at temperatures above 40 K, the probability of energy transfer decreases with the back-transfer resulting from thermal excitation. A 325-nm He–Cd laser was used as the excitation light source. Fig. 3(b) shows the typical spatial distribution of the luminescence emitted from

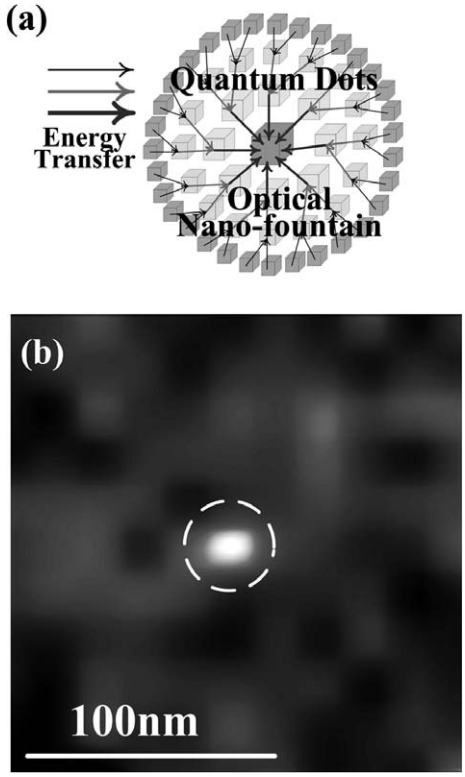

Fig. 3. (a) A schematic explanation of the optical nano-fountain and unidirectional energy transfer. (b) The spatial distribution of the luminescence intensity in an optical nano-fountain. The bright spot surrounded by a broken circle is the focal spot.

QDs that operate as an optical nano-fountain. Here, the collected luminescence photon energy, E_p, was $3.215\ \text{eV} \leqslant E_p \leqslant 3.350\ \text{eV}$, which corresponds to the luminescence from QDs of size $2.5\ \text{nm} \leqslant L \leqslant 10\ \text{nm}$. The bright spot inside the broken circle corresponds to a spurt from an optical nano-fountain, i.e., the focal spot of the nanometric optical condensing device. The diameter of the focal spot was less than 20 nm, which was limited by the spatial resolution of the near-field spectrometer. From the Rayleigh criterion (i.e., resolution $= 0.61 \cdot \lambda/\text{NA}$), we obtained a numerical aperture (NA) of 12 for $\lambda = 385$ nm.

3. A surface plasmon-polariton condenser

Fig. 4(a) and (b) shows scanning electron microscopic (SEM) images of the SPP condenser and nanodot coupler. The nanodot coupler consisted of a linear array of nanoparticles with diameters of 230 nm separated by 70 nm. The SPP condenser consisted of twelve scatterers 700 nm in diameter, aligned on an arc with a diameter of 10 μm.

The spatial distribution of the optical near-field energy was observed using a collection mode near-field optical microscope. A light source with a wavelength of $\lambda =$ 785 nm was used. First, we checked whether the SPP condenser led to efficient scattering and resultant focusing of the SPP by exciting the SPP mode through the grating coupler. Fig. 4(c) and (d) shows a shear-force image of the SPP

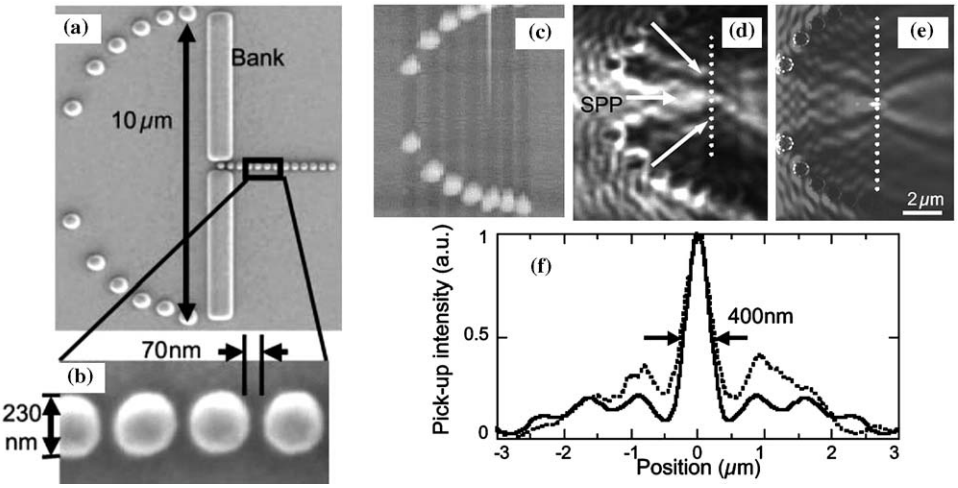

Fig. 4. (a, b) SEM images of the fabricated nanodot coupler and SPP condenser. (c) Shear-force image of the SPP condenser. (d) The near-field energy distribution of (a) taken at $\lambda = 785$ nm. (e) The calculated spatial distribution of the electric-field energy using the FDTD method. The dashed and solid curves in (f) are cross-sectional profiles along the dashed white lines in (d) and (e), respectively.

condenser and the spatial distribution of the optical near-field energy, respectively. As shown in the cross-sectional profile (dashed curve in Fig. 4(f)) through the focal point of the SPP (white dotted line in Fig. 4(d)), the full width at half maximum (FWHM) of the spatial distribution of the SPP was as narrow as 400 nm. Fig. 4(f) shows the spatial distribution of the optical near-field energy in the SPP condenser calculated using the finite difference time domain (FDTD) method. These results imply that our device works as an efficient phased array.

4. Conclusion

An optical near field generated on a nanometric element is free from the diffraction of light and enables the operation and integration of nanometric optical devices. Using the localized optical near field as the signal carrier, which is transmitted from one nanometric element to another, a nanoscale photonic device exceeding the diffraction limit can be realized. The primary advantage of nanophotonics is its capacity to achieve novel functions that are based on local electromagnetic interactions, while realizing nanometer-sized photonic devices. Based on this idea, we introduced a nanometric switch, an optical nano-fountain, and a surface plasmon-polariton condenser in this paper. We also demonstrated these unique devices using an optical near field. In the nanophotonic device, the optical near field is used as a carrier to transmit the signal. Owing to their high spatial density and low power dissipation, nanophotonic devices will play important roles in future photonic systems.

References

[1] M. Ohtsu, K. Kobayashi, T. Kawazoe, S. Sangu, T. Yatsui, IEEE J. Sel. Top. Quant. Electron 8 (2002) 839.
[2] M. Ohtsu, in: Tech. Dig. 18th Congr. Int. Commission for Optics, 1999, SPIE, 3749, 1999, 478.
[3] T. Kawazoe, K. Kobayashi, J. Lim, Y. Narita, M. Ohtsu, Phys. Rev. Lett. 88 (2002) 067404.
[4] S. Sangu, K. Kobayashi, A. Shojiguchi, T. Kawazoe, M. Ohtsu, J. Appl. Phys. 93 (2003) 2937.
[5] K. Kobayashi, S. Sangu, T. Kawazoe, M. Ohtsu, J. Lumin. 112 (2005) 117.
[6] T. Kawazoe, K. Kobayashi, S. Sangu, M. Ohtsu, J. Microsc. 209 (2003) 261.
[7] T. Kawazoe, K. Kobayashi, S. Sangu, M. Ohtsu, Appl. Phys. Lett. 82 (2003) 2957.
[8] T. Kawazoe, K. Kobayashi, M. Ohtsu, Appl. Phys. Lett. 86 (2005) 103102.
[9] W. Nomura, M. Ohtsu, T. Yatsui, Appl. Phys. Lett. 86 (2005) 181108.

Appl. Phys. B 84, 243–246 (2006)
DOI: 10.1007/s00340-006-2234-x

Applied Physics B
Lasers and Optics

T. KAWAZOE[1,✉]
K. KOBAYASHI[2]
K. AKAHANE[3]
M. NARUSE[3]
N. YAMAMOTO[3]
M. OHTSU[1,4]

Demonstration of nanophotonic NOT gate using near-field optically coupled quantum dots

[1] Japan Science and Technology Agency, Machida, Tokyo 194-0004, Japan
[2] Department of Physics, Tokyo Institute of Technology, Meguro-ku, Tokyo 152-8551, Japan
[3] National Institute of Information and Communications Technology, Koganei, Tokyo 184-8795, Japan
[4] Department of Electronics Engineering, University of Tokyo, Bunkyo-ku, Tokyo 113-8656, Japan

Received: 31 December 2005
Published online: 3 May 2006 • © Springer-Verlag 2006

ABSTRACT We propose and demonstrate the operation of a nanometric optical NOT gate using CuCl quantum dots coupled via an optical near-field interaction. The device was smaller than 20 nm and its repeated operation was verified. The operating energy of this device was much lower than that of a conventional photonic device. We also introduce all-optical NAND and NOR gates using coupled quantum dots. Toward an actual nanophotonic device, we discuss the possibility of coupled InAlAs quantum dots. A double layer of InAlAs quantum dots for nanophotonic device operation was prepared using molecular beam epitaxial growth. We obtained a near-field spectroscopy signal, indicating that the InAlAs quantum dots coupled with the optical near field acted as a NOT gate. The experimental results show that the sample has great potential as an actual nanophotonic device.

PACS 78.67.Hc; 07.79.Fc; 42.79.Ta

1 Introduction

It is felt that the size of photonic switching devices should be reduced to a sub-wavelength scale in the next 10 years [1]. As conventional photonic devices have to confine light waves within their cavities or core layers, their minimum sizes are limited by the diffraction limit, and they cannot meet a size requirement beyond the diffraction limit. It is readily apparent that a novel optical nanotechnology, such as nanophotonics, is required in order to surpass the diffraction limit.

The optical near field generated on a nanometric element is free from the diffraction of light and enables the operation and integration of nanometric optical devices, i.e. nanophotonic devices. The above requirements can be met in nanophotonic devices by using a localized optical near field as the carrier, which is transmitted from one nanometric element to another. Based on this idea, we have proposed unique optical nanotechnology that uses the optical near field. So far, we have observed the optically forbidden energy transfer between CuCl quantum dots via an optical near field [2] and proposed several nanometric optical devices, including a nanometric AND gate [3, 4], a surface plasmon–polariton condenser [5], a nanometric XOR logic gate [6], and a nanometric optical condenser (optical nanofountain) [7].

Experimental demonstrations of the operation of these devices, e.g. the AND gate, surface plasmon–polariton condenser, and optical nanofountain, have already been reported. Since a nanophotonic NOT gate is a key device for realizing a functionally complete set of logic gates for nanophotonic systems, we have been researching its operation using a coupled quantum-dot system. In this paper, we propose a nanometric optical NOT gate and demonstrate its operation using CuCl quantum dots. For actual use, we prepared InAlAs quantum dots and discuss a NOT gate using them in order to avoid the weakness of CuCl quantum dots. Finally, the experimental results of NOT-gate operation using the coupled InAlAs quantum dots are presented, which show the promise of InAlAs quantum dots acting as an actual nanophotonic device.

2 Principle of nanophotonic NOT gate

In cubic CuCl quantum dots, the energy eigenvalue of an exciton is given by

$$E_{n_x,n_y,n_z} = E_{\mathrm{B}} + \frac{\hbar^2\pi^2}{2M(L-a_{\mathrm{B}})^2}(n_x^2+n_y^2+n_z^2)\,,$$

where E_{B} is the bulk Z_3 exciton energy, M is the translational mass of the exciton, a_{B} is its Bohr radius, n_x, n_y, and n_z are a set of quantum numbers ($n_x, n_y, n_z = 1, 2, 3, ...$), and $d = L - a_{\mathrm{B}}$ corresponds to the effective side length after considering the dead layer correction [8]. Figure 1 shows a schematic explanation of our nanophotonic NOT gate. $\mathrm{QD_{IN}}$ and $\mathrm{QD_{OUT}}$ correspond to the input and output terminals of the NOT gate, respectively. Assuming a pair of quantum dots with a size ratio of $1+\alpha/\sqrt{2}$ ($\alpha \ll 1$), the quantized energy levels with the set of quantum numbers (2, 1, 1) in $\mathrm{QD_{IN}}$ and (1, 1, 1) in $\mathrm{QD_{OUT}}$ are not resonant with each other. However, they can be made nearly resonant by adjusting the size ratio. The energy from the optical power supply generates an exciton in $\mathrm{QD_{OUT}}$. Without the input signal, the exciton in $\mathrm{QD_{OUT}}$ disappears and emits a photon, which is observed as an output signal, as shown in Fig. 1a (In = 0 and Out = 1). Conversely, by applying the input signal, the energy level (2, 1, 1) in $\mathrm{QD_{IN}}$ becomes resonant to (1, 1, 1) in $\mathrm{QD_{OUT}}$ due to broadening

✉ Fax: +81-42-788-6031, E-mail: kawazoe@ohtsu.jst.go.jp

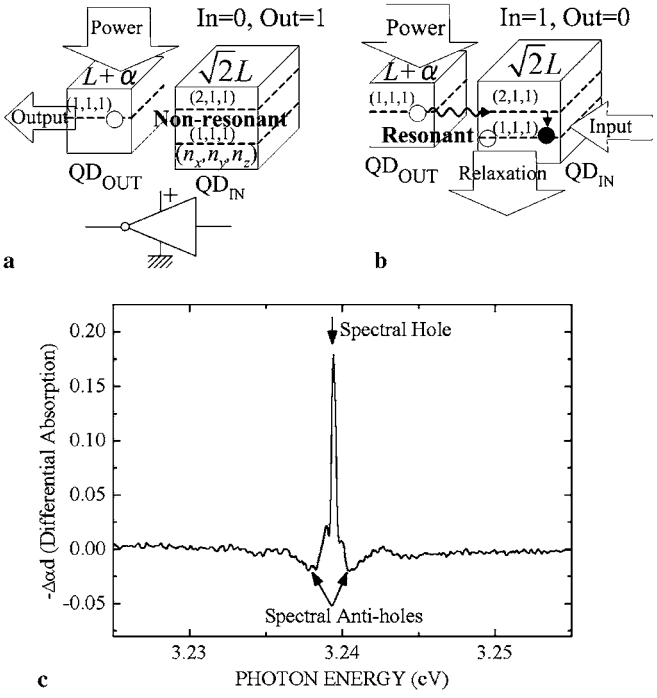

FIGURE 1 (**a**), (**b**) Schematic explanation of the operation of a nanophotonic NOT gate using cubic quantum dots. (**c**) The experimental result of hole burning for CuCl quantum dots embedded in a NaCl matrix at 5 K

of its line width. This broadening was confirmed experimentally for CuCl quantum dots. Figure 1c shows the spectral hole in the absorption spectrum of CuCl quantum dots observed in a far-field hole-burning experiment at 5 K; anti-holes appear on both sides of the spectral hole. This experimental result shows that the excitation broadens the homogeneous line width of quantum dots. This broadening might arise from shortening of the phase-relaxation time of the excitons in quantum dots, due to carrier–carrier scattering. Consequently, the exciton energy in QD_{OUT} is transferred to QD_{IN} via an optical near-field interaction [2], which suppresses output-signal generation (Fig. 1b; In = 1 and Out = 0). As a result, an output signal with temporal behavior that is the inverse of that of the input signal is obtained. These operations correspond to a NOT gate.

3 Demonstration of a nanophotonic NOT gate

3.1 *A nanophotonic NOT gate using CuCl quantum dots*

We used CuCl quantum dots embedded in a NaCl matrix to verify operation of the NOT gate, as CuCl quantum dots offer discrete energy levels similar to the exciton described in Fig. 1 [8]. The mean size of the quantum dots was 4.1 nm and the mean distance between the quantum dots was 25 nm. In the experiment, the second-harmonic generation (SHG) of a continuous-wave (cw) Ti:sapphire laser ($h\nu = 3.2704$ eV) and the SHG of a mode-locked Ti:sapphire laser ($h\nu = 3.2195$ eV) were used as the optical power supply and the input-signal pulse, respectively. The respective power densities of the optical power supply and input signal were 1 and 2 W/cm^2 at the sample surface. In the excitation condition, there were fewer than 0.1 excitons in a quantum

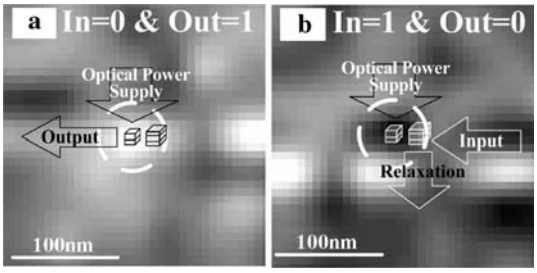

FIGURE 2 The spatial distribution of the output signal from a nanophotonic NOT gate measured using a near-field microscope at Input = 0 (**a**) and Input = 1 (**b**)

dot. This laser light excited the sample from its back and the output signal was observed in the collection-mode operation of a near-field microscope. The sample temperature was controlled at 15 K. In order to find the quantum-dot pair acting as a nanophotonic NOT gate, we mapped the quantum-dot positions by measuring the luminescence distribution on the sample, which was obtained using a near-field spectrometer using He-Cd laser excitation ($h\nu = 3.81$ eV). After several quantum-dot pairs were selected as candidates for nanophotonic NOT-gate operation, we tried to observe the operation signal. Finally, we found a nanophotonic NOT gate and the probability of obtaining a nanophotonic NOT gate was about one device per 1 μm^2 of scanning area. Figure 2a shows the spatial distribution of the optical near-field output-signal intensity without an input signal, i.e. with the optical power supply only. Figure 2b shows the distribution with an input-signal pulse. These images were acquired using a near-field optical spectrometer in one area of the sample. The insets in Fig. 3 are schematic drawings of an existing quantum-dot pair for NOT-gate operation, which was confirmed from the luminescence spectra. The sizes of the two quantum dots, estimated from the wavelengths of their luminescence, were 5.0 and 6.3 nm, which satisfy the NOT gate operation condition, as shown in Fig. 1. Note that the photon energy of the optical power supply ($h\nu = 3.2704$ eV) is not resonant to the (1, 1, 1) exciton level in the 5.0-nm quantum dot ($h\nu = 3.2304$ eV) in order to decrease the artifact of the laser by using narrow-band optical filters and observe the output signal clearly. The optical power was supplied to the 5.0-nm quantum dot from neighboring quantum dots, which were smaller [2, 7]. The NOT-gated sig-

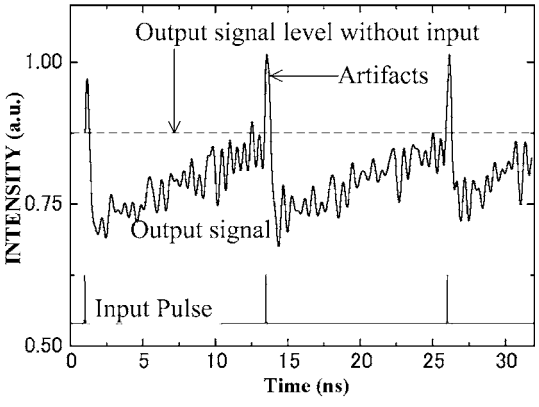

FIGURE 3 The temporal evolution of the output (*upper*) and input (*lower*) pulse signals from and to the nanophotonic NOT gate *circled* in Fig. 2a

nal appeared at the center of the broken circles in Fig. 2, from which the size of the device was estimated to be 20 nm.

The dynamic behavior of the NOT gate was evaluated using the time correlation single photon counting method. Figure 3 shows the temporal evolution of the output signal. The horizontal broken line shows the output-signal level without the input-signal pulses. Without the input pulses, the output-signal level is constant, since a cw laser was used as the optical power supply. With the input pulses, the output signal rises within a time period shorter than the time resolution of 20 ps due to the artifact of the input pulses, and it decreases to a level lower than the initial level. The fall time of the output signal is about 100 ps, which corresponds to the energy-transfer time between quantum dots. The output signal recovers to the level of the broken line within 10 ns. The recovery time is longer than the exciton lifetime in 6.3-nm CuCl quantum dots ($\tau_1 \sim 1$ ns), because the energy transfer from the optical power supply disturbs the recovery. Namely, the recovery time depends on the competition between the exciton lifetime and the energy-transfer time.

The experiment verified that a NOT gate using CuCl quantum dots can operate at a 80-MHz repetition frequency, which is not fast as a photonic device. However, the advantages of this nanophotonic NOT gate are its small size and low power consumption. We estimated that the switching energy of this device was about five orders of magnitude smaller than that of a conventional electronic gate [3].

3.2 *A nanophotonic NOT gate using InAlAs quantum dots*

CuCl quantum dots embedded in a NaCl matrix have the potential to form an optical near-field coupled system [2, 8–10]. However, CuCl is unsuitable for an actual device owing to its chemical instability and the low controllability of dot size and position. Therefore, we attempted to construct actual nanophotonic devices using III-V compound semiconductors. Of the III-V semiconductors, InAlAs is one of the best materials for our purpose. Its band-gap energy can be controlled widely from 0.3 to 2.2 eV and it is easy to prepare samples with a high density of quantum dots. As the first step, we prepared $In_{0.5}Al_{0.5}As$ quantum dots using molecular beam epitaxy (MBE) in S-K mode growth [11] to make the band-gap energy exceed 1.6 eV, at which standard photodetectors have high sensitivity. Figure 4a shows the sample structures and an atomic force microscope (AFM) image after the growth of quantum-dot layers. To operate the nanophotonic device, double-quantum-dot layers were grown. The mean quantum-dot size was 5-nm high and 25 nm in diameter. Using this fabrication method, the quantum dots could be aligned vertically and the sheet density of quantum dots was 10^{11} cm^{-2}. Therefore, both the vertical and horizontal distances between quantum dots were about 30 nm, and vertical and horizontal coupling of quantum dots was expected via the optical near-field interactions.

To investigate the suitability of the fabricated sample as a nanophotonic device, we measured the far- and near-field luminescence spectra. In Fig. 4b, the broken curve shows the far-field luminescence spectrum at 12 K. The luminescence around 1.8 eV comes from the $In_{0.5}Al_{0.5}As$ quantum dots that were broadened owing to their size inhomogeneity. The solid

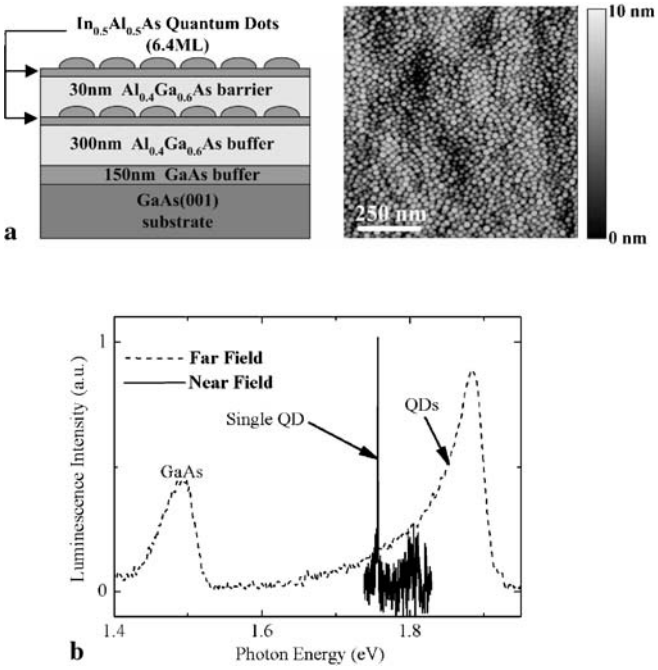

FIGURE 4 (**a**) The structures of InAlAs quantum dots and an atomic force microscope (AFM) image after the growth of quantum-dot layers. (**b**) Far-field (*broken curve*) and near-field (*solid curve*) luminescence spectra of InAlAs quantum dots

curve shows the typical near-field luminescence spectrum at 11 K. For near-field spectroscopy, we used a He-Ne laser ($h\nu = 1.958$ eV) and obtained a luminescence peak from a single quantum dot at 1.7569 eV in illumination–collection mode operation. The spectral line width (FWHM) was less than 500 μeV; it was free from size inhomogeneity and limited by the spectral resolution of the spectrometer. This narrowness of luminescence indicates that the sample was of high quality.

Figure 5 shows the near-field luminescence spectra at different positions on the sample surface. The insets show the intensity distributions of the respective luminescence peaks

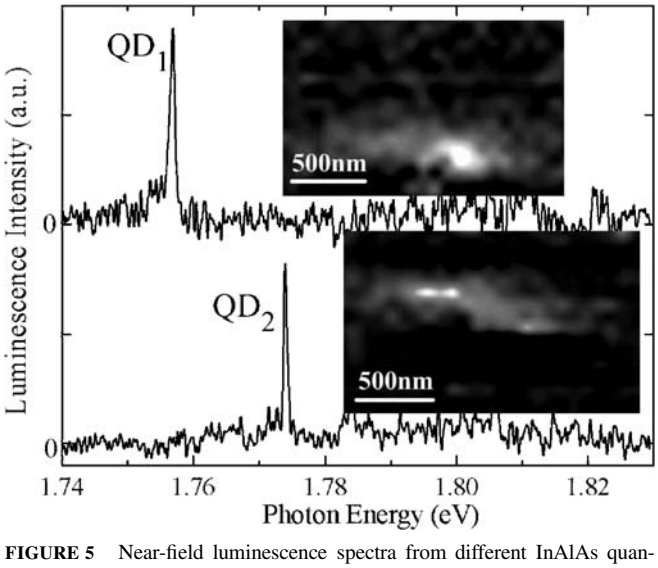

FIGURE 5 Near-field luminescence spectra from different InAlAs quantum dots at different positions. The *insets* show the luminescence intensity distributions on the sample surface

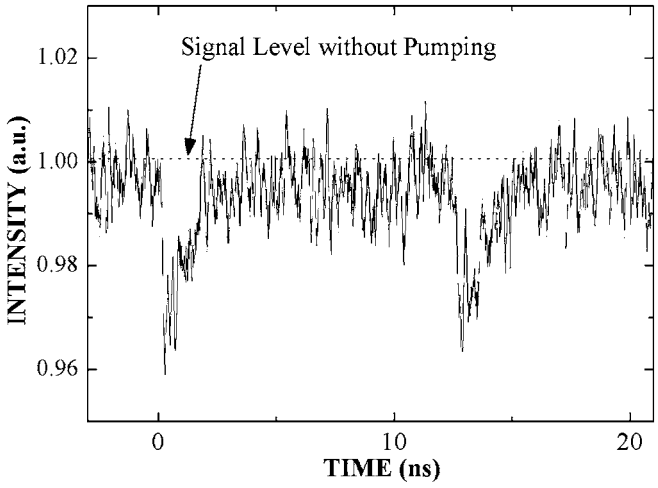

FIGURE 6 Temporal evolution of the output signals from the InAlAs quantum dots acting as a nanophotonic NOT gate

QD_1 and QD_2. As their photon energies and intensity distributions differed, the luminescence peaks QD_1 and QD_2 came from different quantum dots. In this way, we confirmed the existence of several quantum dots within an area of 1 μm^2. The observed density of quantum dots was much lower than the density of the quantum dots measured using AFM. We postulate that energy transfer to the non-radiative relaxation path in the surface quantum-dot layer and non-radiative energy dissipation caused the low quantum-dot density measured using near-field spectroscopy. The luminescence efficiency of quantum dots without a cap layer is very low due to non-radiative recombination [12]. When horizontal and vertical energy transfers to the top quantum-dot layer without a cap layer occur, most of the quantum dots dissipate the excitation energy non-radiatively. This supports the postulate that the sample acted as the desired nanophotonic device, because the energy transfer is necessary for the operation of the nanophotonic device.

Figure 6 shows the temporal evolution of the signal obtained from the InAlAs quantum dots. In the measurement, we adjusted the probe position to the bright region on the sample surface, i.e. the bright spot shown in Fig. 5, and the bright region was excited using a cw He-Ne laser ($h\nu = 1.958$ eV) and a mode-locked Ti:sapphire laser ($h\nu = 1.722$ eV). The photon energy of the luminescence collected using a spectral filter was 1.745–1.796 eV. The output signal decreased synchronously with the excitation pulse of the mode-locked laser and recovered to the signal level without pumping. Specifically, the observed quantum dots acted as a NOT gate. Here, we explain one of the possible mechanisms of this NOT-gate operation observed in the double-layer InAlAs quantum dots. With the cw laser only, part of the scanning region is bright because most of the excitation energy is dissipated via non-radiative relaxation after the energy transfer between quantum dots. Part of the excitation energy can reach the radiative quantum dots. With the cw and mode-locked lasers, the energy-transfer paths to the radiative quantum dots disappear, because other relaxation paths to the non-radiative quantum dots are generated due to spectral broadening by the mode-locked laser pulses. Carrier tunneling and Coulomb coupling are other possible interactions. In order to determine the exact mechanism, more investigations are necessary. In the experimental NOT-gate operation using InAlAs quantum dots, the two-dimensional scanning image was not clear, due to the weak signal intensity of the NOT gate.

4 Conclusion

We demonstrated the operation of a nanometric optical NOT gate with a device size of 20 nm using CuCl quantum dots. This device utilizes the resonant optical near-field energy transfer between quantum dots. For an actual nanophotonic integrated device, we fabricated a double layer of InAlAs quantum dots and observed the luminescence of a single quantum dot. Finally, we demonstrated operation of the NOT gate using InAlAs quantum dots. We believe that quantum dots of III-V materials are suitable for nanophotonic devices using the optical near field, due to the other coupling interactions between quantum dots, such as carrier tunneling, Coulomb coupling, and spin interaction.

REFERENCES

1 M. Ohtsu, K. Kobayashi, T. Kawazoe, S. Sangu, T. Yatsui, IEEE J. Sel. Top. Quantum Electron. **8**, 839 (2002)
2 T. Kawazoe, K. Kobayashi, J. Lim, Y. Narita, M. Ohtsu, Phys. Rev. Lett. **88**, 067 404 (2002)
3 T. Kawazoe, K. Kobayashi, S. Sangu, M. Ohtsu, Appl. Phys. Lett. **82**, 2957 (2003)
4 T. Kawazoe, K. Kobayashi, S. Sangu, M. Ohtsu, J. Microsc. **210**, 247 (2003)
5 W. Nomura, T. Yatsui, M. Ohtsu, Appl. Phys. Lett. **86**, 181 108 (2005)
6 S. Sangu, K. Kobayashi, A. Shojiguchi, M. Ohtsu, Phys. Rev. B **69**, 115 334 (2004)
7 T. Kawazoe, K. Kobayashi, M. Ohtsu, Appl. Phys. Lett. **86**, 103 102 (2005)
8 N. Sakakura, Y. Masumoto, Phys. Rev. B **56**, 4051 (1997)
9 A.I. Ekimov, Al.L. Eflos, A.A. Onushchenko, Solid State Commun. **56**, 921 (1985)
10 T. Itoh, S. Yano, N. Katagiri, Y. Iwabuchi, C. Gourdon, A.I. Ekimov, J. Luminesc. **60–61**, 396 (1994)
11 L. Goldstein, F. Glas, J.Y. Marzin, M.N. Charasse, G. Le Roux, Appl. Phys. Lett. **47**, 1099 (1985)
12 H. Saito, K. Nishi, S. Sugou, Appl. Phys. Lett. **73**, 2742 (1998)

Appl. Phys. B 84, 257–259 (2006)
DOI: 10.1007/s00340-006-2165-6

Applied Physics B
Lasers and Optics

W. NOMURA[1,✉]
T. YATSUI[2]
M. OHTSU[1,2]

Efficient optical near-field energy transfer along an Au nanodot coupler with size-dependent resonance

[1] School of Engineering, The University of Tokyo, 7-3-1 Hongo, Bunkyo-ku, Tokyo, 113-8656, Japan
[2] Solution-Oriented Research for Science and Technology (SORST), Japan Science and Technology Agency, 687-1 Tsuruma, Machida, Tokyo, 194-0004, Japan

Received: 15 December 2005
Published online: 17 March 2006 • © Springer-Verlag 2006

ABSTRACT We confirmed that the light intensity ($\lambda = 785$ nm) scattered from an isolated hemispherical Au nanoparticle was resonantly enhanced at a diameter of 200 nm and a height of 50 nm, as observed experimentally using a collection-mode near-field optical microscope. The experimental results agreed with the calculated results using Mie's theory. Furthermore, we observed resonant energy transfer of the optical near-field energy along a chain of Au nanoparticles. The magnitude of the transferred energy increased resonantly at the size of resonant light scattering for an isolated Au nanoparticle (200 nm diameter with 240 nm center-to-center separation).

PACS 42.82.Et; 73.20.Mf; 78.67.Bf

1 Introduction

Future optical transmission and data processing systems will require advanced photonic devices, as well as their integration, in order to increase data processing rates and capacity. Consequently, these devices will have to be significantly smaller than conventional diffraction-limited photonic devices. To meet this requirement, we have proposed nanometer-scale photonic integrated circuits (nanophotonic ICs) that are composed of nanometer-sized elemental devices (nanophotonic devices) [1]. As representative devices, a nanophotonic switch, an optical nanofountain, and a nanophotonic not-gate were proposed and their operations were demonstrated by controlling the dipole forbidden optical energy transfer among resonant energy states in CuCl quantum cubes via an optical near-field [2, 3]. To fabricate nanophotonic devices, we also developed a near-field optical chemical-vapor deposition technique and self-assembly with nanometer-scale resolution and accuracy in size, position, and separation [4–7]. Theoretical studies of these novel devices and fabrications have also been carried out [8, 9].

For use in future photonic systems, the nanophotonic devices and ICs must be connected to conventional diffraction-limited photonic devices. This connection requires a far/near-field conversion device, such as a nanometer-scale optical waveguide. As such a conversion device, we have already reported a nanodot coupler that consists of a closely spaced metallic nanoparticle chain [10]. We fabricated a linearly aligned Au nanodot coupler and confirmed that the nanodot coupler has a transmission length more than three times longer than that of a metallic core waveguide with the same width of 230 nm at a wavelength of $\lambda = 785$ nm. Furthermore, we confirmed that the zigzag-shaped nanodot coupler has sufficiently low transmission loss at the corner, owing to the efficient coupling of transverse magnetic (TM) and transverse electric (TE) modes through the nanodot coupler (Fig. 1).

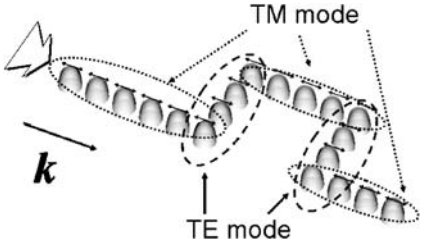

FIGURE 1 Schematic of a zigzag-shaped nanodot coupler

Since a metallic nanoparticle has resonant light scattering due to plasmon resonance [11], we examined the size dependence of Au nanoparticles in this study in order to increase the efficiency of the nanodot coupler. Based on the results, we optimized the efficiency of optical near-field energy transmission along a chain of Au nanoparticles.

2 Experimental

First, in order to check whether Au nanoparticles led to efficient scattering, we fabricated isolated Au nanoparticles using the following three steps:

(i) A 50-nm-thick Au film was deposited on SiO_2 substrate using sputtering (Fig. 2a).
(ii) Carbon hemispheres were deposited on the Au film using a focused ion beam (FIB) (Fig. 2b).
(iii) By irradiating the carbon on the Au film with Ga ions, the shape of the carbon was transferred to Au (FIB milling technique) (Fig. 2c).

Figure 2d shows a scanning electron microscopy (SEM) image of hemispherical Au nanoparticles. They were arranged with sufficiently longer separation in relation to each

✉ Fax: +81-42-788-6031,
E-mail: nomura@nanophotonics.t.u-tokyo.ac.jp

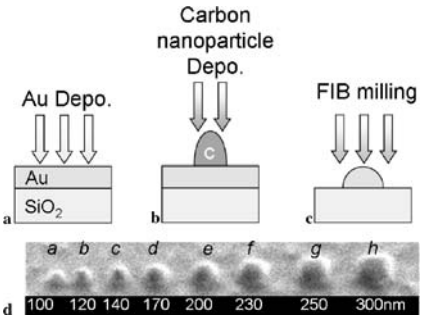

FIGURE 2 (**a**)–(**c**) Cross-sectional images of the fabrication of Au nanoparticles. (**a**) Sputtering Au film (step (i)). (**b**) Carbon nanoparticle deposition using FIB (step (ii)). (**c**) Au film milling using FIB (step (iii)). (**d**) SEM image of the fabricated Au nanoparticles

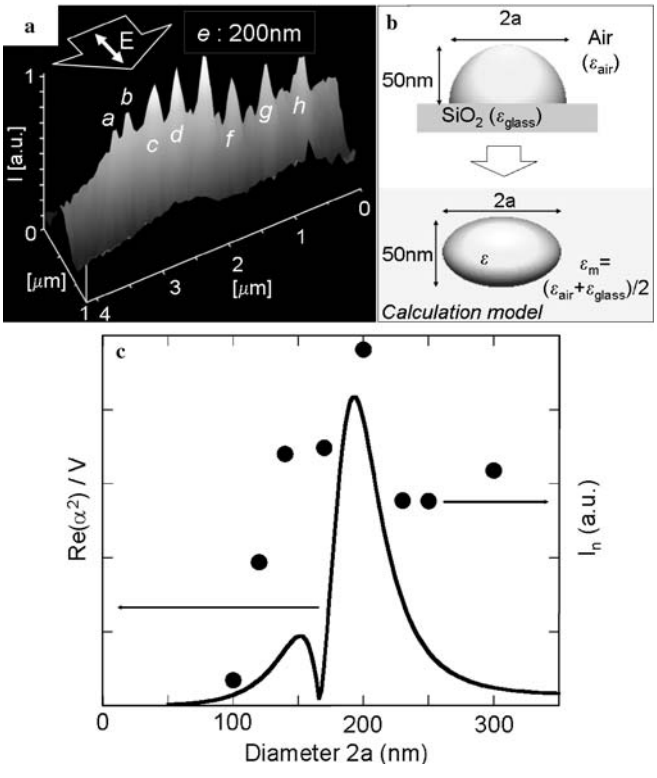

FIGURE 3 (**a**) C-mode NOM image of the scattered light intensity distribution from individual Au nanoparticles. (**b**) Schematic image of the model used for Mie's theory of resonant light scattering. (**c**) Calculated polarizability (*solid curve*) and peak intensity (I_n) obtained at each nanoparticle (*closed circles*)

diameter so that no Au nanoparticle coupled with the neighboring nanoparticles via the optical near-field.

The spatial distribution of the optical near-field intensity at isolated Au nanoparticles in the $2a$ diameter range from 100 to 300 nm was observed using a collection-mode near-field optical microscope (C-mode NOM) at $\lambda = 785$ nm. Figure 3a shows the observed results, in which the optical near-field intensity (I) resonantly takes the maximum for the Au nanoparticle 200 nm in diameter (labelled *e*). In order to find the origin of this size-dependent resonance, we made a calculation based on Mie's scattering theory, in which only the lowest TM mode was considered [12]. A hemispherical Au on SiO_2 substrate was approximated as an oblate spheroid buried in a medium whose dielectric constant (ε_m) is an arithmetic

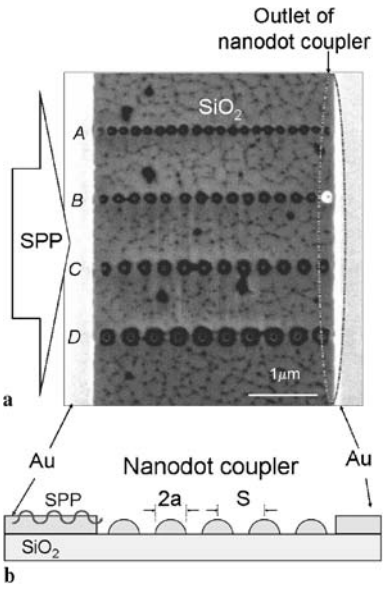

FIGURE 4 (**a**) SEM images of Au nanodot couplers. The diameters of the Au nanoparticles are A: 150, B: 200, C: 250, and D: 300 nm. (**b**) Schematic of a cross-section of the Au nanodot coupler along the *dashed white line* in (**a**)

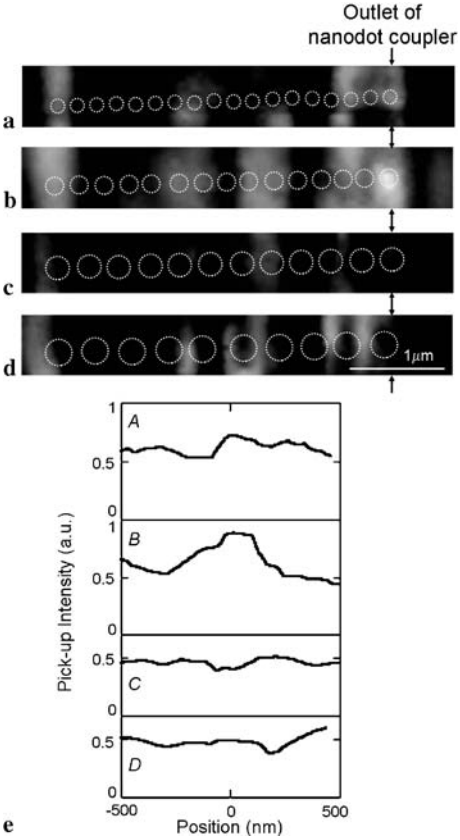

FIGURE 5 C-mode NOM images of nanodot couplers with respective diameters of (**a**) 150, (**b**) 200, (**c**) 250, and (**d**) 300 nm (A–D, respectively). The *white dashed circles* in (**a**)–(**d**) represent the positions of Au nanoparticles. (**e**) Cross-sectional profiles of the detected intensity along the two *arrows* in (**a**)–(**d**)

mean of those of SiO_2 (ε_{glass}) and vacuum (ε_{air}): $\varepsilon_m = (2.25 + 1)/2 = 1.68$ (see Fig. 3b). The solid curve in Fig. 3c represents the real part of the normalized polarizability $\mathrm{Re}(\alpha^2)/V$ (α = polarizability, V = the volume of an Au nanoparticle)

as a function of the diameter $2a$ of the Au oblate spheroid whose short axis was fixed at 50 nm. The closed circles in Fig. 3c show the normalized peak intensity (I_n) experimentally measured for each nanoparticle. Both the solid curve and closed circles exhibit size-dependent resonance, and the calculated resonant diameter (190 nm) is in good agreement with the experimentally confirmed particle size ($2a = 200$ nm) at $\lambda = 785$ nm.

Next, we checked the size dependence of the optical near-field energy transfer efficiency along the Au nanodot coupler. As a nanodot coupler, a linear array of 50-nm-high Au nanoparticles with $2a$ diameters ranging from 150 to 300 nm with center-to-center separations of $S = 2.4a$ was fabricated, using the FIB milling technique. To couple the transferred optical near-field with a two-dimensional surface plasmon polariton (2D SPP) mode for input and output, nanodot couplers were fabricated between 50-nm-thick Au films (Fig. 4). The nanodot couplers labelled A to D correspond to the Au diameter range of 150 to 300 nm. 2D SPP mode was used to excite the plasmon polariton modes along the nanodot couplers and the optical near-field intensity distributions were detected using the C-mode NOM at a wavelength of $\lambda = 785$ nm.

Figures 5a–d show the respective C-mode NOM images of nanodot couplers A–D. Although optical near-field energy was not detected over the nanodot coupler, owing to the low coupling efficiency from the Au nanoparticles to the fiber probe, we detected strong near-field energy at the outlet of the nanodot coupler, which presumably resulted from scattering coupling [13] at the interface of the nanodot coupler and Au film. Note that the output energy was obtained efficiently only for the nanodot coupler labelled B ($2a = 200$ nm), which is consistent with the experimental results shown in Fig. 3a. These results confirm that the efficient energy transfer along the Au nanoparticles originates from near-field coupling between the resonant plasmon polariton modes of neighboring particles.

3 Conclusion

We directly observed the resonant light scattering of an Au metallic nanoparticle 200 nm in diameter at a wavelength of $\lambda = 785$ nm. Furthermore, we confirmed the efficient energy transfer along a nanodot coupler of the resonant size. As the size dependence of the transmission efficiency depends on the photon energy, the results shown here suggest possible applications such as an optical frequency filter.

REFERENCES

1 M. Ohtsu, K. Kobayashi, T. Kawazoe, S. Sangu, T. Yatsui, IEEE J. Sel. Top. Quantum Electron. **8**, 839 (2002)
2 T. Kawazoe, K. Kobayashi, S. Sangu, M. Ohtsu, Appl. Phys. Lett. **82**, 2957 (2003)
3 T. Kawazoe, K. Kobayashi, M. Ohtsu, Appl. Phys. Lett. **86**, 103 102 (2005)
4 Y. Yamamoto, M. Kourogi, M. Ohtsu, V. Polonski, G.H. Lee, Appl. Phys. Lett. **76**, 2173 (2000)
5 Y. Yamamoto, M. Kourogi, M. Ohtsu, T. Kawazoe, IEICE Trans. Electron. E **85-C**, 2081 (2002)
6 T. Yatsui, T. Kawazoe, M. Ueda, Y. Yamamoto, M. Kourogi, M. Ohtsu, Appl. Phys. Lett. **81**, 3651 (2002)
7 T. Yatsui, W. Nomura, M. Ohtsu, Nano Lett. **5**, 2548 (2005)
8 K. Kobayashi, S. Sangu, T. Kawazoe, M. Ohtsu, J. Luminesc. **112**, 117 (2005)
9 G.H. Lee, T. Kawazoe, M. Ohtsu, Appl. Surf. Sci. **239**, 394 (2005)
10 W. Nomura, M. Ohtsu, T. Yatsui, Appl. Phys. Lett. **86**, 181 108 (2005)
11 G.T. Boyd, T. Rasing, J.R.R. Leite, Y.R. Shen, Phys. Rev. B **30**, 519 (1984)
12 H. Kuwata, H. Tamaru, K. Esumi, K. Miyano, Appl. Phys. Lett. **83**, 4625 (2003)
13 D. Marcuse, *Light Transmission Optics* (Van Nostrand–Reinhold, New York, 1972), Chapt. 10

Appl. Phys. B 84, 247–251 (2006)
DOI: 10.1007/s00340-006-2224-z

Applied Physics B
Lasers and Optics

T. KAWAZOE[1,✉]
K. KOBAYASHI[2]
M. OHTSU[1,3]

Near-field optical chemical vapor deposition using $Zn(acac)_2$ with a non-adiabatic photochemical process

[1] Japan Science and Technology Agency, Machida, Tokyo 194-0004, Japan
[2] Department of Physics, Tokyo Institute of Technology, Meguro-ku, Tokyo 152-8551, Japan
[3] Department of Electronics Engineering, University of Tokyo, Bunkyo-ku, Tokyo 113-8656, Japan

Received: 31 January 2006/Revised version: 23 March 2006
Published online: 29 April 2006 •

ABSTRACT We succeeded in depositing nanometric Zn dots using near-field optical chemical vapor deposition (NFO-CVD). Conventional optical CVD is based on an adiabatic photochemical process and requires UV light to excite molecules from the ground electronic state to the excited state for dissociation. By contrast, in near-field optical CVD (NFO-CVD), non-adiabatic photodissociation takes place, even with visible light, as a consequence of the steep spatial gradient of the optical power of an optical near field. This non-adiabatic process, which can be explained using the exciton–phonon polariton model, enables the photodissociation of optically inactive $Zn(acac)_2$. We discuss experimental results using the exciton–phonon polariton model.

PACS 33.80.Gj; 82.50.-m; 81.16.Be

1 Introduction

The fabrication of future electronic and optical devices will require advanced nanofabrication techniques that realize high spatial resolution and high precision in controlling size and position, and that are applicable to various materials. Self-organized growth has been used for nanofabrication [1]; however, its spatial precision is insufficient to meet these requirements. To improve precision, an e-beam [2], a scanning tunneling microscope (STM) [3], and surface modification [4] have been used for site control of the substrate. In situ patterning of nanoscale structures using a scanning probe microscope, such as an STM [5], has also been investigated; however, it has a fatal disadvantage in that the number of materials that can be deposited is limited by the fact that it cannot deal with insulators. In conventional optical chemical vapor deposition (CVD), the vapors of organometallic molecules are dissociated as a result of the photochemical reaction with far-field light; however, it is difficult to deposit subwavelength-sized materials due to the diffraction limit of light.

Near-field optical CVD (NFO-CVD) was proposed to solve these problems by utilizing the high spatial resolution capability of the optical near field. Nanometric Zn, Al, and ZnO dots and loops have been deposited successfully using this method [6–9]. The precision of deposition was as high as 1 nm [8]. As an outstanding advantage, we recently found that photodissociation can take place even under non-resonant conditions for the electronic transition of molecules, which results from the non-adiabatic process arising from the inherent properties of the optical near field [10]. Conventional optical CVD utilizes a two-step process: photodissociation and adsorption. For photodissociation, far-field light must resonate the reacting molecular gases to excite molecules from the ground state to an excited electronic state [11]. The Franck–Condon principle holds that this resonance is essential for excitation. The excited molecules then relax to the dissociation channel, and the dissociated atoms adsorb onto the substrate surface. However, the non-adiabatic photodissociation process, which is observed in NFO-CVD under non-resonant conditions, can violate the Franck–Condon principle, which is for an adiabatic process [12]. In this paper, we discuss non-adiabatic NFO-CVD and explain the experimental results using optically inactive zinc-bis(acetylacetonate) ($Zn(acac)_2$) as a CVD gas source based on the exciton–phonon polariton model.

2 Near-field optical CVD using $Zn(acac)_2$

Figure 1 shows the experimental setup used for NFO-CVD. $Zn(acac)_2$ was used as the source of the reacting molecular gas. An Ar^+ laser ($\lambda = 457$ nm) was used as the light source. The fiber probe used for NFO-CVD was a high-throughput single-tapered fiber probe, which was fabricated by pulling and etching a pure silica core fiber [13]. The cone angle of the fabricated fiber probe was 30 degrees and its apex diameter was 30 nm. To investigate the deposition effect of non-resonant far-field light, a fiber probe without the usual metal coating, i.e. a bare fiber probe, was used for deposition. Therefore, the optical far field was generated by light leaking through the circumference of the fiber probe, while the optical near field was generated at the apex, as shown in Fig. 1. The separation between the fiber probe and the sapphire substrate was controlled to within a few nanometers using a shear-force technique [13]. The laser output power from the fiber probe was measured with a photodiode placed behind the sapphire substrate. The sizes of the deposited Zn dots were measured using shear-force microscopy. During deposition, the pres-

✉ Fax: +81-42-788-6031, E-mail: kawazoe@ohtsu.jst.go.jp

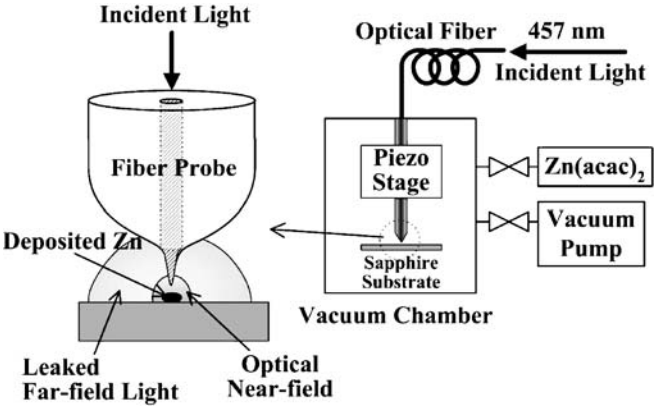

FIGURE 1 Experimental setup for chemical vapor deposition using an optical near field

sure of $Zn(acac)_2$ was 70 mTorr. Details of the Zn deposition procedures have been reported previously [8]. Note that the deposition of Zn on the fiber probe and the resultant decrease in the efficiency of optical near-field generation are negligible because the deposition time is sufficiently short, as pointed out elsewhere [8].

Figure 2 shows shear-force topographical images after NFO-CVD and the cross-sectional profile of a Zn dot deposited on the sapphire substrate. The diameter (full width at half maximum; FWHM) and height of the topographical image were 71 and 2.4 nm, respectively. The incident laser power was 1 mW and the irradiation time was 15 s. Although $Zn(acac)_2$ is optically inactive, we observed the deposition of Zn nanodots on the substrate just below the apex of the fiber probe using NFO-CVD. The absorption spectrum of $Zn(acac)_2$ was observed and its absorption edge was less than 240 nm. Specifically, the light source used was non-resonant for $Zn(acac)_2$, and the deposition of Zn, i.e. the photodissociation of $Zn(acac)_2$, originated from a non-adiabatic photochemical process, even with non-resonant light. This photochemical process occurred directly under the apex of the fiber probe where the optical near field was strong. Furthermore, while the bare fiber probe also leaked strong far-field light, no Zn layer was observed outside the small area under the apex of the fiber probe, because $Zn(acac)_2$ is inactive for far-field light.

It was difficult to observe the chemical composition of the deposited nanodots using X-ray photoelectron spectroscopy, because they were too small. During deposition, a little Zn was also deposited on the fiber probe. We believe that the chemical compositions of the materials deposited on the substrate and at the fiber probe were the same. Therefore, we measured the X-ray spectrum around the apex of the fiber probe after deposition, which indicated that the purity of the Zn exceeded 90%.

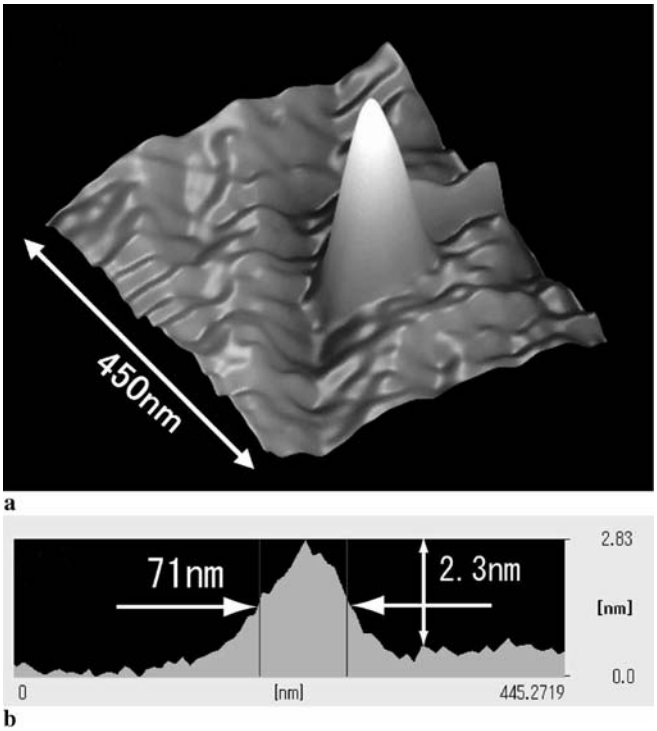

FIGURE 2 Shear-force topographical images after NFO-CVD (**a**) and the cross-sectional profile of a Zn dot deposited on a sapphire substrate (**b**)

3 Exciton–phonon polariton model

Although we used a bare fiber probe, with an optical field that broadened to more than 200 nm in diameter (FWHM), the Zn dots were deposited directly under the apex of the fiber probe. No known photochemical process for an optical far field, such as the Raman process or two-photon absorption, can explain our experimental results. In order to explain our experimental results, we propose the exciton–phonon polariton model.

Figure 3 shows the potential curves of an electron in a typical molecular orbital drawn as a function of the internuclear distance, which is involved in photodissociation [12]. The relevant energy levels of the molecular vibration mode are indicated by the horizontal broken lines in each potential curve. When far-field light is used, photo-absorption (indicated by the white arrow in this figure) triggers typical dissociation [11]. By contrast, when a non-resonant optical near field is used, there are three possible origins of photodissociation,

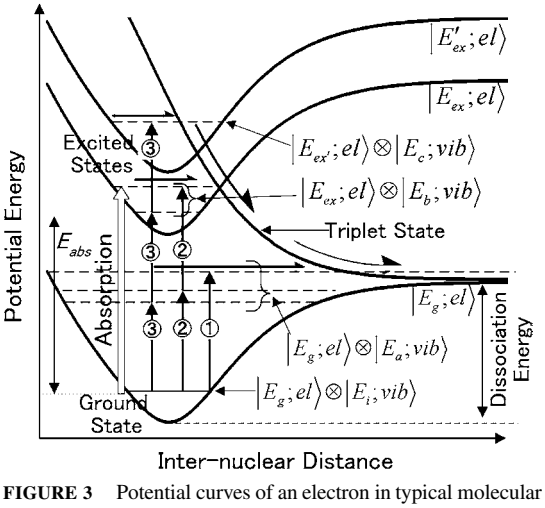

FIGURE 3 Potential curves of an electron in typical molecular orbitals. The relevant energy levels of the molecular vibration modes are indicated by the *horizontal broken lines*

as we proposed elsewhere [10]: (1) a multiple photon absorption process, (2) a multi-step transition process via an intermediate energy level induced by the fiber probe, and (3) a multi-step transition via an excited state of the molecular vibration mode. Possibility (1) is negligible, because the optical power density in the experiment was less than 10 kW/cm^2, which is too low for multiple-photon absorption. Possibility (2) is also negligible, because NFO-CVD is observed for light in the ultraviolet to near-infrared regions, and the molecule used lacks relevant energy levels for such a broad region. As a result, our experimental results strongly support possibility (3), i.e. the physical origin of the photodissociation caused by a non-resonant optical near field is the transition to an excited state via a molecular vibration mode. The three multi-step excitation processes in Fig. 3, labeled ①, ②, and ③, contribute to this. Since we consider the system to be strongly coupled to the vibration state, it must be treated as a non-adiabatic system.

To evaluate these contributions, we propose an exciton–phonon polariton model. In the exciton–phonon polariton model, the optical near field excites the molecular vibration mode due to the steep spatial gradient of the optical near field. Figure 4 shows a schematic of the quasi-particle of the exciton–phonon polariton. For an optical far field, the field intensity is uniform in a neutral molecule smaller than the wavelength. Electrons in the molecule only respond to an electric field with the same phase and intensity. Therefore, an optical far field cannot excite molecular vibration. By contrast, the field intensity is not uniform in a molecule for an optical near field with a steep spatial gradient. The electrons respond non-uniformly, and the molecular vibration modes are excited, because the molecular orbital changes and the molecule is polarized as a result of this non-uniform response of the electrons. We propose the exciton–phonon polariton model to quantify this excitation process. The exciton–phonon polariton is a quasi-particle that is an exciton polariton trailing the phonon (lattice vibration) generated by the steep spatial gradient of its optical field, as shown in Fig. 4. The exciton–phonon polariton model is formulated below.

The optical near field generated on the nanometric probe tip [14] is described in terms of the following model Hamiltonian:

$$
\begin{aligned}
H = & \sum_p \hbar \left[\omega_{\mathrm{p}} a_{\mathrm{p}}^{\dagger} a_{\mathrm{p}} + \omega_{\mathrm{p}}^{\mathrm{ex}} b_{\mathrm{p}}^{\dagger} b_{\mathrm{p}} + \frac{\mathrm{i}\Omega_{\mathrm{c}}}{2} \left(a_{\mathrm{p}}^{\dagger} b_{\mathrm{p}} - a_{\mathrm{p}} b_{\mathrm{p}}^{\dagger} \right) \right] \\
& + \sum_p \hbar \Omega_{\mathrm{p}} c_{\mathrm{p}}^{\dagger} c_{\mathrm{p}} \\
& + \sum_{p,q} \left\{ \mathrm{i}\hbar M\left(p-q\right) b_{\mathrm{p}}^{\dagger} b_{\mathrm{q}} \left[c_{\mathrm{p\text{-}q}} + c_{\mathrm{q\text{-}p}}^{\dagger} \right] + h.c. \right\} \\
= & \sum_p \hbar \omega_{\mathrm{p}}^{\mathrm{pol}} B_{\mathrm{p}}^{\dagger} B_{\mathrm{p}} + \sum_p \hbar \Omega_{\mathrm{p}} c_{\mathrm{p}}^{\dagger} c_{\mathrm{p}} \\
& + \sum_{p,q} \left\{ \mathrm{i}\hbar M'\left(p-q\right) B_{\mathrm{p}}^{\dagger} B_{\mathrm{q}} \left[c_{\mathrm{p\text{-}q}} + c_{\mathrm{q\text{-}p}}^{\dagger} \right] + h.c. \right\},
\end{aligned}
$$

where the creation (annihilation) operators for a photon, exciton, renormalized phonon, and exciton polariton are denoted as $a_{\mathrm{p}}^{\dagger}\left(a_{\mathrm{p}}\right)$, $b_{\mathrm{p}}^{\dagger}\left(b_{\mathrm{p}}\right)$, $c_{\mathrm{p}}^{\dagger}\left(c_{\mathrm{p}}\right)$, and $B_{\mathrm{p}}^{\dagger}\left(B_{\mathrm{p}}\right)$, respectively, and their respective frequencies are ω_{p}, $\omega_{\mathrm{p}}^{\mathrm{ex}}$, Ω_{p}, and $\omega_{\mathrm{p}}^{\mathrm{pol}}$. The photon–exciton coupling, exciton–phonon coupling, and exciton–polariton–phonon coupling are designated Ω_{c}, $M\left(p-q\right)$, and $M'\left(p-q\right)$, respectively. The first line of this description expresses the Hamiltonian for a photon–exciton interacting system and is transformed into the exciton–polariton representation in the third line, while the second line represents the Hamiltonian for a phonon–exciton interacting system. Note that the mode and anharmonic coupling of phonons are considered a renormalized phonon; therefore, multiple phonons can interact with an exciton or an exciton polariton simultaneously.

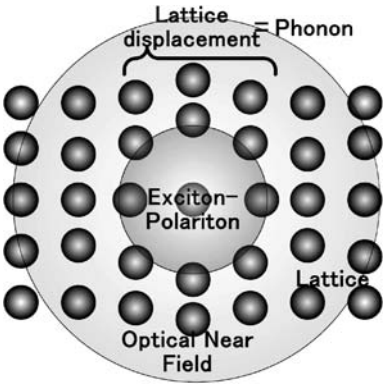

FIGURE 4 Schematic explanation of the exciton–phonon polariton

If the mean-field approximation of exciton polaritons near the probe tip is

$$
\left\langle B_{k_0}^{\dagger} \right\rangle = \left\langle B_{k_0} \right\rangle = \sqrt{I_0\left(\omega_0\right) V},
$$

using the unitary transformation

$$
\begin{pmatrix} B_{\mathrm{p}} \\ c_{\mathrm{p}-k_0} \end{pmatrix} = \begin{pmatrix} \mathrm{i}v_{\mathrm{p}}' & u_{\mathrm{p}}' \\ u_{\mathrm{p}}' & \mathrm{i}v_{\mathrm{p}}' \end{pmatrix} \begin{pmatrix} \xi_{(-)\mathrm{p}} \\ \xi_{(+)\mathrm{p}} \end{pmatrix}
$$

we can diagonalize the Hamiltonian in the quasi-particle (the exciton–phonon polariton) representation as [15]

$$
\begin{aligned}
H = & \sum_p \hbar \omega_{\mathrm{p}}^{\mathrm{pol}} B_{\mathrm{p}}^{\dagger} B_{\mathrm{p}} + \sum_p \hbar \Omega_{\mathrm{p}} c_{\mathrm{p}}^{\dagger} c_{\mathrm{p}} \\
& + \sum_p \left\{ \mathrm{i}\hbar \sqrt{I_0\left(\omega_0\right) V} M'\left(p-k_0\right) \left(B_{\mathrm{p}}^{\dagger} c_{\mathrm{p}-k_0} + B_{\mathrm{p}} c_{\mathrm{p}-k_0}^{\dagger} \right) \right\} \\
= & \sum_p \hbar \omega\left(p\right) \xi_{\mathrm{p}}^{\dagger} \xi_{\mathrm{p}}.
\end{aligned}
$$

Here, $I_0\left(\omega_0\right)$ is the intensity of an incident photon with frequency ω_0 and momentum $\hbar k_0$, and V represents the volume to be considered. The transformation elements u_{p}' and v_{p}' are given by

$$
\begin{aligned}
u_{\mathrm{p}}' = & \frac{1}{\sqrt{2}} \left(1 + \frac{\Delta}{\sqrt{\Delta^2 + (2Q)^2}} \right)^{\frac{1}{2}}, \\
v_{\mathrm{p}}' = & \frac{1}{\sqrt{2}} \left(1 - \frac{\Delta}{\sqrt{\Delta^2 + (2Q)^2}} \right)^{\frac{1}{2}},
\end{aligned}
$$

where the detuning between an exciton polariton and a phonon is denoted as $\Delta = \omega_{\mathrm{p}}^{\mathrm{pol}} - \Omega_{\mathrm{p}-k_0}$, and the effective coupling

constant is expressed as $Q = \sqrt{I_0(\omega_0)\,V}\,M'(p-k_0)$. Therefore, in this model, a molecule located near the probe tip does not absorb simple photons, but absorbs exciton–phonon polaritons whose energies are transferred to the molecule, which excites molecular vibrations or induces electronic transitions.

We will now discuss the dissociation probability of a molecule, assuming that the deposition rate of the metal atoms is proportional to the molecular dissociation rate. We consider the following initial and three final states of a system consisting of the optical near-field probe and a molecule:

$$
\begin{aligned}
&|\mathrm{i}\rangle = |\mathrm{probe}\rangle \otimes \left|E_\mathrm{g};\,\mathrm{el}\right\rangle \otimes |E_\mathrm{i};\,\mathrm{vib}\rangle\,,\\
&|f_\mathrm{first}\rangle = |\mathrm{probe}\rangle \otimes \left|E_\mathrm{g};\,\mathrm{el}\right\rangle \otimes |E_\mathrm{a};\,\mathrm{vib}\rangle\,,\\
&|f_\mathrm{second}\rangle = |\mathrm{probe}\rangle \otimes |E_\mathrm{ex};\,\mathrm{el}\rangle \otimes |E_\mathrm{b};\,\mathrm{vib}\rangle\,,\\
&|f_\mathrm{third}\rangle = |\mathrm{probe}\rangle \otimes |E_\mathrm{ex'};\,\mathrm{el}\rangle \otimes |E_\mathrm{c};\,\mathrm{vib}\rangle\,,
\end{aligned}
$$

where $|\mathrm{probe}\rangle$, $|E_\alpha;\,\mathrm{el}\rangle$, and $\left|E_\beta;\,\mathrm{vib}\right\rangle$ represent the probe state, molecular electronic states with energy E_α $(\alpha = \mathrm{g}, \mathrm{ex}, \mathrm{ex}')$, and molecular vibrational states with energy E_β $(\beta = \mathrm{i}, a, b, c)$, respectively, as shown in Fig. 3. The transitions from the initial to the final states can be formulated using the conventional perturbation method for the interaction Hamiltonian expressed in terms of exciton–phonon polaritons as

$$
\begin{aligned}
H_\mathrm{int} = &-\left\{\mu^\mathrm{el}\left(e+e^\dagger\right)+\mu^\mathrm{nucl}\left(v+v^\dagger\right)\right\}\\
&\times\sum_p \mathrm{i}\sqrt{\frac{2\pi\hbar\omega_\mathrm{p}}{V}}\left\{-v_\mathrm{p}v'_\mathrm{p}\left(\xi_\mathrm{p}-\xi_\mathrm{p}^\dagger\right)\right\}\mathrm{e}^{\mathrm{i}pr}.
\end{aligned}
$$

Here, μ^el and μ^nucl are the electronic and vibrational dipole moments, respectively, and the creation (annihilation) operators of the electronic and vibrational excitations are denoted as $e^\dagger$ (e) and $v^\dagger$ (v), respectively. The incident photon frequency and transformation coefficients are ω_p and v_p (v'_p), respectively. Then, the transition probabilities of one-, two-, and three-step excitation (labeled ①, ②, and ③ in Fig. 3, and denoting the corresponding final states as $|f_\mathrm{first}\rangle$, $|f_\mathrm{second}\rangle$, and $|f_\mathrm{third}\rangle$) can be written as follows:

$$
\begin{aligned}
P_\mathrm{first}\left(\omega_\mathrm{p}\right) &= \frac{2\pi}{\hbar}\left|\langle f_\mathrm{first}|\,H_\mathrm{int}\,|\mathrm{i}\rangle\right|^2\\
&= \frac{(2\pi)^2}{\hbar}v_\mathrm{p}^2 v'^2_\mathrm{p}u'^2_\mathrm{p}\left(\mu^\mathrm{nucl}\right)^2\left(\hbar\omega_\mathrm{p}\right)I_0\left(\omega_\mathrm{p}\right),\\
P_\mathrm{second}\left(\omega_\mathrm{p}\right) &= \frac{2\pi}{\hbar}\left|\langle f_\mathrm{second}|\,H_\mathrm{int}\,|\mathrm{i}\rangle\right|^2\\
&= \frac{(2\pi)^3}{\hbar}\frac{v_\mathrm{p}^4 v'^6_\mathrm{p}u'^2_\mathrm{p}}{\left|\hbar\omega(p)-(E_\mathrm{a}-E_\mathrm{i}+\mathrm{i}\gamma_\mathrm{m})\right|^2}\\
&\quad\times\left(\mu^\mathrm{el}\right)^2\left(\mu^\mathrm{nucl}\right)^2\left(\hbar\omega_\mathrm{p}\right)^2 I_0^2\left(\omega_\mathrm{p}\right),\\
P_\mathrm{third}\left(\omega_\mathrm{p}\right) &= \frac{2\pi}{\hbar}\left|\langle f_\mathrm{third}|\,H_\mathrm{int}\,|\mathrm{i}\rangle\right|^2 = \frac{(2\pi)^4}{\hbar}\\
&\times\frac{v_\mathrm{p}^6 v'^{10}_\mathrm{p}u'^2_\mathrm{p}}{\left|\hbar\omega(p)-(E_\mathrm{a}-E_\mathrm{i}+\mathrm{i}\gamma_\mathrm{m})\right|^2\left|\hbar\omega(p)-\left(E_\mathrm{ex}-E_\mathrm{g}+\mathrm{i}\gamma_\mathrm{m}\right)\right|^2}\\
&\quad\times\left(\mu^\mathrm{el}\right)^4\left(\mu^\mathrm{nucl}\right)^2\left(\hbar\omega_\mathrm{p}\right)^3 I_0^3\left(\omega_\mathrm{p}\right),
\end{aligned}
$$

where u'_p and $I_0\left(\omega_\mathrm{p}\right)$ represent the transformation coefficient and the incident light intensity, respectively. In addition, E_α $\left(\alpha = \mathrm{g}, \mathrm{ex}, \mathrm{ex}'\right)$ and E_β $(\beta = \mathrm{i}, a, b, c)$ represent the molecular electronic and vibrational energies, respectively, as shown in Fig. 3, and γ_m is the line width of the vibrational states. It follows that these near-resonant transition probabilities have the following ratio:

$$
\begin{aligned}
\frac{P_\mathrm{second}\left(\omega_\mathrm{p}\right)/I_0^2\left(\omega_\mathrm{p}\right)}{P_\mathrm{first}\left(\omega_\mathrm{p}\right)/I_0\left(\omega_\mathrm{p}\right)} &= \frac{P_\mathrm{third}\left(\omega_\mathrm{p}\right)/I_0^3\left(\omega_\mathrm{p}\right)}{P_\mathrm{second}\left(\omega_\mathrm{p}\right)/I_0^2\left(\omega_\mathrm{p}\right)}\\
&= \frac{\hbar}{2\pi}\frac{P_\mathrm{first}\left(\omega_\mathrm{p}\right)}{\gamma_\mathrm{m}^2 I_0\left(\omega_\mathrm{p}\right)}\left(\frac{v'^2_\mathrm{p}}{u'^2_\mathrm{p}}\right)\left(\frac{\mu^\mathrm{el}}{\mu^\mathrm{nucl}}\right)^2.
\end{aligned}
$$

Using this ratio, we analyzed the experimental intensity dependence of the deposition rate to clarify possibility (3). Using reasonable values of $\mu^\mathrm{nucl} = 1\,\mathrm{Debye}$, $\mu^\mathrm{el} = 10^{-3}\,\mathrm{Debye}$, $\gamma_\mathrm{m} = 10^{-1}\,\mathrm{eV}$, and $v'^2_\mathrm{p}\big/u'^2_\mathrm{p} = 0.02$, we obtain the following value for the ratio:

$$
\begin{aligned}
\frac{P_\mathrm{second}(\omega)/I_0^2(\omega)}{P_\mathrm{first}(\omega)/I_0(\omega)} &= \frac{P_\mathrm{third}(\omega)/I_0^3(\omega)}{P_\mathrm{second}(\omega)/I_0^2(\omega)}\\
&= \frac{\hbar}{2\pi}\frac{P_\mathrm{first}(\omega)}{\gamma_\mathrm{m}^2 I_0(\omega)}\left(\frac{v'^2_\mathrm{p}}{u'^2_\mathrm{p}}\right)\left(\frac{\mu^\mathrm{el}}{\mu^\mathrm{nucl}}\right)^2\\
&\simeq 10^{-15}. \qquad (1)
\end{aligned}
$$

4 Experimental results and discussion

Figure 5 shows the optical power (photon flux: I) dependency of the rate R of Zn deposition. First, we introduce previous work using diethylzinc (DEZn) as the reacting molecular gas source [12] for three different light sources, which are He-Cd ($h\nu = 3.81\,\mathrm{eV}$), Ar: ($h\nu = 2.54\,\mathrm{eV}$) lasers, and LD ($h\nu = 1.81\,\mathrm{eV}$) using DEZn and the broken curves are the fitted results using the third-order function $R = aI + bI^2 + cI^3$. The respective values of $a_{\hbar\omega}$, $b_{\hbar\omega}$, and $c_{\hbar\omega}$ are $a_{3.81} = 5.0\times10^{-6}$, $b_{3.81} = 0$, and $c_{3.81} = 0$ for $h\nu =$

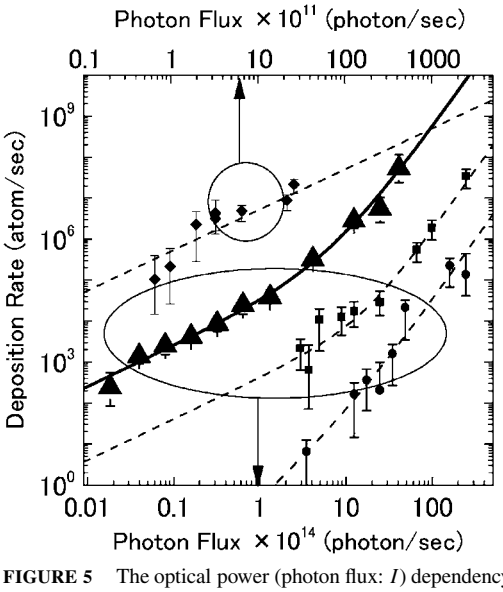

FIGURE 5 The optical power (photon flux: I) dependency of the rate of Zn deposition (R). The *solid* and *broken curves* fit the results using $R = aI + bI^2 + cI^3$

3.81 eV; $a_{2.54} = 4.1 \times 10^{-12}$, $b_{2.54} = 2.1 \times 10^{-27}$, and $c_{2.54} = 1.5 \times 10^{-42}$ for $h\nu = 2.54$ eV; $a_{1.81} = 0$, $b_{1.81} = 4.2 \times 10^{-29}$, and $c_{1.81} = 3.0 \times 10^{-44}$ for $h\nu = 1.81$ eV. These values support the theoretical result, i.e. (1), because the ratio of the values satisfy the relation $a : b \cong b : c \cong 10^{-15}$. In addition, the experimental results using $Zn(acac)_2$ indicated by the fitting curve (the solid curve in Fig. 5) also support the theory, i.e. the exciton–phonon polariton model. Here, the fitting values were $a = 2.5 \times 10^{-10}$, $b = 8 \times 10^{-25}$, and $c = 5 \times 10^{-40}$ for $Zn(acac)_2$.

Note that the intensity gradient of the optical field is important in the non-adiabatic process because the intensity gradient generates the possibility of a non-adiabatic transition. In the experiment, we used a bare fiber probe, because the apex diameter of the bare fiber probe is smaller than that of a metal-coated fiber probe and its field gradient is steeper. In addition, the spatial resolution of the topographical image is high for a bare fiber probe.

5 Conclusion

In conclusion, we demonstrated NFO-CVD of nanometric Zn dots based on the photodissociation of optically inactive $Zn(acac)_2$ using an optical near field under non-resonant conditions. To clarify the physical origin of this process, the optical power dependency of the deposition rate was measured. We explain the dependency using a multi-step excitation process via the molecular vibration mode and the exciton–phonon polariton model, i.e. a non-adiabatic photochemical process. In this model, the enhanced coupling between the optical field and molecular vibration originates from the steep spatial gradient of the optical power of the optical near field. Such a non-adiabatic photochemical process violates the Franck–Condon principle, and can be applied to other photochemical phenomena. The process involved in the photochemical reaction based on an optical near field reported here will open new methods in nanotechnology [16–18].

REFERENCES

1 D. Leonard, M. Krishnamurthy, C.M. Reaves, S.P. Denbaars, P.M. Petroff, Appl. Phys. Lett. **63**, 3203 (1993)
2 T. Tsutsui, K. Kawasaki, M. Mochizuki, T. Matsubara, Microelectron. Eng. **47**, 135 (1999)
3 S. Kohmoto, H. Nakamura, T. Ishikawa, K. Asakawa, Appl. Phys. Lett. **75**, 3488 (1999)
4 E. Kuramochi, J. Temmyo, T. Tamamura, H. Kamada, Appl. Phys. Lett. **71**, 1655 (1997)
5 R. Wiesendanger, Appl. Surf. Sci. **54**, 271 (1992)
6 V.V. Polonski, Y. Yamamoto, M. Kourogi, H. Fukuda, M. Ohtsu, J. Microsc. **194**, 545 (1999)
7 V.V. Polonski, Y. Yamamoto, J.D. White, M. Kourogi, M. Ohtsu, Jpn. J. Appl. Phys. **38**, 826 (1999)
8 Y. Yamamoto, M. Kourogi, M. Ohtsu, V. Polonski, G.H. Lee, Appl. Phys. Lett. **76**, 2173 (2000)
9 G.H. Lee, Y. Yamamoto, M. Kourogi, M. Ohtsu, Proc. SPIE **3791**, 132 (1999)
10 T. Kawazoe, Y. Yamamoto, M. Ohtsu, Appl. Phys. Lett. **79**, 1184 (2001)
11 J.G. Calvert, J.N. Patts Jr., *Photochemistry* (Wiley, New York, 1996)
12 T. Kawazoe, K. Kobayashi, S. Takubo, M. Ohtsu, J. Chem. Phys. **122**, 024715 (2005)
13 M. Ohtsu, *Near-Field Nano/Atom Optics and Technology* (Springer, Tokyo Berlin Heidelberg New York, 1998)
14 K. Kobayashi, S. Sangu, H. Ito, M. Ohtsu, Phys. Rev. A **63**, 0138061-1-9 (2001)
15 J.J. Hopfield, Phys. Rev. **112**, 1555 (1958)
16 M. Ohtsu, K. Kobayashi, T. Kawazoe, S. Sangu, T. Yatsui, IEEE J. Sel. Top. Quantum Electron. **8**, 839 (2002)
17 T. Kawazoe, K. Kobayashi, S. Sangu, M. Ohtsu, Appl. Phys. Lett. **82**, 2957 (2003)
18 T. Kawazoe, K. Kobayashi, M. Ohtsu, Appl. Phys. Lett. **86**, 103102 (2005)

Appl. Phys. B 84, 265–267 (2006)
DOI: 10.1007/s00340-006-2328-5

Applied Physics B
Lasers and Optics

T. YATSUI[1,✉]
Y. NAKAJIMA[2]
W. NOMURA[2]
M. OHTSU[1,2]

High-resolution capability of optical near-field imprint lithography

[1] Solution-Oriented Research for Science and Technology (SORST), Japan Science and Technology Agency, 687-1 Tsuruma, Machida, Tokyo, 194-0004, Japan
[2] School of Engineering, The University of Tokyo, 7-3-1 Hongo, Bunkyo-ku, Tokyo, 113-8656, Japan

Received: 15 December 2006/Revised version: 2 May 2006
Published online: 22 June 2006 •

ABSTRACT We propose a novel method to increase the resolution of imprint lithography by introducing strong localization of the optical near-field intensity, depending on the mold structure. By optimizing the thickness of the metallic film on a SiO_2 line-and-space (LS) mold without a sidewall coating, we confirmed that the optical near-field strongly localizes at the edge of the mold, using a finite-difference time-domain calculation method. Based on the calculated results, we performed optical near-field imprint lithography using a mold with metallized (20-nm-thick Al without a sidewall coating) SiO_2 LS with a 300-nm half-pitch that was 200-nm deep with illumination using the g-line ($\lambda = 436$ nm), and obtained features as narrow as 50 nm wide.

PACS 81.16.Nd; 81.16.Rf

1 Introduction

As next-generation lithography (NGL) for the 32-nm node and below, ArF immersion lithography, extreme ultraviolet lithography (EUVL), and electron projection lithography (EPL) have been studied. However, a practical problem is the increasing cost and size of NGL tools. To solve these problems, optical near-field lithography has been developed by introducing tri-layer resist. The fabrication of sub-50 nm features has been realized using the i-line ($\lambda = 365$ nm) [1], with conventional photolithography facilities.

A further decrease in feature size has been reported with the introduction of imprint lithography [2], which resulted in the fabrication of 14-nm pitch features [3]. Although conventional imprint lithography results in the same mold structure, the use of the optical near-field intensity distribution should realize features smaller than the mold structure, since a nano-scale mold has a nano-scale optical field distribution at its edge.

✉ Fax: +81-42-788-6031, E-mail: yatsui@ohtsu.jst.go.jp

In this study, we propose and demonstrate optical near-field imprint lithography to introduce its ability to obtain a higher resolution than the size of the mold features.

2 Optimizing the mold structure

To realize the efficient excitation of an optical near-field on a mold, the thickness of the metallic film and the coverage were optimized using the finite-difference time-domain (FDTD) method [4]. For comparison with a conventional photolithographic mask, the optical field distribution for 80-nm half-pitch, 200-nm-deep Cr line-and-space (LS) on the SiO_2 ($n = 1.5$) substrate was calculated at a wavelength of 436 nm (g-line). Here, the refractive index of Cr was assumed to be $n = 1.78 + i2.69$ [5], and the line was parallel to the y-axis (Fig. 1a). Since the imprint mold used in this study was fabricated using SiO_2, we also calculated the optical field distribution of 80-nm half-pitch, 200-nm-deep SiO_2 LS, coated with aluminum film ($n = 0.56 + i5.2$) [5] (Fig. 1b–d). The minimum cell size was $5 \times 12.5 \times 5$ nm.

Figure 1e shows the cross-sectional profile along the x-axis 10 nm from the mold. The optical field intensity distribution of the Cr LS used for conventional photolithography resulted in a single peak corresponding to the space of the Cr mask, which resulted from reducing the optical field intensity through the 200-nm-thick Cr film (curve 1a in Fig. 1e). By contrast, coating the SiO_2 LS with a 20-nm-thick Al film (Fig. 1b and c) enhanced the electric field intensity at the edge of the mold (curves 2a and 3a in Fig. 1e). Higher localization at the edge of the mold was realized without a sidewall coating (Fig. 1b and curve 2a in Fig. 1e). Since this localization was not observed for the thicker coating (a 50-nm-thick Al film on top of SiO_2 and a 20-nm-thick Al film on the sidewall) and was not observed in the y-polarization (curve y in Fig. 1f), this localized optical near-field originated from the edge effect. Since efficient excitation of the surface plasmon is obtained with a 15-nm-thick aluminum coating on glass in the Kretschmann configuration [6], this size-dependent feature is attributed to localized surface plasmon resonance on the Al film. Furthermore, the localization of the optical field intensity to an area as narrow as 25-nm in curve 2a in Fig. 1e

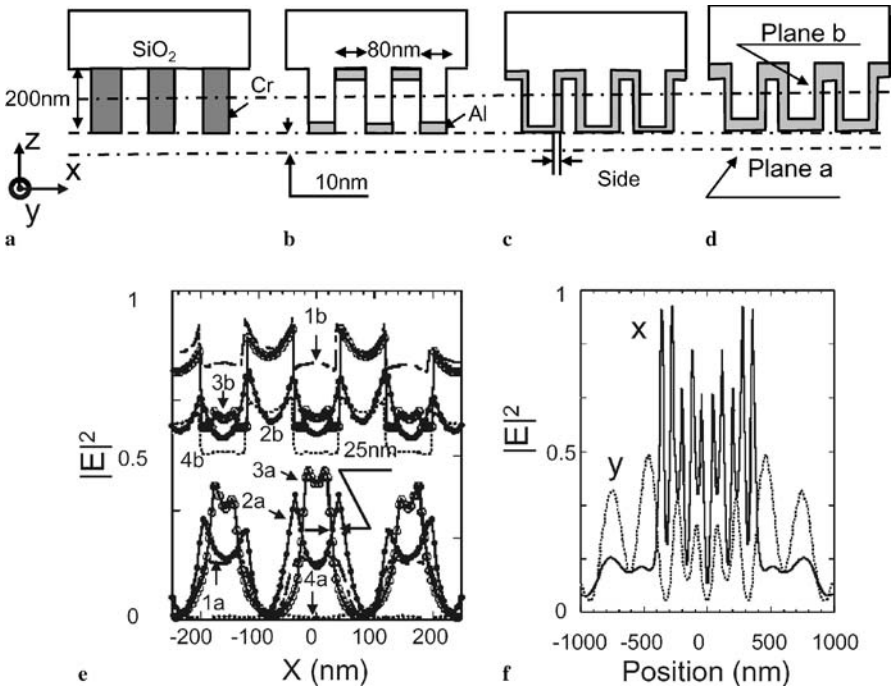

FIGURE 1 Schematic of the calculation models. (**a**) Cr LS on SiO_2 substrate. (**b–d**) SiO_2 LS coated with (b) 20-nm Al without a sidewall coating, (**c**) 20-nm Al with a sidewall coating, and (**d**) 50-nm Al at the top and 20-nm Al on the sidewall. (**e**) Curves 1a–4a show the cross-sectional profiles along the *x*-axis 10 nm from the mold (plane a) with five grooves in the mold. Curves 1b–4b show the cross-sectional profiles along the *x*-axis 10 nm from the bottom of the mold (plane b). The beam width at $1/e^2$ of incident light with a Gaussian shape was 1000 nm. The *x*-coordinate is perpendicular to the grating in (**a–d**). (**f**) The polarization dependence of the cross-sectional profiles for *x*- (perpendicular to the LS direction) and *y*- (parallel to the LS direction) polarization for the mold with five grooves in the mold. The beam width at $1/e^2$ of incident light with a Gaussian shape was 2000 nm ($1/e^2$)

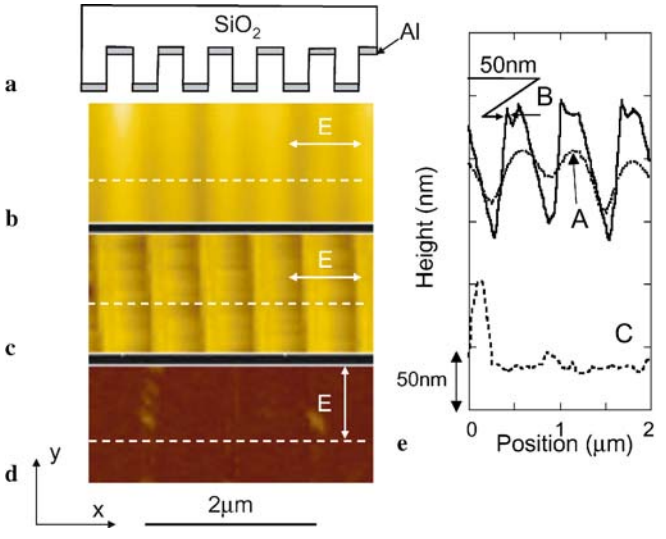

FIGURE 2 (**a**) Mold position before its release from PAK01. (**b–d**) show AFM images of the surface of the PAK01 using a bare mold with *x*-polarization (perpendicular to the LS direction), an Al-coated mold with *x*-polarization, and an Al-coated mold with *y*-polarization (parallel to the LS direction), respectively. (**d**) Curves A, B, and C show the cross-sectional profiles along the *dashed white lines* in (**b**), (**c**), and (**d**), respectively

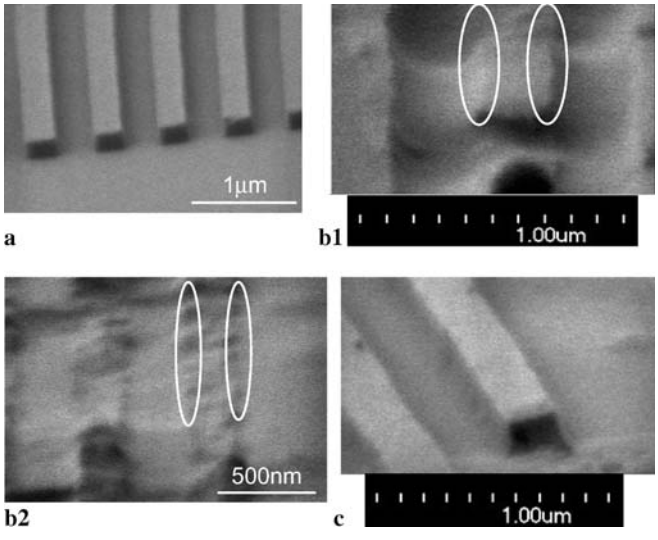

FIGURE 3 Tilted (30°) SEM images using (**a**) a bare mold with *x*-polarization (perpendicular to the LS direction), (**b**.1) (**b**.2) an Al-coated mold with *x*-polarization, and (**c**) an Al-coated mold with *y*-polarization

infers the realization of a resolution higher than the mold size. This localization was also observed in curve 2b (Fig. 1e) obtained in the plane along the *x*-axis 10 nm from the bottom of the mold.

3 Experiment

We performed imprint lithography to confirm the higher resolution capability using an optical near-field, as discussed above. Commercial photocurable acryl PAK01 resin (blended by Toyo Gosei) was used; it is composed of tri-propylene-glycol-diacrylate monomer with dimethoxy-phenyl-acetophenon as the photo-initiator and has good release properties [7]. Polycarbonate (PC) substrate was spin-coated with PAK01. We used 300-nm half-pitch, 200-nm-deep SiO_2 LS as the mold.

To obtain the optimum structure shown in Fig. 1b (20-nm-thick Al film with no sidewall coating), the mold was coated with Al using vacuum evaporation (Fig. 2a). The mold was pressed into the liquid polymer on PC substrate under a pressure of 70 kPa using a conventional contact mask aligner (MJB3, SUSS MicroTec KK). It was irradiated with UV light (g-line: 436 nm, power density: 30 mW/cm^2) for 30 s from the back of the mold, while maintaining the imprint pressure during exposure. After pressing the mold and UV curing, we separated the PC substrate from the mold, and the pattern was transferred.

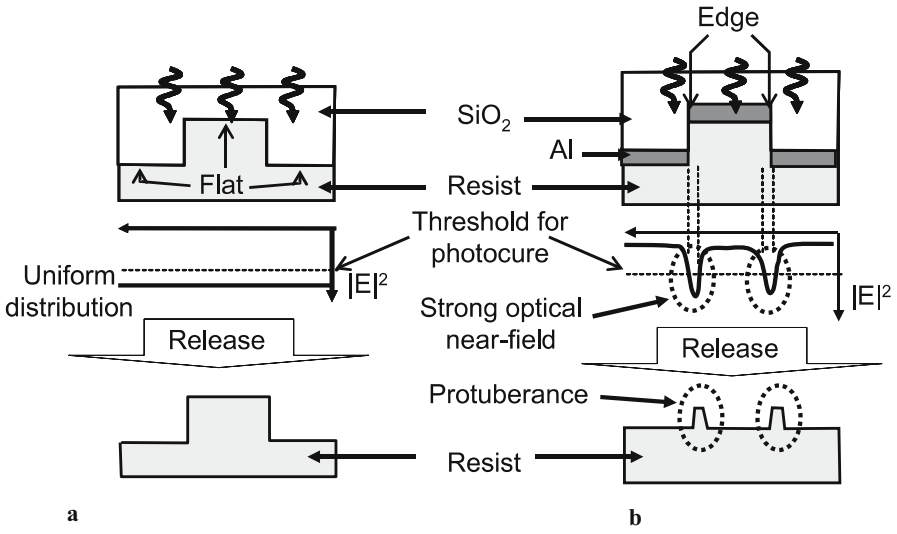

FIGURE 4 Schematics of (**a**) conventional imprint lithography and (**b**) optical near-field imprint lithography

4 Results and discussion

First, we obtained topographic atomic force microscopy (AFM) images of the surface of PAK01 after release of the mold. Figure 2b–d show AFM images of a bare SiO_2 mold with x-polarization (perpendicular to the LS direction), an Al-coated SiO_2 mold with x-polarization, and an Al-coated SiO_2 mold with y-polarization (parallel to the LS direction), respectively. Although the bare mold resulted in a single pitch corresponding to the mold pitch (Fig. 2b and curve A in Fig. 2e), we obtained sharp (50 nm) protruding structures at the edge of the Al-coated SiO_2 mold, when the mold was pressed under x-polarization (Fig. 2c and curve B in Fig. 2e). Although the pitch differs between the numerical and experimental results, these profiles with protruding structures seen at the edge of the Al-coated SiO_2 mold are in good agreement with those calculated using FDTD (curve 2a of Fig. 1e). The calculated value at the point next to the interface is unstable in the FDTD calculation due to the drastic change in the refractive index. Furthermore, since the distribution of the optical near-field along the z-axis is as large as that along the x-axis, the optical near-field is believed to be localized to a region small as 20-nm along the z-axis. Therefore, we compared the profiles at the second point from the interface (10 nm apart from the interface). Although the calculated and obtained profiles differ, the protuberances were obtained only with x-polarization with an Al coating; therefore, we believe that the protuberances originated from the plasmon resonance, as predicted by the FDTD calculation. These results indicate that the resolution was higher than the pitch of the mold.

Next, we obtained scanning electron microscope (SEM) images of the transferred pattern (Fig. 3a–c). As shown in the AFM images, the SEM images confirmed that there were protuberances where the edge of the mold was pressed (inside the white solid ellipses in Fig. 3b.1 and b.2) using the Al-coated mold with x-polarization.

The field distribution calculated using the FDTD method did not predict the resist structure after release of the mold. However, the correspondence between the AFM and SEM images showed that protuberances were formed at positions where a strong optical near-field was localized. Based on these results, we concluded that using conventional imprint lithography, a strong uniform optical field intensity resulted in the formation of the same pitch as that of the mold (Fig. 4a). In contrast, with optical near-field imprint lithography, the resist was deformed in the underexposed condition where the flat surface of the mold was press, which was due to the Al coating of the mold, and the resist was remained in the overexposed condition arising from the strong optical near-field, which was due to the edge effect from where the edge of the mold was pressed. This enhancement originated from the resonant excitation of the surface plasmon on the Al film, which resulted in protuberances smaller than the pitch of the mold (see Fig. 4b). Future evaluations, which will include the effects of power and irradiation time, are required to explain the optimum dose for the higher contrast of the protuberances.

5 Conclusion

We performed optical near-field imprint lithography to increase the resolution over conventional imprint lithography. By introducing local field enhancement of the optical near-field using a metallized LS SiO_2 mold (300-nm half-pitch and 200-nm deep) without sidewall coating, we obtained features as small as 50-nm wide on illumination with the g-line ($\lambda = 436$ nm). The resolution could be increased further by surface treatment with Al or other durable metals or semiconductors.

REFERENCES

1 T. Ito, M. Ogino, T. Yamada, Y. Inao, T. Yamaguchi, T. Mizutani, R. Kuroda, J. Photopoly. Sci. Technol. **18**, 435 (2003)
2 S.Y. Chou, P.R. Krauss, W. Zhang, L. Guo, L. Zhuang, J. Vac. Sci. Technol. B **15**, 2897 (1997)
3 M.D. Austin, H. Ge, W. Wu, M. Li, Z. Yu, D. Wasserman, S.A. Lyon, S.Y. Chou, Appl. Phys. Lett. **84**, 5299 (2004)
4 The computer simulations in this paper are performed by a FDTD-based program, Poynting for Optics, a product of Fujitsu, Japan
5 E.D. Palik (Ed.), *Handbook of Optical Constants of Solids* (Academic, New York, 1985)
6 H. Raether (Ed.), *Surface Plasmons* (Springer-Verlag, Berlin, 1988)
7 J. Haisma, M. Verheijen, K. van den Heuvel, J. van den Berg, J. Vac. Sci. Technol. B **14**, 4124 (1996)

Quantum confinement effect in $ZnO/Mg_{0.2}Zn_{0.8}O$ multishell nanorod heterostructures

Eue-Soon Jang, Jun Young Bae, Jinkyoung Yoo, Won Il Park, Dong-Wook Kim, and Gyu-Chul Yi[a)]
National CRI Center for Semiconductor Nanorods and Department of Materials Science and Engineering, Pohang University of Science and Technology (POSTECH), San-31 Hyoja-dong, Pohang, Gyeongbuk 790-784, Korea

T. Yatsui and M. Ohtsu[b)]
Solution-Oriented Research for Science and Technology (SORST), Japan Science and Technology Agency, Machida, Tokyo 194-0004, Japan

(Received 23 May 2005; accepted 15 November 2005; published online 9 January 2006)

We report on photoluminescence measurements of $Mg_{0.2}Zn_{0.8}O/ZnO/Mg_{0.2}Zn_{0.8}O$ multishell layers on ZnO core nanorods. Dominant excitonic emissions in the photoluminescence spectra show a blueshift depending on the ZnO shell layer thickness attributed to the quantum confinement effect in the nanorod heterostructure radial direction. Furthermore, near-field scanning optical microscopy clearly shows sharp photoluminescence peaks from the individual nanorod quantum structures, corresponding to subband levels. © *2006 American Institute of Physics*. [DOI: 10.1063/1.2162695]

Recent progress in semiconductor nanowire and nanorod heterostructure synthesis allows us to explore high-performance electronic, optoelectronic, and sensing nanodevices.[1–6] Especially, composition-modulated nanowire/nanorod heterostructures have great potential as building blocks for the fabrication of quantum devices, such as high electron mobility transistors.[7] Composition modulation in the radial direction can efficiently confine both the carriers and emitted photons: coaxial nanorod heterostructures are expected to suppress surface state mediated nonradiative recombination and to decrease thermal quenching of emission intensity.[8] Although there have been some reports on coaxial nanowire and nanorod heterostructures, including Ge/Si, Si/CdSe, and GaP/GaN,[9–11] a quantum confinement effect in a multishell nanorod heterostructure has not been reported. The shell layer thicknesses of the reported multishell nanorod heterostructures are a few tens of nm,[3,9,11] which is generally too thick to confine charge carriers in the shell layer.[12,13] Moreover, many of the coaxial nanowire heterostructures show large lattice mismatches between their core and shell layer components (for instance, 11% for Si/CdSe and 71% for GaP/GaN). This will result in strain-induced crystal defects at the interface, which hinders the appearance of quantum confinement.[14] Precise control of shell thickness and a negligible lattice mismatch in $ZnO/Mg_{0.2}Zn_{0.8}O$ coaxial nanorod heterostructures enable us to successfully demonstrate the quantum confinement effect in multishell quantum structures.

We fabricated $ZnO/Mg_{0.2}Zn_{0.8}O/ZnO/Mg_{0.2}Zn_{0.8}O$ multishell nanorod heterostructures on $Al_2O_3(0001)$ and Si(100) substrates using catalyst-free metalorganic vapor phase epitaxy (MOVPE). For core ZnO nanorod synthesis, we used diethylzinc and oxygen as the reactants with argon as the carrier gas.[1,14] Subsequent $Mg_{0.2}Zn_{0.8}O$ shell layers were deposited by introducing bis-cyclopentadienyl-Mg as the Mg precursor. Energy dispersive x-ray spectroscopy analysis confirmed Mg concentration in the $Mg_{0.2}Zn_{0.8}O$ layers. The multishell nanorod heterostructures, as schematically depicted in Fig. 1, were prepared by repeated alternate deposition of ZnO and $Mg_{0.2}Zn_{0.8}O$ layers. The nanorods with various ZnO quantum well (QW) widths, L_W, were prepared in order to investigate the quantum confinement effect. Such distinctive coaxial nanorod structures were realized by precise control of L_W and L_B in angstrom scale using a computer-controlled gas valve system in our MOVPE system. In particular, the formation of interfacial intermediate alloy layers was prevented by purging the system with pure

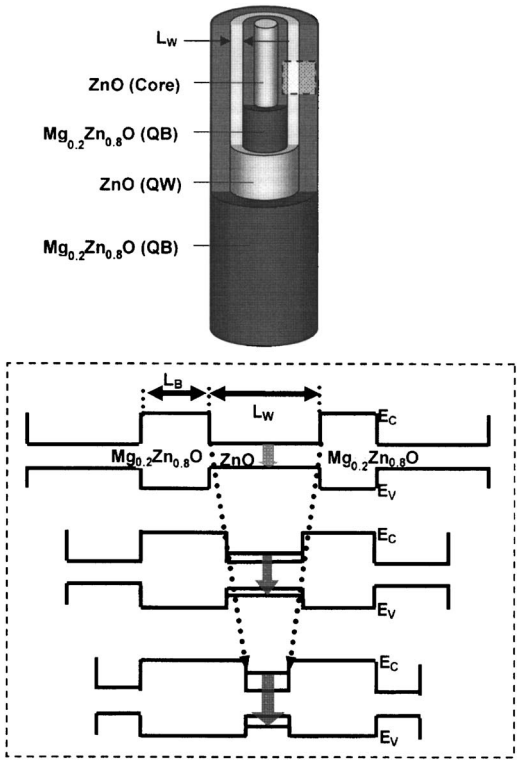

FIG. 1. Schematic illustration of a $ZnO/Mg_{0.2}Zn_{0.8}O/ZnO/Mg_{0.2}Zn_{0.8}O$ multishell nanorod heterostructure and its band diagrams for different ZnO (QW) shell widths (L_W).

[a)]Author to whom correspondence should be addressed; electronic mail: gcyi@postech.ac.kr
[b)]Also at: the School of Engineering, University of Tokyo, 7-3-1 Hongo, Bunkyo-ku, Tokyo 113-8656, Japan.

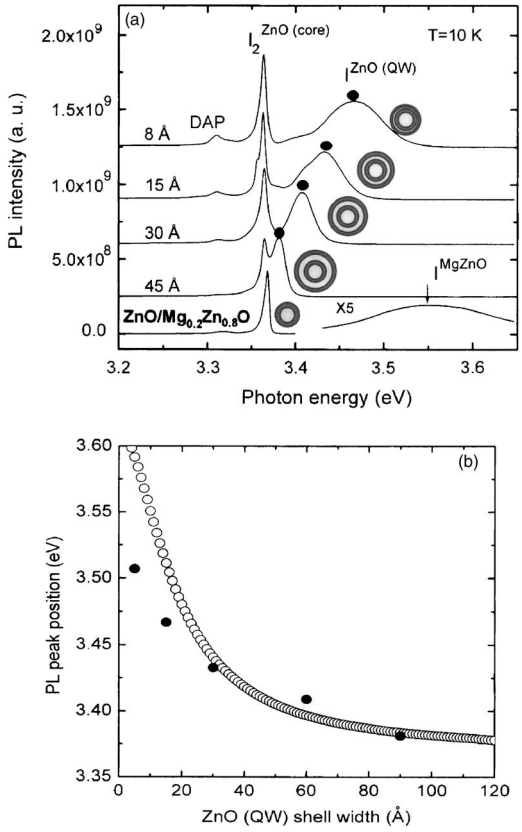

FIG. 2. (a) PL spectra (10 K) of $ZnO/Mg_{0.2}Zn_{0.8}O$ core/shell nanorod heterostructures and $ZnO/Mg_{0.2}Zn_{0.8}O/ZnO/Mg_{0.2}Zn_{0.8}O$ multishell nanorod quantum structures with different ZnO (QW) shell widths of 45, 30, 15, 8 Å. (b) Well-width dependent PL peak positions in $ZnO/Mg_{0.2}Zn_{0.8}O$ coaxial quantum structures (solid circles) and theoretically calculated values (open circles) in one period of one-dimensional square potential wells. In this calculation, we employed the following parameters: 0.28 and 1.8 m_o for the effective masses of electron and hole, respectively, a ratio of conduction and valence band offsets ($\triangle E_c/\triangle E_v$) of 9, and a band gap offset ($\triangle E_g$) of 250 meV.

argon whenever the reactants were delivered into the system, leading to formation of clean and abrupt interfaces as confirmed by high resolution transmission electron microscopy. A small lattice mismatch ($<1\%$) between ZnO and $Mg_{0.2}Zn_{0.8}O$ layers is also helpful to reduce defects in the interface.[1,8]

Far-field photoluminescence (PL) measurements were performed using the 325 nm line of a He–Cd laser as an excitation source at 10 K with an optical resolution of 1 Å.[1] To obtain optical spectra from a single nanorod, near-field scanning optical microscopy (NSOM) was used: a sharpened ultraviolet (UV) fiber, coated with a 50-nm-thick aluminum film, was used as a scanning probe, and a He–Cd laser light ($\lambda=325$ nm) was a light source to excite individual $ZnO/Mg_{0.2}Zn_{0.8}O/ZnO/Mg_{0.2}Zn_{0.8}O$ multishell nanorods through the UV fiber probe.[15] The fiber probe was used not only for excitation but also for collecting PL signals from the nanorods. The fiber probe was kept in close proximity to the sample surface ($\sim$10 nm) using the shear-force feedback technique. The probe collected light signal was analyzed by a monochromator and the intensity was measured by a cooled charge coupled device.

The general morphology of the nanorod heterostructures was investigated using field-emission scanning electron microscopy. The mean diameter and length of bare ZnO nanorods, grown at 800 °C for 2 h, are 26 nm and 2.5 μm, respectively. Subsequent growth processes of the ZnO (QW) and $Mg_{0.2}Zn_{0.8}O$ (QB) shell layers gradually increased the nanorod diameter: a growth time of QB layer of 30, 60, and 180 s produced nanorod heterostructures with various diameters of 51, 52, and 58 nm, respectively. Growth rates of the ZnO (QW) and $Mg_{0.2}Zn_{0.8}O$ (QB) shells were roughly 0.25 and 0.33 Å/s.

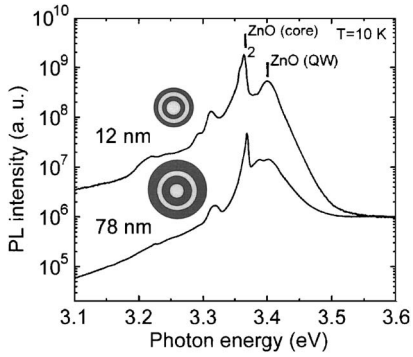

FIG. 3. PL spectra (10 K) of $ZnO/Mg_{0.2}Zn_{0.8}O/ZnO/Mg_{0.2}Zn_{0.8}O$ multishell nanorods upon variation of different $Mg_{0.2}Zn_{0.8}O$ (QB) shell widths of 12 and 78 nm. The $Mg_{0.2}Zn_{0.8}O$ (QB) shell layer thickness was fixed at 120 Å. Cross-sectional views, ZnO (QW) shell widths, and $Mg_{0.2}Zn_{0.8}O$ (QB) barrier widths of coaxial nanorod heterostructures are depicted in the inset, respectively.

Figure 2(a) shows 10 K PL spectra of the $ZnO/Mg_{0.2}Zn_{0.8}O$ core/shell and $ZnO/Mg_{0.2}Zn_{0.8}O/ZnO/Mg_{0.2}Zn_{0.8}O$ multishell nanorod heterostructures. The schematic diagrams of the heterostructures are also shown in Fig. 2(a). PL spectra of the $ZnO/Mg_{0.2}Zn_{0.8}O$ core/shell nanorods exhibited two dominant PL peaks at 3.364 and 3.553 eV corresponding to excitonic emissions from ZnO core nanorods ($I_2^{ZnO(core)}$) and $Mg_{0.2}Zn_{0.8}O$(I^{MgZnO}) shell layers, respectively.[1,16–18] Except for these PL peaks, no PL peak is shown in the range between 3.364 and 3.553 eV, strongly suggesting that there is no significant intermediate layer formation between ZnO core and $Mg_{0.2}Zn_{0.8}O$ shell layers. If there is an intermediate layer between the ZnO core and $Mg_{0.2}Zn_{0.8}O$ shell layers, there should be at least one additional PL peak between 3.364 and 3.553 eV.

Meanwhile, $ZnO/Mg_{0.2}Zn_{0.8}O/ZnO/Mg_{0.2}Zn_{0.8}O$ core/multishell nanorod heterostructures with various L_W, from 8 to 45 Å, and fixed L_B of 120 Å, showed a new PL peak marked by $I^{ZnO(QW)}$. The $I^{ZnO(QW)}$ peak energy increases from 3.382 to 3.467 eV, as the L_W is decreased from 45 to 8 Å. All the $I^{ZnO(QW)}$ peaks blueshift toward higher energy, compared with 3.364 eV of $I^{ZnO(core)}$. Such a blueshift of the PL emission peak can be well understood by the fact that quantized sublevel states are created due to the quantum size effect in core/multishell nanorod heterostructures and quantized energy levels increase by decreasing the embedded ZnO (QW) shell layer width, L_W.[19,20] Figure 2(b) also shows the dominant PL peak positions obtained from experiments and theoretical predictions in finite periodic square-well potential of $ZnO/Mg_{0.2}Zn_{0.8}O/ZnO/Mg_{0.2}Zn_{0.8}O$ core/multishell nanorods. As shown in Fig. 2(b), the experimental values agree well with the theoretical calculation except small deviation for the samples with the narrow quantum well widths below 20 Å, indicating that the systematic increase in PL emission energy with reducing well width is consistent with the quantum confinement effect.

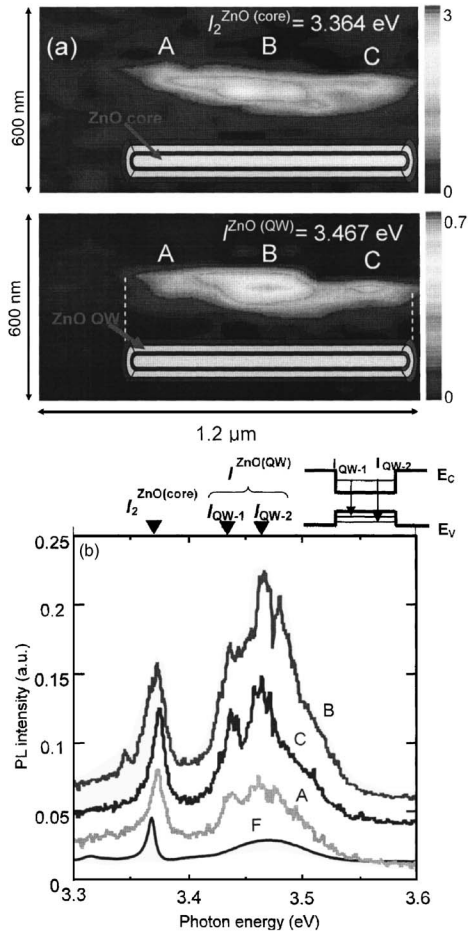

FIG. 4. (a) Monochromatic PL images of $ZnO/Mg_{0.2}Zn_{0.8}O/ZnO/Mg_{0.2}Zn_{0.8}O$ multishell nanorods measured at different emission energies of 3.364($I_2^{ZnO(core)}$) and 3.467($I^{ZnO(QW)}$) eV. In the $ZnO/Mg_{0.2}Zn_{0.8}O$ core/multishell nanorod quantum structures, ZnO (QW) and $Mg_{0.2}Zn_{0.8}O$ shell widths are 8 and 120 Å, respectively. (b) Near-field PL spectra taken at different positions marked by A, B, and C in (a). The black solid curve (F) is the far-field spectrum.

Compositional intermixing of ZnO and $Mg_{0.2}Zn_{0.8}O$ at the interface also may cause a blueshift of the PL peaks. To rule out this possibility, we prepared $ZnO/Mg_{0.2}Zn_{0.8}O/ZnO/Mg_{0.2}Zn_{0.8}O$ multishell nanorods with two different L_W (12 and 78 nm) and fixed L_B (30 Å). Intermixing at the interface may cause a couple of effects: (1) the Mg mole fraction in the alloy becomes higher by increasing the $Mg_{0.2}Zn_{0.8}O$ shell layer thickness (or growth time), resulting in a larger PL peak blueshift;[21] (2) effective ZnO (QW) shell thickness can be altered. As shown in Fig. 3, the $I^{ZnO(QW)}$ peak positions of the two nanorods are nearly the same, ruling out the intermixing possibility.

Furthermore, we examined spatially resolved PL properties of a single nanorod quantum structure by near-field scanning optical microscopy (NSOM). Figures 4(a) and 4(b) show the near-field images and spectra of a $ZnO/Mg_{0.2}Zn_{0.8}O/ZnO/Mg_{0.2}Zn_{0.8}O$ multishell nanorod with L_W of 8 Å and L_B of 120 Å. As shown in Fig. 4(a), near-field PL intensity distribution taken at two photon energies of 3.364 (corresponding to $I_2^{ZnO(core)}$) and 3.467 eV (corresponding to $I^{ZnO(QW)}$) are very similar, except for topographically induced emission intensity variation. This indicates that uniform ZnO core and shell layers form along the axial direction of the multishell nanorod. In addition, near-field PL spectra, collected from different positions as denoted by *A*, *B* and *C* in Fig. 4(a), were obtained as shown in Fig. 4(b). This result demonstrates that constituent layers of the multishell nanorod, ZnO and $Mg_{0.2}Zn_{0.8}O$, are homogeneously grown throughout the entire nanorod heterostructures.

It is worth noting that near-field PL spectra show two distinct peaks at 3.435(I_{QW-1}) and 3.460(I_{QW-2}) eV [Fig. 4(b)] [far-field PL spectra exhibited only a single peak at 3.467 eV [Fig. 2(a)]. The I_{QW-1} and I_{QW-2} are PL emission peaks due to the ground state of the electrons and the two different valence band states of the holes as depicted in the upper right side of Fig. 4(b).

In conclusion, catalyst-free MOVPE demonstrates fabrication of high quality $ZnO/Mg_{0.2}Zn_{0.8}O/ZnO/Mg_{0.2}Zn_{0.8}O$ multishell nanorod quantum structures by fine tuning the ZnO (QW) and $Mg_{0.2}Zn_{0.8}O$ (QB) shell thicknesses. From both far-field and near-field PL spectra of the nanorod quantum structures, systematic PL blueshifts with decreasing well layer widths were observed, resulting from the quantum confinement effect. This controlled growth of coaxial multishell nanorod quantum structures realizes the artificial design of a kind of semiconductor nanorod quantum structures, which could open up significant opportunities for exploring high performance electronic and photonic nanodevices.

This work was financially supported through the National Creative Research Initiative Project by the KOSEF and the Air Force Office of Scientific Research (FA5209-04-P-0325), USA.

[1] W. I. Park, G.-C. Yi, M. Kim, and S. J. Pennycook Adv. Mater. (Weinheim, Ger.) **15**, 526 (2003).
[2] S. W. Jung, W. I. Park, G.-C. Yi, and M. Kim, Adv. Mater. (Weinheim, Ger.) **15**, 1358 (2003).
[3] J. Hu, Y. Bando, Z. Liu, T. Sekiguchi, D. Goldberg, and J. Zhan, J. Am. Chem. Soc. **125**, 11306 (2003).
[4] D. Li, Y. Wu, R. Fan, P. Yang, and A. Majumdar, Appl. Phys. Lett. **83**, 3186 (2003).
[5] X. Wang, C. J. Summers, and Z. L. Wang, Adv. Mater. (Weinheim, Ger.) **16**, 1215 (2004).
[6] C. Thelander, T. Mårtensson, M. T. Björk, B. J. Ohlsson, M. W. Larsson, L. R. Wallenberg, and L. Samuelson, Appl. Phys. Lett. **83**, 2052 (2003).
[7] Y. Wu, J. Xiang, C. Yang, W. Lu, and C. M. Lieber, Nature (London) **430**, 61 (2004).
[8] W. I. Park, S. J. An, G.-C. Yi, and M. Kim, *Fourth IEEE Conference Proceeding on Nanotechnology* (IEEE, New York, 2004), p. 83.
[9] L. J. Lauhon, M. S. Gudiksen, D. Wang, and C. M. Lieber, Nature (London) **57**, 420 (2002).
[10] Q. Li and C. Wang, J. Am. Chem. Soc. **125**, 9892 (2003).
[11] H.-M. Lin, Y.-L. Chen, J. Yang, Y.-C. Liu, K.-M. Yin, J. J. Kai, F.-R. Chen, L.-C. Chen, Y.-F. Chen, and C.-C. Chen, Nano Lett. **3**, 537 (2003).
[12] K. K. Nanda, F. E. Kruis, and H. Fissan, Nano Lett. **1**, 605 (2001).
[13] H. Yu, J. Li, R. A. Loomis, L.-W. Wang, and W. E. Buhro, Nat. Mater. **2**, 517 (2003).
[14] S. J. An, W. I. Park, G.-C. Yi, Y.-J. Kim, H.-B. Kang, and M. Kim, Appl. Phys. Lett. **84**, 3612 (2004).
[16] W. I. Park, S. J. An, J. L. Yang, G.-C. Yi, S. Hong, T. Joo, and M. Kim, J. Phys. Chem. B **108**, 15457 (2004).
[15] T. Yatsui, J. Lim, M. Ohtsu, S. J. An, and G.-C. Yi, Appl. Phys. Lett. **85**, 727 (2004).
[17] S. Fujita, T. Takagi, H. Tanaka, and S. Fujita, Phys. Status Solidi B **241**, 599 (2004).
[18] H. Kato, M. Sano, K. Miyamoto, and T. Yao, Phys. Status Solidi B **241**, 612 (2004).
[19] A. Ohtomo, K. Tamura, I. Ohkubo, H. Koinuma, T. Yasuda, and Y. Segawa, Appl. Phys. Lett. **75**, 980 (1999).
[20] T. Makino, C. H. Chia, Ng. T. Tuan, H. D. Sun, Y. Segawa, M. Kawasaku, A. Ohtomo, K. Tamura, and H. Koinuma, Appl. Phys. Lett. **77**, 975 (2000).
[21] W. I. Park, G.-C. Yi, and H. M. Jang, Appl. Phys. Lett. **79**, 2022 (2001).

NANO LETTERS

2005
Vol. 5, No. 12
2548−2551

Self-Assembly of Size- and Position-Controlled Ultralong Nanodot Chains using Near-Field Optical Desorption

Takashi Yatsui,*,† Wataru Nomura,‡ and Motoichi Ohtsu†,‡

Solution-Oriented Research for Science and Technology (SORST), Japan Science and Technology Agency, Machida, Tokyo, 194-0004 Japan, and School of Engineering, The University of Tokyo, Bunkyo-ku, Tokyo, 113-8656 Japan

Received September 23, 2005; Revised Manuscript Received October 23, 2005

ABSTRACT

We report the self-assembly of a size- and position-controlled ultralong nanodot chain using a novel effect of near-field optical desorption. A sub-100-nm dot chain with a deviation of 5 nm forms at a size based on plasmon resonance, depending on the photon energy; the resulting structure forms a high-transmission-efficiency nanoscale waveguide. Using this method with simple lithographically patterned substrates allows one to increase the throughput of the production of nanoscale structures dramatically at all scales.

Future optical transmission systems will require advanced photonic switching device arrays and advanced photonic integrated circuits (ICs) in order to increase data transmission rates and capacity. Consequently, these devices will need to be significantly smaller than conventional diffraction-limited photonic devices. To fulfill this requirement, we propose a nanometer-scale photonic IC consisting of sub-100-nm scale dots and lines.[1] As a representative device, a nanophotonic switch can be realized by controlling the dipole forbidden optical energy transfer among resonant energy states in CuCl quantum cubes via an optical near field.[2]

However, coupling these photonic devices with external conventional diffraction-limited photonic devices requires a nanometer-scale optical waveguide for far/near-field conversion. To realize this, it has been suggested that electromagnetic energy can be guided along a nanodot coupler consisting of chains of closely spaced metallic nanoparticles.[3−5] The energy transfer in the nanodot coupler relies on dipole−dipole coupling between neighboring nanoparticles. To realize a nanodot coupler consisting of 50-nm gold nanoparticles with 50-nm separation, it is estimated that the dispersion of their separation must be as small as 10 nm to obtain an efficiency equivalent to 50% that of an ordered array.[3]

Promising components for integrating such nanometer-sized photonic devices include chemically synthesized nanocrystals, such as metallic nanocrystals,[6] semiconductor quantum dots,[7] and nanorods[8] because they have uniform size, controlled shape, defined chemical composition, and tunable surface chemical functionality. However, position- and size-controlled deposition methods have not yet been developed. For greater precision, electron beams[9] and scanning probe microscopes[10−12] have been used to control the site on the substrate. However, these techniques have inherent low throughput ratios for production.

To fabricate nanophotonic devices at all scales, we propose a self-assembling method that builds nanodot chains by controlling desorption with an optical near-field. Our approach is illustrated schematically in Figure 1A. A nanodot chain of metallic nanoparticles was fabricated using radio frequency (RF) sputtering under illumination on a glass substrate. To realize self-assembly, a simple groove 100-nm wide and 30-nm deep was fabricated on the glass substrate. During deposition of the metal, linear polarized light illuminating the groove directly above (E_{90}) was used to excite a strong optical near-field at the edge of the groove (see Figure 1B), which induced the desorption of the deposited metallic nanoparticles.[13] A metallic dot has a strong optical absorption because of plasmon resonance,[14,15] which depends strongly on particle size. This can induce desorption of the deposited metallic nanodot when it reaches the resonant diameter.[16,17] As the deposition of metallic dots proceeds, the growth is governed by a tradeoff between deposition and desorption, which determines dot size, depending on the photon energy of the incident light. Consequently, the metallic nanoparticles should align along the groove (Figure 1B and C).

* Corresponding author. E-mail: yatsui@ohtsu.jst.go.jp.
† SORST, Japan Science and Technology Agency.
‡ School of Engineering, The University of Tokyo.

10.1021/nl051898z CCC: $30.25
Published on Web 11/15/2005

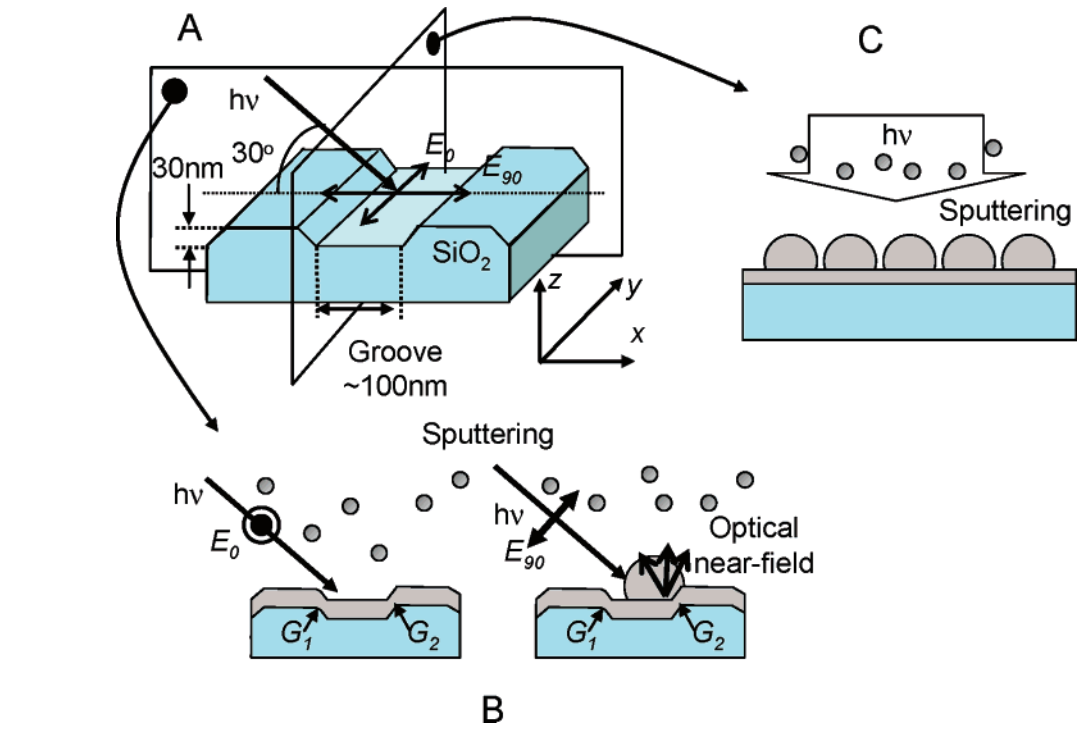

Figure 1. (A) Size- and position-controlled ultralong nanodot chain formation. The slanted light had a spot diameter of 1 mm. The groove parallels axis *y*. E_{90} and E_0 are perpendicular and parallel to axis *y*, respectively. (B and C) Cross-sections in planes *XZ* and *YZ*, respectively.

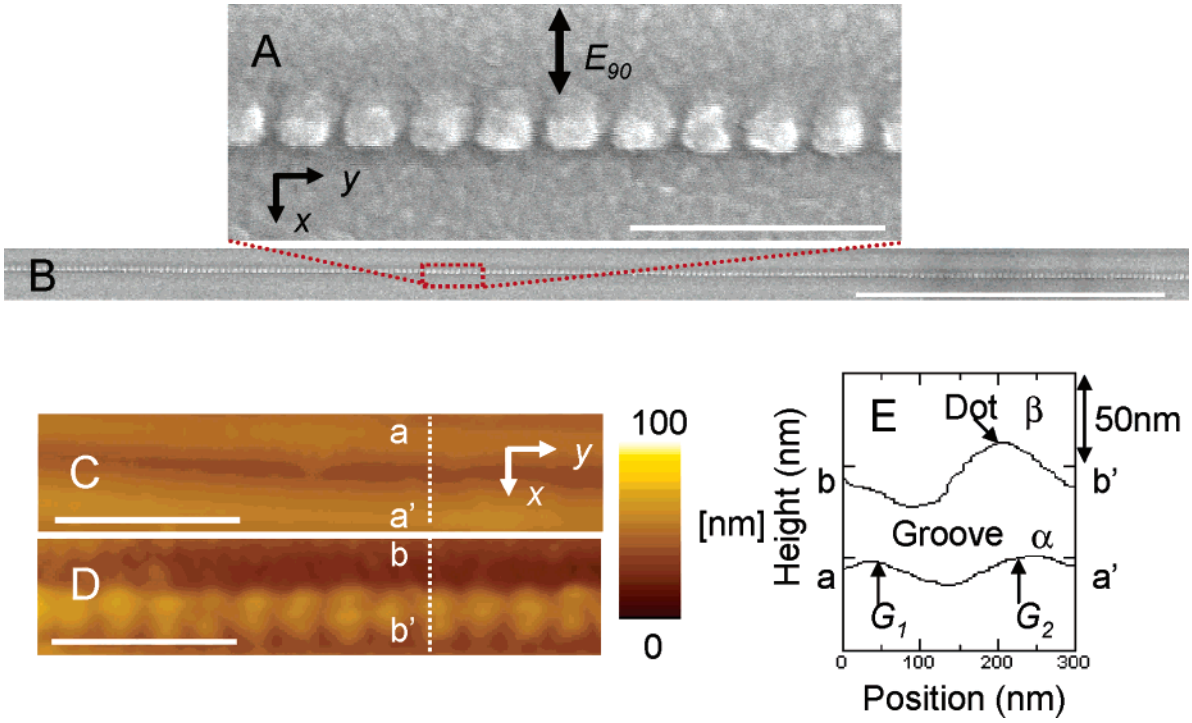

Figure 2. (A and B) SEM images of deposited aluminum with perpendicular polarization E_{90} ($h\upsilon = 2.33$ eV). (C and D) Respective AFM images of the surface of the glass substrate before and after aluminum deposition, at the same position. (E) Curves α and β show the respective cross-sectional profiles of AFM images along dashed white lines a−a' in C and b−b' in D. Scale bars: (A) 500 nm, (B) 10 μm, (C and D) 500 nm.

Illumination with 2.33-eV light (50 mW) during the deposition of aluminum resulted in the formation of 99.6-nm-diameter aluminum nanodot chains with 27.9-nm separation that were as long as 100 μm in a highly size- and position-controlled manner (see Figure 2A and B). The deviation of both nanodot size and separation, determined from scanning electron microscopy (SEM) images, were as small as 5 nm. Such a small deviation of 5% meets the requirement of the nanodot coupler for an efficiency equivalent to 50% of that of an ordered array. To identify

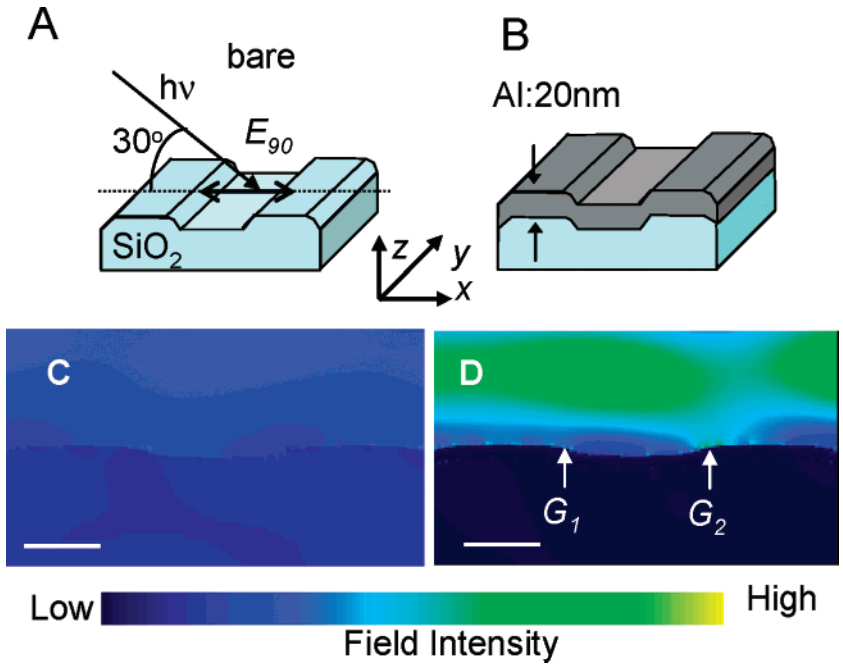

Figure 3. The field intensities ($|E|^2$) calculated using the FDTD method for the bare glass substrate (A and C) and glass coated with 20-nm-thick aluminum film (B and D). Scale bars: (C and D) 100 nm.

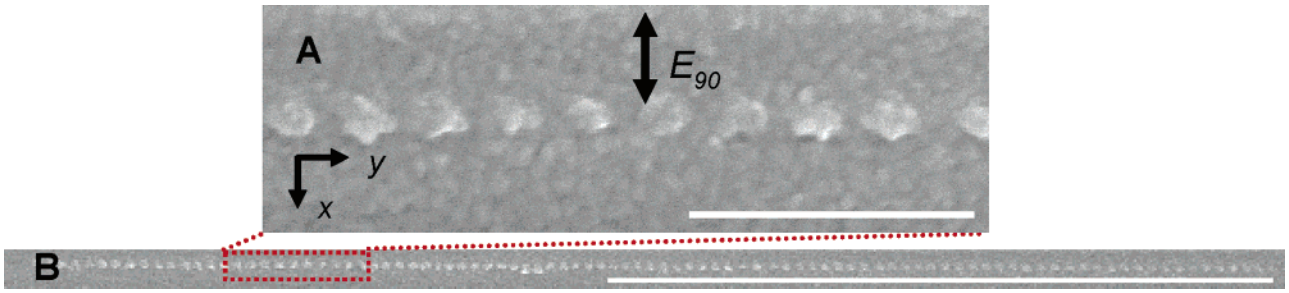

Figure 4. (A and B) SEM images of deposited aluminum with $E_{9.0}$ ($h\upsilon = 2.62$ eV). Scale bars: (A) 500 nm and (B) 5 μm.

the position of the chain, we compared topographic atomic force microscopy (AFM) images of the surface of the glass substrate before (Figure 2C) and after (Figure 2D) aluminum deposition, at the same position. Curves α and β in Figure 2E show the respective cross-sectional profiles along dashed white lines a−a' in Figure 2C and b−b' in Figure 2D. Comparison of these profiles showed that the nanodot chain formed around edge G_2. Furthermore, illumination with parallel polarization along groove E_0 resulted in film growth along the groove structure and no dot structure was obtained. Because the near-field intensity with E_{90} was enhanced strongly at the metallic edge of the groove in comparison with E_0 owing to edge enhancement of the electrical field (see Figure 1B), a strong near-field intensity results in nanodot chain formation.

Dot formation at the one-sided edge originates from the asymmetric electric-field intensity distribution, owing to the slanted illumination. To confirm this prediction, we calculated the electric field intensity using a finite-difference time-domain (FDTD) based simulator (*Poynting for Optics*, a product of Fujitsu, Japan). We compared the electric field intensity distribution between a bare glass groove (100-nm wide and 30-nm deep) and one coated with 20-nm-thick aluminum ($n = 0.867 + i6.42$) with slanted (30°) illumination at a photon energy of 2.33 eV (Figure 3A and B). Although the bare groove in the glass does not induce localization of the electric field intensity (Figure 3C), we found that the slanted illumination enhanced the electric field intensity strongly at the backside of metallized groove G_2 (Figure 3D) only, inducing desorption of the metallic nanoparticles. It is reasonable to assume that the desorption was excited after the deposition of the aluminum film. The oscillations in the electric field perpendicular to the edge induce charges on the metallized edge of the groove, and these induced charges generate a strong electric field and the associated scattering.[18]

Aluminum-dot chain formation was also observed with RF sputtering of aluminum under illumination with 2.62-eV light (100 mW) with E_{90} using the same grooved (100-nm wide and 30-nm deep) glass substrate, which resulted in the formation of 84.2-nm nanodots with 48.6-nm separation (see Figure 4A and B). Although the deviation of both nanodot size and separation were as large as 10 nm, the dot size was reduced in proportion to the increase in the photon energy (99.6 nm × (2.33/2.62) = 88.5 nm ≈ 84.2 nm). This result indicates that the obtained size is determined by the

photon energy and that the size-controlled dot-chain formation originates from photodesorption of the deposited metallic nanoparticles.[13] The period under 2.62-eV light illumination (132.8 nm) was longer than that (127.5 nm) for fabrication using the 2.33-eV light. However, the ratios of the center−center distance (d) and radius (a) of the nanodots (d/a = 2.56 and 3.15 obtained under 2.33-eV and 2.62-eV light illumination, respectively) are similar to the optimum value, which is in the range of 2.4−3.0, for the efficient transmission of the optical energy along the chain of spherical metal dots calculated using Mie's theory,[19] which is determined by the tradeoff between the increase in the transmission loss in the metal and the reduction in the coupling loss between adjacent metallic nanoparticles as the separation increases. Future theoretical analysis, which will include the effect of a continuous metallic film below the nanodot chain, is required to explain the optimum separation of the nanoparticles depending on the photon energy. However, our preliminary results imply that the center−center distance is set at the optimum distance for efficient energy transfer of the optical near-field, given that such a strong optical near-field can induce desorption of the deposited metallic nanoparticles and result in position-controlled dot-chain formation.

We believe that the resulting structure should have high transmission efficiency for optical near-field energy, which is suitable for a nanodot coupler, given that the nanodot chain forms at a size based on plasmon resonance, and we have already reported the efficient energy transfer along a nanodot chain involving a continuous metallic film below the nanodot chain.[5] Furthermore, because our deposition method is based on a photodesorption reaction, illumination at multiple photon energies using the simple lithographically patterned substrate could realize the simultaneous fabrication of size- and position-controlled nanoscale structures with different particle sizes and with other metals or semiconductors. The use of the self-assembling method with a simple lithographically patterned substrate will increase the throughput of the production of nanoscale structures dramatically, which is required by future systems.

References

(1) Ohtsu, M.; Kobayashi, K.; Kawazoe, T.; Sangu, S.; Yatsui, T. *IEEE J. Sel. Top. Quantum Electron.* **2002**, *8*, 839.
(2) Kawazoe, T.; Kobayashi, K.; Sangu, S.; Ohtsu, M. *Appl. Phys. Lett.* **2003**, *82*, 2957.
(3) Krenn, J. R.; Dereux, A.; Weeber, J. C.; Bourillot, E.; Lacroute, Y.; Goudonnet, J. P.; Schider, G.; Gotschy, W.; Leitner, A.; Aussenegg, F. R.; Girard, C. *Phys. Rev. Lett.* **1999**, *82*, 2590.
(4) Maier, S. A.; Kik, P. G.; Atwater, H. A.; Meltzer, S.; Harel, E.; Koel, B. E.; Requicha, A. A. G. *Nat. Mater.* **2003**, *2*, 229.
(5) Nomura, W.; Yatsui, T.; Ohtsu, M. *Appl. Phys. Lett.* **2005**, *86*, 181108.
(6) Brust, M.; Kiely, C. J. *Colloids Surf., A* **2002**, *202*, 175.
(7) Alivisatos, A. P. *Science* **1996**, *271*, 933.
(8) Yang, P. *Nature* **2003**, *425*, 243.
(9) Ishikawa, T.; Kohmoto, S.; Asakawa, K. *Appl. Phys. Lett.* **1998** *73*, 1712.
(10) Kohmoto, S.; Nakamura, H.; Ishikawa, T.; Asakawa, K. *Appl. Phys. Lett.* **1999**, *75*, 3488.
(11) Ara, M.; Graaf, H.; Tada, H. *Appl. Phys. Lett.* **2002**, *80*, 2565.
(12) Yatsui, T.; Kawazoe, T.; Ueda, M.; Yamamoto, Y.; Kourogi, M.; Ohtsu, M. *Appl. Phys. Lett.* **2002**, *81*, 3651.
(13) Yatsui, T.; Takubo, S.; Lim, J.; Nomura, W.; Kourogi, M.; Ohtsu, M. *Appl. Phys. Lett.* **2003**, *83*, 1716.
(14) Wokaun, A.; Gordon, J. P.; Liao, P. F. *Phys. Rev. Lett.* **1982**, *48*, 957.
(15) Boyd, G. T.; Rasing, T.; Leite, J. R. R.; Shen, Y. R. *Phys. Rev. B* **1984**, *30*, 519.
(16) Bosbach, J.; Martin, D.; Stietz, F.; Wenzel, T.; Träger, F. *Appl. Phys. Lett.* **1999**, *74*, 2605.
(17) MacDonald, K. F.; Fedotov, V. A.; Pochon, S.; Ross, K. J.; Stevens, G. C.; Zheludev, N. I.; Brocklesby, W. S.; Emel'yanov, V. I. *Appl. Phys. Lett.* **2002**, *80*, 1643.
(18) Sommerfeld, A. *Optics*; Academic Press: New York, 1954.
(19) Quinten, M.; Leitner, A.; Krenn, J. R.; Aussenegg, F. R. *Opt. Lett.* **1998**, *23*, 1331.

NL051898Z

Optical interconnects based on optical far- and near-field interactions for high-density data broadcasting

Makoto Naruse

National Institute of Information and Communications Technology, 4-2-1 Nukui-kita, Koganei, Tokyo 184-8795, Japan
naruse@nict.go.jp

Tadashi Kawazoe

Japan Science and Technology Agency, 687-1 Tsuruma, Machida, Tokyo 194-0004, Japan
kawazoe@ohtsu.jst.go.jp

Suguru Sangu

Ricoh Co. Ltd., 16-1 Shinei-cho, Tsuzuki-ku, Yokohama, Kanagawa 224-0035, Japan
suguru.sangu@nts.ricoh.co.jp

Kiyoshi Kobayashi

Tokyo Institute of Technology, 2-12-1 Ookayama, Meguro-ku, Tokyo 152-8551, Japan
kkoba@phys.titech.ac.jp

Motoichi Ohtsu

The University of Tokyo, 7-3-1 Hongo, Bunkyo-ku, Tokyo 113-8656, Japan
ohtsu@ee.t.u-tokyo.ac.jp

Abstract: Ultrahigh-density data-broadcasting optical interconnects are proposed and experimentally demonstrated using optical near-field interactions between quantum dots, which cannot be driven by far-field light, allowing sub-wavelength device operation, and far-field excitation for global interconnects. The proposed scheme helps to solve interconnection difficulties experienced in nano-scale device arrays since components for individually guiding light from external systems are not required. Combining the broadcasting mechanism with switching and summation architectures will allow nano-scale integration of parallel processing devices.

OCIS codes: (200.4650) Optical interconnects; (270.0270) Quantum optics; (070.6020) Signal processing

References and links

1. International Technology Roadmap for Semiconductors, http://public.itrs.net/
2. D. A. B. Miller, "Rationale and challenges for optical interconnects to electronic chips," in Proceedings of e IEEE **88**, 728-749 (2000).
3. N. McArdle, M. Naruse, H. Toyoda, Y. Kobayashi, and M. Ishikawa, "Reconfigurable optical interconnections for parallel computing," in Proceedings of IEEE **88**, 829-837 (2000).
4. M. Ohtsu, K. Kobayashi, T. Kawazoe, S. Sangu, and T. Yatsui, "Nanophotonics: design, fabrication, and operation of nanometric devices using optical near fields," IEEE J. Sel. Top Quantum Electron. **8**, 839-862 (2002).
5. T. Yatsui, M. Kourogi, and M. Ohtsu, "Plasmon waveguide for optical far/near-field conversion," Appl. Phys. Lett. **79**, 4583-4585 (2001).

#8596 - $15.00 USD Received 26 August 2005; revised 22 December 2005; accepted 22 December 2005

6. J. Takahara, Y. Suguru, T. Hiroaki, A. Morimoto, and T. Kobayashi, "Guiding of a one-dimensional optical beam with nanometer diameter," Opt. Lett. **22**, 475-477 (1997).
7. W. Nomura, M. Ohtsu, and T. Yatsui, "Nanodot coupler with a surface plasmon polariton condenser for optical far/near-field conversion," Appl. Phys. Lett. **86**, 181108-1-3 (2005).
8. J. W. Goodman, A. R. Dias, and L. M. Woody, "Fully parallel, high-speed incoherent optical method for performing discrete Fourier transforms," Opt. Lett. **2**, 1-3 (1978).
9. P. S. Guilfoyle and D. S. McCallum, "High-speed low-energy digital optical processors," Opt. Eng. **35**, 436-442 (1996).
10. B. Li, Y.Qin, X. Cao, and K. M. Sivalingam, "Photonic packet switching: Architecture and performance," Optical Networks Magazine **2**, 27-39 (2001).
11. K. Kobayashi and M. Ohtsu, "Quantum theoretical approach to a near-field optical system," J. Microsc. **194**, 249-254 (1999).
12. K. Kobayashi, S. Sangu, H. Ito, and M. Ohtsu, "Near-field optical potential for a neutral atom," Phys. Rev. A **63**, 013806-1-9 (2001).
13. T. Kawazoe, K. Kobayashi, J. Lim, Y. Narita, and M. Ohtsu, "Direct observation of optically forbidden energy transfer between CuCl Quantum Cubes via near-field Optical Spectroscopy," Phys. Rev. Lett. **88**, 067404-1-4 (2002).
14. T. Kawazoe, K. Kobayashi, S. Sangu, and M. Ohtsu, "Demonstration of a nanophotonic switching operation by optical near-field energy transfer," Appl. Phys. Lett. **82**, 2957-2959 (2003).
15. T. Kawazoe, K. Kobayashi, and M. Ohtsu, "The optical nano-fountain: a biomimetic device that concentrates optical energy in a nanometric region," Appl. Phys. Lett. **86**, 103102-1-3 (2005).
16. M. Naruse, T. Miyazaki, F. Kubota, T. Kawazoe, K. Kobayashi, S. Sangu, and M. Ohtsu, "Nanometric summation architecture using optical near-field interaction between quantum dots," Opt. Lett. **30**, 201-203 (2005).
17. E. A. De Souza, M. C. Nuss, W. H. Knox, and D. A. B. Miller, "Wavelength-division multiplexing with femtosecond pulses," Opt. Lett. **20**, 1166-1168 (1995).
18. N. Sakakura and Y. Masumoto, "Persistent spectral-hole-burning spectroscopy of CuCl quantum cubes", Phys. Rev. B **56**, 4051-4055 (1997).
19. Z. K. Tang, A. Yanase, T. Yasui, Y. Segawa, and K. Cho, "Optical selection rule and oscillator strength of confined exciton system in CuCl thin films," Phys. Rev. Lett. **71**, 1431-1434 (1993).
20. T. Itoh, Y. Iwabuchi, and M. Kataoka, "Study on the size and shape of CuCl microcrystals embedded in alkali-chloride matrices and their correlation with exciton confinement," Phys. Status Solidi B **145**, 567-577 (1988).

1. Introduction

Interconnects are a critical issue for information processing devices and systems [1], and optical interconnects have been thoroughly investigated for their ability to overcome the limitations of their electrical counterparts [2, 3]. Nanophotonics requires yet another type of interconnect since it is based on local electromagnetic interactions between a few nanometer-size particles, such as quantum dots (QDs), via optical near fields, which in turn allows device integration at densities beyond the diffraction limit [4]. For the interconnects in such high-density nanophotonic devices, far- and near-field conversion devices are required, as shown in Fig. 1(a); for instance, plasmon waveguides [5, 6] and nano-dot couplers [7] have been successfully demonstrated. However, since many of such conversion devices are needed for all nanophotonic devices distributed within a sub-wavelength scale region, such interconnection is another serious bottleneck for system integration. In this paper, we propose an interconnection method based on both far- and near-field interactions for data broadcasting purposes, meaning that multiple nanophotonic devices are supplied with the same input data.

2. Broadcast interconnects

We first describe the application of data-broadcasting interconnects to nanophotonic circuits and their physical principles. Data broadcasting is a fundamental functionality required for computing operations such as matrix-vector products [8, 9] and switching operations, such as those used in a broadcast-and-select architecture [10], where multiple functional blocks require the same input data, as schematically shown in Fig. 1(a). For example, consider a matrix-vector multiplication given by $\boldsymbol{v} = A\boldsymbol{s}$, where $\boldsymbol{v} = (v_1, \cdots, v_m)$, $\boldsymbol{s} = (s_1, \cdots, s_n)$, and A is an $m \times n$ matrix. Here, to compute every v_j from the input data $\boldsymbol{s}$, broadcast interconnects

#8596 - $15.00 USD Received 26 August 2005; revised 22 December 2005; accepted 22 December 2005

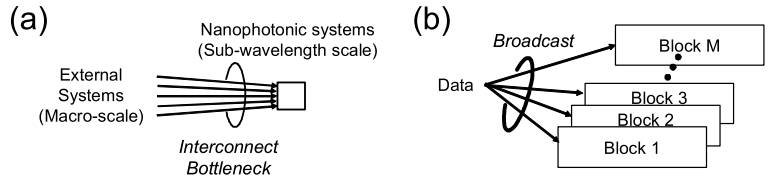

Fig. 1. (a) Interconnections from macro-scale external systems to sub-wavelength-scale nanophotonic systems. (b) Broadcast interconnects.

are required if each v_j is calculated in distinct processing hardware. Optics is in fact well suited to such broadcast operations in the form of simple imaging optics [8, 9] or in optical waveguide couplers thanks to the nature of optical wave propagation. However, the integration density is physically limited by the diffraction limit, which leads to bulky system configurations.

3. Operating principle

The physical operating principle of broadcasting is described here. An irreversible energy transfer between neighboring QDs is possible via local optical near-field interactions and intrasublevel relaxation, as schematically shown in Fig. 2(c) [4, 11-13]. This unique feature enables nonlinear functions, such as optical switching [14], convergence of energy [15], and data summation [16], as well as extremely high integration density. From the viewpoint of interconnects, however, it places stringent requirements on individual addressability since the devices are arrayed on the sub-wavelength scale, as mentioned in the introduction. However, data broadcasting allows another interconnection scheme. Suppose that arrays of nanophotonic circuit blocks, such as the nanophotonic switches described later, are distributed within an area whose size is comparable to the wavelength, as shown in Fig. 2(a). Here, for broadcasting, multiple input QDs simultaneously accept identical input data carried by diffraction-limited far-field light by tuning their optical frequency so that the light is coupled to energy sublevels that are associated with the input of each block, while not affecting the output and internal operations of each block, as illustrated in Fig. 2(b) and described in more detail below. In a frequency multiplexing sense, this interconnection method is similar to multi-wavelength chip-scale interconnects [17]. Known methods require a physical space comparable to the number of diffraction-limited input channels, due to wavelength demultiplexing, whereas in our proposed scheme, the device arrays are integrated on the sub-wavelength scale, and multiple frequencies are multiplexed in the far-field light supplied to the device.

Here we explain the far- and near-field coupling mentioned above based on a model assuming CuCl QDs, which are also employed in experiments described below. The potential barrier of CuCl QDs in an NaCl crystal can be regarded as infinitely high, and the energy eigenvalues for the quantized exciton energy level (n_x, n_y, n_z) in a CuCl QD with side of length L are given by

$$E_{(n_x,n_y,n_z)} = E_B + \frac{\hbar^2\pi^2}{2M(L-a_B)^2}(n_x^2+n_y^2+n_z^2) \tag{1}$$

where E_B is the energy of the bulk Z_3 exciton, M is the mass of the exciton for the motion of the center of mass (C. M.), a_B is its Bohr radius, n_x, n_y, and n_z are quantum numbers for the C. M. motion ($n_x, n_y, n_z = 1,2,3,\ldots$), and $a = L - a_B$ corresponds to an effective side length taking into account so-called dead layer correction [18]. According to Eq. (1), there exists a resonance between the quantized exciton energy sublevel of quantum number (1, 1, 1) for the

#8596 - $15.00 USD Received 26 August 2005; revised 22 December 2005; accepted 22 December 2005

QD with effective side length a and that of quantum number (2, 1, 1) for the QD with effective side length $\sqrt{2}a$. (For simplicity, we refer to the QDs with effective side lengths a and $\sqrt{2}a$ as "QD a" and "QD $\sqrt{2}a$", respectively.) Energy transfer between QD a and QD $\sqrt{2}a$ occurs via optical near fields [11-13]. It should be noted here that the optical selection rule tells us that the exciton energy levels with even quantum numbers do not contribute to the optical transition, meaning that the electric dipole transitions between the ground state and the states with even quantum numbers are prohibited for far-field light [18, 19]. Optical near-fields, on the other hands, allow excitation of such states having even quantum numbers thanks to the local steep variation of electric field, as illustrated in Fig. 2(c). (Details are shown in Ref. [4].) In this paper, we call exciton states with even quantum numbers "*dipole-forbidden*" states (or equivalently, dipole-forbidden energy sublevels) and states with odd quantum numbers "*dipole-allowed*" states (or equivalently, dipole-allowed energy sublevels). Far-field light can couple to dipole-allowed energy sublevels but cannot couple to dipole-forbidden energy sublevels.

In order to easily understand the principle of the broadcast interconnects shown later, here we introduce a *frequency-and-quantum-dot-size diagram* in Fig. 2(d), where the horizontal axis shows QD size and the vertical axis shows energy level or its equivalent optical frequency. The 3-digit sets in the diagram are the quantum numbers of the exciton states. In the example shown in Fig. 2(d), the (1, 1, 1)-level of the QD a and the (2, 1, 1)-level of the QD $\sqrt{2}a$ exist at the same vertical position.

We note that the input energy level for the QDs, that is, the (1, 1, 1)-level, can also couple to the far-field excitation. We utilized this fact for data broadcasting. One of the design restrictions is that energy-sublevels for input channels do not overlap with those for output channels. Also, if there are QDs internally used for near-field coupling, dipole-allowed energy sublevels for those QDs cannot be used for input channels since the inputs are provided by far-field light, which may lead to misbehavior of internal near-field interactions if resonant levels exist. Therefore, frequency partitioning among the input, internal, and output channels is important. The frequencies used for broadcasting, denoted by $\Omega_i = \{\varpi_{i,1}, \varpi_{i,2}, \cdots, \varpi_{i,A}\}$, should

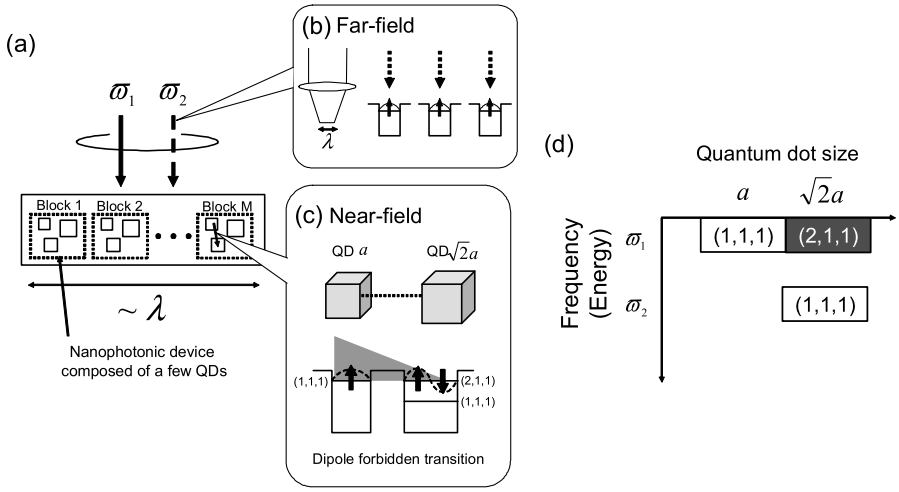

Fig. 2. (a) Broadcast-type interconnects to nanophotonic device arrays. (b) Near-field interaction between quantum dots for internal functions. (c) Far-field excitation for identical data input (broadcast) to nanophotonic devices within a diffraction-limit-sized area. (d) Frequency-and-quantum-dot-size diagram.

be distinct values and should not overlap with the output channel frequencies $\Omega_o = \{\varpi_{o,1}, \varpi_{o,2}, \cdots, \varpi_{o,B}\}$. A and B indicate the number of frequencies used for input

#8596 - $15.00 USD Received 26 August 2005; revised 22 December 2005; accepted 22 December 2005

and output channels, respectively. Also, there will be frequencies needed for internal device operations that are not used for either input or output (discussed later in the sum of product example), denoted by $\Omega_n = \{\varpi_{n,1}, \varpi_{n,2}, \cdots, \varpi_{n,C}\}$, where C is the number of those frequencies. In other words, the design criteria for global data broadcasting is to exclusively assign input, output, and internal frequencies, Ω_i, Ω_o, and Ω_n, respectively. Figure 3 illustrates two examples of frequency partitioning using frequency-and-quantum-dot-size diagrams.

In the example shown in Fig. 3(a), we used a nanophotonic switch (2-input AND gate) composed of three QDs with a size ratio of $1:\sqrt{2}:2$. The two input channels are assigned to QD a and QD $2a$, and the output appears from QD $\sqrt{2}a$. The underlining principles are the irreversible signal transfer via resonant energy levels, which was described earlier. When the (1, 1, 1)-level of the QD $2a$ is occupied (state filling), an exciton in QD a will be transferred to the (1,1,1)-level of QD $\sqrt{2}a$ and dissipated. Therefore, the output from QD $\sqrt{2}a$ is at a high level. On the other hand, when the (1, 1, 1)-level of the QD $2a$ is not occupied, an exciton in QD a will be transferred to the (1,1,1)-level of QD $2a$ and dissipated, and so the output from the QD $\sqrt{2}a$ is at a low level. The details of the switching principle are shown in Ref. [14]. Here, multiple input dots QD a and QD $2a$ can accept identical input data via far-field light for broadcasting purposes.

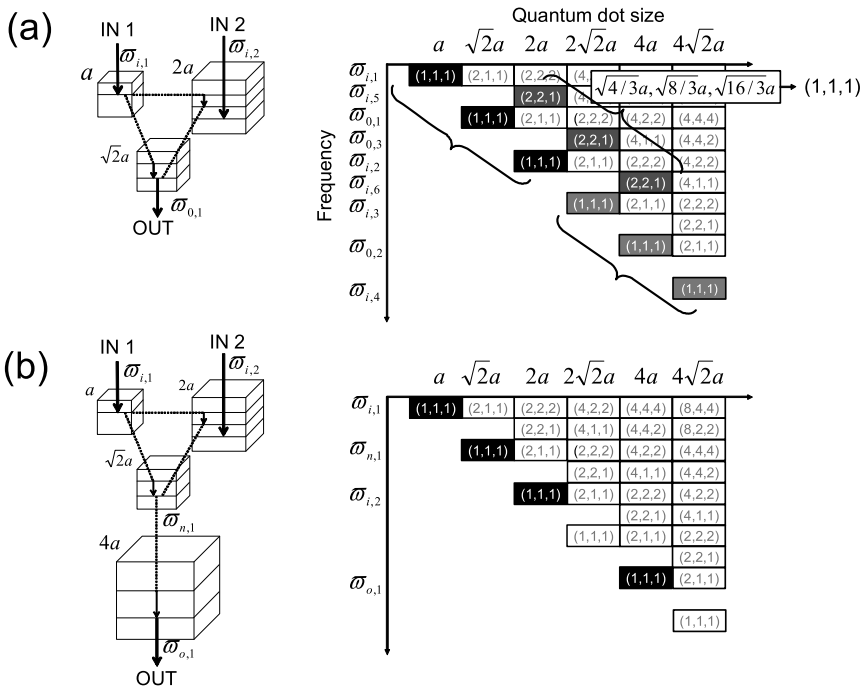

Fig. 3. Frequency partitioning among external and internal channels, and examples in (a) multiple implementations of 3-dot nanophotonic switches, and (b) 4-dot configuration for sum of products.

Adding more optical switches for different channels means adding different size dots, for instance, by multiplying the scale of the QDs by a constant while maintaining the ratio $1:\sqrt{2}:2$, such as a QD trio of $2\sqrt{2}a$, $4a$, and $4\sqrt{2}a$, so that the corresponding far-field

#8596 - $15.00 USD Received 26 August 2005; revised 22 December 2005; accepted 22 December 2005

resonant frequencies do not overlap with the other channels. More dense integration is also possible by appropriately configuring the size of the QDs. As an example, consider a QD whose size is $\sqrt{4/3}a$. The (1, 1, 1)-level in this QD $\sqrt{4/3}a$ can couple to the far-field excitation. It should be noted that this particular energy level is equal to the (2, 2, 1)-level in QD 2*a*, which is an already-used input QD; however, the far-field excitation in this particular energy level cannot couple to QD 2*a* since the (2, 2, 1)-level in QD 2*a* is a dipole-forbidden energy sublevel. Therefore, a QD trio composed of QDs of size $\sqrt{4/3}a$, $\sqrt{8/3}a$, and $\sqrt{16/3}a$ can make up another optical switch, while not interfering with other channels even though all of the input light is irradiated in the same area.

Another situation where an internally used frequency exists is a sum of products operation. A simplified example is shown in Fig. 3(b). The QD *a* and QD 2*a* operate on two inputs and their product appears in the (1, 1, 1)-level in QD $\sqrt{2}a$, which is further coupled to the sublevel (4,2,2) in QD 4*a*. The QD 4*a* is the output dot. Here, the QD $\sqrt{2}a$ is internally used; thus any frequency that could couple to QD $\sqrt{2}a$ cannot be used for other input channels.

We now briefly discuss the operation speed and the number of channels. (i) Speed: The operation speed of such systems involving optical near-field interactions is typically on the order of nanoseconds if the system involves a radiative dissipation process at the output QD. The internal operation speed is determined by optical near-field interactions between neighboring QDs, which is typically around one hundred picoseconds [4]. (ii) Total number of channels available: This depends on many factors, such as inhomogeneous and homogeneous broadening of the QDs, the linewidth of the input light, the configuration of the system (or the configuration of the QDs, such as the examples shown in Fig. 3), and so forth. Therefore, as an ultimate limiting factor, here we theoretically deal with the maximum size of the QD based on Eq. (1). The energy difference between the (2, 1, 1)-level and the (1, 1, 1)-level, or the intrasublevel relaxation, is derived from Eq. (1) as

$$E_{(2,1,1)} - E_{(1,1,1)} = \frac{3\pi^2\hbar^2}{2M(L-a_B)^2}, \tag{2}$$

which decreases as the QD becomes larger, but it should be larger than the intrasublevel relaxation constant in order to resolve those two energy levels. In the case of CuCl QDs, assuming M=2.3m_e [18] and an intrasublevel relaxation constant of $\hbar\Gamma$ with Γ^{-1} around 1 ps [4], the maximum QD size is around 30 nm. This will act as a limitation in the design of the system.

4. Experiment

To verify the broadcasting method, we performed the following experiments using CuCl QDs in an NaCl matrix at a temperature of 22 K. To operate a 3-dot nanophotonic switch (2-input AND gate), we irradiated at most two input light beams (IN1 and IN2). The experimental setup is summarized in Fig. 4(a). The input light IN1 and IN2 were assigned to 325 nm and 384.7 nm, which were coupled to QD *a* and QD 2*a,* respectively. They were irradiated over the entire sample (global irradiation) via far-field light. The spatial intensity distribution of the output signal, at 382.6 nm, which was obtained from QD $\sqrt{2}a$, was measured by scanning a near-field fiber probe. There were several nanophotonic switches (or AND gates) within an approximately 1 μm × 1 μm area, as schematically shown in Fig. 4(b). As described in Sec. 3, the output of the AND gate should appear only when both of the inputs are supplied. In Fig. 5(a), when only IN1 was applied to the sample, the output of the AND gate was ZERO (low-level), whereas in Fig. 5(b), when both inputs were irradiated, the output was ONE (high-level). Note the regions marked by ■, ●, and ◆. In those three regions, the output signal levels were respectively low and high in Figs. 5(a) and (b), which indicates that multiple AND

#8596 - $15.00 USD Received 26 August 2005; revised 22 December 2005; accepted 22 December 2005

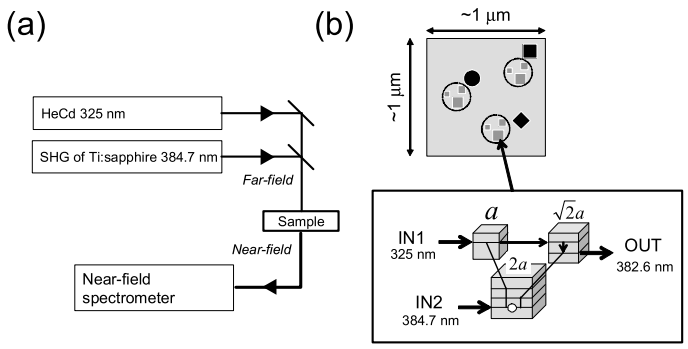

Fig. 4. (a) Experimental setup. (b) Three nanophotonic switches (3-dot AND gates) are distributed within 1 μm × 1 μm area in the sample.

gates were integrated at densities beyond the scale of the globally irradiated input beam area. That is to say, broadcast interconnects to nanophotonic switch arrays were accomplished by diffraction-limited far-field light.

The following is a description of the sample used in terms of the number of switches observed, namely, three, as demonstrated above. The CuCl QDs were inhomogeneously distributed in an NaCl matrix by using the Bridgman method [20], which was also employed in previous demonstrations [14-16]. Absorption and emission spectra of the sample measured at 5 K are shown in Fig. 5(c) by the thin and thick lines, respectively. The vertical dotted lines in the figure show photon energies that correspond to the (1, 1, 1)-levels of QDs of different size, as specified units of monolayers (ML), where 1 ML is equal to 0.2705 nm. Clear absorption and photoluminescence peaks were observed at a photon energy corresponding to a QD size of 17 ML, and thus, the output energy level was set to 3.24 eV for the output QD $\sqrt{2}a$, as shown above. Accordingly, the size of QD 2*a*, which couples to IN2, corresponded to a photon energy of 3.22 eV. The average distance between QDs was estimated at around 20 nm since the CuCl concentration was 1 mol% and the average dot size was around 4 nm. Therefore, the number of QDs in the observed volume of 1 μm × 1 μm × 30 nm was approximately 3,000. From the emission spectrum, it was estimated that QD $\sqrt{2}a$ (3.24 eV) and QD 2*a* (3.22 eV) respectively occupied approximately 4% and 1% of all QDs, and hence the numbers of QD $\sqrt{2}a$ and QD 2*a* in the scanned sample volume were 120 and 30, respectively. Here, if we virtually divide the entire sample into unit volumes of 30 nm × 30 nm × 30 nm, called a voxel, which is the volume occupied by a single 3-dot nanophotonic switch, there are in total 900 such voxels. Since the other input, IN1, was assigned to 325 nm, it excited all QDs in the sample, and hence there was at least one QD that functioned as IN1 in a voxel. Therefore, the expected number of 3-dot nanophotonic switches (i.e., the expected number of voxels in which an appropriate-size QD trio resides simultaneously) within a volume of 1 μm × 1 μm × 30 nm will be approximately (120/900) × (30/900) × 900 (=4), which is in good agreement with the experimental observation in Figs. 5(a) and (b).

5. Summary

In summary, broadcast interconnects for nanophotonic devices have been proposed and experimentally demonstrated using far- and near-field interactions. Combining this broadcasting mechanism with switching [14] and summation [16] will allow nano-scale integration of optical parallel processing devices, which have conventionally resulted in bulky systems.

#8596 - $15.00 USD Received 26 August 2005; revised 22 December 2005; accepted 22 December 2005

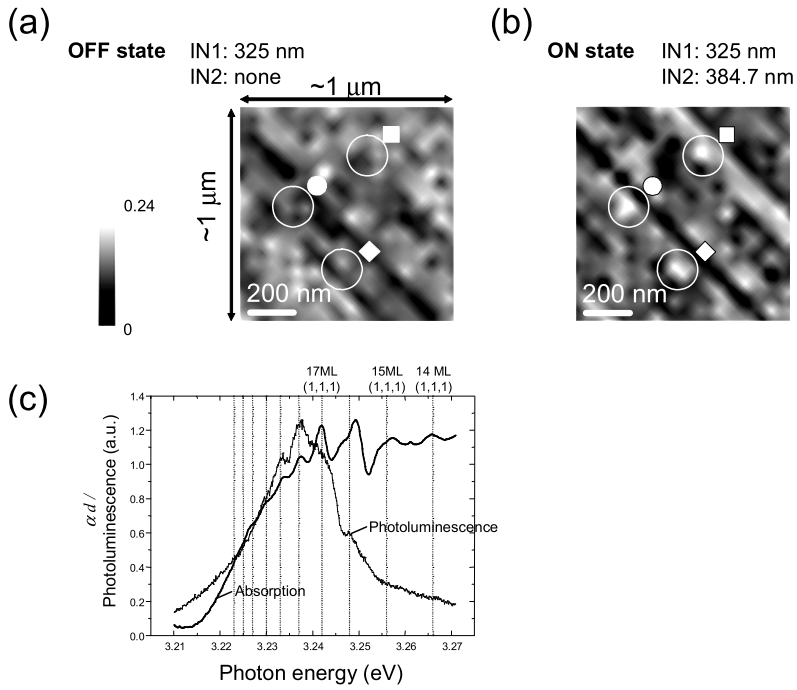

Fig. 5. Experimental results. (a, b) Spatial intensity distribution of the output of 3-dot AND gates. (a) Output level: low (1 AND 0 = 0), and (b) output level: high (1 AND 1 = 1). (c) Absorption and photoluminescence spectrum of the sample.

#8596 - $15.00 USD Received 26 August 2005; revised 22 December 2005; accepted 22 December 2005

Hierarchy in optical near-fields and its application to memory retrieval

Makoto Naruse

National Institute of Information and Communications Technology
4-2-1 Nukui-kita, Koganei, Tokyo 184-8795, Japan
naruse@nict.go.jp

Takashi Yatsui

Japan Science and Technology Agency, 687-1 Tsuruma, Machida, Tokyo 194-0004, Japan
yatsui@ohtsu.jst.go.jp

Wataru Nomura, Nobuaki Hirose, and Motoichi Ohtsu

The University of Tokyo, 7-3-1 Hongo, Bunkyo-ku, Tokyo 113-8656, Japan
ohtsu@ee.t.u-tokyo.ac.jp

Abstract: Optical near-field interactions exhibit different behavior at different scales, which we term scale-dependent physical hierarchy. Using the intrinsic logical hierarchy of information and a simple digital coding scheme, scale-dependent optical memory accesses are associated with different levels of the information hierarchy. The basic principle is demonstrated by finite-different time-domain simulations and experiments using metal nanoparticles.

OCIS codes: (210.4680) Optical memories; (070.6020) Signal processing; (180.5810) Scanning microscopy; (260) Physical optics; (260.2110) Electromagnetic theory

References and links

1. M. Ohtsu, K. Kobayashi, T. Kawazoe, S. Sangu, and T. Yatsui, "Nanophotonics: design, fabrication, and operation of nanometric devices using optical near fields," IEEE J. Sel. Top. Quantum Electron. **8**, 839-862 (2002).
2. M. Naruse, T. Miyazaki, T. Kawazoe, K. Kobayashi, S. Sangu, F. Kubota, and M. Ohtsu, "Nanophotonic computing based on optical near-field interactions between quantum dots," IEICE Trans. Electron. **E88-C**, 1817-1823 (2005).
3. T. Inoue and H. Hori, "Representations and transforms of vector field as the basis of near-field optics," Opt. Rev. **3**, 458-462 (1996).
4. K. Kobayashi and M. Ohtsu, "Quantum theoretical approach to a near-field optical system," J. Microsc. **194**, 249–254 (1999).
5. M. Ohtsu and H. Hori, *Near-Field Nano-Optics* (Kluwer Academic/Plenum Publishers, New York 1999).
6. K. Baba, R. Yamada, S. Nakao, and M. Miyagi, "Multifrequency three-dimensional optical read-only memory disks using metallic island films: preliminary experiments," Appl. Opt. **32**, 3137-3143 (1993).
7. H. Ditlbacher, J. R. Krenn, B. Lamprecht, A. Leitner, and F. R. Aussenegg, "Spectrally coded optical data storage by metal nanoparticles," Opt. Lett. **25**, 563-565 (2000).
8. M. Ohtsu and K. Kobayashi, *Optical Near Fields* (Springer, Belin, 2004).
9. H. Tamaru, H. Kuwata, and K. Miyano, "Resonant light scattering from individual Ag nanoparticles and particle pairs," Appl. Phys. Lett. **80**, 1826-1828 (2002).
10. W. Rechberger, A. Hohenau, A. Leitner, J. R. Krenn, B. Lamprecht, and F. R. Aussenegg, "Optical properties of two interacting gold nanoparticles," Opt. Commun. **220**, 137-141 (2003).

1. Introduction

Recent advances in the field of optical near-field interactions between sub-wavelength-size objects allow the design of optical devices and systems at densities beyond those conventionally limited by the diffraction limit of light [1, 2]. This higher integration density,

#8905 - $15.00 USD Received 26 September 2005; revised 30 October 2005; accepted 31 October 2005

however, is only one of benefits of optical near-fields over electronics. Another benefit is that optical near-fields are physically based on the flow of excitation, not electron transfer. Based on these features, theoretical frameworks for signal transfer via optical near-fields have been proposed, such as angular spectrum representations [3] or the virtual photon model [4]. Another aspect that could be exploited in devices and systems is the physical hierarchy of optical near-fields, meaning that the system exhibits different physical behavior at different scales [5]. More concretely, a certain nanostructure may appear differently depending on how we observe it, for example, depending on the size of a fiber probe used to measure it. In this paper, we demonstrate one of the simplest forms of such a hierarchy in optical near-fields and associate it with an information hierarchy.

Hierarchy of information can be found, for example, in terms of its meaning, quality, or level of importance, such as detailed and abstract information, high-resolution and low-resolution information, high-security and less-critical information, and so forth. One of the most simple and fundamental structures in such a hierarchy that we will discuss in this paper is one where several data items in a "detailed" layer are categorized as a single data item in an "abstract" layer. Such a hierarchy can be considered as an additional degree-of-freedom in conventional data multiplexing technologies used to record multiple independent data items in a recording medium [6, 7].

This paper is organized as follows. In Section 2, we discuss the physical hierarchy in optical near-fields considered in this paper. Section 3 discusses a logical model applied to two-mode optical memory retrieval. Section 4 shows numerical simulations and experimental results. Section 5 concludes the paper.

2. A scale-dependent hierarchy in optical near-fields

The hierarchy we consider in this paper is the scale-dependency of optical near-field interactions. We begin with a physical model of optical near-fields based on dipole-dipole interactions [8]. Suppose that a probe, which is modeled by a sphere of radius r_P, is placed close to a sample to be observed, which is modeled as a sphere of radius r_S. Figure 1(a) shows three different sizes for the probe and the sample. When they are illuminated by incident light whose electric field is $\boldsymbol{E}_0$, electric dipole moments are induced in both the probe and the samples; these moments are respectively denoted by $\boldsymbol{p}_P=\alpha_P\boldsymbol{E}_0$ and $\boldsymbol{p}_S=\alpha_S\boldsymbol{E}_0$. The electric dipole moment induced in the sample, $\boldsymbol{p}_S$, then generates an electric field, which changes the electric dipole moment in the probe by an amount $\Delta\boldsymbol{p}_P=\Delta\alpha_P\boldsymbol{E}_0$. Similarly, $\boldsymbol{p}_P$ changes the electric dipole moment in the sample by $\Delta\boldsymbol{p}_S=\Delta\alpha_S\boldsymbol{E}_0$. These electromagnetic interactions are called dipole-dipole interactions. The scattering intensity induced by these electric dipole moments is given by

$$\begin{aligned} I &= \left|\boldsymbol{p}_P+\Delta\boldsymbol{p}_P+\boldsymbol{p}_S+\Delta\boldsymbol{p}_S\right|^2 \\ &\approx (\alpha_P+\alpha_S)^2\,|E_0|^2+4\Delta\alpha(\alpha_P+\alpha_S)\,|E_0|^2 \end{aligned} \tag{1}$$

where $\Delta\alpha=\Delta\alpha_S=\Delta\alpha_P$ [8]. The second term in Eq. (1) shows the intensity of the scattered light generated by the dipole-dipole interactions, containing the information of interest, which is the relative difference between the probe and the sample. The first term in Eq. (1) is the background signal for the measurement. Therefore, the ratio of the second term to the first term of Eq. (1) corresponds to a signal contrast, which will be maximized when the sizes of the probe and the sample are the same ($r_P=r_S$), as shown in Fig. 1(b). (Detailed derivation is found in reference [8].) Accordingly, the spatial resolution varies depending on the sizes of the probe and the sample. Figure 1(c) shows normalized signal intensity profiles corresponding to three cases where the sum r_S+r_P is respectively D, $3D$, and $6D$ (D=80 nm). Thus, we can see a scale-dependent physical hierarchy in this framework, where a small probe, say $r_P=D/2$, can nicely resolve objects with a comparable resolution, whereas a large probe, say $r_P=3D/2$, cannot resolve detailed structure but it can resolve structure with a resolution comparable to the probe size. Therefore, although a large diameter probe cannot detect smaller-scale structure, it could detect certain features that are associated with a nanostructure; we discuss this aspect in more detail below.

#8905 - $15.00 USD Received 26 September 2005; revised 30 October 2005; accepted 31 October 2005

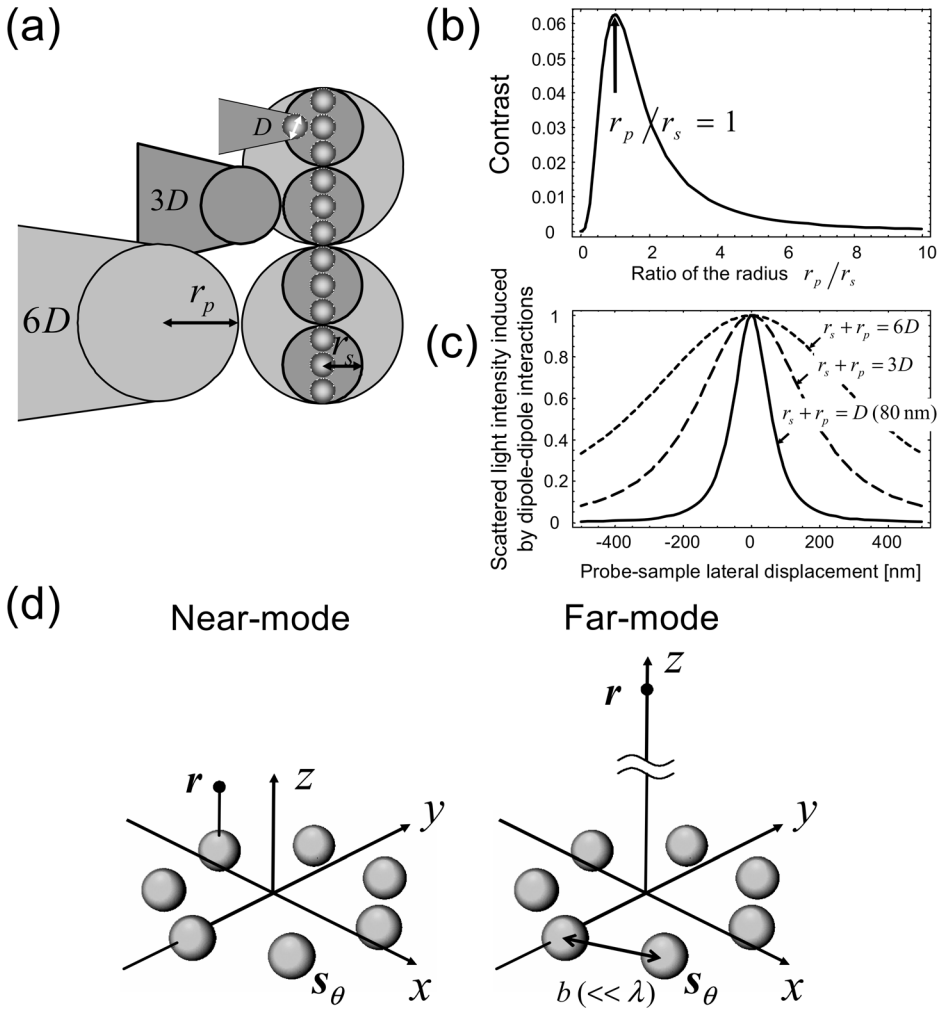

Fig. 1. A simple spatial hierarchy observed in optical near-fields. (a) Dipole-dipole interaction. (b) Signal contrast as a function of the ratio of the radius of the sample and the probe. (c) Spatial resolution varies depending on the scale of the sample and the probe. (d) Array of dipole moments distributed on sub-wavelength scale and its observation in *near-mode* and *far-mode*.

We consider the observation of an array of small particles distributed with sub-wavelength pitch using a probe whose diameter is substantially larger than that of observed particles. As discussed earlier, the spatial distribution of the particles can be obtained by using a fiber probe of comparable size. (We call this situation the "*near-mode*".) On the other hand, the distribution cannot be resolved by a large fiber probe. (We call this situation the "*far-mode*".) This far-mode is approximately equivalent to a case where we observe an array of dipole moments distributed with sub-wavelength scale in a far-field. Here, as schematically shown in Fig. 1(d), each of the dipole moments is assumed to be induced in a small particle centered on a circle on the *xy* plane, and the minimum distance between adjacent particles is *b*. The electric field at position $\boldsymbol{r}$ in Fig. 1(d) is given by

$$E(\boldsymbol{r}) = \sum_{\theta} E_\theta e^{-i\alpha + ik|\boldsymbol{r}-\boldsymbol{s}_\theta|} \frac{1}{|\boldsymbol{r}-\boldsymbol{s}_\theta|} \tag{2}$$

#8905 - $15.00 USD Received 26 September 2005; revised 30 October 2005; accepted 31 October 2005

where ω is the operating frequency, k is the wave number, and $\boldsymbol{s}_\theta$ represents the position of a dipole specified by θ (where θ = 1, 2, …). The existence of the dipole at position $\boldsymbol{s}_\theta$ is indicated by a *near-code*, which will be introduced later in Section 3, that is

$$E_\theta = \begin{cases} 0 & \text{near-code}(\theta) = 0 \\ E_0 & \text{near-code}(\theta) = 1 \end{cases}. \tag{3}$$

If we assume that $b \ll \lambda \ll r$, which corresponds to the far-mode, Eq. (2) is simplified to

$$E(\boldsymbol{r}) = E_0 \frac{e^{-i\omega t + ikr}}{r} \sum_\theta \text{near-code}(\theta) \tag{4}$$

which means that the electric field intensity at position $\boldsymbol{r}$ is proportional to the number of dipole moments given by the near-code. When the near-code consists of n bits, the number of dipole moments can range from zero to n. Therefore, n+1 different signal levels appear in the signal obtained in far-mode. On the other hand, the total number of bit combinations in the near-code is 2^n, which are resolvable in the near-mode.

3. A logical model for hierarchical memory systems

We focus on the differences in the number of signal levels and combinations discussed in Section 2 using a simple digital coding scheme.

A two-layer hierarchical memory based on concepts that we call *far-codes* and *near-codes* is described in this section. The far-code depends on an array of bits distributed within a certain area and is determined logically to be either ZERO or ONE. Consider an (N+1)-bit digital code, where N is an even number. Now, let the far-code be defined depending on the number of ONEs (or ZEROs) contained in the (N+1)-bit digital code according to

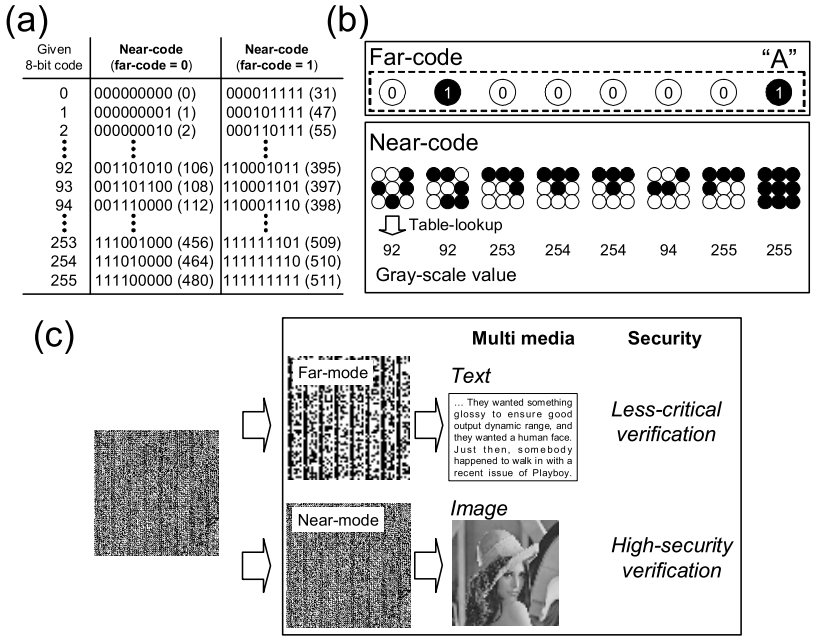

Fig. 2. Example of logical model for the near-code and far-code. (a) Original 8-bit information is coded differently in the near-code depending on its corresponding far-code, which is either ZERO or ONE. (b) Example of the near-codes and far-codes. (c) Using such encoding and decoding principles, nanoparticle arrangements associated with different levels of the information hierarchy.

#8905 - $15.00 USD Received 26 September 2005; revised 30 October 2005; accepted 31 October 2005

$$far-code=\begin{cases}1 & \text{If the number of ONEs} > N/2\\ 0 & \text{otherwise}\end{cases} \quad (5)$$

The (N+1) digits provide a total of 2^{N+1} possible permutations, or codes. Here, we note that half of them, namely 2^N permutations, have more than N/2+1 ONEs among the (N+1) digits (i.e., far-code = 1), and the other half, also 2^N permutations, have more than N/2+1 ZEROs (i.e., far-code = 0). In other words, 2^N different codes could be assigned to two (N+1)-bit digital sequences so that their corresponding far-codes are ZERO and ONE, respectively. We call this (N+1)-bit code a near-code.

Example near-codes are listed in Fig. 2 for N = 8. The correspondence between 2^N original codes and the (N+1)-bit near-codes is arbitrary. Therefore, we use a table-lookup when decoding an (N+1)-bit near-code to obtain the original code. The example near-codes shown in Fig. 2(a) are listed in ascending order, but other lookup-tables or mappings are also possible.

Figure 2(b) schematically demonstrates example codes in which a 9-bit near-code is represented as a 3×3 array of circles, where black and white mean ONE and ZERO, respectively. Here, if the number of ONEs in the near-code is larger than five, then the far-code is ONE, otherwise the far-code is ZERO. Suppose, for example, that the far-code stores text data and the near-code stores 256-level (8-bit) image data. Consider a situation where the far-code should represent an ASCII code for "A", whose binary sequence is "0100001". Here, we assume that the gray levels of the first two pixels, which will be coded in the near-code, are the same value. (Here, they are "92".) However, the first two far-codes are different (ZERO followed by ONE). Referring to the rule shown in Fig. 2(a), and noticing that the first far-code is ZERO and the near-code should represent "92", the first near-code should be "001101010". In the same way, the second near-code is "110001011", which represents "92", whereas its corresponding far-code is ONE. Based on such an encoding and decoding scheme, the near-codes and far-codes could be respectively associated with image and text data for multimedia applications, or with high-security and less-critical verifications for security applications, as schematically shown in Fig. 2(c).

4. Simulations and experiments

Simulations were performed to verify the principles of hierarchical access to memory devices by assuming ideal isotropic metal particles to see how the scattering light varies depending on the number of particles in the far-code by using a Finite Difference Time Domain (FDTD)-based simulator (*Poynting for Optics*, a product of Fujitsu, Japan). Here we assume that 80-nm-diameter particles are distributed around a 200-nm-radius circle with a constant angular interval, as shown in Fig. 3(a). Seven particles at most can be arranged in the ring. The wavelength used in the simulation was 600 nm. The solid squares in Fig. 3(b) show calculated scattering cross-sections as a function of the number of particles in the ring. The scattering cross-section increases nearly linearly with the number of particles in the ring. This result is expected from the physical model described in Section 2.

In order to experimentally demonstrate this behavior, we measured far-mode intensity distributions of an array of Au particles, each with a diameter around 80 nm, distributed on a SiO_2 substrate in a 200-nm-radius circle. The inset of Fig. 1(a) shows an SEM image of one such particle distribution. These particles were fabricated by a liftoff technique using electron-beam (EB) lithography with a Cr buffer layer. Multiple groups of Au particles were separated by 2 μm. In the SEM image shown in Fig. 3(d), the values indicate the number of particles within each group. In order to illuminate all Au particles in each group and collect the scattered light from them, we used a near-field optical microscope in an illumination collection setup with an apertured fiber probe having a diameter (D) of 500 nm, as shown in Fig. 3(c). The light source used was a laser diode with an operating wavelength of 680 nm. The distance between the substrate and the probe was maintained at 750 nm. Figure 3(e) is an intensity pattern captured by the probe, from which the information in the far-mode is retrieved. The solid circles in Fig. 3(b) indicate the peak intensity of each section, which increased substantially linearly. The signal level difference in the far-mode is small when the

#8905 - $15.00 USD Received 26 September 2005; revised 30 October 2005; accepted 31 October 2005

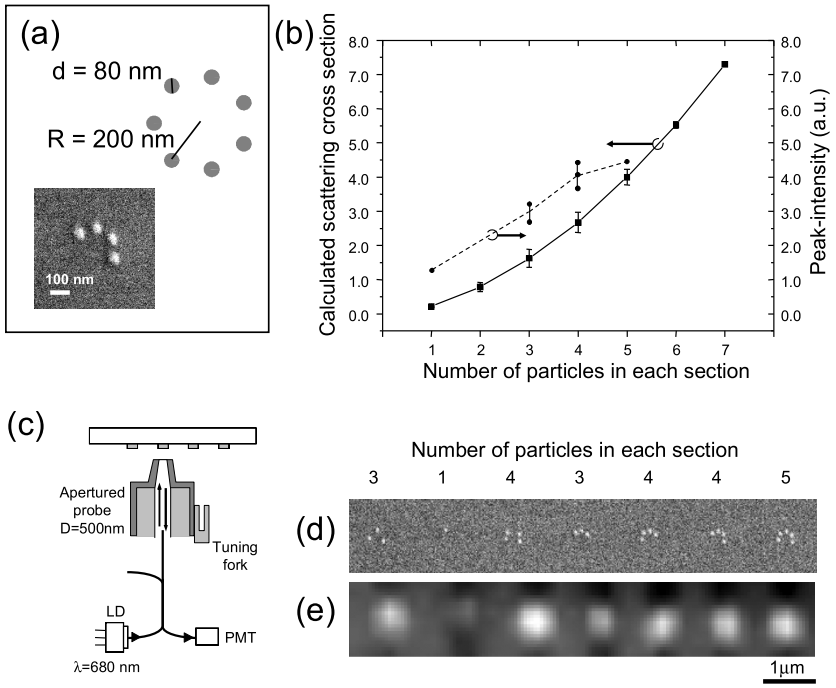

Fig. 3. (a) Each section consists of small particles. (b, square marks) Scattering cross-sections are calculated depending on the number of particles in each section. (b, circular marks) Peak-intensity of each section in intensity profile shown in (e). (c) Experimental setup. (d) SEM picture of an Au particle array. (e) Intensity pattern captured for the far-code.

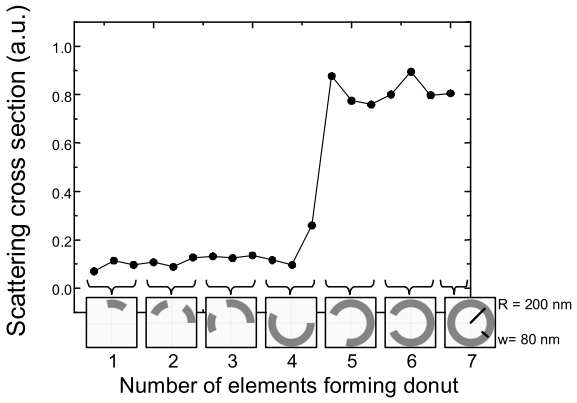

Fig. 4. Scattering cross-section as a function of number of elements forming donut.

difference in the number of particles is small, and therefore, a better way of resolving signals in the far-mode will be required. However, the experimental results shown here demonstrate that this is one fundamental architecture that can exploit the physical hierarchy.

Concerning the size and the pitch of the particles used in the simulation and experiments, the electric field enhancement due to closely placed neighboring particles is negligible [9, 10];

#8905 - $15.00 USD Received 26 September 2005; revised 30 October 2005; accepted 31 October 2005

this is one condition to ensure that a particular far-mode signal level does not significantly differ depending on the distribution of the particles so long as the number of particles is the same, as shown by the solid squares in Fig. 3(b). Such electric field enhancement, however, could provide another degree-of-freedom in the design of hierarchical systems. For example, when we choose a donut-shape, instead of a point particle, for each of the bits in near-code, the far-mode signals could show a step-like response instead of a nearly linear response, according to the number of elements forming the donut. Fig. 4 shows scattering cross-sections obtained by FDTD simulations assuming an 80-nm-wide (W), 200-nm-radius (R) donut shape. In this example, we arrange the combination of elements forming the donut so that the signal increases significantly when the number of elements forming the donut is larger than five. This indicates that the digitization procedure, for instance required in Eq. (5), can be physically realized by engineering the shape of each bit on the nanometer scale.

5. Summary

Optical near-field interactions are observed differently depending on the physical scale of the observation. Noticing that information also has an inherent hierarchy, we present a hierarchical memory access scheme in which the so-called near-mode is used to read detailed dipole distributions, whereas the far-mode is used to detect features within a region-of-interest. Simulations and experimental results using metal nanoparticles are also shown. With a simple coding scheme, different physical accesses to the media are associated with different hierarchical information. Further studies on hierarchies in optical near-fields, regarding their fundamental theory [3], experimental realization, applications, and so forth, are currently underway.

#8905 - $15.00 USD Received 26 September 2005; revised 30 October 2005; accepted 31 October 2005

IEICE TRANS. ELECTRON., VOL.E88–C, NO.9 SEPTEMBER 2005

LETTER *Special Section on Nanophotonics and Related Techniques*

Observation of Faraday Rotation and Magnetic Circular Dichroism in an Optical Near-Field Probe Coated with Fe

Tadashi KAWAZOE[†a)], **Shinya MARUYAMA**[††], ***Nonmembers***, **Kiyoshi KOBAYASHI**[††], ***and*** **Motoichi OHTSU**[†,†††], ***Members***

SUMMARY We demonstrate a novel fiber device exhibiting magnetic circular dichroism (MCD) and Faraday rotation in sharpened optical fibers coated with Fe. The degree of MCD was 0.68 in a magnetic field of 0.35 T and the Faraday rotation angle was as great as 110 degrees. Such great magneto-optical effect is due to optical near-field interactions in the subwavelength region, i.e., in the tip of the near-field fiber probe. These effects can be attributed to the large magnitude of the magneto optical coefficient of Fe.

key words: *polarization, optical near-field, magneto-optical effect, optical properties of magnetic materials, plasmon*

1. Introduction

Optical fiber and guided wave techniques have brought high efficiency, additional function (e.g., optical switch), and small size to optical devices. The demand for downsizing is particularly strong, and several approaches have already been reported [1], [2]. A nanophotonic integrated circuit [2], is composed of nanophotonic devices much smaller than the light wavelength. In order to integrate the important photonic device, such as the optical isolator, circulator (i.e., three-terminal-type directional coupler), and so on, into the nanophotonic integrated circuit, subwavelength-sized polarization controller is necessary. However, current polarization controllers are too large to integrate in the nanophotonic circuits and unsuitable to control the polarization of a signal carrier, i.e., an optical near field, used in the nanophotonic device, because they use optical anisotropy in material and require their sizes larger than light wavelengths. Recently, several groups reported the preparation of an optical anisotropy using fabricated shape instead of anisotropy of the optical crystal to decrease in the size of the polarization control devices [3], [4]. They devised the structural shape of near-field probes and asymmetric nano-dots to control the polarization of an optical near field.

In this study, we propose another approach to control the polarization of light in a nanometric region. The magneto-optical effect of Fe is more than 10^4 times greater than that of glass. For a thin Fe film of 1 μm thick, the degree of polarization and the Faraday rotation angle of transmitted light are more than 0.9 and 30 degrees respectively, at saturation magnetic flux density [5], [6]. We expected such large magneto-optical effect of Fe enable the subwavelength polarization controller for the nanophotonic devices. The depth of Fe penetration is less than 100 nm for light with a wavelength of 600 nm, so the large magneto-optical effect of Fe is certainly unsuitable for conventional optical devices [7]. However, since nanophotonic devices are smaller than the penetration depth of Fe [8], [9], the optical loss is not a serious problem. In the tip of the probe, the optical field passes through a waveguide covered with Fe, which is narrower than the light wavelength, as shown in Fig. 1. The polarization of light passing through the tip changes owing to the strong magneto-optical effect of the Fe coating, and can be controlled using the intensity of the external magnetic field.

In order to develop a polarization controller for nanophotonic device that uses the magneto-optical effect of Fe, we reported the preparation of an optical near-field fiber probe coated with Fe [10]. However, we did not verify the operation of the probe as a polarization controller in the previous work. In this paper, we verify and demonstrate the operation as the polarization controller using optical near-field probes, coated with Fe and Fe/Au/Fe/Au, by measurements of the degree of polarization of magnetic circular dichroism

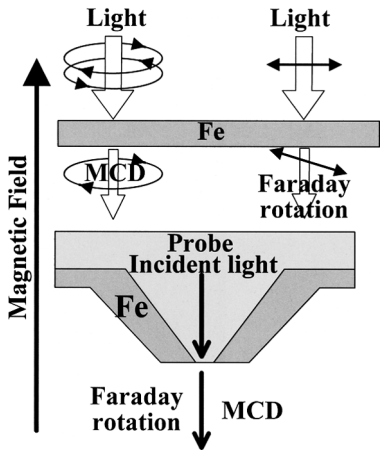

Fig. 1 Schematic explanation of the strong magneto-optical effect of Fe and an optical near-field probe coated with Fe.

Manuscript received April 18, 2005.
Manuscript revised May 31, 2005.

[†]The authors are with Japan Science and Technology Agency, Machida-shi, 194-0004 Japan.
[††]The authors are with Tokyo Institute of Technology, Tokyo, 152-8550 Japan.
[†††]The author is with the University of Tokyo, Tokyo, 113-8656 Japan.
a) E-mail: kawazoe@ohtsu.ist.go.jp

DOI: 10.1093/ietele/e88–c.9.1850

(MCD) and Faraday rotation angle.

2. Preparation and Experiments

Figure 2 shows typical SEM images of fabricated optical fibers that were sharpened by chemical etching and coated with Fe and a metallic multi-layer coating. First, we fabricated a fiber tip coated only with a 150-nm thick Fe layer. When the aperture diameter is much smaller than the diffraction limit of light, the majority of the incident optical power is transferred as a plasmon polariton mode at the boundary between the glass fiber and the Fe layer. The plasmon polariton mode is reconverted to an optical field at the aperture. Therefore, the polarization of the output light passing through the fiber tip can be controlled by the magneto-optical effect of Fe layer. The detailed fabrication procedure was reported in the previous work [10].

Next, we fabricated a probe tip coated with Au/Fe/Au/Fe layers (10 nm, 1 nm, 80 nm, and 100 nm, respectively), to achieve stronger magneto-optical effect by using the quantum size effect of Au/Fe/Au quantum well structures [11]. The 100-nm Fe layer, which is outside the quantum well structure, gives the magnetic coercivity for the probe. The apertures of the probes were fabricated by using a focused ion beam (FIB).

In the experiment, we used a He-Ne laser (λ=632.8 nm) as the light source; the total fiber length was 5 cm. Fe has the greatest magneto-optical effect on light in this wavelength region [6]. The anisotropy of fiber tip is considerable. Therefore, we adjusted the polarization of input light to cancel out the anisotropy of the fiber tip at 0 T, i.e., without external magnetic field. An external magnetic field, B, was applied with a permanent magnet; the direction of the field was parallel to the fiber axis. The polarization of the output light was measured using a set of wave plates and polarizer in front of the photodetector.

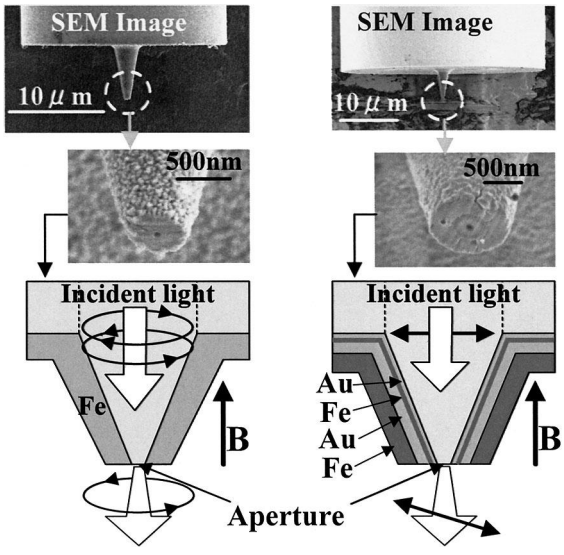

Fig. 2 SEM images of typical fabricated fiber probes and schematics of their structures.

3. Experimental Results

3.1 Magnetic Circular Dichroism

Figure 3(a) shows the experimental results of MCD measurements. Here, we used probes with a 50-nm diameter aperture. The degree of polarization of the output light from the probe coated with Fe increased with an increase in the intensity of the external magnetic field, shown by closed circles and squares. However, the degree of polarization of the conventional near-field probe coated with 160-nm thick Au was independent of magnetic field intensity, and was close to 0, shown by closed triangles. This indicates that the MCD of an Fe-coated probe comes from the MCD of Fe. The MCD of the probe coated with Au/Fe/Au/Fe layers was greater than that of the probe coated with only Fe. We consider this increase in the MCD comes from the quantum size effect of Au/Fe/Au quantum well structures. The difference was especially great in weak magnetic fields. At 0.05 T, the probe coated with Au/Fe/Au/Fe layers had magnitude of MCD 40 times greater than that of the probe coated only with Fe. The maximum degree of polarization (0.68) was observed at a magnetic flux density of 0.35 T.

Figure 3(b) shows the aperture diameter dependence of the degree of polarization with a magnetic field of 0.46 T. The output light form the probe consists of two components. One is a component that propagates as the light wave in the probe tip. Another is a converted component from plasmon polariton mode in the probe tip. The latter is susceptible to

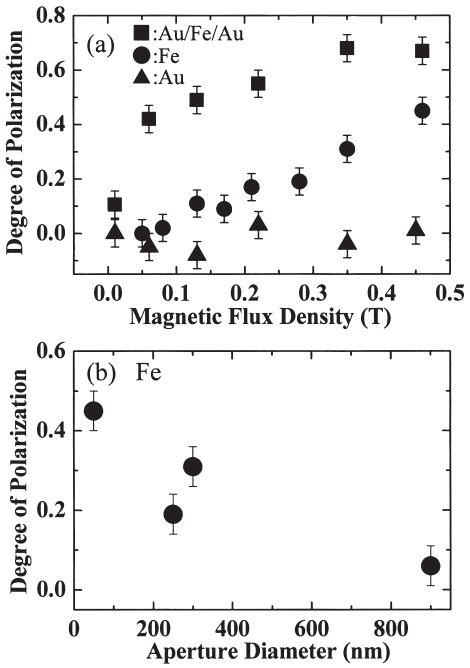

Fig. 3 (a) The magnetic flux density dependence of the degree of polarization in the fabricated probes. (b) The aperture diameter dependence of the degree of polarization with a magnetic field of 0.46 T for an Fe-coated probe.

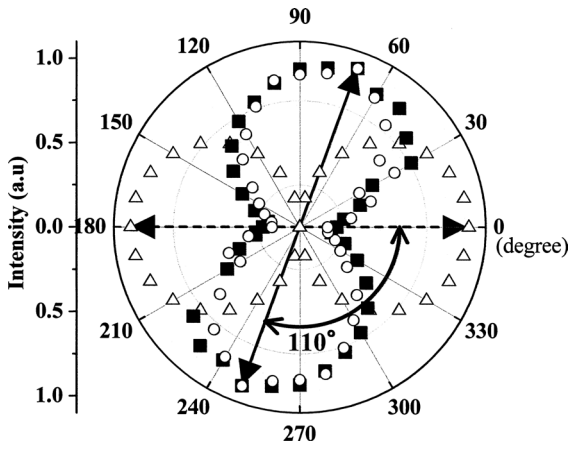

Fig. 4 Polarization of output light for Au/Fe/Au/Fe coated fiber tip with a 50-nm aperture.

influences of the magneto-optical effect of Fe coating and its ratio decrease with increase in the aperture diameter. Thus, the degree of polarization decreases as the aperture diameter increases.

3.2 Faraday Rotation

Figure 4 shows the experimental results of the Faraday rotation measurement. The polar angle and radial axis show the angle of the polarizer and detected intensity, respectively. The open triangles show the polarization of output light from the Au/Fe/Au/Fe coated probe before the magnetic field was applied. For a probe with an aperture larger than 200 nm, the Faraday rotation angle was small. And, we observed Faraday rotation angles in a probe with an aperture of less than a 200 nm; this is much smaller than the light wavelength. We obtained a Faraday rotation angle of 110 degrees for the Au/Fe/Au/Fe-coated probe with a 50-nm diameter aperture at B=0.35 T, shown by open circles in Fig. 4. This rotation angle is sufficient for an optical isolator and circulator. For a probe with a 300-nm diameter aperture, the Faraday rotation angle was less than 10 degrees. Therefore, the Faraday rotation occurs in a small region near the apex of the probe, which is subwavelength in size. Since the Au/Fe/Au/Fe-coated probe had a coercively magnetized Fe layer, it did not require an external magnetic field after magnetization. Thus, the Faraday rotation angle was preserved even after the external magnetic field was removed, shown by closed squares in Fig. 4. Needlessness of the magnet gives us advantages, such as the increase in the integration density of nanophotonic devices and the adverse effect of leaked magnetic field.

4. Conclusion

We verify and demonstrated a polarization controller that uses MCD and Faraday rotation in sharpened optical fibers coated with Fe. We achieved a degree of polarization of 0.68 in MCD using a Au/Fe/Au-coated probe and a rotation angle of 110 degrees in a magnetic field of 0.35 T. Finally, we succeeded in preserving of the rotation angle using a coercively magnetized layer. We consider that these strong magneto-optical effects come from the large magnitude of the magneto optical coefficient of Fe and the quantum well structure (Au/Fe/Au) increases in the magneto-optical effect. The active region of the device is within the apex of the probe, which is subwavelength size. Therefore, this polarization controller can be applied and integrated into a nanophotonic integrated circuit, to act as an optical isolator, circulator, and so on [2].

References

[1] S. Noda, M. Yokoyama, M. Imada, A. Chutinan, and M. Mochizuki, "Polarization mode control of two-dimensional photonic crystal laser by unit cell structure design," Science, vol.293, pp.1123–1125, 2001.
[2] M. Ohtsu, K. Kobayashi, T. Kawazoe, S. Sangu, and T. Yatsui, "Nanophotonics: Design, fabrication, and operation of nanometric devices using optical near fields," IEEE J. Sel. Top. Quantum Electron., vol.8, pp.839–862, July/Aug. 2002.
[3] T. Saiki and Y. Narita, "Nano-optical imaging spectroscopy: Recent advances in near-field scanning optical microscopy," Jap. Soc. Appl. Phys. International, no.5, pp.22–29, 2002.
[4] B.K. Canfield, S. Kujala1, K. Jefimovs, T. Vallius, J. Turunen, and M. Kauranen, "Polarization effects in the linear and nonlinear optical responses of gold nanoparticle arrays," J. Opt. A: Pure Appl. Opt., vol.7, pp.S110–S117, 2005.
[5] Landolt-Boenstein: Zahlenwerte und Funktionen II-9, Magnetischen Eigenschaften 1.
[6] G.S. Krinchik and V.A. Artemev, "Magneto-optical properties of Ni, Co, and Fe in the ultraviolet, visible, and infrared parts of the spectrum," Sov. Phys. JETP, vol.26, pp.1080–1085, 1968.
[7] P.B. Johnson and R.W. Christy, "Optical constants of transition metals: Ti, V, Cr, Mn, Fe, Cu, Ni, and Pd," Phys. Rev. B, vol.9, pp.5056–5070, June 1974.
[8] T. Kawazoe, K. Kobayashi, S. Sangu, and M. Ohtsu, "Demonstration of a nanophotonic switching operation by optical near-field energy transfer," Appl. Phys. Lett., vol.82, pp.2957–2959, May 2003.
[9] T. Kawazoe, K. Kobayashi, and M. Ohtsu, "The optical nanofountain: A biomimetic device that concentrates optical energy in a nanometric region," Appl. Phys. Lett., vol.86, 103102, March 2005.
[10] J. Lim, T. Kawazoe, T. Yatsui, and M. Ohtsu, "Fabrication of a ferromagnetic-coated fiber probe with a double-layer structure," IEICE Trans. Electron., vol.E85, no.12, pp.2077–2080, Dec. 2002.
[11] Y. Suzuki, T. Katayama, S. Yoshida, K. Tanaka, and K. Sato, "New magneto-optical transition in ultrathin Fe(100) films," Phys. Rev. Lett., vol.68, pp.3355–3358, June 1992.

PAPER Special Section on Nanophotonics and Related Techniques

Anti-Parallel Dipole Coupling of Quantum Dots via an Optical Near-Field Interaction

Tadashi KAWAZOE[†a)], *Nonmember*, **Kiyoshi KOBAYASHI**[††], *and* **Motoichi OHTSU**[†,†††], *Members*

SUMMARY We observed the optically forbidden energy transfer between cubic CuCl quantum dots coupled via an optical near-field interaction using time-resolved near-field photoluminescence (PL) spectroscopy. The energy transfer time and exciton lifetime were estimated from the rise and decay times of the PL pump-probe signal, respectively. We found that the exciton lifetime increased as the energy transfer time fell. This result strongly supports the notion that near-field interaction between QD makes the anti-parallel dipole coupling. Namely, a quantum-dots pair coupled by an optical near field has a long exciton lifetime which indicates the anti-parallel coupling of QDs forming a weakly radiative quadrupole state.

key words: *optical near-field interaction, anti-parallel electric dipole pair, near-field spectroscopy, coupled quantum dots*

1. Introduction

The unique optical properties of a quantum dot (QD) system, i.e., the quantum size effect that originates from the electronic state in QDs, are of major research interest. A coupled QD system has more interesting and unique properties than a single QD system, including the Kondo effect [1], Coulomb blockade [2], spin interaction [3], and so on. Furthermore, the optical near-field interaction is also one of the mechanisms to couple the QDs. It is possible to control the coupling strength of the optical near-field coupled QDs, and to realize unique optical device operation. We have observed an optically-forbidden energy transfer between neighboring cubic CuCl QDs via an optical near field [4]. The breaking of the dipole selection rule in the sub-wavelength region has been discussed theoretically [5]. It is based on the fact that the point-dipole descriptions of QDs and long-wave approximation are not suitable for the system that the dots approach each other in a nanometric region. The magnitude of this nanometric dipole-dipole interaction, i.e., the optical near-field interaction, can be estimated by measuring the energy transfer time [6].

The energy transfer between QDs is not only of physical interest, but is also applicable to the novel technology of nanophotonics [7]. We have proposed and demonstrated a nanometric all-optical switch using an optical near field, i.e., the nanophotonic switch [8], [9] and an optical nano-fountain, i.e., a nanometric optical condenser [10]. Since the operation times of these devices depend strongly on the energy transfer time, observations of the energy transfer time are important for designing nanophotonic devices, and for understanding the phenomenon of energy transfer via an optical near field. It is also important to measure the lifetime of the excitons in a coupled QD pair, because the optical near-field interaction influences the exciton lifetime, and the frequency of the repetitive device operation is limited by the exciton lifetime [6].

First, we consider the two QDs coupled via optical near field in the classic simple model. In the classical image, the optical near field around a QD in an excited state is described as the electromagnetic field generated by the many vibrational polarizations of the each cells in material [11]. In the exact near-field theory, all of such vibrational polarizations should be treated as many individual dipoles couple each other. Here, we simplified and represented them as a single dipole in a single QD. Figure 1 shows schematic drawings of the typical states of coupled QDs, which are much smaller than the wavelength of light. When their electric dipoles are parallel, the coupled state exerts a cooperative radiative transition and the carrier lifetime decreases due to the increase in the total oscillator strength, as shown in Fig. 1(a). Conversely, when their electric dipoles are anti-parallel, the coupled state shows quadrupole state, which is destructive interference of radiation. Thus, their carrier lifetime increases, because the total oscillator strength de-

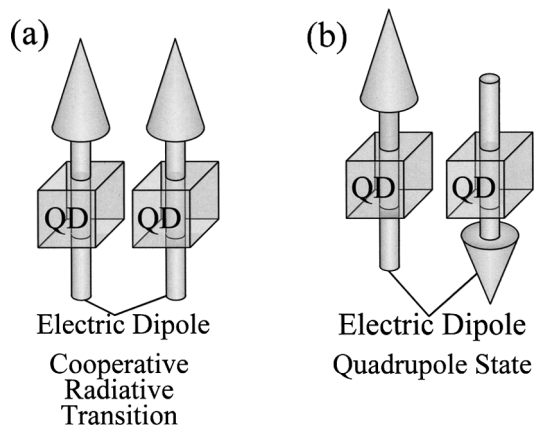

Fig. 1 Schematic drawing of a quantum dot (QD) pair and its electric dipoles. (a) The electric dipoles are parallel to each other. (b) The dipoles are anti-parallel, i.e., the quadrupole state.

Manuscript received April 5, 2005.
Manuscript revised May 31, 2005.

[†]The authors are with Japan Science and Technology Agency, Machida-shi, 194-0004 Japan.
[††]The author is with Tokyo Institute of Technology, Tokyo, 152-8550 Japan.
[†††]The author is with the University of Tokyo, 113-8656 Japan.
a) E-mail: kawazoe@ohtsu.ist.go.jp

DOI: 10.1093/ietele/e88–c.9.1845

creases, as shown in Fig. 1(b).

In this paper, we report the observed energy transfer rate from the exciton state in a CuCl QD to the optically forbidden exciton state in another CuCl QD, using time-resolved optical near-field spectroscopy. We also show the nature of the anti-parallel dipole-coupling feature of the optical near-field interaction experimentally.

2. Experimental

Cubic CuCl QDs embedded in NaCl are suitable for studying the optical near-field interaction, because the possibility of energy transfer due to carrier tunneling and Coulomb coupling can be excluded, since the potential depth exceeds 4 eV and the binding energy of exciton is more than 200 meV with its Bohr radius of 0.68 nm [12]. We fabricated cubic CuCl QDs embedded in a NaCl matrix using the Bridgman method and successive annealing, and found that the average side length size of the cubic QDs was L = 4.2 nm [13]. A 325-nm CW He-Cd laser and 385-nm SHG of CW and mode-locked Ti-sapphire lasers (repetition rate: 80 MHz) were used as the light sources. To achieve the selective excitation of the discrete energy levels in the QDs, the duration of the transform-limited pulse of the mode-locked laser was set at 10 ps. A double-tapered fiber probe with a 150-nm aluminum coating and a 40-nm diameter aperture was fabricated by chemical etching and the pounding method [14], [15]. At the scanning of near field image, the sample-probe distance was regulated within 10 nm by using the shear force technique [16]. The fiber probe was fixed in several seconds at every scanning point, and the spectrum of the output from the fiber probe was measured using the spectrometer with the cooled charge coupled device (CCD) detector for the every scanning points. The near-field image was reconstructed from the stored spectrum datum for the every scanning point after the simple data processing, such as a spectral filtering (i.e., a selecting the wavelength) and a noise reduction. For the measurement of the energy transfer rate between QDs, the temporal evolution of the photoluminescence (PL) pump-probe signal was observed using the time correlation single photon counting method with a 15-ps time resolution. For this measurement, we found the position where the QD pair exists in the inhomogeneous size-dispersed sample first. Next, the fiber probe was fixed at the position, and the output signal from the fiber probe was measured for about 1000 seconds.

3. Results and Discussions

Figures 2(a) shows the spatial distribution of the luminescence intensity by using the near-field microscope with the spectral window, which is 1-nm bandwidth and 385-nm center wavelength. Figure 2(b) shows the PL spectrum at the inside in the broken circle in Fig. 2(a), where we fix the near-field fiber probe at the center in the broken circle and the spectrum of the optical output of fiber probe was measured by the spectrometer with the liquid cooled

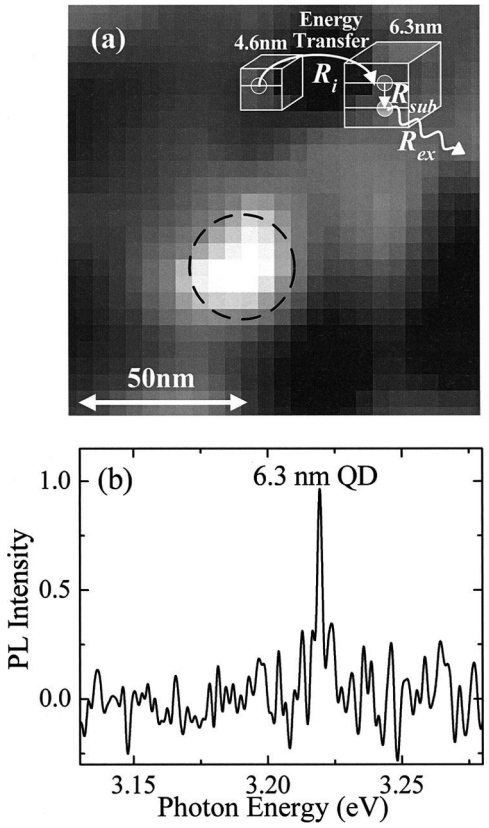

Fig. 2 (a) The spatial distribution of the luminescence intensity from the 6.3-nm QD with the 325-nm CW probe light only. The inset shows the observed QD pair and the energy flow. (b) The near-field PL spectrum measured at the inside in the broken circle in (a).

charge coupled device (CCD) detector. Here, the sample temperature was 15 K and the excitation light source was the 325-nm CW light only, which excited the band-to-band transition in the sample. The inset in Fig. 2(a) shows the QDs exist in the broken circle and explains the energy transfer between the observed QDs, i.e., from 4.6- to 6.3-nm QDs, where R_i, R_{sub}, and R_{ex} are the energy transfer rate, inter-sub-level transition rate, and exciton recombination rate, respectively. The energy transfer time τ_i, the inter-sub-level transition time τ_{sub}, and the exciton lifetime τ_{ex} are give by the inverses of R_i, R_{sub}, and R_{ex}, respectively. The energy eigenvalues for the quantized Z_3 exciton energy level in a cubic CuCl QD with size L are given by $E_{n_x,n_y,n_z} = E_B + \hbar^2\pi^2(n_x^2 + n_y^2 + n_z^2)/2M\,(L - a_B)^2$, where E_B is the bulk Z_3 exciton energy, M is the translational mass of the exciton, a_B is its Bohr radius, n_x, n_y, and n_z are quantum numbers (n_x, n_y, n_z =1, 2, 3, ...). Here, $d = (L - a_B)$ gives the effective confinement size for an exciton in a cubic QD and is called the effective size, which is obtained by considering the dead layer correction [13], and that gives the confinement size for a center of mass of an exciton in a QD. According to the equation, there was resonance between the quantized exciton energy level of quantum number (1,1,1) in the 4.6-nm QDs and the quantized exciton energy level of quantum number (2,1,1) in the 6.3-nm QDs at 15 K, where

the exciton homogeneous linewidth is 1 meV. Note that the transition, induced by the propagating light, between ground state to (2,1,1) excited state is dipole-forbidden. However, optical near-field energy transfer is allowed with the coupling energy represented by the following Yukawa function: [16], [17]. Here, r is the separation between the two QDs, A is the coupling coefficient, and is the inverse decay length of the Yukawa function, which correspond to the effective mass of our published effective interaction theory [16], [17]. For the L = 4.6- and 6.3-nm QD pair with 10-nm separation, the estimated τ_i is about 50 ps, which is much shorter than τ_{ex}, which is a few ns. Since τ_{sub} is generally less than a few ps and is much shorter than τ_i [18], luminescence of a 4.6-nm QD decreases, because the faster energy transfer to 6.3-nm QD occurs instead of the slower radiation of excitonic recombination in a 4.6-nm QD. On the other hand, luminescence of a 6.3-nm QD increases due to the supply of the excitation energy from the neighboring 4.6-nm QD. As a result, the PL signal from the 6.3-nm QD was observed as the spectral peak, as shown in Fig. 2(b).

Figures 3(a) and (b) show the spatial distribution of the luminescence intensity from the 4.6-nm QD and the differential PL spectrum and at 15 K, respectively taken with the 325-nm CW probe light and the 385-nm 10-ps pump pulse. Here, the differential PL spectral intensity is given by $\mathrm{PL_{diff}} = \mathrm{PL_{pump\&probe}} - \mathrm{PL_{pump}} - \mathrm{PL_{probe}}$. Here $\mathrm{PL_{diff}}$ is the differential PL spectral intensity, and $\mathrm{PL_{pump\&probe}}$, $\mathrm{PL_{pump}}$, and $\mathrm{PL_{probe}}$ are the PL spectral intensity which are observed using the both of pump and probe light, the probe light only, and the pump light only, respectively. The upward pointing arrow in Fig. 3(b) shows the photon energy of the pump pulse tuned to the (1,1,1) exciton energy level in the 6.3-nm QD. The inset in Fig. 3(a) shows the energy transfer between the QDs when the pump pulse excites the 6.3-nm QD. In this case, because the exciton energy in the 4.6-nm QD cannot be transferred to the (1,1,1) exciton energy level in the 6.3-nm QD due to the state filling effect, the exciton energy flows back and forth between the (1,1,1) exciton energy level in the 4.6-nm QD and (2,1,1) exciton energy level in the 6.3-nm QD [6], [19], and some excitons recombine in the 4.6-nm QD. Therefore, the PL signal from the 4.6-nm QD was detected as the spectral peak indicated by the arrow in Fig. 3(b). The temporal evolution of this PL signal strongly depends on the R_i and R_{ex} of the coupled QD system.

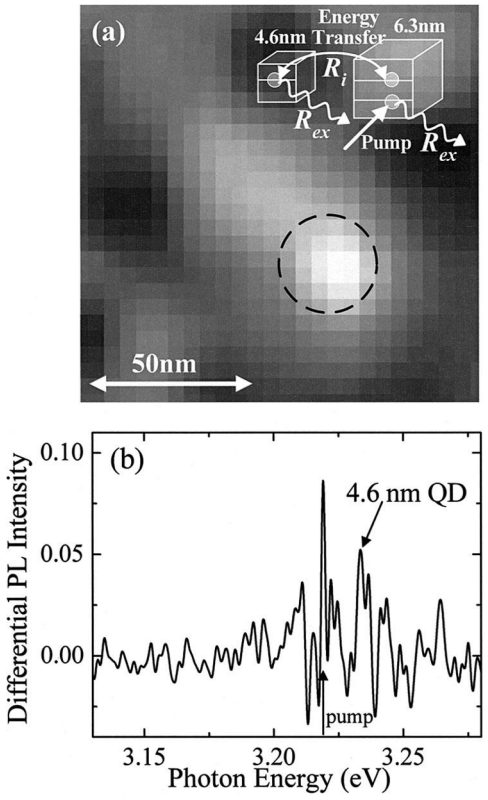

Fig. 3 (a) The spatial distribution of the luminescence intensity from the 4.6-nm QD with the 325-nm CW probe light and the 385-nm 10-ps pump pulse. Here we used the narrow band-pass filter (FWHM:8 meV), whose optical density in the stop-band is more than 6. The inset shows the observed QD pair and the energy flow. (b) The differential near-field PL spectrum measured at the inside in the broken circle in (a).

Figures 4(a) and (b) show the temporal evolution of the PL peak intensity from 4.6-nm QDs indicated for different time scales: (a) from −300 ps to 4000 ps, (b) from −70 ps to 350 ps. The open squares (P1), circles (P2), and triangles (P3) correspond to the experimental results observed for three different 4.6- and 6.3-nm QDs pairs. In Fig. 4(a), the longitudinal axis has a logarithmic scale. The solid, broken, and dotted curves are fitted to the experimental values based on the rate equation, which is given by

$$\begin{cases} \frac{dI_{4.6}}{dt} = I_0 - R_i \cdot I_{4.6} - R_{ex\_4.6} \cdot I_{4.6} + R_i \cdot I_{6.3} + I_{probe} \\ \frac{dI_{6.3}}{dt} = I_0 - R_i \cdot I_{6.3} - R_{ex\_6.3} \cdot I_{6.3} + R_i \cdot I_{6.3} + I_{probe} \end{cases}. \quad (1)$$

Here, $I_{4.6}$ and $I_{6.3}$ are the exciton populations in the 4.6- and 6.3-nm QDs, respectively, and I_{probe} is the exciton population created by the probe laser. I_0 is the equilibrium population of the relaxation and the creation of excitons by the recombination of exciton and the pump-probe light, respectively. In our experimental condition, I_0 is necessary, because the experimental results were obtained by the accumulation of repetitive events of 10^{11} times (the repetition rate of pump pulse was 80 MHz and the accumulation time was about 1000 s) and the equilibrium population remained in QDs due to the memory effect coming form the many repetitive events before the observation. The exciton population in the 6.3-nm QD is increased due to the pump pulse at t=0. The exciton population in the 4.6-nm QD is also increased, because the energy transfer to the 6.3-nm QD is regulated by the filling effect. This increase in the exciton population of the 4.6-nm QD corresponds to the increase in the PL intensity from the 4.6-nm QD. In Fig. 4(a), the solid, broken, and dotted lines show the decay time of the PL for QD pairs P1, P2, and P3, respectively, and the respective decay time are 6.7, 4.2, and 2.9 ns. The rise-time of the PL intensity from the 4.6-nm QD strongly depends on the energy transfer time τ_i. The energy transfer times (τ_i) for P1, P2, and P3 were 25, 90, and 180 ps, respectively, which were estimated from the best fit of the experimental data, as shown

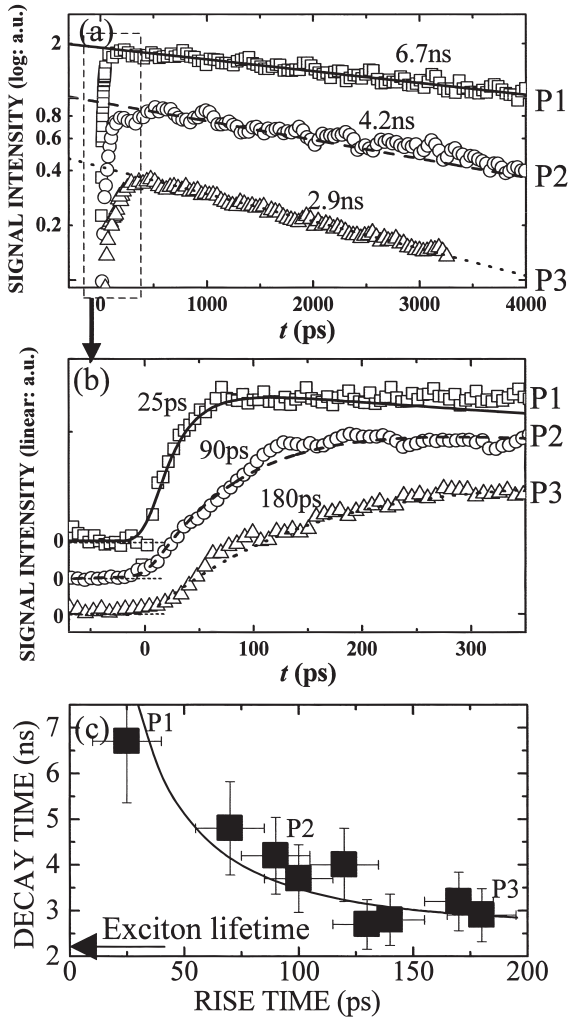

Fig. 4 Time evolutions of the PL peak signal intensity in Fig. 3(a) observed at different positions in the sample, i.e., different QD pairs, (P1: □, P2: ○, and P3: △). (a) Evolution in the range $-300\,\text{ps} \leqq t \leqq 4000\,\text{ps}$ with a logarithmic longitudinal axis. (b) Evolution in the range $-70\,\text{ps} \leqq t \leqq 350\,\text{ps}$ with a linear longitudinal axis. (c) Relationship between the energy transfer and decay times for the PL pump-probe signal. Closed squares show the experimental results, which were fitted using the solid curve.

in Fig. 4(b). Here the longitudinal axis has a linear scale. These energy transfer times agree with them estimated using our proposed near-field interaction theory [17]. Here, we also consider scaling by $1/r^3$ (dipole-dipole interaction) or e^{-r}/r (near-field interaction). The energy transfer time of 0.8 ps was obtained in the light-harvesting antenna complex of photosynthetic purple bacteria [5], whose system is about one fifth the size of the CuCl QD system. The respective energy transfer times of CuCl QD system are expected to be 100 ps ($0.8 \times (1/5)^{-1}$ ps) and 590 ps ($0.8 \times (\exp(-5)/5)^{-1}$) in considering scaling by the dipole-dipole interaction and near-field interaction and are in the same orders as our experimental results. Differences in the rise times of P1, P2, and P3 are attributed to the differences in the separations of the 4.6- and 6.3-nm QDs.

The solid squares in Fig. 4(c) are the experimental results for the relation between the decay and rise times of the PL from the 4.6-nm QD for several QD pairs including P1, P2, and P3. The decay time exceeds the exciton lifetime (2.2 ns) of the isolated 6.3-nm QD measured experimentally, and increases as the rise time falls. Rate Eq. (1) indicates that the decay time is determined by the exciton lifetimes (i.e., physical properties constant) in the 6.3-nm and 4.6-nm QD. The other dissipative pathways can be negligible in consideration of the exciton luminescence efficiency. Therefore the experimental result in Fig. 4(c) means that the exciton lifetime in the QDs increases with the optical near-field interaction. This increase in the exciton lifetime can be explained by the features of a QD pair coupled with an optical near field, which has the feature of the anti-parallel dipole-dipole coupling. When the variation of the exciton recombination rate R_{ex} is proportional to the strength of optical near-field interaction, the decay time of the PL intensity from the 4.6-nm QD, which equals the exciton lifetime τ_{ex}, is given by $\tau_{ex} = 1/R_{ex} = 1/[R_0\{1 - \exp(-a/R_i)\}]$, where R_0 and a are the exciton lifetime of an isolated QD and the fitting parameter, respectively. The solid curve in Fig. 4(c) is the fitted result based on this assumption, and it agrees well with the experimental results.

In order to clarify the physical mechanisms of anti-parallel feature of the optical near-field coupled QD, more detailed examinations are necessary. We consider that although there are two possible eigenstates of the mutual arrangements of the dipoles in excitons, i.e., parallel and anti-parallel, as shown in Figs. 1(a) and 1(b), the occurrence probability of the anti-parallel state exceeds that of the parallel state because the total energy of the system for the anti-parallel state is lower than that for the parallel state. This anti-parallel feature of the optical near-field coupled QDs reduces the recombination of excitons. Consequently, the exciton lifetime increases with the optical near-field interaction.

4. Conclusion

We measured the optically forbidden energy transfer time between cubic CuCl QDs via the optical near-field interaction directly using a PL pump-probe technique. The signal rise time, which corresponds to the energy transfer time, was from 25 to 180 ps. We also showed that the decay time increased as the energy transfer time fell; this was attributed to the anti-parallel dipole-coupling feature of the near-field interaction between the QDs. These features are of interest physically and are applicable to photonic devices, such as optical nanometric sources, long phosphorescence devices, and optical battery cells.

References

[1] D. Goldhaber-Gordon, H. Shtrikman, D. Mahalu, D. Abusch-Magder, U. Meirav, and M.A. Kastner, "Kondo effect in a single-electron transistor," Nature, vol.391, pp.156–159, Jan. 1998; D. Goldhaber-Gordon, J. Göres, M.A. Kastner, H. Shtrikman, D.

Mahalu, and U. Meirav, "From the Kondo regime to the mixed-valence regime in a single-electron transistor," Phys. Rev. Lett., vol.81, pp.5225–5228 Dec. 1998.
[2] F.R. Waugh, M.J. Berry, D.J. Mar, R.M. Westervelt, K.L. Campman, and A.C. Gossard, "Single-electron charging in double and triple quantum dots with tunable coupling," Phys. Rev. Lett., vol.75, pp.705–708, July 1995.
[3] G. Burkard, G. Seelig, and D. Loss, "Spin interactions and switching in vertically tunnel-coupled quantum dots," Phys. Rev. B, vol.62, pp.2581–2592, July 2000.
[4] T. Kawazoe, K. Kobayashi, J. Lim, Y. Narita, and M. Ohtsu, "Direct observation of optically forbidden energy transfer between CuCl quantum cubes via near-field optical spectroscopy," Phys. Rev. Lett., vol.88, 067404, Jan. 2002.
[5] K. Mukai, S. Abe, and H. Sumi, "Theory of rapid excitation-energy transfer from B800 to optically-forbidden exciton states of B850 in the antenna system LH2 of photosynthetic purple bacteria," J. Phys. Chem. B, vol.103, pp.6096–6102, July 1999.
[6] S. Sangu, K. Kobayashi, T. Kawazoe, A. Shojiguchi, and M. Ohtsu, "Quantum-coherence effect in a quantum dot system coupled by optical near fields," Trans. Mat. Res. Soc. Jpn., vol.28, pp.1035–1038, Dec. 2003.
[7] M. Ohtsu, K. Kobayashi, T. Kawazoe, S. Sangu, and T. Yatsui, "Nanophotonics: Design, fabrication, and operation of nanometric devices using optical near fields," IEEE J. Sel. Top. Quantum Electron., vol.8, pp.839–862, July/Aug. 2002.
[8] T. Kawazoe, K. Kobayashi, S. Sangu, and M. Ohtsu, "Demonstration of a nanophotonic switching operation by optical near-field energy transfer," Appl. Phys. Lett., vol.82, pp.2957–2959, May 2003.
[9] T. Kawazoe, K. Kobayashi, S. Sangu, and M. Ohtsu, "Demonstrating nanophotonic switching using near-field pump-probe photoluminescence spectroscopy of CuCl quantum cubes," J. Microscopy, vol.209, pp.261–266, March 2002.
[10] T. Kawazoe, K. Kobayashi, and M. Ohtsu, "The optical nanofountain: A biomimetic device that concentrates optical energy in a nanometric region," Appl. Phys. Lett., vol.86, 103102, March 2005.
[11] M. Ohtsu, ed., Near-Field Nano/Atom Optics and Technology, Springer, Tokyo, Berlin, Heidelberg, New York, 1998.
[12] A.D. Yoffe, "Semiconductor quantum dots and related system: Electronic, optical, luminescence and related properties of low dimensional systems," Adv. Phys., vol.50, pp.1–208, Jan. 2001.
[13] N. Sakakura and Y. Masumoto, "Persistent spectral-hole-burning spectroscopy of CuCl quantum cubes," Phys. Rev. B, vol.56, pp.4051–4055, Aug. 1997.
[14] T. Saiki, S. Mononobe, M. Ohtsu, N. Saito, and J. Kusano, "Tailoring a high-transmission fiber probe for photon scanning tunneling microscope," Appl. Phys. Lett., vol.68, pp.2612–2614, May 1996.
[15] T. Saiki and K. Matsuda, "Near-field optical fiber probe optimized for illumination-collection hybrid mode operation," Appl. Phys. Lett., vol.74, pp.2773–2775, May 1999.
[16] K. Kobayashi, S. Sangu, H. Ito, and M. Ohtsu, "Near-field optical potential for a neutral atom," Phys. Rev. A, vol.63, 013806, Jan. 2000.
[17] S. Sangu, K. Kobayashi, A. Shojiguchi, T. Kawazoe, and M. Ohtsu, "Excitation energy transfer and population dynamics in a quantum dot system induced by optical near-field interaction," J. Appl. Phys., vol.93, pp.2937–2945, March 2003.
[18] T. Suzuki, T. Mitsuyu, K. Nishi, H. Ohyama, T. Tomimasu, S. Noda, T. Asano, and A. Sasaki, "Observation of ultrafast all-optical modulation based on intersubband transition in n-doped quantum wells by using free electron laser," Appl. Phys. Lett., vol.69, pp.4136–4138, Dec. 1996.
[19] K. Kobayashi, S. Sangu, T. Kawazoe, and M. Ohtsu, "Exiton dynamics and logic operations in a near-field optically coupled quantum-dot system," J. Luminescence, vol.112, pp.117–121, April 2005.

Tadashi Kawazoe received the B.E., M.E., and Ph.D. degrees in physics from University of Tsukuba, Tsukuba, Japan, in 1990, 1993, and 1996, respectively. Since 1991, he has studied spin relaxation in semiconductor quantum wells and optical nonlinearities in semiconductor quantum dots at the Institute of Physics, University of Tsukuba, Tsukuba-city, Japan. In 1996, he joined in the Faculty of Engineering, Yamagata University, Yamagata, Japan, as a Research Associate, engaged in research on nonlinear optical materials and devices. Since April 2000, he has been with Japan Science and Technology Agency, Tokyo, Japan. His current research interests are in the areas of optical properties of nano materials, optical near field, and nano-photonic devices. Dr. Kawazoe is a member of the Physical Society of Japan and the Japan Society of Applied Physics.

Kiyoshi Kobayashi was born in Okayama, Japan, on November 25, 1953. He received the D.S. degree in Physics from the University of Tsukuba, Tsukuba, Japan, in 1982. After graduating from the University of Tsukuba, he joined IBM Japan as a Research Staff Member at Tokyo Research Laboratory. Since 1998 he has been the theoretical group leader of the "Localized Photon" project for the Exploratory Research for Advanced Technology (ERATO) at the Japan Science and Technology Corporation (JST), Tokyo. His main fields of interest are theory on near field optics and its application to nano/atom photonics. In 2004, he became a Professor at the Tokyo Institute of Technology. Dr. Kobayashi is a member of the Physical Society of Japan, the Japan Society of Applied Physics, the American Physical Society, and the Optical Society of America.

Motoichi Ohtsu received the B.E., M.E., and Dr.E. degrees in electronics engineering from the Tokyo Institute of Technology, Tokyo, Japan, in 1973, 1975, and 1978, respectively. In 1978, he was appointed a Research Associate, and in 1982, he became an Associate professor at the Tokyo Institute of Technology. From 1986 to 1987, while on leave from the Tokyo Institute of Technology, he joined the Crawford Hill Laboratory, AT&T Bell Laboratories, Holmdel, NJ. In 1991, he became a Professor at the Tokyo Institute of Technology. Since 1993, he has been concurrently the Leader of the "Photon Control" project of the Kanagawa Academy of Science and Technology, Kanagawa, Japan. Since 1998, he has been concurrently the Leader of the "Localized Photon" project of ERATO, JST, Japan. Since 2003, he has been concurrently the Leader of the "Localized Photon" project of SORST, JST, Japan. He has written over 400 papers and received 100 patents. He is the author and co-author of 50 books. His main fields of interests are the nano-photonics and atom-photonics. Dr. Ohtsu is a member of the Japan Society of Applied Physics, the Institute of Electrical Engineering of Japan, the Optical Society of America, and American Physical Society. He has been awarded more than ten prizes from academic institutions, including the Issac Koga Gold Medal of URSI in 1984, the Japan IBM Science Award in 1988, two awards from the Japan Society of Applied Physics in 1982 and 1990, the Inoue Science Foundation Award in 1999, and Medal with Purple Ribbon in 2004.

IEICE TRANS. ELECTRON., VOL.E88–C, NO.9 SEPTEMBER 2005

PAPER Special Section on Nanophotonics and Related Techniques

Observation of Size-Dependent Resonance of Near-Field Coupling between a Deposited Zn Dot and the Probe Apex during Near-Field Optical Chemical Vapor Deposition

Jungshik LIM[†a)], **Takashi YATSUI**[††], *Nonmembers*, *and* **Motoichi OHTSU**[††,†††], *Member*

SUMMARY We investigated the initial stage of Zn dot growth using near-field optical chemical vapor deposition. The dependence of the rate of Zn dot deposition on dot size revealed that the deposition rate was maximal when the dot grew to a size equivalent to the probe apex diameter. Such observed size-dependent resonance was in good agreement with theoretical results for dipole-dipole coupling with a Förster field between the deposited Zn dot and the probe apex.

key words: *optical near-field, self-assembly, nanoparticles*

1. Introduction

Future optical transmission systems require ultrahigh integration of photonic devices. To meet this requirement, we have proposed nanophotonic devices and their integrated circuits (ICs). These consist of nanometer-scale dots and wires, and use an optical near field as the signal carrier [1]. Operation of a nanophotonic switch, a representative device, has been confirmed by controlling the dipole forbidden optical energy transfer among resonant energy states in a three-CuCl-quantum-dot system via an optical near field [2]. In order to fabricate these devices, their size and position on the substrate must be controlled with nanometer-scale accuracy because they are composed of sub-100-nm scale dots and wires.

To realize such controllability, we have proposed and demonstrated near-field optical chemical vapor deposition (NFO-CVD) [3], [4], which is applicable to various materials, including semiconductors, metals, and insulators. Using NFO-CVD, nanometer-scale Zn and Al dots have been successively deposited on the same substrate by changing the reactant molecules during deposition [5].

A nanometer-scale ZnO dot is a promising material for realizing nanophotonic devices operating at room temperature, owing to its large exciton binding energy (60 meV) [6], [7]. Since high-quality ZnO nanocrystallites can be obtained by oxidizing Zn nuclei [8], NFO-CVD is a powerful tool for their fabrication.

By considering the amount of the energy shift of the ground state of the exciton in ZnO nanocrystallites owing to the quantum confinement effect at room temperature, it is estimated that the size accuracy in ZnO nanocrystallites deposition must be as low as ±10% to realize efficient near-field energy transfer among the resonant energy states in a nanophotonic switch composed of 5-, 7-, and 10-nm dots [2].

To realize sub-10-nm scale controllability in size, we report here the precise growth mechanism of Zn dots with NFO-CVD. We directly observe that the deposition rate is maximal when the dot grew to a size equivalent to the probe apex diameter. This dependence is well accounted for by the theoretically calculated dipole-dipole coupling with a Förster field. The theoretical support and experimental results indicate the potential advantages of this technique for improving regulation of the size and position of deposited nanometer-scale dots.

2. NFO-CVD

Figure 1(a) shows a schematic of NFO-CVD. To deposit Zn dots, diethylzinc (DEZn) was used as the reactive molecular gas and argon (Ar) as the carrier gas.

A (0001) sapphire was used as the substrate for Zn dot deposition. The total pressure in the NFO-CVD chamber was 2.5 Torr, and the partial pressure of DEZn was 50 mTorr. A He-Cd laser (λ=325 nm) was used as the light source. We used a sharpened UV fiber probe with a pure silica core to generate the optical near field efficiently [9]. Figure 1(b) shows a scanning electron microscopic (SEM) image of the fiber probe. The estimated apex diameter $2a_p$ was 9 nm by referring to the fitted broken circle. Although the long (more than 30 minutes) irradiation time results in the deposition of the dissociated metal organic molecules also on the probe tip [10], the decrease in the throughput of optical near-field generation on depositing Zn on the fiber probe was negligible, since the laser irradiation time for the deposition of Zn dots as small as several-ten-nm scale was sufficiently short (less than 60 seconds). The He-Cd laser light was coupled to the other end of the fiber probe. The separation between the fiber probe and substrate was kept within a few nanometers by shear-force feedback control. A DEZn molecule ad-

Manuscript received December 13, 2004.
Manuscript revised April 21, 2005.

[†]The author is with Interdisciplinary Graduate School of Science and Engineering, Tokyo Institute of Technology, Yokohama-shi, 226-8502 Japan.
[††]The authors are with Solution-Oriented Research for Science and Technology, Japan Science and Technology Agency, Machida-shi, 194-0004 Japan.
[†††]The author is with the School of Engineering, The University of Tokyo, Tokyo, 113-8656 Japan.
a) E-mail: jslim@ae.titech.ac.jp

DOI: 10.1093/ietele/e88–c.9.1832

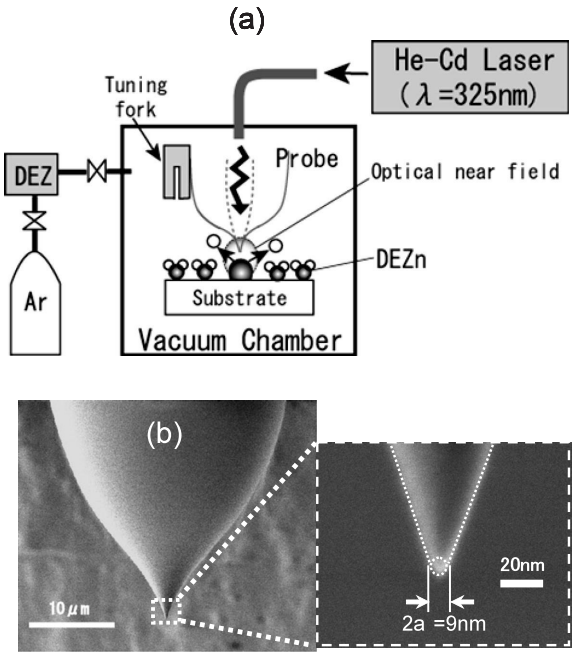

Fig. 1 (a) Schematic of NFO-CVD. (b) A SEM image of the fiber probe apex. $2a_p$: apex diameter.

sorbed on the substrate was selectively dissociated by the optical near field; as a result, Zn atoms were deposited on the substrate [11]. After depositing Zn dots, their sizes and shapes were measured using in situ vacuum shear-force microscopy, with the same fiber probe used for deposition [3].

3. Results and Discussion

Figure 2(a) shows a shear-force image of four Zn dots deposited with irradiation times of 60, 30, 10, and 5 s (dots A to D, respectively) with a laser output power, P, of 5 μW. We tried to deposit dots with 260-nm separation along the x-axis by servo-controlling the position of the fiber probe. As shown in the cross-sectional profiles in Fig. 2(b), Zn dots as small as 20 nm in size (S, defined by the full-width at the half-maximum on this profile) were fabricated. Their separation was 269 and 262 nm, confirming high positional accuracy (< 10 nm). The majority of this residual inaccuracy arises from the hysteresis of the PZT actuator used for scanning the fiber probe; this can be decreased by selecting the actuator carefully.

Figure 3(a) plots the normalized deposition rate, R, of Zn dots, as a function of dot size, S. As the measured dot size, S', was a convolution of the probe apex diameter, $2a_p$, and the real size, S, S was estimated as $S = S' - 2a_p$. Note that R is maximal at $S = 2a_p$. This indicates that the magnitude of the near-field optical interaction between the deposited Zn dot and the probe apex was enhanced resonantly with respect to S, resulting in the resonant increase in R. In other words, the near-field optical interaction exhibited size-dependent resonance characteristics.

To identify the origin of this size-dependent resonance,

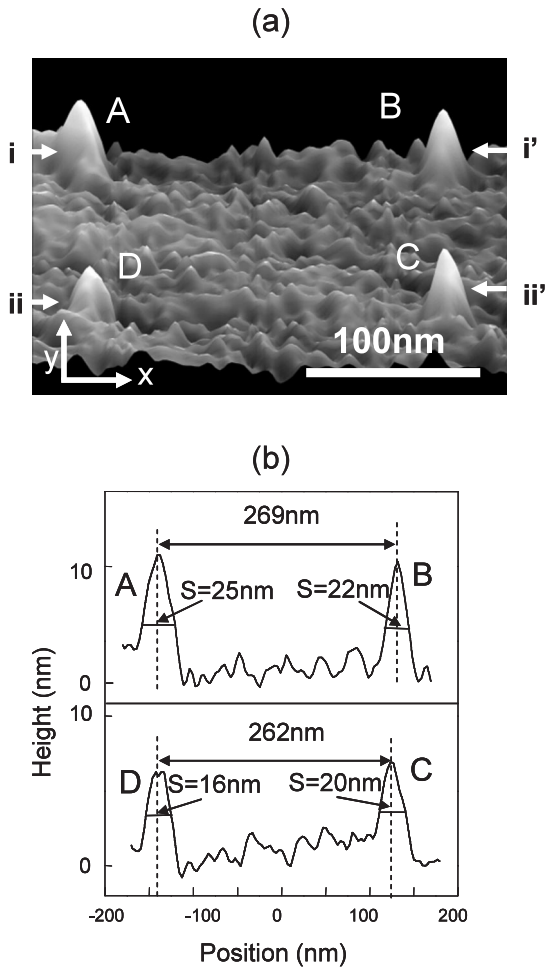

Fig. 2 (a) A shear-force image of deposited Zn dots. The laser irradiation times of dots A-D were 60, 30, 10, and 5 s, respectively. (b) The upper and lower curves show the cross-sectional profile along the line indicated by arrows i-i′ and ii-ii′, respectively.

theoretical considerations were performed. Since the deposition rate can be proportional to the intensity of the light scattered from the closely spaced probe tip and deposited Zn dot, we calculated the magnitude of the near-field optical interaction between them (Fig. 3(b)). In this calculation, since the optical near-field is generated at the probe apex, the probe tip was assumed as sphere p. The sphere s represents Zn dot. As the separation between two particles is much narrower than the wavelength, the Förster field (proportional to R^{-3}, where R is the distance from the dipole) is dominant in the oscillating dipole electric field. In this quasistatic model, I_s, the intensity of the light scattered from the two closely spaced spheres p and s, is given by [12]

$$I_s = I_1 + I_2 = \left(\alpha_p + \alpha_s\right)^2 |E|^2 + 4\Delta\alpha\left(\alpha_p + \alpha_s\right)|E|^2, \quad (1)$$

where $\alpha_i = 4\pi\varepsilon_0(\varepsilon_i - \varepsilon_0)/(\varepsilon_i + 2\varepsilon_0)\, a_i^3$ is the polarizability of sphere i (= p, s) with diameter a_i. The first and second terms, I_1 and I_2, represent the light intensity scattered from the spheres, and the light owing to the dipole-dipole interaction induced by the Förster field. Therefore, the light

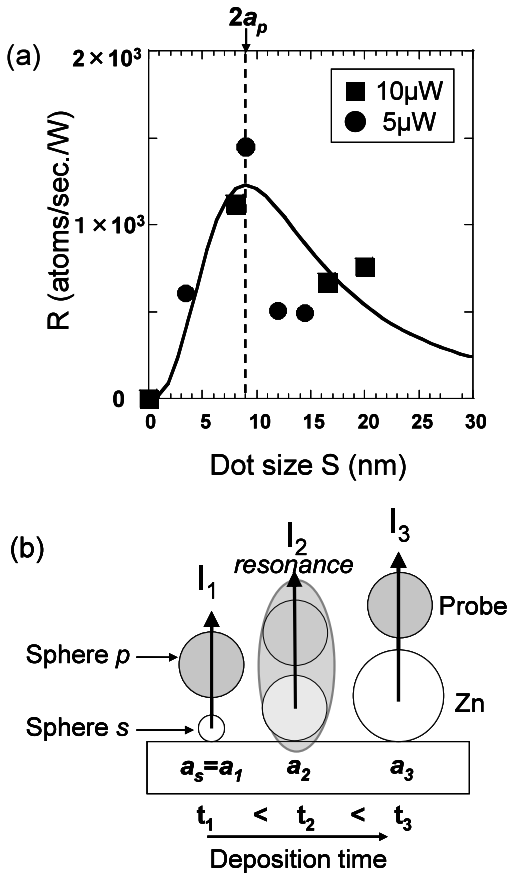

Fig. 3 (a) The time-dependent deposition rate R. Solid squares and circles indicate the normalized deposition rate at P =10 and 5 μW, respectively. The solid curve indicates the calculated value of I_2/I_1. (b) Schematic of the growth of a Zn dot.

intensity under study, normalized to I_1, is given by

$$I_2/I_1 = \frac{G_p A_p^3}{(A_p+1)^3(G_p A_p^3+1)}, \tag{2}$$

where $A_p = a_p/a_s$ and $G_p = (\varepsilon_p - 1)(\varepsilon_s + 2)/(\varepsilon_p + 2)(\varepsilon_s - 1)$. For deposition by the fiber probe, the dielectric constants of Zn and the fiber probe are $\varepsilon_s = (0.6+i4)^2$ [13] and $\varepsilon_p = 1.5^2$, respectively. The diameter ($2a_p$) of sphere p was 9 nm (see Fig. 1(b)). The solid curve in Fig. 3(a) shows the calculated value of I_2/I_1 as a function of the Zn dot size, S (= $2a_s$), which agrees very well with the experimental results. This agreement indicates that the increase in R originates from dipole-dipole coupling with the Förster field at a dot size equivalent to the probe apex diameter.

4. Conclusion

We investigated the growth mechanism of Zn dots with NFO-CVD, and found that the deposition rate was maximal when the dot grew to a size equivalent to the probe apex diameter, owing to resonant near-field coupling between the deposited Zn dot and the probe apex. The experimental results and suggested mechanisms show the potential advantages of this technique for realizing nanophotonic ICs.

Acknowledgement

The authors would like to thank Dr. S. Sangu of Ricoh Company for useful discussions.

References

[1] M. Ohtsu, K. Kobayashi, T. Kawazoe, S. Sangu, and T. Yatsui, "Nanophotonics: Design, fabrication, and operation of nanometric devices using optical near fields," IEEE J. Sel. Top. Quantum Electron., vol.8, no.4, pp.839–862, July/Aug. 2002.

[2] T. Kawazoe, K. Kobayashi, S. Sangu, and M. Ohtsu, "Demonstration of a nanophotonic switching operation by optical near-field energy transfer," Appl. Phys. Lett., vol.82, no.18, pp.2957–2959, May 2003.

[3] Y. Yamamoto, M. Kourogi, M. Ohtsu, V. Polonski, and G.H. Lee, "Fabrication of nanometric zinc pattern with photodissociated gas-phase diethylzinc by optical near field," Appl. Phys. Lett., vol.76, no.16, pp.2173–2175, April 2000.

[4] T. Yatsui, S. Takubo, J. Lim, W. Nomura, M. Kourogi, and M. Ohtsu, "Regulating the size and position of deposited Zn nanoparticles by optical near-field desorption using size-dependent resonance," Appl. Phys. Lett., vol.83, no.9, pp.1716–1718, Sept. 2003.

[5] Y. Yamamoto, M. Kourogi, M. Ohtsu, G.H. Lee, and T. Kawazoe, "Lateral integration of Zn and Al dots with nanometer-scale precision by near field optical chemical vapor deposition using a sharpened optical fiber probe," IEICE Trans. Electron., vol.E85-C, no.12, pp.2081–2085, Dec. 2002.

[6] M.H. Huang, S. Mao, H. Feick, H. Yan, Y. Wu, H. Kind, E. Weber, R. Russo, and P. Yang, "Room-temperature ultraviolet nanowire nanolasers," Science, vol.292, pp.1897–1899, June 2001.

[7] A. Ohtomo, K. Tamura, M. Kawasaki, T. Makino, Y. Segawa, Z.K. Tang, G.K.L. Wong, Y. Matsumoto, and H. Koinuma, "Room-temperature stimulated emission of exitons in ZnO/(Mg,Zn)O superlattices," Appl. Phys. Lett., vol.77, no.14, pp.2204–2206, Oct. 2000.

[8] S. Cho, J. Ma, Y. Kim, Y. Sun, G. Wong, and J.B. Ketterson, "Photoluminescence and ultraviolet lasing of polycrystalline ZnO thin films prepared by the oxidation of the metallic Zn," Appl. Phys. Lett., vol.75, no.18, pp.2761–2763, Nov. 1999.

[9] M. Ohtsu, ed., Near-Field Nano/Atom Optics and Technology, Springer-Verlag, Tokyo, 1999.

[10] Y. Yamamoto, G.H. Lee, K. Matsuda, T. Shimizu, M. Kourogi, and M. Ohtsu, "Fabrication of an ultraviolet light-emitting functional probe of sub-micron size by photochemical vapor deposition," Opt. Rev., vol.7, no.6, pp.486–488, Dec. 2000.

[11] T. Yatsui, T. Kawazoe, M. Ueda, Y. Yamamoto, M. Kourogi, and M. Ohtsu, "Fabrication of nanometric single zinc and zinc oxide dots by the selective photodissociation of adsorption-phase diethylzinc using a nonresonant optical field," Appl. Phys. Lett., vol.81, no.19, pp.3651–3653, Nov. 2002.

[12] M. Ohtsu and K. Kobayashi, Optical Near Fields, Springer-Verlag, Berlin, 2003.

[13] R.G. Yarovaya, I.N. Shklyarevsklii, and A.F.A. El-Shazly, "Temperature dependence of the optical properties and the energy spectrum of zinc," Sov. Phys. JETP, vol.38, no.2, pp.331–334, Feb. 1974.

Jungshik Lim was born in Seoul, Korea, on October 17, 1971. He received the B.E. and M.E. degrees from Tokyo Institute of Technology, Tokyo, Japan, in 2001 and 2003, respectively. He is a Ph.D. student of Tokyo Institute of Technology, Tokyo, Japan. Mr. Lim is a member of the Japan Society of Applied Physics.

Takashi Yatsui was born in Tokyo, Japan, on January 21, 1972. He received the B.E. degree from Keio University, Tokyo, Japan, in 1995, and M.E. and D.E. degrees from Tokyo Institute of Technology, Tokyo, Japan, in 1997 and 2000, respectively. From 1999 to 2000, he was a Research Fellow of the Japan Society for the Promotion of Science. Since 2000, he has been a Researcher at the Japan Science and Technology Corporation, Tokyo. Since 2003, he has been a Researcher at the Japan Science and Technology Agency, Tokyo. His current research interests include nanofabrication using optical near-field. Dr. Yatsui received first prize in Paper Contest from IEEE Student Branch at Tokyo Institute of Technology in 1998, and the excellent research presentation award from the Japan Society of Applied Physics in 2000, and Tejima Doctoral Dissertation Award from Tejima Foundation in 2001. Dr. Yatsui is a member of the Japan Society of Applied Physics.

Motoichi Ohtsu received the B.E., M.E., and Dr.E. degrees in electronics engineering from the Tokyo Institute of Technology, in 1973, 1975, and 1978, respectively. In 1978, he was appointed a Research Associate, and in 1982, he became an Associate professor at the Tokyo Institute of Technology. From 1986 to 1987, while on leave from the Tokyo Institute of Technology, he joined the Crawford Hill Laboratory, AT&T Bell Laboratories. In 1991, he became a Professor at the Tokyo Institute of Technology. In 2004, he moved to the University of Tokyo. Since 1993, he has been concurrently the leader of the "Photon Control" project of the Kanagawa Academy of Science and Technology. Since 1998, he has been concurrently the leader of the "Localized Photon" project of ERATO. Since 2002, he is a leader of the national project on "Ultrahigh density optical storage" sponsored by METI. He has written over 320 papers and received 87 patents. He is the author and co-author of 39 books. In 2000, he was the President of the IEEE/LEOS Japan Chapter. From 2000, he is an executive director of the Japan Society of Applied Physics. In 2001, he served as a Technical Program Co-chair for the 4th CLEO/PR01. He has been a tutorial lecturer o the SPIE and the OSA. He is a member of several boards of the MEXT, METI, and so on. Prof. Ohtsu is a Fellow of the OSA, a senior member of IEEE, and member of several academic societies. He has been awarded ten prizes from academic institutions, including the I. Koga Gold Medal of URSI in 1984, the Japan IBM Science Award in 1988, two awards from the JSAP in 1982 and 1990, and the Inoue Science Foundation Award in 1999. In 2004, he was awarded a purple ribbon medal from Japanese government.

IEICE TRANS. ELECTRON., VOL.E88–C, NO.9 SEPTEMBER 2005

PAPER Special Section on Nanophotonics and Related Techniques

Nanophotonic Devices and Fundamental Functional Operations*

Suguru SANGU[†a)], *Nonmember*, **Kiyoshi KOBAYASHI**[††], *and* **Motoichi OHTSU**[†††,††††], *Members*

SUMMARY In nanophotonic device operations, characteristic features on a nanometer scale, such as locally excited states, dependence on the excitation number, and spatial symmetry of a system, play an important role. Using these features, selective excitation energy transfer via an optical near field is shown for a quantum-dot system with discrete energy levels. This selectivity strongly depends on a dipole-inactive state of an exciton, which cannot be excited by the far-field light. Operation principles of logic gates, photon storage, and quantum information processing device, which are based on the selectivity, are proposed, and the temporal dynamics are investigated analytically and numerically by using quantum theory. Nanophotonic devices, which are constructed from quantum mechanical and classical dissipative systems, are expected to become one of a key technologies in future device architecture.

key words: *nanophotonics, quantum states, logic gates, photon storage, quantum information processing*

1. Introduction

Nanophotonics has been one of promising technologies to develop future integrated optical devices [1], [2], which overcome critical limits of conventional devices. The optical devices based on wave optics have faced a limit for miniaturization of the device elements on a nanometer scale due to the diffraction limit of light. An optical near field, which is free from the diffraction limit, and is localized in the order of nanometric material size [3], plays an important role in nanophotonic devices. Electronic devices also have the limits; energy consumption in accordance with device miniaturization and a wiring problem [4]. Since nanophotonic devices do not operate via electric charge but excitation energy transfer, energy consumption is quite lower than the electronic devices [5]. These characteristic properties, such as local interaction and excitation transfer, require careful consideration for application to operation of nanophotonic devices, which are quite different from those for conventional optical and electronic devices.

Exploratory studies on nanophotonic devices have been carried out in recent years [6]–[10]. In 2003, Kawazoe et al. [9] had experimentally demonstrated a nanophotonic switching operation, in which three quantum dots with certain size ratios couple with each other via the optical near field. In this switch, they used irreversible energy transfer due to fast relaxation among the sublevels in a CuCl quantum dot and dipole-forbidden energy transfer that is allowed by a steep gradient of the optical near field. Aiming at further applications of nanophotonics, Naruse et al. [10] has proposed a content addressable memory or matching architecture in the field of optical communication, in which they also utilized the irreversible dynamics among several quantum dots. In this manner, inherent phenomena in the optical near field are strongly related to characteristic operations of nanophotonic devices.

In this paper, we emphasize three characteristic features in nanophotonics; (1) locally excited states, (2) dependence on the excitation (exciton) number, and (3) spatial symmetry in a several quantum-dot system, which are utilized for novel functional operations inherent in nanophotonic devices, as well as conventional ones. We investigate realization of key fundamental functional operations of nanophotonic devices, theoretically and numerically. Enumeration of feasible functional operations is quite important to develop future device technologies that overcome the above critical limits. Our proposed system consists of several quantum dots with discrete energy levels or energy sublevels. Note that such a system contains resonant energy transfer among quantum dots via the optical near field, which holds quantum coherence for a period before energy dissipation via energy sublevels coupled with lattice vibration. Fundamental structure of nanophotonic devices, we consider, consists of the quantum mechanical and classical parts [11], and is schematically illustrated in Fig. 1. In the

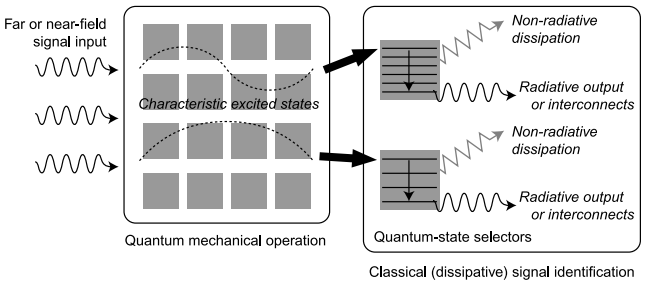

Fig. 1 Conceptual structure of nanophotonic devices, which consists of a quantum mechanical part and a classical part. The quantum mechanical part builds up characteristic excited states, and the classical part with dissipation identifies certain states and connects to outer detection systems.

Manuscript received December 13, 2004.

[†]The author is with the Research and Development Center, Ricoh Co., Ltd., Yokohama-shi, 224-0035 Japan.

[††]The author is with the Department of Physics, Tokyo Institute of Technology, Tokyo, 152-8551 Japan.

[†††]The author is with the Department of Electrical Engineering, the University of Tokyo, Tokyo, 113-8656 Japan.

[††††]The author is also with the Japan Science and Technology Agency.

*This work was part of the ERATO "Localized Photon" project at Japan Science and Technology Agency from 1998 to 2003.

a) E-mail: suguru.sangu@nts.ricoh.co.jp

DOI: 10.1093/ietele/e88–c.9.1824

quantum mechanical part, some characteristic excited states are created, and then, these states are extracted selectively from the quantum mechanical part to the classical one for connecting signals to an outer detection system, which is a key process to drive nanophotonic devices. Simple examples realized in a three or four-quantum-dot system are described in this paper, on the basis of such concepts.

This paper is organized as follows; details of the characteristic features mentioned above are given in Sect. 2. In Sect. 3, conventional logic gates, which are realized by using three quantum-dot systems, are demonstrated theoretically. Section 4 devotes photon storage or photon buffer memory by using dipole-inactive state for propagating far-field light. In Sect. 5, we discuss an application to quantum information processing. Finally, conclusions are given in Sect. 6.

2. Characteristic Features in Nanophotonics

2.1 Locally Excited States

Owing to localization of an optical near field, we cannot only observe but also access an individual quantum dot in a nanometric quantum-dot system, which is impossible for far-field light because of the diffraction limit of light. For the following discussions, we consider two identical quantum dots coupled via the optical near field. In this case, an exciton prepared in the system goes back and forth between two quantum dots for the period in the order of 100 ps, which we call near-field optical nutation, and the period is estimated experimentally [12] and theoretically [13]. If the pumping time is much shorter than the period of the near-field optical nutation, we can create locally excited states in this system.

The locally excited states with an exciton in the system, which are referred to as one-exciton states, can be written by appropriate bases to describe excitation dynamics in a coupled quantum-dot system as

$$|e\rangle_{\mathrm{QD-A}}|g\rangle_{\mathrm{QD-B}} = (|e\rangle_{\mathrm{S}} + |e\rangle_{\mathrm{A}})/\sqrt{2}, \tag{1a}$$

$$|g\rangle_{\mathrm{QD-A}}|e\rangle_{\mathrm{QD-B}} = (|e\rangle_{\mathrm{S}} - |e\rangle_{\mathrm{A}})/\sqrt{2}, \tag{1b}$$

where e and g represent the exciton and crystal ground states, respectively, and the subscripts on the left hand sides are the indices of two quantum dots (QD-A and B). The subscripts S and A on the right hand sides denote symmetric and anti-symmetric states, respectively, which are the appropriate bases in a coupled quantum-dot system.

2.2 Dependence on the Excitation Number

In addition to the symmetric and anti-symmetric states in Eq. (1), we can prepare a two-exciton state, in which two excitons exist in the system, such as

$$|e\rangle_{\mathrm{QD-A}}|e\rangle_{\mathrm{QD-B}} = |2e\rangle_{\mathrm{P}}, \tag{2}$$

where the pre-factor 2 on the right hand side means the two-exciton state. Strictly speaking, an exciton in a quantum dot is neither fermion nor boson because of presence of many-body interactions among electrons and holes in a single quantum dot [14]. Here we assume a fermionic exciton in the following discussion, since the many-body effect cannot be neglected as the size of a quantum dot decreases. Thus two excitons are assumed not to occupy the same energy level in a quantum dot, which is equivalent to the Pauli principle. We have found that calculations based on this assumption is good agreement with experimental results [16].

In order to evaluate energies of these states given in Eqs. (1) and (2), we first consider the Hamiltonian for the two identical quantum-dot system, which is expressed as

$$\hat{H} = \hat{H}_0 + \hat{H}_{\mathrm{int}}, \tag{3a}$$

$$\hat{H}_0 = \hbar\Omega\hat{A}^\dagger\hat{A} + \hbar\Omega\hat{B}^\dagger\hat{B}, \tag{3b}$$

$$\hat{H}_{\mathrm{int}} = \hbar U_{\mathrm{AB}}(\hat{A}^\dagger\hat{B} + \hat{B}^\dagger\hat{A}), \tag{3c}$$

where $\hat{H}_0$ and $\hat{H}_{\mathrm{int}}$ represent the unperturbed Hamiltonian and the interaction Hamiltonian. Creation and annihilation operators for an exciton in QD-A and B are represented as $(\hat{A}^\dagger, \hat{A})$ and $(\hat{B}^\dagger, \hat{B})$, respectively, and the eigenenergies of both QD-A and B are $\hbar\Omega$. The coupling strength via the optical near field is denoted as U_{AB}. Readers who are interested in the details refer to Refs. [13] and [15], where exciton-polaritons mediate the coupling between two quantum dots, and the couplings to dipole-allowed state and dipole-forbidden state for the far-field light with the help of steep gradient optical near field are theoretically investigated. Similar discussions have been presented in Refs. [17] and [18].

The energies of the three states are given from Eq. (3a) as follows:

$${}_{\mathrm{S}}\langle e|\hat{H}|e\rangle_{\mathrm{S}} = \hbar(\Omega + U_{\mathrm{AB}}), \tag{4a}$$

$${}_{\mathrm{A}}\langle e|\hat{H}|e\rangle_{\mathrm{A}} = \hbar(\Omega - U_{\mathrm{AB}}), \tag{4b}$$

$${}_{\mathrm{P}}\langle 2e|\hat{H}|2e\rangle_{\mathrm{P}} = 2\hbar\Omega. \tag{4c}$$

From Eqs. (4a) and (4b), the energies of the coupled states depend on the coupling strength via the optical near field, and the energy shift oppositely appears for both states. The energy states given by Eqs. (4a) and (4b) are illustrated in Fig. 2. Note that the energy levels in the coupled system are split for the one-exciton state, while they are degenerate for the two-exciton state. This is a quite important feature to sweep any information into an output system with the help of resonant energy transfer between input and output systems, which will be described in the next subsection.

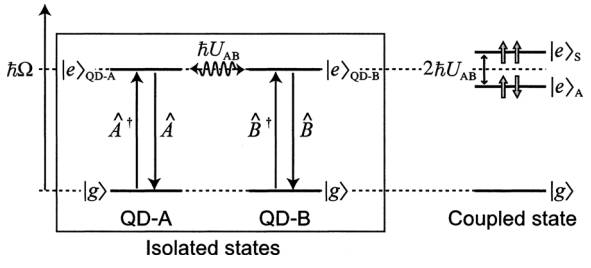

Fig. 2 Energy levels of isolated quantum dots (left) and those of a coupled system via an optical near field (right).

2.3 Spatial Symmetry

In order to detect such three excited states selectively, we prepare the third quantum dot (QD-C) with energy sublevels, in which the energy-sublevel spacing is generally less than 10 meV in a sub-10 nm CuCl quantum dot [19], and thus, non-radiative relaxation occurs mediating the coupling between exciton and lattice vibration. This enables irreversible energy transfer from input to output systems.

Let us consider transition matrix elements in such a system, where no exciton exists in QD-C in the initial state, and an exciton exists in the final state. The transition matrix elements in this situation read

$$_{\text{QD-C}}\langle e|\langle g|\hat{H}'_{\text{int}}|e\rangle_{\text{S}}|g\rangle_{\text{QD-C}} = \sqrt{2}\hbar\frac{U_{\text{CA}}+U_{\text{BC}}}{2}, \tag{5a}$$

$$_{\text{QD-C}}\langle e|\langle g|\hat{H}'_{\text{int}}|e\rangle_{\text{A}}|g\rangle_{\text{QD-C}} = \sqrt{2}\hbar\frac{U_{\text{CA}}-U_{\text{BC}}}{2}, \tag{5b}$$

where $|g\rangle = |g\rangle_{\text{S}} = |g\rangle_{\text{A}}$, and the interaction Hamiltonian $\hat{H}'_{\text{int}}$ in the three-quantum-dot system is given by adding the term $\hbar U_{\text{CA}}(\hat{A}^{\dagger}\hat{C}+\hat{C}^{\dagger}\hat{A})+\hbar U_{\text{BC}}(\hat{B}^{\dagger}\hat{C}+\hat{C}^{\dagger}\hat{B})$ to that of two-quantum-dot system described in Eq. (3c), with U_{CA} and U_{BC} being the coupling strengths via the optical near field between QD-A and C, and QD-B and C, respectively.

The transition matrix elements for the two-exciton states, in which the initial state is $|2e\rangle_{\text{P}}|g\rangle_{\text{QD-C}}$ and the final states are $|e\rangle_{\text{S}}|e\rangle_{\text{QD-C}}$ and $|e\rangle_{\text{A}}|e\rangle_{\text{QD-C}}$, are completely the same, but the output state is expressed by the symmetric and anti-symmetric states.

It follows from Eq. (5b) that the energy transfer from the input part (QD-A and B) to the output part (QD-C) is strongly related to spatial configuration of three quantum dots. The spatial configuration becomes important in nanophotonics, because two identical quantum dots on a nanometer space can be spatially resolved only by the optical near field, not by the far-field light. Therefore, consideration of spatial arrangement of each quantum dot is a unique point for investigation of nanophotonic device operations.

Schematic illustration of the energy transfer process is given in Fig. 3, where the left part corresponds to the initial input state (see Eq. (4)) and the right is the final output state. We can readily understand an interesting character of selective energy transfer for the one and two-exciton states, that is, the resonant conditions are reversed between the symmetric and anti-symmetric states. Appropriately arranging the spatial symmetry of QD-C against a pair of QD-A and B as well as the energy level in QD-C by adjusting the size, this selectivity can be controlled. For example, the right part in Fig. 3 corresponds to the output state with the positive detuning in QD-C. In this situation, the energy transfer from the states $|e\rangle_{\text{S}}|g\rangle_{\text{QD-C}}$ to $|g\rangle|e\rangle_{\text{QD-C}}$ becomes dominant for the one-exciton state. On the other hand, in the case of two-exciton state, dominant energy transfer inversely occurs between the states $|2e\rangle_{\text{P}}|g\rangle_{\text{QD-C}}$ and $|e\rangle_{\text{A}}|e\rangle_{\text{QD-C}}$. If we consider a symmetrically arranged system, i.e., $U_{\text{CA}} = U_{\text{BC}}$, these states do not couple with each other because the transition matrix element is equal to zero. (See Eq. (5b)) Therefore, the output signal cannot be obtained. Such fundamental property is useful for logic operations as shown in the next section.

3. Logic Gates

In this section, we discuss two typical logic gates as examples of nanophotonic devices that we easily recognize the principles of operation. The system for the two logic gates similarly consists of two identical quantum dots and a larger quantum dot with energy sublevels, where the larger quantum dot is symmetrically located against a pair of the other two as illustrated in Fig. 4. Functionality of the spatial symmetry is to hinder the energy transfer via the anti-symmetric states, as shown in Eq. (5b). We also utilize the difference of resonance conditions for one and two-exciton states between the input part (QD-A and B) and the output part (QD-C) with energy detuning. In the following, nanophotonic logic operations are discussed on the basis of the exciton population dynamics, which is solved analytically in the symmetrically arranged quantum-dot system [13].

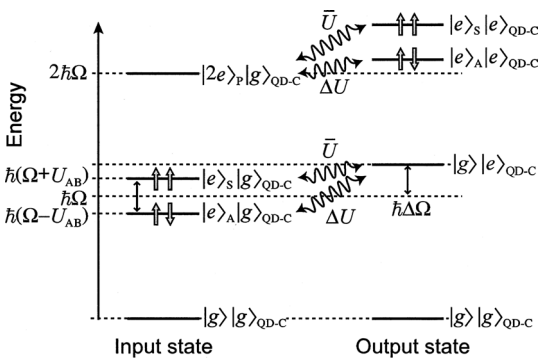

Fig. 3 Energy diagram in a coupled three-quantum-dot system. The left part corresponds to the initial input state with one or two excitons in QD-A and B, and the right is the final output state with existence of an exciton in QD-C.

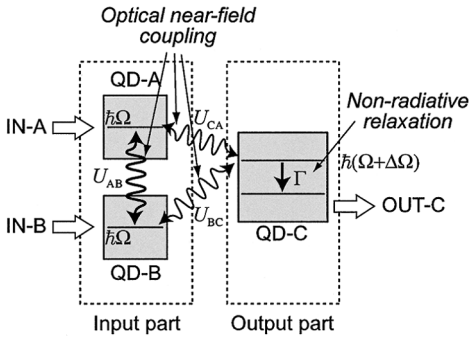

Fig. 4 Schematic illustration of symmetrically arranged quantum-dot system. The input and output parts consist of two identical quantum dots (QD-A and B) and a larger quantum dot (QD-C) with energy sublevels, respectively. With the energy detuning of the upper energy level in QD-C, logic operations are changed selectively.

3.1 AND Logic Gate

When the upper energy level in QD-C is negatively shifted, which corresponds to $\hbar(\Omega - U_{\mathrm{AB}})$, we can realize an AND-logic gate. Figure 5(a) represents energy diagram in the system with the negative detuning in QD-C. It follows from Fig. 5(a) that the resonant energy transfer occurs only for the two-exciton state via the output symmetric state, while the energy transfer for the one-exciton state is forbidden because the energy level in QD-C is resonant to the input anti-symmetric state that is dipole inactive with respect to QD-C arranged symmetrically. This characteristic selective energy transfer assures an AND-logic operation.

The temporal evolution of the exciton population on the lower energy level in QD-C is plotted in Fig. 5(b). This result is obtained from the density matrix formalism for the appropriate bases described in Eqs. (1) and (2), with the Hamiltonian in Eq. (3) used. Non-radiative relaxation due to the exciton-lattice vibration coupling is included under the Born-Markov approximation [20] for phonon reservoir. In the theoretical derivation, the coupling to far-field light is neglected because our interests are fast population dynamics due to the optical near-field coupling, which is of the order of 100 ps. Detailed derivation and discussion can be found in Ref. [13]. In Fig. 5(b), the exciton population is almost occupied in about 100 ps for the two-exciton state, which is determined by the coupling strength $U_{\mathrm{CA}}(U_{\mathrm{BC}})$ between QD-A and C (QD-B and C). The coupling strength or energy detuning is set as 89 μeV, which is faster than the coupling from the input to output system (14 μeV). Non-radiative relaxation time is also set as 10 ps, which is obtained from experimental estimation [21].

From Fig. 5(b), the output population can be observed only for the two-exciton state as expected, because the coupling occurs via the output symmetric state. On the other hand, OFF-level for the one-exciton state increases very slowly. This is caused by the weak coupling between the input symmetric state and the output state. The state-filling time is much longer than the exciton recombination time, which is omitted from the calculation, and thus, the exciton population for the one-exciton state does not affect the output signal. In this manner, these operations for the one and two-exciton states surely correspond to the AND-logic gate, where the size of the system considered is much smaller than the diffraction limit of light.

3.2 XOR Logic Gate

Contrary to the AND-logic gate, suppose a system in which the upper energy level in QD-C is positively shifted. Energy diagram in the system is illustrated in Fig. 6(a). Here the symmetric state in the input part is resonant with the one-

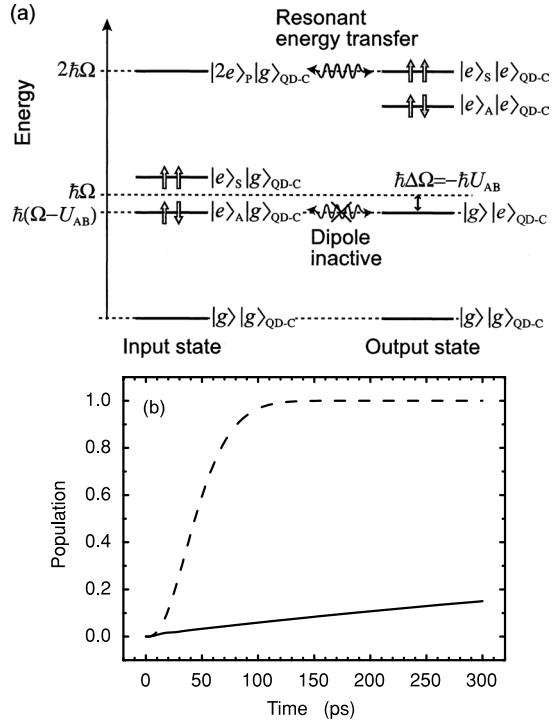

Fig. 5 (a) Energy diagram in a coupled three quantum-dot system with the negative energy detuning in QD-C, and (b) temporal evolution of exciton population on the lower energy level (output level) in QD-C. The solid and dashed curves represent the cases for the one and two-exciton states, respectively. The coupling strength between QD-A and B is set as $\hbar U_{\mathrm{AB}} = 89\,\mu$eV, and that between QD-B and C (QD-A and C) is $\hbar U_{\mathrm{BC(CA)}} = 14\,\mu$eV.

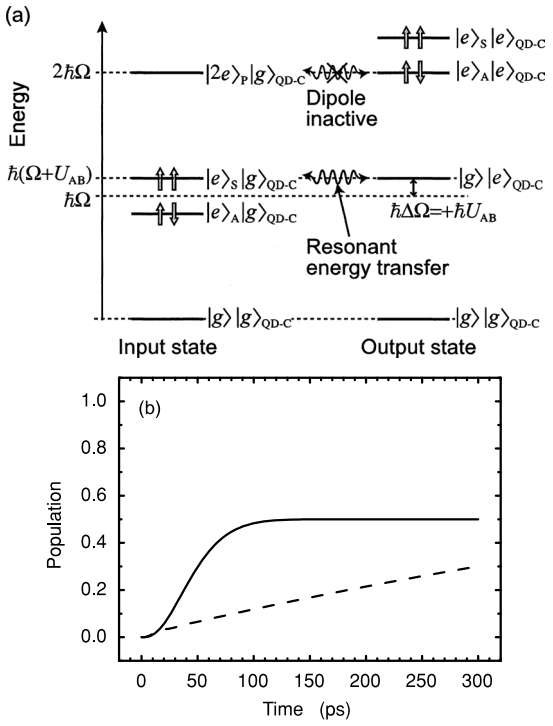

Fig. 6 (a) Energy diagram in a coupled three quantum-dot system with the positive energy detuning in QD-C, and (b) temporal evolution of exciton population on the lower energy level (output level) in QD-C. The solid and dashed curves represent the cases for the one and two-exciton states, respectively. The coupling strength between QD-A and B is set as $\hbar U_{\mathrm{AB}} = 89\,\mu$eV, and that between QD-B and C (QD-A and C) is $\bar{U}_{\mathrm{BC(CA)}} = 14\,\mu$eV.

exciton state in the output part, while the anti-symmetric state is resonant with the two-exciton state. The excitation energy is resonantly transferred from the input to output parts only if a single exciton exists in the system, while it is forbidden for the two-exciton state because the anti-symmetric state is resonant but inactive in the symmetrically arranged quantum-dot system.

Figure 6(b) shows theoretical curves of the temporal evolution for the one and two-exciton states. The given parameters, such as the coupling strength via the optical near field, non-radiative relaxation time, are completely the same as those in Fig. 5(b). From Fig. 6(b), the output population appears for the one-exciton state, while a slow increase in the population is observed for the two-exciton state. The state-filling time for the one-exciton state is related to the coupling strength between QD-A and C or QD-B and C, which is the same as the AND-logic gate mentioned above. Here the following question might be raised; why does the exciton population reach a half of the maximum for the one-exciton state? This is because a one-side quantum dot in the input part is locally excited as an initial condition, which means that both the symmetric and anti-symmetric states are simultaneously excited with the same occupation probability as described in Eq. (1). On the other hand, slow growth of exciton population for the two-exciton state (dashed curve in Fig. 6(b)), which is the OFF-operation, is faster than that for the AND-logic gate given by the solid curve in Fig. 5(b). This also originates from the same reason; in Fig. 5(b), the symmetric state in the input part with an exciton is occupied half of the maximum at the initial time, while full of the initial exciton population for the two-exciton state can couple to QD-C in the positively detuned case, and thus, the state-filling time becomes as twice fast as the AND-logic gate.

This behavior, i.e., the output population is detected when a one-side quantum dot in the input part is initially excited, corresponds to a XOR-logic gate as a stochastic meaning. It indicates that the output state cannot be fully occupied in a single exciton process, and thus, we require iterative observations.

4. Photon Storage

Since the anti-symmetric state has no total dipole, it cannot be excited by the far-field light, and cannot radiate the far-field light. Using this dipole-inactive nature, we can realize an interesting operation, in which exciton-polariton or incident photon energy is retained in the system for a long time. We refer to this type of device as photon storage or photon buffer memory.

The three-quantum-dot system is the simplest configuration to obtain a complete anti-symmetric state for a photon storage, which is illustrated in Fig. 7(a). According to Fig. 3, the energy transfer from the two-exciton states $|2e\rangle_{\rm P}|g\rangle_{\rm QD-C}$ to $|e\rangle_{\rm A}|e\rangle_{\rm QD-C}$ is active when QD-C is located asymmetrically and the upper energy level in QD-C is positively shifted by $\Delta\Omega = +U_{\rm AB}$, which is the resonance condition between the input and output parts in the asymmetrically arranged quantum-dot system. In this system, the anti-symmetric state for the one-exciton state is not directly excited, because both of the symmetric and anti-symmetric states are simultaneously excited. However, if the two-exciton state is initially excited in the input part, one-exciton energy is transferred to the lower energy level in QD-C via resonant upper energy level, and then, the state reaches the two-exciton anti-symmetric state. In this state, the total dipole moment in the input part is zero, and thus, no coupling to the far-field light occurs even if the exciton in the lower energy level in QD-C is released via far-field emission, which corresponds to the off-resonant condition of the anti-symmetric state for the one-exciton state. Therefore, the input photon energy is stored as an exciton in this system.

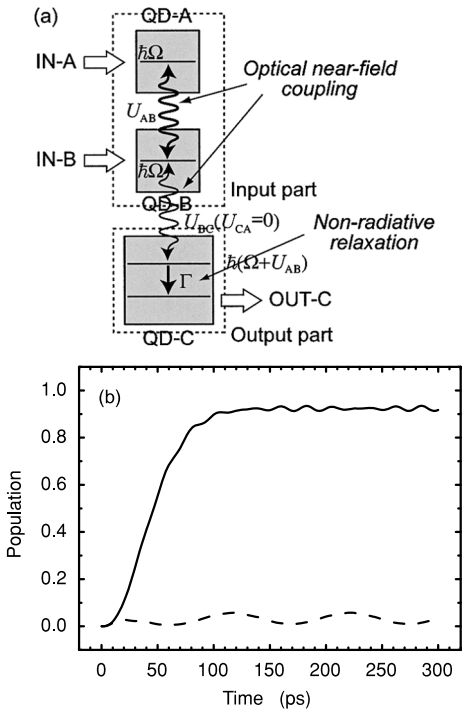

Fig. 7 (a) Schematic illustration of asymmetrically arranged quantum quantum-dot system. Two identical quantum dots, QD-A and B, makes dipole-inactive state for the far-field light, which corresponds to the anti-symmetric state. (b) Temporal evolution of exciton population for the two-exciton state. The solid and dashed curves represent for the anti-symmetric and symmetric states, respectively. The coupling strength between QD-A and B is set as $\hbar U_{\rm AB} = 89\,\mu$eV, and that between QD-B and C (QD-A and C) is $\hbar U_{\rm BC(CA)} = 14\,\mu$eV.

Figure 7(b) represents a numerical result of the time evolution obtained in a similar manner as the previous section. The solid curve in Fig. 7(b) corresponds to the exciton population for the one and two-exciton anti-symmetric states, which holds zero total dipole moment for the far-field light. On the other hand, the exciton population for the symmetric states is plotted by the dashed curve in Fig. 7(b), which keeps almost zero value since the initial time. Actually, we cannot keep the dipole-inactive state for infinite time because a direct coupling between the anti-symmetric

and symmetric states, and the energy transfer from the symmetric state to the state with an exciton on the lower energy level in QD-C induces a weak radiative decay that we neglected in the calculation. Oscillating behavior is observed for the both curves in Fig. 7(b), which is caused by the coupling of the anti-symmetric and symmetric states.

The above discussion is devoted to a writing process in the photon storage, or how to prepare the anti-symmetric state in the coupled quantum-dot system. However, in a general system, we need to consider a mechanism for reading information in addition to the writing process, which will be discussed elsewhere.

5. Application to Quantum Information Processing

In the above discussions, we have focused on realization of conventional functional devices on a nanometer scale. Note that our proposed functional devices consist of two parts; quantum mechanical part and classical part as illustrated in Fig. 1. The quantum mechanical part maintains matter coherence for the period that the exciton population moves to the classical part via energy dissipation. In other words, the output quantum dot acts as a selector to identify a certain quantum state by using resonant energy transfer and spatial symmetry of the quantum-dot system. Therefore, such a system is helpful for detecting information about quantum entanglement. In this section, we propose a special signal splitting device against the quantum-entangled state, where the competition between quantum and classical processes is a novel inherent concept originating from nanophotonics.

Figure 8 shows schematic illustration of the device, in which two output terminal quantum dots, QD-C and D, exist. The QD-C is located symmetrically regarding two identical quantum dots, and the upper energy level is set with the positive detuning by U_{AB}. The QD-D is configured maximally asymmetrically with the negative energy detuning. From the resonance conditions, QD-C can extract the exciton population from the quantum mechanical part via the symmetric state, while QD-D resonantly selects the anti-symmetric state, where resonant energy transfer is allowed because symmetry breaking. (See Fig. 7(b)) In this system, an initially quantum-entangled state, $|\phi\rangle = c_1|e\rangle_{\mathrm{S}} + c_2|e\rangle_{\mathrm{A}}$, is distinguishable and information of weight coefficients c_1 and c_2 is converted to optical frequency or wavelength of the far-field light released after the lifetime of excitons, which is estimated as several ns.

Numerical results in the system are given in Fig. 8(b) in a similar way as mentioned in Sects. 3 and 4. The top in Fig. 8(b) is the time evolution in the case of $|c_1|^2 = 2/3$ and $|c_2|^2 = 1/3$ as an initial condition, and the bottom is that of $|c_1|^2 = 1/3$ and $|c_2|^2 = 2/3$. Such initially quantum-entangled states can be established by using asymmetrically located optical near-field source against a pair of identical quantum dots (QD-A and B), or by connecting to some quantum computing devices. Both in Fig. 8(b) show that, the exciton population on the energy levels in QD-C and D well reflects the initial weight coefficients, where the horizontal

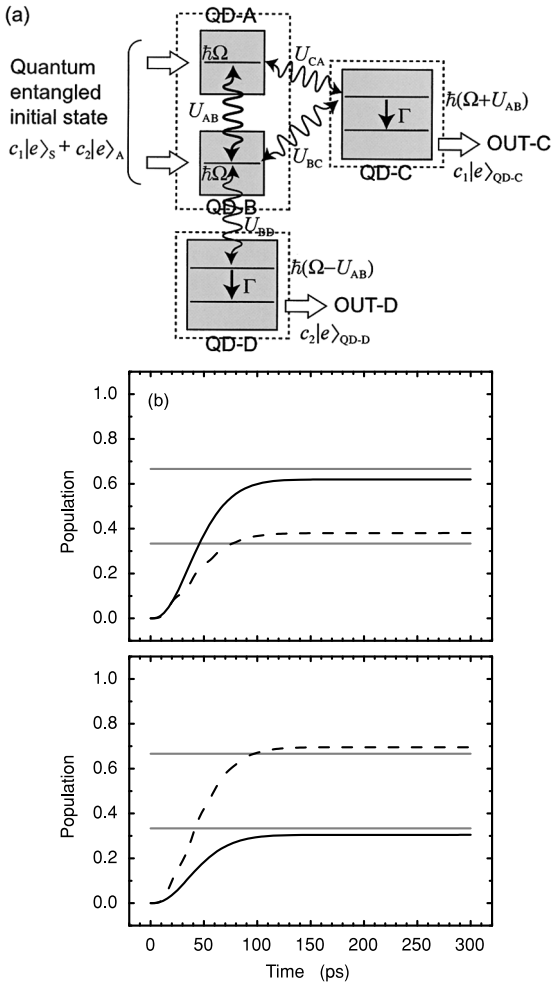

Fig. 8 (a) Schematic illustration of a signal splitting device reflected quantum entangled states, which consists of a symmetrically arranged system with the positive detuning and a maximally asymmetrically arranged system with the negative detuning. Two identical quantum dots, QD-A and B, hold quantum mechanical motion, whose system is called as the quantum mechanical part, and QD-C and D correspond to the classical part. (b) Temporal evolution of exciton population on the lower energy level in QD-C (solid curve) and that in QD-D (dashed curve). The top and bottom figures represent the cases of the weight coefficients $|c_1|^2 = 2/3$, $|c_2|^2 = 1/3$, and $|c_1|^2 = 1/3$, $|c_2|^2 = 2/3$, respectively. The coupling strength between QD-A and B is set as $\hbar U_{\mathrm{AB}} = 89\,\mu$eV, and that between QD-B and C (QD-A and C, QD-A and D, QD-B and D) is $\hbar U_{\mathrm{BC(CA)}} = 14\,\mu$eV.

gray lines in Fig. 8(b) indicate the expected values. Note that the deviation from the expected values becomes large, as the weight coefficient of symmetric state c_1 increases. This is caused by the off-resonant energy transfer from the quantum mechanical part to the classical part slightly, which occurs in the asymmetrically arranged quantum-dot system. When QD-C is located symmetrically, the off-resonant energy transfer from anti-symmetric state to the output QD-C is completely forbidden. Therefore, a part of the exciton population, which should flow into symmetrically arranged system, moves into asymmetrically arranged QD-D. This results in the difference depending on these weight coefficients.

To use quantum and classical processes is one of characteristic device operations inherent in nanophotonic devices, and we expect further investigation on useful applications, from the system architectural viewpoint.

6. Conclusions

In this paper, we have discussed three typical nanophotonic devices that consist of several quantum dots coupled via the optical near field. All of these are based on the locally excited states, dependence of the excitation number, and spatial symmetry of a system, which cannot be utilized in the conventional optics using the propagating far-field light. In a symmetrically arranged quantum-dot system, we showed AND and XOR-logic operations by using selective energy transfer due to resonance and forbidden conditions for the symmetric and anti-symmetric states in two identical quantum dots. The anti-symmetric state has an important role, which is not coupled with the far-field light. This is quite useful to store photon energy in a system. We have proposed a way to excite the anti-symmetric state by using three quantum dots asymmetrically arranged, so-called photon buffer memory. The third is an application to quantum information processing devices. The competition of symmetrically and asymmetrically arranged quantum-dot systems enables us to divide the input signal into two quantum dots with different energy levels reflecting information about quantum entanglement between the symmetric and anti-symmetric states. This includes a very interesting character that nanophotonic devices operate temporally quantum mechanical and finally classical. We expect that such device operations with both quantum and classical aspects open up novel device architectures that have not considered in the present days. Nanophotonics becomes one of promising technologies in the future, which is not only to realize miniaturization of optical devices but also to develop novel functionalities with qualitative innovations.

References

[1] M. Ohtsu, K. Kobayashi, T. Kawazoe, S. Sangu, and T. Yatsui, "Nanophotonics: Design, fabrication, and operation of nanometric devices using optical near fields," IEEE J. Sel. Top. Quantum. Electron., vol.8, no.4, pp.839–862, July/Aug. 2002.

[2] M. Ohtsu, ed., Progress in Nano-Electro-Optics I–III, Springer-Verlag, Berlin, 2003/2004.

[3] M. Ohtsu, ed., Near-Field Nano/Atom Optics and Technology, Springer-Verlag, Tokyo, 1998; M. Ohtsu and H. Hori, Near-Field Nano-Optics: From Basic Principles to Nano-Fabrication and Nano-Photonics, Kluwer Academic/Plenum Publishers, New York, 1999; M. Ohtsu and K. Kobayashi, Optical Near Fields: Introduction to Classical and Quantum Theories of Electromagnetic Phenomena at the Nanoscale, Springer-Verlag, Berlin, 2003.

[4] International technology roadmap for semiconductors, 2004, <http://public.itrs.net>.

[5] C.S. Lent, P.D. Tougaw, W. Porod, and G.H. Bernstein, "Quantum cellular automata," Nanotechnology, vol.4, no.1, pp.49–57, Jan. 1993; P.D. Tougaw and C.S. Lent, "Logical devices implemented using quantum cellular automata," J. Appl. Phys., vol.75, no.3, pp.1818–1825, Feb. 1994.

[6] T. Kawazoe, K. Kobayashi, J. Lim, Y. Narita, and M. Ohtsu, "Direct observation of optically forbidden energy transfer between CuCl quantum cubes via near-field optical spectroscopy," Phys. Rev. Lett., vol.88, no.6, pp.067404-1–4, Jan. 2002.

[7] T. Yatsui, M. Kourogi, and M. Ohtsu, "Plasmon waveguide for optical far/near-field conversion," Appl. Phys. Lett., vol.79, no.27, pp.4583–4585, 2001.

[8] M.L. Brongersma, J.W. Hartman, and H.A. Atwater, "Electromagnetic energy transfer and switching in nanoparticle chain arrays below the diffraction limit," Phys. Rev. B, vol.62, no.24, pp.R16356–R16359, Dec. 2000.

[9] T. Kawazoe, K. Kobayashi, S. Sangu, and M. Ohtsu, "Demonstration of a nanophotonic switching operation by optical near-field energy transfer," Appl. Phys. Lett., vol.82, no.18, pp.2957–2959, May 2003.

[10] M. Naruse, T. Miyazaki, F. Kubota, T. Kawazoe, K. Kobayashi, S. Sangu, and M. Ohtsu, "Nanometric summation architecture using optical near-field interaction between quantum dots," Opt. Lett., vol.30, no.2, pp.201–203, Jan. 2005.

[11] H. Hori, "Electronic and electromagnetic properties in nanometer scales," in Optical and Electronic Process of Nano-Matters, ed. M. Ohtsu, pp.1–55, KTK Scientific, Tokyo/Kluwer Academic, Dordrecht, 2001.

[12] T. Kawazoe, K. Kobayashi, S. Sangu, and M. Ohtsu, "Demonstrating nanophotonic switching using near-field pump-probe photoluminescence spectroscopy of CuCl quantum cubes," J. Microscopy, vol.209, pt.3, pp.261–266, March 2003.

[13] S. Sangu, K. Kobayashi, A. Shojiguchi, and M. Ohtsu, "Logic and functional operations using a near-field optically coupled quantum-dot system," Phys. Rev. B, vol.69, no.11, pp.115334–1–13, March 2004.

[14] H. Haken, Quantum Field Theory of Solids: An Introduction, Elsevier, Amsterdam, 1983.

[15] K. Kobayashi, S. Sangu, H. Itoh, and M. Ohtsu, "Near-field optical potential for a neutral atom," Phys. Rev. A., vol.63, no.1, pp.013806-1–9, Jan. 2001; K. Kobayashi and M. Ohtsu, "Quantum theoretical approach to a near-field optical system," J. Microscopy, vol.194, pt.2/3, pp.249–254, May/June 1999.

[16] S. Sangu, K. Kobayashi, A. Shojiguchi, and M. Ohtsu, "Quantum-coherence effect in a quantum dot system coupled by optical near fields," Trans. Mat. Res. Soc. Jpn., vol.28, no.4, pp.1035–1038, Dec. 2002.

[17] K. Cho, Y. Ohfuti, and K. Arima, "Theory of resonant SNOM (scanning near-field optical microscopy): Breakdown of the electric dipole selection rule in the reflection mode," Surf. Sci., vol.363, no.1-3, pp.378–384, Aug. 1996.

[18] G.W. Bryant, "Probing quantum nanostructures with near-field optical microscopy and vice versa," Appl. Phys. Lett., vol.72, no.7, pp.768–770, Feb. 1998.

[19] N. Sakakura and Y. Masumoto, "Persistent spectral-hole-burning spectroscopy of CuCl quantum cubes," Phys. Rev. B, vol.56, no.7, pp.4051–4055, Aug. 1997.

[20] H.J. Carmichael, Statistical Methods in Quantum Optics 1, Springer-Verlag, Berlin, 1999.

[21] Y. Masumoto, M. Ikezawa, B.-R. Hyun, K. Takemoto, and M. Furuya, "Homogeneous width of confined excitons in quantum dots at very low temperatures," Phys. Status Solidi, vol.224, no.3, pp.613–619, March 2001.

Suguru Sangu was born in Hokkaido in 1971. He received the B.E. degree from Muroran Institute of Technology in 1994, and the M.E. and Ph.D. degrees in electronics and information engineering from Hokkaido University in 1996 and 1999, respectively. From 1999 to 2003, he joined the ERATO "Localized Photon" project at the Japan Science and Technology Agency. Since 2003, he has been a Researcher of the Research and Development Center, Ricoh Company, Ltd. His current research interests are the theory on near-field optics and its application to nanophotonics.

Kiyoshi Kobayashi was born in Okayama in 1953. He received the Dr.Sc. degree in physics from University of Tsukuba in 1982. After graduation, he joined IBM Japan as a Research Staff at Tokyo Research Laboratory. In 1998, he became the theoretical group leader of the ERATO "Localized Photon" project at Japan Science and Technology Agency. Since 2004, he has been a professor with the COE21, Nanometer-scale Quantum Physics, Department of Physics, Tokyo Institute of Technology. His main fields of interest are quantum optical near-field theory and its application to nano/atom photonics.

Motoichi Ohtsu received the B.E., M.E., and Dr.E. degrees in electronics engineering from the Tokyo Institute of Technology, Tokyo, Japan, in 1973, 1975, and 1978, respectively. In 1978, he was appointed a Research Associate, and in 1982, he became an Associate Professor at the Tokyo Institute of Technology. From 1986 to 1987, while on leave from the Tokyo Institute of Technology, he joined the Crawford Hill Laboratory, AT&T Bell Laboratories. In 1991, he became a Professor at the Tokyo Institute of Technology. In 2004, he moved to the University of Tokyo. Since 1993, he has been concurrently the Leader of the "Photon Control" project of the Kanagawa Academy of Science and Technology. Since 1998, he has been concurrently the Leader of the "Localized Photon" project of ERATO. Since 2002, he is a leader of the national project on "Ultrahigh density optical storage" sponsored by METI. He has authored more than 320 papers and holds 87 patents. He is the author and coauthor of 39 books. In 2000, he was the President of the IEEE/LEOS Japan Chapter. From 2000, he is an executive director of the Japan Society of Applied Physics. In 2001, he served as a Technical Program Co-chair for the 4th CLEO/PR01, 2001. He has been a tutorial lecturer of the SPIE and the OSA. He is a member of several boards of the MEXT, METI and so on. Prof. Ohtsu is a Fellow of the OSA, a senior member of IEEE, and member of several academic societies. He has been awarded ten prizes from academic institutions, including the I. Koga Gold Medal of International URSI in 1984, the Japan IBM Science Award in 1988, two awards from JSAP in 1982 and 1990, the Inoue Science Foundation Award in 1999. In 2004, he was awarded a Purple Ribbon Medal from Japanese government.

PAPER Special Section on Nanophotonics and Related Techniques

Nanophotonic Computing Based on Optical Near-Field Interactions between Quantum Dots

Makoto NARUSE[†a)], **Tetsuya MIYAZAKI**[†], *Members*, **Tadashi KAWAZOE**[††], **Suguru SANGU**[†††], *Nonmembers*, **Kiyoshi KOBAYASHI**[††††], *Member*, **Fumito KUBOTA**[†], *Fellow*, *and* **Motoichi OHTSU**[†††††], *Member*

SUMMARY We approach nanophotonic computing on the basis of optical near-field interactions between quantum dots. A table lookup, or matrix-vector multiplication, architecture is proposed. As fundamental functionality, a data summation mechanism and digital-to-analog conversion are experimentally demonstrated using CuCl quantum dots. Owing to the diffraction-limit-free nature of nanophotonics, these architectures can achieve ultrahigh density integration compared to conventional bulky optical systems, as well as low power dissipation.

key words: *nanophotonics, optical signal processing, optical near-field, information processing, nanophotonic computing*

1. Introduction

To accommodate the continuously growing amount of data traffic in communication systems [1], optics is expected to further enhance the overall system performance by performing certain functional behavior [2]. In this regard, so-called all-optical packet switching has been thoroughly investigated. Also, the application of optical features, such as parallelism, in computing systems has been investigated since the 1970s [3], [4]. However, many technological difficulties remain to be overcome; one problem is the poor integrability of the hardware due to the diffraction limit of light, which is much larger than the gate width in VLSI circuits. This results in relatively bulky hardware configurations.

Nanophotonics, on the other hand, is free from the diffraction limit since it is based on local electromagnetic interactions between a few nanometric particles, such as quantum dots (QDs), via optical near-fields [5]. From an architectural perspective, this drastically changes the fundamental design rules of optical functional systems.

In this paper, we propose a nanophotonic computing architecture composed of table-lookup operations, as schematically shown in Fig. 1. A large amount of lookup-table (routing table) data can be recorded by configuring the sizes and positions of QDs, and by implementing the required logical operation mechanisms for each entry, based on near-field interactions. Since the internal device functions are based on uni-directional energy transfer via near-field interactions, which is prohibited for far-field light, as discussed in Sect. 3, input query data to the nanophotonic lookup table may be supplied globally by far-field light by tuning its operating frequency so that it does not interfere with the internal device operations.

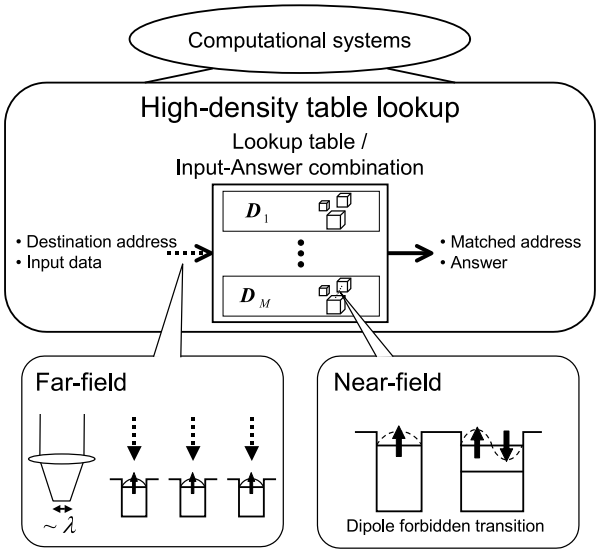

Fig. 1 An architecture for nanophotonic computing: High-density parallel table lookup based on nanophotonics. Internal device operation is based on near-field interactions between quantum dots, whereas input data can be either globally irradiated via far-field light or individually addressed through far- to near-field conversion.

This paper is organized as follows. In Sect. 2, we relate the table lookup operations and arbitrary digital computations to inner product operations with an appropriate data representation. Section 3 discusses their nanophotonic implementation. As an important sub-function, a data summation mechanism based on optical near-field interactions between QDs is shown. Also, its proof-of-principle experiment is demonstrated using CuCl QDs in a NaCl matrix. As an extension of the table lookup operation, or matrix-vector multiplication, Sect. 4 discusses digital-to-analog conversion by configuring the coupling strength between QDs. Its experimental verification is also shown. Finally, Sect. 5 concludes the paper.

Manuscript received December 1, 2004.
Manuscript revised April 30, 2005.

[†]The authors are with the National Institute of Information and Communications Technology, Koganei-shi, 184-8795 Japan.
[††]The author is with Japan Science and Technology Agency, Machida-shi, 194-0004 Japan.
[†††]The author is with Ricoh Co., Ltd., Yokohama-shi, 224-0035 Japan.
[††††]The author is with Tokyo Institute of Technology, Tokyo, 152-8551 Japan.
[†††††]The author is with the University of Tokyo, Tokyo, 113-8656 Japan.
a) E-mail: naruse@nict.go.jp
DOI: 10.1093/ietele/e88–c.9.1817

2. Nanophotonic Computing Architecture Based on High-Density Table Lookup

This section discusses the overall processing architecture. We begin with a concrete example of a packet forwarding application, which is an important function in routers; in this application, the output port for an incoming packet is determined based on a routing table. For such functions, a content addressable memory (CAM) [6] or its equivalent is used; in a CAM, an input signal (content) serves as a query to a lookup table and the output is the address of data matching the input. All optical means for implementing such functions have been proposed, for instance, by using planar lightwave circuits [7]. However, since we need separate optical hardware for each table entry if based on today's known methods, if the number of entries in a routing table is on the order of 10,000 or more, the overall physical size of the system becomes unfeasibly large. On the other hand, by using diffraction-limit-free nanophotonic principles, huge lookup table can be configured compactly.

First, we begin by relating the table lookup problem to an inner product operation. We assume an N-bit input signal $\boldsymbol{S} = (s_1, \cdots, s_N)$ and reference data $\boldsymbol{D} = (d_1, \cdots, d_N)$. Here the inner product $\boldsymbol{S} \bullet \boldsymbol{D} = \sum_{i=1}^{N} s_i \bullet d_i$ will provide a maximum value when the input perfectly matches the reference data. However, the inner product is, in fact, not enough to determine correct matching of the input and reference. This can be demonstrated as follows. Assume, for example, a 4-bit input $\boldsymbol{S}$ = (1010), and two items of reference data $\boldsymbol{D}_1$ = (1010) and $\boldsymbol{D}_2$ = (1110). Both inner products result in a value of 2, but the correctly matching data is only $\boldsymbol{D}_1$. That is to say, the exclusiveness of the matching operations should also be considered. Correct matching can be achieved by calculating also the inner product of the *inverted* input signal and reference data. Inversion is, however, a difficult function to implement optically. One possible option is to properly design the modulation format [8], for instance, by representing a logical level by two digits, such as Logic 1="10" and Logic 0="01." Then, an N-bit logical input is physically represented by $2N$ bits, which makes the inner product equivalent to the matching operation.

For packet data transfer, an operation known as longest prefix matching is important [9]. In this operation, a "don't care" state is required. In the above format, it can be simply coded by "11." Then, the resultant multiplication of a don't-care bit with an input bit will be 1 for either Logic 0 or 1.

Suppose that the reference data in the memory $\boldsymbol{D}_j$ ($j = 1, \cdots, M$) and the input $\boldsymbol{S}$ are represented in the above format. Then, the function of the CAM will be to derive j that maximizes $\boldsymbol{S} \bullet \boldsymbol{D}_j$. A nanophotonic implementation of such a function can be implemented in a highly dense form, as shown in Sect. 3. In addition, a large array of such inner product operations will allow a massively parallel processing system to be constructed.

Consequently, multiple inner products are equivalent to a matrix-vector multiplication, which is capable of implementing a wide range of parallel computations [4]. As a simple example, digital-to-analog conversion will be demonstrated by tuning the near-field interaction strength, as discussed in Sect. 4.

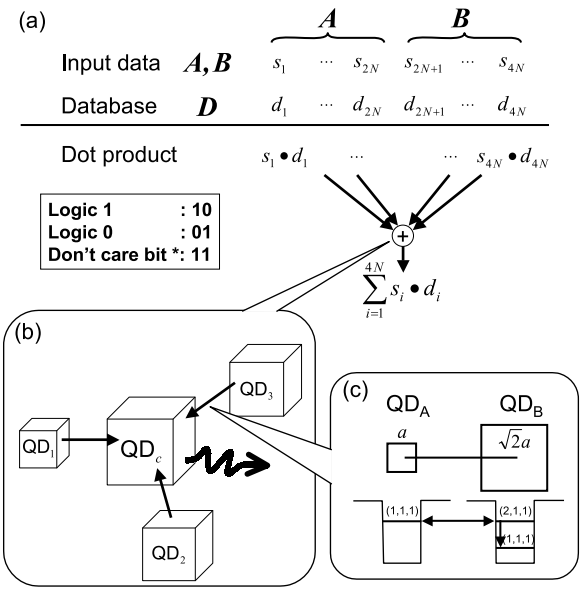

Fig. 2 (a) Inner product operation as a table lookup. (b) Summation mechanism in quantum dots. (c) Inter-dot interaction via an optical near-field.

Furthermore, arbitrary combinational logic can be reformulated as a table lookup operation; more specifically, any computation is equivalent to performing a lookup in a table where all possible input/answer combinations are prerecorded. For example, consider a two-input, two-bit ADD operation, $\boldsymbol{A} + \boldsymbol{B}$. In the ADD operation, the third-bit of the output (the carry bit) should be logical 1 when the second bits (that is, the 2^1 bit positions) of both inputs are 1, regardless of their first bits, that is, when ($\boldsymbol{A}$, $\boldsymbol{B}$) = (1*, 1*). Therefore, following the data representation format introduced above (Logic 1 = 10, Logic 0 = 01, and don't care = 11), the table lookup entry $\boldsymbol{D}$ should be (10111011) so that any input combination satisfying ($\boldsymbol{A}$, $\boldsymbol{B}$) = (1*, 1*) will provide a maximum inner product $\boldsymbol{S} \bullet \boldsymbol{D}$. This procedure is summarized in Fig. 2(a).

3. Data Summation Using Near-Field Interactions

As discussed in Sect. 2, the inner product operations are the key functionality of the present architecture. The multiplication of two bits, namely $x_i = s_i \bullet d_i$, has already been demonstrated by a combination of three quantum dots [10], [11]. Therefore, one of the key operations remaining is the summation, or data gathering scheme, denoted by Σx_i, where all data bits should be taken into account.

In known optical methods, wave propagation in free-space or in waveguides, using, for example, focusing lenses or fiber couplers, well matches such a data gathering scheme because the physical nature of propagating light is inherently suitable for global functionality such as global sum-

mation. However, the level of integration of these methods is restricted due to the diffraction limit of light. In nanophotonics, on the other hand, the near-field interaction is inherently physically local, although functionally global behavior is required.

Here we implement a global data gathering mechanism, or summation, based on the uni-directional energy flow via an optical near field, as schematically shown in Fig. 2(b), where surrounding excitations are transferred towards a quantum dot QD_C located at the center. As a fundamental case, we assume two quantum dots QD_A and QD_B, as shown in Fig. 2(c). The ratio of the sizes of QD_A and QD_B is $1 : \sqrt{2}$. There is a resonant quantized energy sublevel between those two dots, which are coupled by an optical near-field interaction [10]–[12]. Therefore, the exciton population in the (1,1,1)-level in QD_A is transferred to the (2,1,1)-level in QD_B [10], [12]. It should be noted that this interaction is forbidden for far-field light [13]. Since the intra-sublevel relaxation via exciton-phonon coupling is fast, the population is quickly transferred to the lower (1,1,1)-level in QD_B. Similar energy transfers may take place among the resonant energy levels in the dots surrounding QD_C so that energy flow can occur. One may worry that if the lower energy level of QD_B is occupied, another exciton cannot be transferred to that level due to the Pauli exclusion principle. Here, thanks again to the nature of the optical near-field interaction, the exciton population goes back and forth in the resonant energy level between QD_A and QD_B, which is called optical nutation [10]–[12]. Finally, both excitons can be transferred to QD_B. The lowest energy level in each quantum dot is coupled to a free photon bath to sweep out the excitation radiatively. The output signal is proportional to the (1,1,1)-level population in QD_B.

Numerical calculations were performed based on quantum master equations in the density matrix formalism. The model Hamiltonian of the coupled two-dot system is given by

$$H = \hbar \begin{pmatrix} \Omega_A & U \\ U & \Omega_B \end{pmatrix} \tag{1}$$

where $\hbar U$ is the optical near-field interaction, and $\hbar\Omega_A$ and $\hbar\Omega_B$ respectively refer to the eigenenergies of QD_A and QD_B. The equation of motion is given by the Liouville equation:

$$\dot{\rho}(t) = -\frac{i}{\hbar}[H, \rho(t)] \tag{2}$$

where ρ is the density operator. We used seven bases where either zero, one, or two excitons occupy the (1,1,1) level in QD_A, the (2,1,1) level in QD_B, and the (1,1,1) level in QD_B. Assuming inter-dot near-field coupling (U), exciton-phonon coupling (Γ), and relaxation to the radiation photon bath (γ_A for QD_A and γ_B for QD_B), within the Born-Markov approximation [14], we can derive multiple differential equations. In the following, we assume $U^{-1} = 50\,\text{ps}$, $\Gamma^{-1} = 10\,\text{ps}$, $\gamma_A^{-1} = 2\sqrt{2}\,\text{ns}$, and $\gamma_B^{-1} = 1\,\text{ns}$ as a typical parameter set.

First, we consider an initial condition where there are two excitons in the system: one in QD_A and the other in QD_B (two-exciton system). The population of the (1,1,1)-level in QD_B is related to the output signal, whose time evolution is shown by the solid curve in Fig. 3. Incidentally, the population when QD_A has an exciton is denoted by the dotted curve in Fig. 3. Nutation is observed as expected since the lower level of QD_B is likely to be occupied and the inter-dot near-field interaction is faster than the radiative relaxation at each dot.

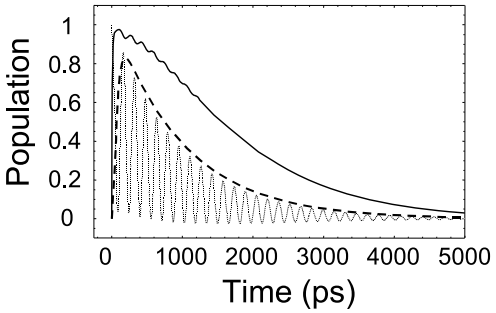

Fig. 3 Time evolution of the population of the lower level of QD_B in a two-exciton system (solid curve) and a one-exciton system (dashed curve). Dotted curve shows the population when QD_A has an exciton in a two-exciton system; Nutation is observed.

We then compare the population dynamics between one- and two-exciton systems. The dashed curve in Fig. 3 shows the time evolution of the population in the lower level of QD_B, where, as an initial condition, one exciton exists only in QD_A. Physically the output signal is considered to be the radiative relaxation from the lowest energy level of the output QD, which is related to integration of the population in the lower level of QD_B. By numerically integrating the population between 0 and 5 ns, we can obtain the ratio of the output signals between the two- and one-exciton systems, namely, 1.86:1, which reflects the number of initial excitons, or the summation mechanism.

A proof-of-principle experiment was performed to verify the nanoscale summation using CuCl quantum dots in a NaCl matrix, which has also been employed for demonstrating nanophotonic switches [10] and optical nano-fountains [15]. We selected a quantum dot arrangement where small QDs (QD_1 to QD_3) surrounded a "large" QD (QD_C), as schematically shown in Fig. 4(a). Here, we irradiate at most three light beams with different wavelength, 325 nm, 376 nm, and 381.3 nm, which respectively excite the quantum dots QD_1 to QD_3 having sizes of 1 nm, 3.1 nm, and 4.1 nm, respectively. The excited excitons are transferred to QD_C, and its radiation is observed by a near-field fiber probe. Notice the output signal intensity at a photon energy level of 3.225 eV in Fig. 4(b), which corresponds to a wavelength of 384 nm or a QD_C size of 5.9 nm. The intensity varies approximately as 1:2:3 depending on the number of excited QDs in the vicinity, as observed in Fig. 4(b). The spatial intensity distribution was measured by scanning the fiber probe, as shown in Fig. 4(c), where the energy is converged at the center. Hence, this architecture works as a

summation mechanism, counting the number of input channels, based on exciton energy transfer via optical near-field interactions.

Such a quantum-dot-based data gathering mechanism is also extremely energy efficient compared to other optical methods such as focusing lenses or optical couplers. For example, the transmittance between two materials with refractive indexes n_1 and n_2 is given by $4n_1n_2/(n_1 + n_2)^2$; this gives a 4% loss if n_1 and n_2 are 1 and 1.5, respectively. The transmittance of an N-channel guided wave coupler is $1/N$ from the input to the output if the coupling loss at each coupler is 3 dB. In nanophotonic summation, the loss is attributed to the dissipation between energy sublevels, which is significantly smaller. Incidentally, it is energy- and space-efficient compared to electrical CAM VLSI chips [16]–[18], as shown in Table 1.

We should also note, in terms of interconnections, that the input data should be commonly applied to all lookup table entries, which allows another possible interconnection mechanism. Since the internal functionality is based on energy transfer via optical near-field interactions and it is forbidden for far-field light, global input data irradiation, that is, broadcast interconnects, via far-field light may be possible; this is now being investigated [19].

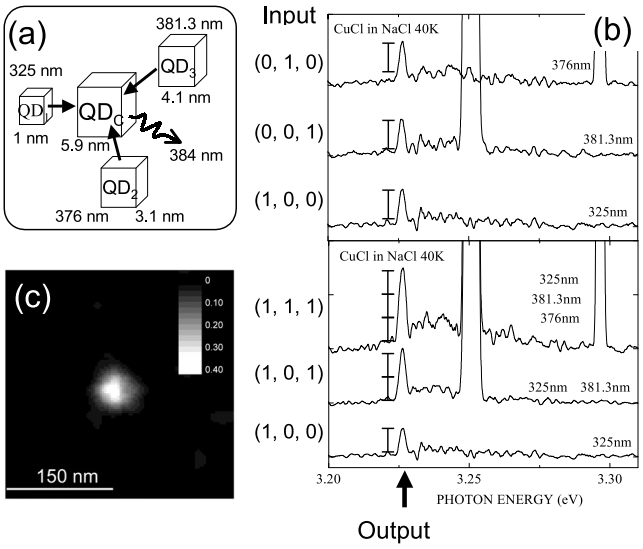

Fig. 4 Experimental results of the nanometric summation. (a) A quantum dot arrangement. (b) Luminescence intensity for three different numbers of excited QDs. (c) Spatial intensity distribution of the output photon energy.

Table 1 Power dissipation and cell size comparison with electrical CAM VLSI chips and optical waveguides.

	Power dissipation (fJ / bit / search)	Cell size (μm^2)
CAM chip[16]	3.4	-
CAM chip[17]	2.1	17.54
CAM chip[18]	1.3	17.46
Optical waveguide	-	~ 1,000
Nanophotonic	0.0002	0.01

4. Digital-to-Analog Conversion Using Near-Field Interactions

In the summation mechanism shown in Sect. 3, the coupling strengths between the input QDs and the output QD is uniform. However, these coupling strengths can be independently configured, for instance, by modifying the relative distances. Theoretically, this corresponds to configuring U of the Hamiltonian in Eq. (1). For instance, consider three input QDs, QD_0 to QD_2, as schematically shown in Fig. 5(a). By choosing U^{-1} of 410 ps, 240 ps, and 50 ps between QD_0 to QD_2 and the output QD, respectively, the simulated time evolution of the output population is summarized in Fig. 5(b). The time integral of the output populations originating from QD_0 to QD_2 between 0 and 5 ns is approximately in a ratio of 1:2:4. This leads to a digital-to-analog conversion formula given by

$$d = 2^0 s_0 + 2^1 s_1 + 2^2 s_2 \tag{3}$$

where d is the output, and s_0, s_1, and s_2 represent the presence/absence of excitations in QD_0 to QD_2 respectively. Here each of the inputs s_i is optically applied to the system whose frequency is resonant with the (1,1,1)-level in QD_i. It should be noted that they are not coupled to the other QDs (i.e., input QD_j ($j \neq i$) and the output QD) since the corresponding energy levels are optically forbidden for the other QDs. Also, the initial state of the system is considered to be one in which an exciton is excited at each dot.

In the experiment, CuCl QDs in a NaCl matrix were used, as in Sect. 3, and three different input light frequencies were assigned to the three-bit input. Here, the output signal is considered to be the radiative relaxation from the lowest energy level of the output QD, which is observed with a near-field fiber probe at a wavelength of 384 nm. One re-

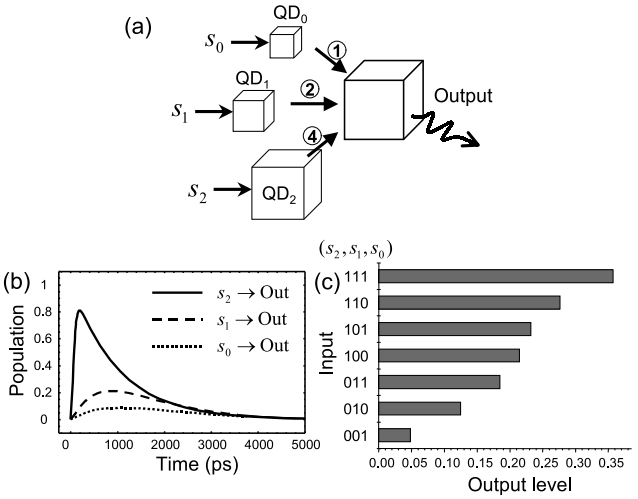

Fig. 5 (a) Digital-to-analog (DA) conversion. The near-field coupling is tuned so as to satisfy the relation for DA conversion. (b) Time evolution from each of the input bits to the output. (c) Experimental results of the output intensity level as a function of 3-bit input combinations.

mark here is that not every excited exciton produces the output signal; for instance there will be loss due to relaxation at each of the input QDs when the output energy level is occupied. However, such effects may not be serious since, as discussed in Sect. 3, nutation occurs among resonant energy levels and the relaxation rate at the output QD, which is the largest in the system in terms of size, is smaller than that at the input QDs. Figure 5(c) shows output signal intensity as a function of the presence (1) or absence (0) of the input excitation, as specified by (s_2, s_1, s_0), which were respectively 381.3 nm, 376 nm, and 325 nm. The output intensity is approximately linearly correlated to the input bit set combination, which indicates the validity of the digital-to-analog conversion mechanism. Compared to known optical approaches, such as those based on space-domain filtering and focusing lenses [3], [4], or optical waveguides and intensity filters [20], the nanophotonic approach achieves a significant higher spatial density.

5. Discussion

In summary, an architecture for nanophotonic computing is proposed; the architecture is based on table lookup using near-field interactions between quantum dots (QDs). As well as content addressable memories, digital logic and matrix-vector multiplication can be implemented in this architecture. As fundamental functional elements, a data summation mechanism and digital-to-analog conversion are presented, and their proof-of-principle experiments are demonstrated using CuCl QDs. Owing to its high spatial density and low power dissipation, a massive array of such functional components will be useful in applications such as massive table lookup operations in networking and information processing systems.

Generality of processing remains an open issue since it requires random access memories, and other design strategies, such as binary decision diagrams [21], are another possible candidates. Memory is also an extremely important subject for optical networks to replace the bulky optical fiber loops used for buffering [22]; the possibility of using nanophotonic devices in these applications is now being pursued [11]. The extremely high spatial density will also lead to novel system design concepts, for instance, in redundancy or fault tolerance [23]. In addition, further investigation of system application issues is indispensable, such as interconnections [24], [25], the fabrication limitations of nanostructures [26], and new applications unachievable by other technologies.

References

[1] 2004 WHITE PAPER, Information and Communications in Japan, Ministry of Internal Affairs and Communications (MIC), Japan.
[2] S. Yao, B. Mukherjee, and S. Dixit, "Advances in photonic packet switching: An overview," IEEE Commun. Mag., vol.38, no.2, pp.84–94, 2000.
[3] J.W. Goodman, A.R. Dias, and L.M. Woody, "Fully parallel, high-speed incoherent optical method for performing discrete Fourier transforms," Opt. Lett., vol.2, pp.1–3, 1978.
[4] P.S. Guilfoyle and D.S. McCallum, "High-speed low-energy digital optical processors," Opt. Eng., vol.35, pp.436–442, 1996.
[5] M. Ohtsu, K. Kobayashi, T. Kawazoe, S. Sangu, and T. Yatsui, "Nanophotonics: Design, fabrication, and operation of nanometric devices using optical near fields," IEEE J. Sel. Top. Quantum Electron., vol.8, no.4, pp.839–862, 2002.
[6] H. Liu, "Routing table compaction in ternary CAM," IEEE Microw., vol.22, no.1, pp.58–64, 2002.
[7] A. Grunnet-Jepsen, A.E. Johnson, E.S. Maniloff, T.W. Mossberg, M.J. Munroe, and J.N. Sweetser, "Fibre Bragg grating based spectral encoder/decoder for lightwave CDMA," Electron. Lett., vol.35, pp.1096–1097, June 1999.
[8] M. Naruse, H. Mitsu, M. Furuki, I. Izumi, Y. Sato, S. Tatsuura, M. Tian, and F. Kubota, "Terabit all-optical logic based on ultrafast two-dimensional transmission gating," Opt. Lett., vol.29, pp.608–610, 2004.
[9] K. Kitayama and M. Murata, "Versatile optical code-based MPLS for circuit, burst, and packet switchings," IEEE J. Lightwave Technol., vol.21, no.11, pp.2753–2764, 2003.
[10] T. Kawazoe, K. Kobayashi, S. Sangu, and M. Ohtsu, "Demonstration of a nanophotonic switching operation by optical near-field energy transfer," Appl. Phys. Lett., vol.82, pp.2957–2959, 2003.
[11] S. Sangu, K. Kobayashi, A. Shojiguchi, and M. Ohtsu, "Logic and functional operations using a near-field optically coupled quantum-dot system," Phys. Rev. B, vol.69, pp.115334-1–13, 2004.
[12] T. Kawazoe, K. Kobayashi, J. Lim, Y. Narita, and M. Ohtsu, "Direct observation of optically forbidden energy transfer between CuCl quantum cubes via near-field optical spectroscopy," Phys. Rev. Lett., vol.88, pp.067404-1–4, 2002.
[13] Z.K. Tang, A. Yanase, T. Yasui, Y. Segawa, and K. Cho, "Optical selection rule and oscillator strength of confined exciton system in CuCl thin films," Phys. Rev. Lett., vol.71, pp.1431–1434, 1993.
[14] H.J. Carmichael, Statistical Methods in Quantum Optics I, Springer-Verlag, Berlin, 1999.
[15] T. Kawazoe, K. Kobayashi, and M. Ohtsu, "Optical nanofountain: A biomimetic device that concentrates optical energy in a nanometric region," Appl. Phys. Lett., vol.86, pp.103102-1–3, 2005.
[16] I. Arsovski and A. Sheikholeslami, "A current-saving match-line sensing scheme for content-addressable memories," 2003 IEEE International Solid-State Circuits Conference, Digest of Technical Papers, vol.1, pp.304–494, 2003.
[17] I. Arsovski, T. Chandler, and A. Sheikholeslami, "A ternary content-addressable memory (TCAM) based on 4T static storage and including a current-race sensing scheme," IEEE J. Solid-State Circuits, vol.38, no.1, pp.155–158, 2003.
[18] P.-F. Lin and J.B. Kuo, "A 1-V 128-kb four-way set-associative CMOS cache memory using wordline-oriented tag-compare (WLOTC) structure with the content-addressable-memory (CAM) 10-transistor tag cell," IEEE J. Solid-State Circuits, vol.36, no.4, pp.666–675, 2001.
[19] M. Naruse, F. Kubota, T. Kawazoe, S. Sangu, K. Kobayashi, and M. Ohtsu, "Optical interconnects using optical far- and near-field interactions for high-density data broadcasting," Conference on Lasers and Electro-Optics (CLEO) 2005, paper CWF6.
[20] T. Saida, K. Okamamoto, K. Uchiyama, K. Takiguchi, T. Shibata, and A. Sugita, "Integrated optical digital-to-analogue converter and its application to pulse pattern recognition," Electron. Lett., vol.37, pp.1237–1238, 2001.
[21] S.B. Akers, "Binary decision diagram," IEEE Trans. Comput., vol.C-27, no.6, pp.509–516, 1978.
[22] D.K. Hunter, M.C. Chia, and I. Andonovic, "Buffering in optical packet switches," IEEE J. Lightwave Technol., vol.16, no.12, pp.2081–2094, 1998.
[23] K. Nikolic, A. Sadek, and M. Forshaw, "Fault-tolerant techniques for nanocomputers," Nanotechnology, vol.13, pp.357–362, 2002.
[24] T. Yatsui, M. Kourogi, and M. Ohtsu, "Plasmon waveguide for op-

tical far/near-field conversion," Appl. Phys. Lett., vol.79, pp.4583–4585, 2001.

[25] J. Takahara, Y. Suguru, T. Hiroaki, A. Morimoto, and T. Kobayashi, "Guiding of a one-dimensional optical beam with nanometer diameter," Opt. Lett., vol.22, pp.475–477 1997.

[26] T. Yatsui, S. Takubo, J. Lim, W. Nomura, M. Kourogi, and M. Ohtsu, "Regulating the size and position of deposited Zn nanoparticles by optical near-field desorption using size-dependent resonance," Appl. Phys. Lett., vol.83, pp.1716–1718, 2003.

Makoto Naruse was born in Tokyo, Japan, in 1971. He received the B.E., M.E., and Dr. Eng. degrees from the University of Tokyo in 1994, 1996, and 1999, respectively. From 1999 to 2000, he was a postdoctoral researcher of the Japan Society for the Promotion of Science. From 2000 to 2002, he was a research associate at the University of Tokyo. In 2002, he joined the Ultrafast Photonic Network Group at the National Institute of Information and Communications Technology (formerly the Communications Research Laboratory). From 2003, he is a senior researcher. From 2001 to 2005, he was concurrently serving as a researcher of the PRESTO program of the Japan Science and Technology Agency. He is currently engaged in optical communication and information processing systems based on novel optical devices and architectures. He received an Inoue Research Award for Young Scientist from the Inoue Foundation for Science and a Research Award from Research Foundation for Opto-Science and Technology in 2000. Dr. Naruse is a member of the OSA, the Japan Society of Applied Physics and the Society of Instrument and Control Engineers.

Tetsuya Miyazaki was born in Chiba, Japan, in 1962. He received the B.S. degree in physics from the University of Tsukuba, Ibaraki, Japan, in 1985 and the M.S. and Dr.Eng. degrees in information processing from the Tokyo Institute of Technology, Tokyo, Japan, in 1987 and 1997, respectively. In 1987, he joined KDDI Research and Development (R&D) Laboratories, Saitama, Japan, where he worked on coherent optical communications. From 1993 to 1996, he was with ATR Optical and Radio Communications Research Laboratories, where he worked on fiber amplifiers for optical inter-satellite links. From 1996 to 2002, he was with KDDI R&D Laboratories, where he was engaged in work on WDM optical networks. Since April 2002, he has been with Communications Research Laboratory (currently NICT) where he is involved in research on ultra-fast photonic networks. Currently, he is group leader of the ultra-fast photonic network group. Dr. Miyazaki is a member of the IEEE Laser and Electro-Optic Society (IEEE LEOS).

Tadashi Kawazoe was born in Kochi in 1967. He received the B.E., M.E., and Ph.D. degrees in physics from University of Tsukuba, Tsukuba, Japan, in 1990, 1993, and 1996, respectively. He is a researcher at Solution Oriented Research for Science and Technology (SORST) project of Japan Science and Technology Agency. In 1996, he joined the Faculty of Engineering, Yamagata University, Yamagata, Japan, as a Research Associate, engaged in research on nonlinear optical materials and devices. Since April 2000, he has been with Japan Science and Technology Agency. His current research interests are in the areas of optical properties of nano materials, optical near field, and nanophotonic devices. Dr. Kawazoe is a member of the Japan Society of Applied Physics and the Physical Society of Japan.

Suguru Sangu was born in Hokkaido, Japan, in 1971. He received the B.E. degree from the Muroran Institute of Technology, Hokkaido, Japan, in 1994, and the M.E. and Ph.D. degrees in electronics and information engineering from Hokkaido University, Hokkaido, Japan, in 1996 and 1999, respectively. From 1999 to 2003, he joined the "Localized Photon" project for the Exploratory Research for Advanced Technology (ERATO) at the Japan Science and Technology Agency. Since 2003, he has been a Researcher of the Research and Development Center, Ricoh Company Ltd. His current research interests are the theory on near-field optics and its application to nano-photonics. Dr. Sangu is a member of the Japan Society of Applied Physics.

Kiyoshi Kobayashi was born in Okayama in 1953. He received the D.S. degree in physics from the University of Tsukuba, Tsukuba, Japan, in 1982. After graduation, he joined IBM Japan as a Research Staff Member at Tokyo Research Laboratory, Tokyo, Japan. Since 1998, he has been the theoretical group leader of the "Localized Photon" project for the Exploratory Research for Advanced Technology (ERATO) at the Japan Science and Technology Agency, Tokyo. Since 2004, he has been a Professor with the 21 Century Center of Excellence Program, Nanometer-scale Quantum Physics, Department of Physics, Tokyo Institute of Technology, Tokyo, Japan. His main fields of interest are quantum optical near-field theory and its application to nano/atom photonics. Dr. Kobayashi is a member of the Physical Society of Japan, the Japan Society of Applied Physics, and the American Physical Society.

Fumito Kubota received a B.E. in Instrumentation Engineering from Keio University, Japan and a Ph.D. in Computer Science and Electronics from the Kyushu Institute of Technology, Japan. He joined the Radio Research Laboratories, Ministry of Posts and Telecommunications (presently National Institute of Information and Communications Technology (NICT)). Since then, he has been involved in research on mobile communications and advanced networks. From 1982 through 1983, he engaged in research on digital mobile communications at the Nancy 1 University in France. Currently, he is a Research Supervisor in the Information and Network Systems Department at NICT. Concurrently, he functions in the capacity of Guest Professor at both the National Institute of Multimedia Education (NIME) since 1996 and the Japan Advanced Institute of Science and Technology (JAIST), Hokuriku since 1999. He is a member of IEEE.

Motoichi Ohtsu received the B.E., M.E., and Dr.E. degrees in electronics engineering from the Tokyo Institute of Technology, in 1973, 1975, and 1978, respectively. In 1978, he was appointed a Research Associate, and in 1982, he became an Associate professor at the Tokyo Institute of Technology. From 1986 to 1987, while on leave from the Tokyo Institute of Technology, he joined the Crawford Hill Laboratory, AT&T Bell Laboratories. In 1991, he became a Professor at the Tokyo Institute of Technology. In 2004, he moved to the University of Tokyo. Since 1993, he has been concurrently the leader of the "Photon Control" project of the Kanagawa Academy of Science and Technology. Since 1998, he has been concurrently the leader of the "Localized Photon" project of ERATO. Since 2002, he is a leader of the national project on "Ultrahigh density optical storage" sponsored by METI. He has written over 320 papers and received 87 patents. He is the author and co-author of 39 books. In 2000, he was the President of the IEEE/LEOS Japan Chapter. From 2000, he is an executive director of the Japan Society of Applied Physics. In 2001, he served as a Technical Program Co-chair for the 4th CLEO/PR01. He has been a tutorial lecturer o the SPIE and the OSA. He is a member of several boards of the MEXT, METI, and so on. Prof. Ohtsu is a Fellow of the OSA, a senior member of IEEE, and member of several academic societies. He has been awarded ten prizes from academic institutions, including the I. Koga Gold Medal of URSI in 1984, the Japan IBM Science Award in 1988, two awards from the JSAP in 1982 and 1990, and the Inoue Science Foundation Award in 1999. In 2004, he was awarded a purple ribbon medal from Japanese government.

IEICE TRANS. ELECTRON., VOL.E88–C, NO.9 SEPTEMBER 2005

PAPER Special Section on Nanophotonics and Related Techniques

Size-, Position-, and Separation-Controlled One-Dimensional Alignment of Nanoparticles Using an Optical Near Field

Takashi YATSUI[†a)], **Wataru NOMURA**[††], *Nonmembers*, *and* **Motoichi OHTSU**[†,††], *Member*

SUMMARY Particles several tens of nanometers in size were aligned in the desired positions in a controlled manner by using capillary force interaction and suspension flow. Latex beads 40-nm in diameter were aligned linearly around a 10-μm-hole template fabricated by lithography. Further control of their position and separation was realized using colloidal gold nanoparticles by controlling the particle-substrate and particle-particle interactions using an optical near field generated on the edge of a Si wedge, in which the separation of the colloidal gold nanoparticles was controlled by the direction of polarization.

key words: *optical near-field, self-assembly, nanoparticles*

1. Introduction

For future optical transmission and signal processing systems with high data transmission rates and capacity, we have proposed nanometer-sized photonic integrated circuits (i.e., nanophotonics ICs) [1]. As a representative device, the operation of a nanophotonic switch was demonstrated by controlling the dipole forbidden optical energy transfer among resonant energy states in CuCl quantum cubes via an optical near field [2]. The switch is made of three CuCl quantum cubes with a size ratio of 1: $\sqrt{2}$:2 on a sub-10-nm scale, and the size and position of the cubes on the substrate must be controlled with nanometer-scale accuracy.

Coupling these nanophotonic devices and ICs with external conventional diffraction-limited photonic devices requires a nanometer-sized optical waveguide for far-/near-field conversion. To realize this, we reported a plasmon waveguide that uses a metallized Si wedge structure that converts far-field light into an optical near-field via a metallic core waveguide [3]. Furthermore, it has been suggested that electromagnetic energy can be guided along a nano-dot coupler, which consists of chains of closely spaced metallic nanoparticles [4]. Energy transfer in the nano-dot coupler relies on dipole-dipole coupling between neighboring nanoparticles. To realize a nano-dot coupler consisting of 50-nm gold nanoparticles with 50-nm separation, the dispersion of their separation is estimated to be as small as 10 nm to obtain an efficiency equivalent 50% that of an ordered array [4].

Manuscript received November 18, 2004.
Manuscript revised May 7, 2005.

[†]The authors are with Solution-Oriented Research for Science and Technology, Japan Science and Technology Agency, Machida-shi, 194-0004, Japan.
[††]The authors are with the School of Engineering, The University of Tokyo, Tokyo, 113-8656 Japan.
a) E-mail: yatsui@ohtsu.jst.go.jp

DOI: 10.1093/ietele/e88–c.9.1798

Promising components for integrating these nanometer-sized photonic devices include chemically synthesized nanocrystals, such as metallic nanocrystals [5], semiconductor quantum dots [6], and nanorods [7], because they have uniform size, controlled shape, defined chemical composition, and tunable surface chemical functionality. However, position- and size-controlled deposition methods have not yet been developed. Since several methods have been developed to prepare nanometer-sized templates reproducibly [8], it is expected that the self-assembly of colloidal nanostructures into a lithographically patterned substrate will enable precise control at all scales [9]. Capillary forces play an important role, because colloidal nanostructures are synthesized in solution. Recently, successful integration of polymer or silica spheres [10], [11] and complex nanostructures such as nanotetrapods [11] into templates by controlling the capillary force using appropriate template structures has been reported, although their size and separation are typically uniform.

To fabricate nanophotonic devices, we propose a novel method of assembling nanoparticles by controlling the capillary force interaction and suspension flow. Further control of the positioning and separation of the nanoparticles is realized by controlling the particle-particle and particle-substrate interactions using an optical near field.

2. One-Dimensional Alignment of Latex Beads

To control position and separation very accurately, preliminary experiment was performed on a patterned Si substrate, where an array of 10-μm holes in 100- nm-thick SiO_2 was fabricated using photolithography (Fig. 1(a)). Subsequently, a suspension containing latex beads with a mean diameter of 40 nm was dispersed on the substrate and the latex beads were aligned after solvent evaporation. The deposited latex beads were not subjected to any surface treatment and were dispersed in pure water at 0.001 wt%. Although the 10-μm-sized template resulted in low selectivity in the position of the latex beads (Figs. 1(b) and 1(c)), the beads were deposited only on the SiO_2 surface owing to its higher capillarity.

For higher positional selectivity, the suspension containing latex beads was dropped onto a lithographically patterned Si substrate that was spinning at 3,000 revolutions per minute (rpm). As shown in Fig. 1(d), the suspension flow split into two branches at the SiO_2 hole. Scanning electron microscope (SEM) images (Figs. 1(e)–(g)) show that

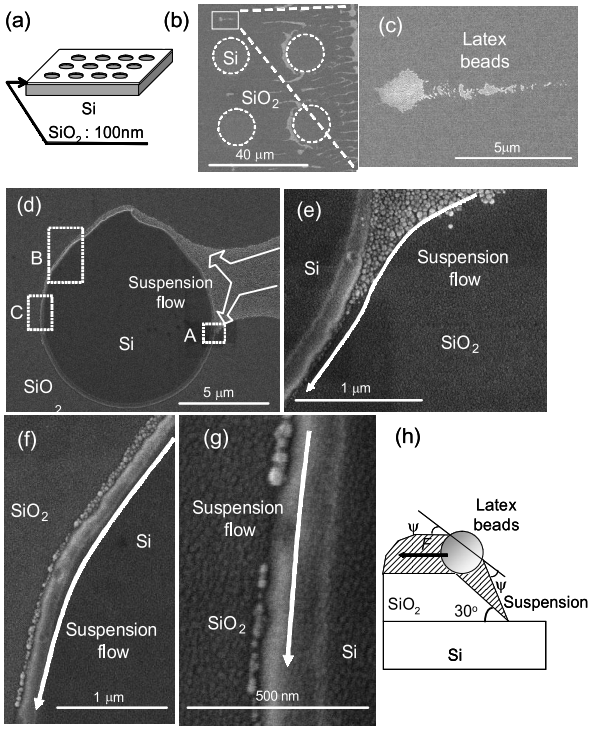

Fig. 1 (a) Schematic of lithographically patterned Si substrate. (b and c) SEM images of latex beads dispersed on the lithographically patterned Si substrate. (d) SEM image of latex beads dispersed on the lithographically patterned Si substrate rotated at 3,000 rpm. Higher magnification SEM images of white squares A (e), B (f), and C (g) in (d). (h) Schematic illustrating of the particle-assembly process driven by the capillary force and suspension flow.

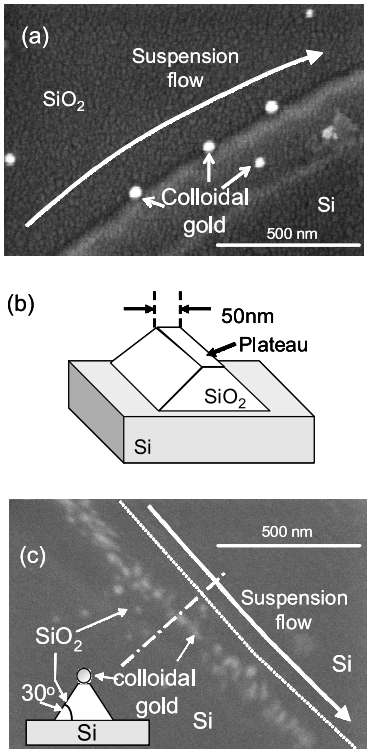

Fig. 2 (a) SEM image of colloidal gold nanoparticles dispersed on the lithographically patterned Si substrate rotated at 3,000 rpm. (b) Schematic of the SiO_2 line structure fabricated on the Si substrate. (c) SEM images of colloidal gold nanoparticles dispersed on the SiO_2 line rotated at 3,000 rpm. Inset; cross-section of the substrate along the white line (dashes and dots).

the chain of colloidal beads was aligned at the Si/SiO_2 interface. Note that the number of rows of latex beads decreased (Figs. 1(e) and 1(f)) and only the smallest beads, which were 20 nm in diameter, reached the end of the suspension flow (Fig. 1(g)). Assuming the same particle-suspension contact angle (denoted ψ in Fig. 1(h)) for various particles diameters, the flow speed of the larger latex beads had greater deceleration since the magnitude of the force pushing the particles on the SiO_2 (denoted F in Fig. 1(h)) owing to evaporation of the solvent is proportional to the particle diameter [11]. In other ward, the size selection was realized.

3. Self-Assembly of Au Nanoparticles Using an Optical Near Field

Based on the results of preliminary deposition, we tried assembling metallic nanoparticles because they are the material used to construct nano-dot couplers [4]. In this trial, we investigated the assembly of colloidal gold nanoparticles with a mean diameter of 20 nm dispersed in citrate solution at 0.001%. The nanoparticles were prepared by the citric acid reduction of gold ions and terminated by a carboxyl group (approximate length is 0.2 nm) with a negative charge [12]. However, they could not be aggregated using the same deposition process as for the latex beads (Fig. 2(a)). To aggregate these particles, we fabricated a SiO_2 line structure with a plateau width of 50 nm on the Si substrate using photolithography (Fig. 2(b)). The solvent containing the colloidal gold nanoparticles was dropped onto this substrate at 3,000 rpm. Then, the colloidal gold nanoparticles aggregated along the plateau of the SiO_2 line (Figs. 2(b) and 2(c)). This indicates that the capillary force induced by the lithographically patterned substrate, which is caused by the higher wettability of SiO_2 than that of the Si, was larger than the repulsive force owing to the negative charge of the carboxyl group on the colloidal gold nanoparticles. Furthermore, the gold nanoparticles were aligned along the plateau of the SiO_2. Such aggregation is caused by its wedge structure. This is because the suspension at the edge is thinner than that on the slope of the SiO_2 owing to its low capillarity, and this causes the convective transport of particles toward the edge [13], which resulted in the aggregation and alignment of the colloidal gold nanoparticles at high density.

To further control size, separation, and positioning, we examined the aggregation of colloidal gold nanoparticles under illumination, because the colloidal gold nanoparticles have strong optical absorption. Strong absorption should desorb the carboxyl group from the colloidal gold nanoparticles and result in their aggregation. Such an aggregation of colloidal gold nanoparticles were confirmed by the illumination of light. Figure 3(a) shows the aggregated gold nanoparticles over the pyramidal Si substrate under the 690-

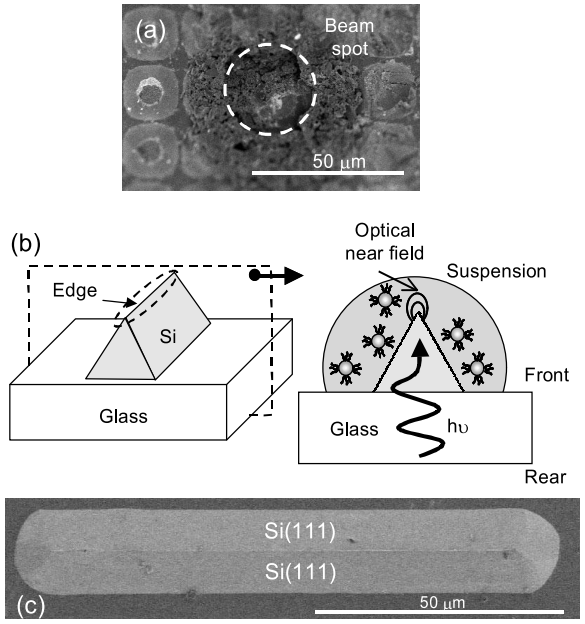

Fig. 3 (a) Aggregated colloidal gold nanoparticles with frontal illumination under 690-nm light (25 mW/mm^2) for 60 seconds. (b) Schematic of the experimental setup. (c) SEM image of the fabricated Si wedge structure.

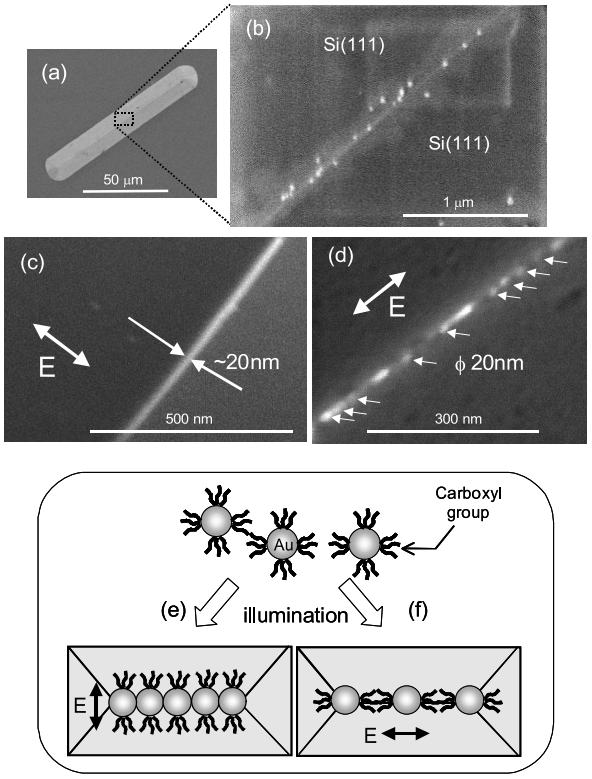

Fig. 4 (a) Overview of the Si wedge structure. (b) SEM image of colloidal gold nanoparticles deposited on the edge of the Si wedge structure without illumination. SEM images of colloidal gold nanoparticles on the Si wedge structure under illumination with polarization perpendicular (c) and parallel (d) to the edge. Schematic diagrams of the aggregation of colloidal gold nanoparticles along the edge of the Si wedge with polarization perpendicular (e) and parallel (f) to the edge.

nm-light illumination for 60 seconds. However, since the light was illuminated through the droplet of the colloidal gold nanoparticles, aggregated colloidal gold nanoparticles were spread outside the beam spot. In order to realize selective aggregation of the gold nanoparticles at the desired position, the suspension was illuminated from behind (Fig. 3(b)). Furthermore, we used a Si wedge, because this is a suitable structure for a far-/near-field conversion device [3]. The Si wedge structure was fabricated in three steps:

(i) A (100)-oriented silicon-on-insulator (SOI) wafer was bonded to the glass substrate using anodic bonding.
(ii) After removing the Si substrate from the SOI wafer by wet etching, the SiO_2 layer was patterned using photolithography.
(iii) The Si wedge was fabricated by anisotropic etching (40 g KOH + 60 g H_2O + 40 g isopropyl alcohol, 80°C). Maintaining the Si wedge height at less than 10 μm also kept its propagation loss sufficiently low.

Figure 3(c) shows an SEM image of the fabricated Si wedge structure after removing the SiO_2 layer.

For this structure, colloidal gold nanoparticles were deposited around the edge after evaporating the suspension without illumination (Figs. 4(a) and 4(b)). Such aggregation is caused by its wedge structure, as observed for the SiO_2 wedge structure (Fig. 2(c)) [13]. Further selective alignment along the edge of the Si wedge was realized using rear illumination. Figures 4(c) and 4(d) show the deposited colloidal gold nanoparticles with illumination under 690-nm light (25 mW/mm^2) for 60 seconds. Since the optical near-field energy is enhanced at the edge owing to the high refractive index of Si (see Fig. 3(b)) [14], selective aggregation along the edge with higher density is seen in these figures. This is due to the desorption of the carboxyl group by the absorption of light by the colloidal gold nanoparticles.

Note that the colloidal gold nanoparticles were closely aggregated and aligned linearly to form a wire shape when the polarization was perpendicular to the edge axis (Fig. 4(c)), while they were aligned with separation of several tens of nanometers in the parallel polarization (Fig. 4(d)). As the optical near-field energy for parallel polarization is higher than that for perpendicular polarization [3], greater aggregation is expected for parallel polarization. Nevertheless, the parallel polarization resulted in less aggregation. The low resolution of SEM images does not determine the distribution of the carboxyl molecules. However, such a repulsive force for disaggregation is caused by the carboxyl molecules which remained on the colloidal gold nanoaprticles. Thus, we believe that the difference in the degree of aggregation originated from differences in the charge distribution induced inside the gold nanoparticles. Based on the polarization dependence of the aggregation, it is reasonable to consider that the aggregation along the edge with perpendicular polarization is owing to partially adsorbed carboxyl groups (Fig. 4(e)), while the disaggregation with the parallel polarization resulted from the repulsive force in-

duced by the partially attached carboxyl group on the colloidal gold nanoparticles (Fig. 4(f)).

4. Conclusion

We present experimental results that demonstrate the controlled assembly of 40-nm latex particles in desired positions using capillary force interaction. Further controllability in separation and positioning was demonstrated using colloidal gold nanoparticles by introducing the Si wedge structure and controlling the direction of polarization. The experimental results and suggested mechanisms described here show the potential advantages of this technique in improving the regulation of the separation and positioning of nanoparticles, and possible application to realize a nano-dot coupler for far-/near-field conversion.

Acknowledgement

The authors thank Prof. H. Hori, University of Yamanashi, for valuable discussions.

References

[1] M. Ohtsu, K. Kobayashi, T. Kawazoe, S. Sangu, and T. Yatsui, "Nanophotonics: Design, fabrication, and operation of nanometric devices using optical near fields," IEEE J. Sel. Top. Quantum Electron., vol.8, no.4, pp.839–862, 2002.
[2] T. Kawazoe, K. Kobayashi, S. Sangu, and M. Ohtsu, "Demonstration of nanophotonic switching by optical near-field energy transfer," Appl. Phys. Lett., vol.82, no.18, pp.2957–2959, 2003.
[3] T. Yatsui, M. Kourogi, and M. Ohtsu, "Plasmon waveguide for optical far/near-field conversion," Appl. Phys. Lett., vol.79, no.27, pp.4583–4585, 2001.
[4] S.A. Maier, P.G. Kik, H.A. Atwater, S. Meltzer, E. Harel, B.E. Koel, and A.G. Requicha, "Local detection of electromagnetic energy transport below the diffraction limit in metal nanoparticle plasmon waveguides," Nature Materials, vol.2, pp.229–232, 2003.
[5] M. Brust and C.J. Kiely, "Some recent advances in nanostructure preparation from gold and silver particles: Short topical review," Colloids Surf. A, vol.202, pp.175–186, 2002.
[6] A.P. Alivisatos, "Semiconductor clusters, nanocrystals, and quantum dots," Science, vol.271, pp.933–937, 1996.
[7] P. Yang, "Wires on water," Nature, vol.425, pp.243–244, 2003.
[8] M.D. Austin, H. Ge, W. Wu, M. Li, Z. Yu, D. Wasserman, S.A. Lyon, and S.Y. Chou, "Fabrication of 5 nm linewidth and 14 nm pitch features by nanoimprint lithography," Appl. Phys. Lett., vol.84, no.26, pp.5299–5301, 2004.
[9] G.M. Whitesides and B. Grzybowski, "Self-assembly at all scales," Science, vol.295, pp.2418–2421, 2002.
[10] Y. Yin, Y. Lu, and Y. Xia, "Assembly of monodispersed spherical colloids into one-dimensional aggregates characterized by well-controlled structures and length," J. Mater. Chem., vol.11, pp.987–989, 2001.
[11] Y. Cui, M.T. Björk, J.A. Liddle, C. Sönnichsen, B. Boussert, and A.P. Alivisatos, "Integration of colloidal nanocrystals into lithographically patterned devices," Nano Lett., vol.4, no.6, pp.1093–1098, 2004.
[12] G. Frens, "Controlled nucleation for the regulation of the particle size in monodisperse gold suspensions," Nature Phys. Sci., vol.241, pp.20–22, 1973.
[13] N.D. Denkov, O.D. Velev, P.A. Kralchevsky, I.B. Ivanov, H. Yoshimura, and L. Nagayama, "Two-dimensional crystallization," Nature, vol.361, p.26, 1993.
[14] T. Yatsui, K. Itsumi, M. Kourogi, and M. Ohtsu, "Metallized pyramidal silicon probe with extremely high throughput and resolution capability for optical near-field technology," Appl. Phys. Lett., vol.80, no.13, pp.2257–2259, 2002.

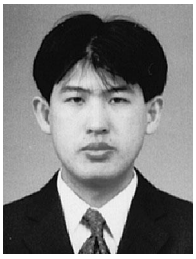

Takashi Yatsui was born in Tokyo, Japan, on January 21, 1972. He received the B.E. degree from Keio University, Tokyo, Japan, in 1995, and M.E. and D.E. degrees from Tokyo Institute of Technology, Tokyo, Japan, in 1997 and 2000, respectively. From 1999 to 2000, he was a Research Fellow of the Japan Society for the Promotion of Science. Since 2000, he has been a Researcher at the Japan Science and Technology Corporation, Tokyo. Since 2003, he has been a Researcher at the Japan Science and Technology Agency, Tokyo. His current research interests include nanofabrication using optical near-field. Dr. Yatsui received 1st prize in Paper Contest from IEEE Student Branch at Tokyo Institute of Technology in 1998, and the excellent research presentation award form the Japan Society of Applied Physics in 2000, and Tejima Doctoral Dissertation Award from Tejima Foundation in 2001. Dr. Yatsui is a member of the Japan Society of Applied Physics.

Wataru Nomura was born in Kanagawa, Japan, on December 17, 1979. He recieved the B.E. and M.E. degrees from Tokyo Institute of Technology, Tokyo, Japan, in 2002 and 2004, respectively. He is a Ph.D. student of The University of Tokyo, Tokyo, Japan.

Motoichi Ohtsu received the B.E., M.E., and Dr.E. degrees in electronics engineering from the Tokyo Institute of Technology, in 1973, 1975, and 1978, respectively. In 1978, he was appointed a Research Associate, and in 1982, he became an Associate professor at the Tokyo Institute of Technology. From 1986 to 1987, while on leave from the Tokyo Institute of Technology, he joined the Crawford Hill Laboratory, AT&T Bell Laboratories. In 1991, he became a Professor at the Tokyo Institute of Technology. In 2004, he moved to the University of Tokyo. Since 1993, he has been concurrently the leader of the "Photon Control" project of the Kanagawa Academy of Science and Technology. Since 1998, he has been concurrently the leader of the "Localized Photon" project of ERATO. Since 2002, he is a leader of the national project on "Ultrahigh density optical storage" sponsored by METI. He has written over 320 papers and received 87 patents. He is the author and co-author of 39 books. In 2000, he was the President of the IEEE/LEOS Japan Chapter. From 2000, he is an executive director of the Japan Society of Applied Physics. In 2001, he served as a Technical Program Co-chair for the 4th CLEO/PR01. He has been a tutorial lecturer o the SPIE and the OSA. He is a member of several boards of the MEXT, METI, and so on. Prof. Ohtsu is a Fellow of the OSA, a senior member of IEEE, and member of several academic societies. He has been awarded ten prizes from academic institutions, including the I. Koga Gold Medal of URSI in 1984, the Japan IBM Science Award in 1988, two awards from the JSAP in 1982 and 1990, and the Inoue Science Foundation Award in 1999. In 2004, he was awarded a purple ribbon medal from Japanese government.

Importance of Multiple-Phonon Interactions in Molecular Dissociation and Nanofabrication Using Optical Near Fields

Kiyoshi Kobayashi, Tadashi Kawazoe, and Motoichi Ohtsu, *Senior Member, IEEE*

***Abstract*—A quasi-particle (exciton–phonon polariton) model, as a simple model of an optical near-field probe, is proposed to investigate an unresolved problem in photochemical processes, i.e., why a vapor molecule can be dissociated by an incident photon with less energy than the dissociation energy only if, not a propagating far field, but an optical near field is used, and what is the mechanism leading to the photon flux dependence of the deposition rates. Incident photon energy and intensity dependences of Zn deposition rates are analyzed, and good agreement between the theoretical and experimental results is obtained. It suggests that the probe system plays an important role in vibrational transitions as well as electronic transitions in photodissociation processes, and that the couplings between the optical near field and molecular vibrations are enhanced to permit a nonresonant photodissociation inherent in the optical near field.**

***Index Terms*—Molecular dissociation, multiple-phonon interaction, nanofabrication, optical near field, probe model, quasi-particle.**

I. Introduction

PHOTONIC devices must be ultra-highly integrated in order to fulfill the demands for an increase in communication capacity and information processing and, thus, the size of each functional block will be so small that it is far beyond the diffraction limit of incident light. All-optical switches are one of the key devices for such requirements, and the interferometer type switch has attracted considerable attention because ultrafast switching is possible by using optical nonlinearity. This kind of approach utilizes wave phenomena, and the device size and its integration are still constrained by the diffraction limit of light. A nanophotonic switch operated and controlled by an optical near field has been proposed in order to avoid the constraints, and the principles of operation have been verified theoretically and experimentally [1]–[5]. Toward implementation of such a nanophotonic device, it is mandatory to fabricate a collection of nanometric quantum dots on a substrate to a precision of a few nanometers. A number of approaches have been proposed, and among them, optical near-field fabrication methods seem promising because an optical near field possesses several notable features such as high spatial resolution originating from the highly localized field far beyond the diffraction limit of light. In fact, it has been reported that a zinc (Zn) dot or a few dots in sub-50 nm are successfully deposited on the sapphire substrate after dissociation of diethylzinc (DEZn) molecules by optical near fields [6], [7].

In particular, in [6], a fiber probe without the usual metal coating was used for the deposition of Zn dots in order to investigate effects of both near- and far-field light simultaneously. As is well known, the propagating far field is generated by light leaking through the circumference of the fiber, while the optical near field is mainly generated at the apex. The following three types of photon energy were essentially used for the experiment.

- Case 1) 5.08 eV (corresponding wavelength $\lambda = 244$ nm), which is close to the electronic excitation energy (5 eV) of a DEZn molecule.
- Case 2) 2.54 eV (corresponding wavelength $\lambda = 488$ nm), which is larger than the dissociation energy of the molecule (2.26 eV), but much smaller than the electronic excitation energy.
- Case 3) 1.81 eV (corresponding wavelength $\lambda = 684$ nm), which is smaller than both the dissociation and electronic excitation energies.

They showed in Case 1) that a Zn dot with a full width at a half maximum of 30 nm is deposited by the optical near field, and that tails of 4-nm high are also observed on both sides of the dot due to the leaked far-field light. On the other hand, they found in Case 2) that a 30-nm Zn dot without tails is deposited only by the near field whose energy is less than the electronic excitation energy. Regarding Case 3), no significant dot deposition were reported in [6] due to the weak photon intensity. Here, it is not known why an incident photon with less energy than the electronic excitation energy of a molecule can resolve it into composite atoms and deposit them as a nanometric dot. Such a mechanism is not allowed in a conventional photochemical vapor deposition (CVD) using a propagating light because the propagating light must resonate the reacting molecular gasses for photodissociation in order to excite molecules from the ground state to an excited electronic state [8], [9].

Manuscript received July 12, 2004; revised January 10, 2005. The work of K. Kobayashi was supported in part by a 21st Century COE Program at the Tokyo Institute of Technology "Nanometer-Scale Quantum Physics" and by a Grant-in-Aid for Scientific Research from the Ministry of Education, Sports, Science, and Technology, Japan.

K. Kobayashi was with Solution Oriented Research for Science and Technology, Japan Science and Technology Agency, Tokyo 194-0004, Japan. He is now with the Department of Physics, Tokyo Institute of Technology, Tokyo 152-8551, Japan (e-mail: kkoba@phys.titech.ac.jp).

T. Kawazoe is with Solution Oriented Research for Science and Technology, Japan Science and Technology Agency, Tokyo 194-0004, Japan (e-mail address: kawazoe@ohtsu.jst.go.jp). .

M. Ohtsu is with the Department of Electronics Engineering, University of Tokyo, Tokyo 113-8656, Japan and also with Solution Oriented Research for Science and Technology, Japan Science and Technology Agency, Tokyo 194-0004, Japan (e-mail address: ohtsu@ee.t.u-tokyo.ac.jp).

Digital Object Identifier 10.1109/TNANO.2005.851406

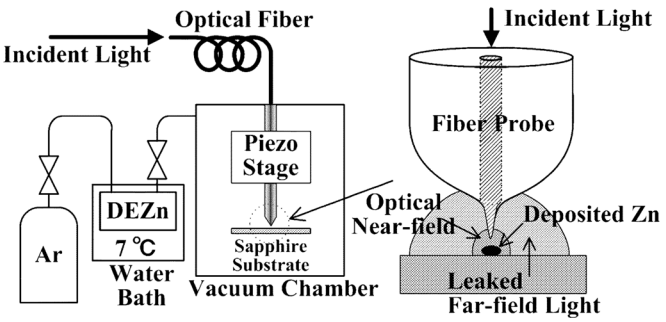

Fig. 1. Experimental setup for NFO CVD. The DEZn bottle and CVD chamber were kept at 7 °C and 25 °C, respectively, to prevent the condensation of DEZn on the sapphire substrate. During deposition, the partial pressure of DEZn was 100 mtorr and the total pressure in the chamber was 8 torr. Incident wavelength and power of the laser, as well as the irradiation time were: (a) 325 nm, 2.3 μW, and 60 s, (b) 488 nm, 360 μW, and 180 s, and (c) 684 nm, 1 mW, and 180 s, respectively.

In order to further investigate the mechanism of the photochemical process, they measured deposition rates depending on photon energy and intensity [10]. Experimental setup and conditions are illustrated in Fig. 1. As an optical near-field probe, a glass fiber is chemically etched to have a nanometric sized probe apex without metal coating usually employed, which is similar to the one used in [6]. However, to our best knowledge, no theoretical analysis has been reported yet, and the mechanism of the dissociation and deposition of molecules has still not been clearly understood. It is thus essential to understand this process in order to fabricate nanometric dots while controlling position and size; pairs of such dots could then be used to build nanophotonic devices such as those that we proposed in our previous study [1]–[5]. In this paper, we address this issue, propose a simple model of an optical near-field probe, and clarify the mechanism of the photochemical processes involved in using such a probe, comparing the theoretical results with Zn-dot deposition data.

This paper is organized as follows. Section II outlines our simple model for an optical near-field probe. In Section III, molecular dissociation processes using optical near field are theoretically analyzed, and the results are compared with experimental data on the deposition rates of Zn dots in Section IV. Finally, concluding remarks are presented in Section V.

II. Model

We propose a quasi-particle (exciton–phonon polariton) model as a simple model of an optical near-field probe in order to investigate the physical mechanisms of the chemical vapor deposition using an optical near field (NFO CVD). We assume that exciton–phonon polaritons, the quanta of which are transferred from the optical near-field probe tip to both gas and adsorbed molecules, are created at the apex of the optical near-field probe. Here it should be noted that the quasi-particle transfer is valid only if the molecules are very close to the probe tip because the optical near field is highly localized near the probe tip. The optical near field generated on the nanometric probe tip, which is a highly mixed state with material excitation rather than the propagating light field [11], is described in terms of the following model Hamiltonian:

$$\begin{aligned} H &= \sum_p \hbar \left[\omega_p a_p^\dagger a_p + \omega_p^{\mathrm{ex}} b_p^\dagger b_p + \frac{i\Omega_c}{2}(a_p^\dagger b_p - a_p b_p^\dagger) \right] \\ &\quad + \sum_p \hbar\Omega_p c_p^\dagger c_p + \sum_{p,q} \Big\{ i\hbar M(p-q) b_p^\dagger b_q \\ &\qquad \times \left[c_{p-q} + c_{q-p}^\dagger \right] + h.c. \Big\} \\ &= \sum_p \hbar\omega_p^{\mathrm{pol}} B_p^\dagger B_p + \sum_p \hbar\Omega_p c_p^\dagger c_p \\ &\quad + \sum_{p,q} \left\{ i\hbar M'(p-q) B_p^\dagger B_q \left[c_{p-q} + c_{q-p}^\dagger \right] + h.c. \right\} \end{aligned} \tag{1}$$

where the creation (annihilation) operators for a photon, an exciton, a renormalized phonon, and an exciton polariton are denoted, respectively, as $a_p^\dagger(a_p), b_p^\dagger(b_p), c_p^\dagger(c_p)$, and $B_p^\dagger(B_p)$, and their frequencies are $\omega_p, \omega_p^{\mathrm{ex}}, \Omega_p$, and ω_p^{pol}, respectively. The subscripts p and q indicate the momenta of the relevant particle in the momentum representation such as a photon, an exciton, a renormalized phonon, an exciton polariton, or an exciton–phonon polariton. Each coupling between a photon and an exciton, a phonon and an exciton, and an exciton polariton and a phonon is designated as $\Omega_c, M(p-q)$, and $M'(p-q)$, respectively. The first line of this description expresses the Hamiltonian for a photon-exciton interacting system and is transformed into the exciton-polariton representation, as shown in the third line [12], while the second line represents the Hamiltonian for a phonon-exciton interacting system. Note that electronic excitations near the probe tip, driven by photons incident into the fiber probe, cause mode–mode couplings or anharmonic couplings of phonons, and that they are taken into account as a renormalized phonon; therefore, multiple phonons as coherently squeezed phonons in the original representation can interact with an exciton or an exciton polariton simultaneously. In the model, quasi-particles (exciton–phonon polaritons) in bulk material (glass fiber) are approximately used and, thus, their states are specified by the momentum. Strictly speaking, momentum is not a good quantum number to specify the quasi-particle states at the apex of the probe, from the symmetry consideration, and they should be a superposition of such momentum-specified states with different weights. Instead of this kind of treatment, we simply assume that the quasi-particles specified by the momentum are transferred to a vapor or adsorbed molecule that is located near the probe tip, utilizing highly spatial localization of the optical near field.

Now we assume that exciton polaritons near the probe tip are expressed in the mean field approximation as

$$\langle B_{k_0}^\dagger \rangle = \langle B_{k_0} \rangle = \sqrt{\frac{I_0(\omega_0)V}{\hbar\omega_0 d}}. \tag{2}$$

Here, $I_0(\omega_0)$ is the photon intensity inside the probe tip with frequency ω_0 and momentum $\hbar k_0$, and V represents the volume to be considered while the probe tip size is denoted as d. Using the unitary transformation as

$$\begin{pmatrix} B_p \\ c_{p-k_0} \end{pmatrix} = \begin{pmatrix} iv_p' & u_p' \\ u_p' & iv_p' \end{pmatrix} \begin{pmatrix} \xi_{(-)p} \\ \xi_{(+)p} \end{pmatrix} \tag{3}$$

we can diagonalize the Hamiltonian in the exciton–phonon polariton representation [13] as

$$H = \sum_p \hbar\omega_p^{\rm pol} B_p^\dagger B_p + \sum_p \hbar\Omega_p c_p^\dagger c_p + \sum_p \left\{ i\hbar\sqrt{\frac{I_0(\omega_0)V}{\hbar\omega_0 d}} M'(p-k_0)\left(B_p^\dagger c_{p-k_0} - B_p c_{p-k_0}^\dagger\right)\right\} = \sum_p \hbar\omega(p)\,\xi_p^\dagger \xi_p \quad (4)$$

where the creation (annihilation) operator for an exciton–phonon polariton and the frequency are denoted as $\xi_p^\dagger(\xi_p)$ and $\omega(p)$, respectively. The suffix $(-)$ or $(+)$ indicates the lower or upper branch of the exciton–phonon polariton. The transformation coefficients u_p' and v_p' are given by

$$u_p'^2 = \frac{1}{2}\left(1 + \frac{\Delta}{\sqrt{\Delta^2 + (2Q)^2}}\right)$$
$$v_p'^2 = \frac{1}{2}\left(1 - \frac{\Delta}{\sqrt{\Delta^2 + (2Q)^2}}\right) \quad (5)$$

where the detuning between an exciton polariton and a phonon is denoted as $\Delta = \omega_p^{\rm pol} - \Omega_{p-k_0}$, and the effective coupling constant is expressed as $Q = \sqrt{I_0(\omega_0)V/(\hbar\omega_0 d)}M'(p-k_0)$. Therefore, in this model, a molecule located near the probe tip does absorb not simple photons, but exciton–phonon polaritons whose energies are transferred to the molecule, which excite molecular vibrations, as well as electronic transitions.

III. Dissociation Probability

We now discuss the dissociation probability of a molecule, postulating that the deposition rate of the metal atoms is proportional to the molecular dissociation rate. Since the experimental intensity dependence of the deposition rate is up to the third order, as will be discussed in Section IV, we consider multiple-step transitions via vibrational levels in the electronic ground state. For the purpose, the following initial and three final states of a total system $|i\rangle, |f_{\rm first}\rangle, |f_{\rm second}\rangle$, and $|f_{\rm third}\rangle$, consisting of the optical near-field probe and a molecule, are prepared:

$$|i\rangle = |\text{probe}\rangle \otimes |E_g;\text{el}\rangle \otimes |E_i;\text{vib}\rangle \quad (6a)$$
$$|f_{\rm first}\rangle = |\text{probe}\rangle \otimes |E_g;\text{el}\rangle \otimes |E_a;\text{vib}\rangle \quad (6b)$$
$$|f_{\rm second}\rangle = |\text{probe}\rangle \otimes |E_{\rm ex};\text{el}\rangle \otimes |E_b;\text{vib}\rangle \quad (6c)$$
$$|f_{\rm third}\rangle = |\text{probe}\rangle \otimes |E_{\rm ex'};\text{el}\rangle \otimes |E_c;\text{vib}\rangle \quad (6d)$$

where $|\text{probe}\rangle$ represents probe states expressed by eigenstates of (4), and $|E_\alpha;\text{el}\rangle$ and $|E_\beta;\text{vib}\rangle$ denote molecular electronic and vibrational states, respectively. As shown in Fig. 2, molecular electronic states are classified into ground $(\alpha = g)$, first excited $(\alpha = \text{ex})$, and second excited $(\alpha = \text{ex}')$ states with energy E_α, while vibrational ground and excited states in the electronic ground state are $|E_i;\text{vib}\rangle$ and $|E_a;\text{vib}\rangle$, and vibrational states in the first and second electronic excited states are represented as $|E_b;\text{vib}\rangle$ and $|E_c;\text{vib}\rangle$, respectively. The direct product is designated as $\otimes$. The transitions from the initial to final states can be formulated according to the conventional perturbation method for the interaction Hamiltonian that is given by

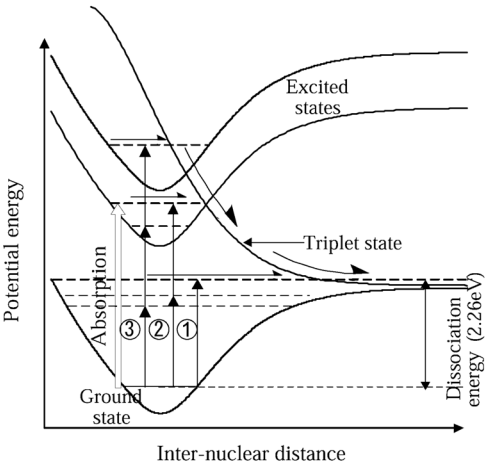

Fig. 2. Schematic drawing of potential energy of a DEZn molecule as a function of inter-nuclear distance. The solid curves depict the electronic ground state and three excited states, while the dashed lines denote the vibrational levels. Three labeled transitions marked by the arrows are considered for the dissociation of the molecules.

the multipolar quantum electrodynamics (QED) Hamiltonian in the dipole approximation [14] for an optical near-field–molecule interaction as

$$H_{\rm int} = -\int \boldsymbol{\mu}(\boldsymbol{r})\cdot\boldsymbol{D}^\perp(\boldsymbol{r})d^3r \quad (7a)$$

$$\boldsymbol{D}^\perp(\boldsymbol{r}) = i\sum_p \left(\frac{2\pi\hbar\omega_p}{V}\right)^{1/2}\boldsymbol{\varepsilon}_p\left[a_p e^{i\boldsymbol{p}\cdot\boldsymbol{r}} - a_p^\dagger e^{-i\boldsymbol{p}\cdot\boldsymbol{r}}\right]. \quad (7b)$$

Here, $\boldsymbol{\mu}(\boldsymbol{r})$ and $\boldsymbol{D}^\perp(\boldsymbol{r})$ denote the electric dipole operator and electric displacement vector at position $\boldsymbol{r}$, respectively. The polarization unit vector of a photon is designated as $\boldsymbol{\varepsilon}_p$. Rewriting the photon operators $(a_p, a_p^\dagger)$ in terms of the exciton–phonon polariton operators $(\xi_p, \xi_p^\dagger)$ discussed in Section II, and noticing that the electric dipole operator consists of the two components (electronic $\boldsymbol{\mu}^{\rm el}$ and vibrational $\boldsymbol{\mu}^{\rm nucl}$), we have the interaction Hamiltonian expressed in the exciton–phonon polariton representation as

$$H_{\rm int} = \left\{\mu^{\rm el}\left(e + e^\dagger\right) + \mu^{\rm nucl}\left(v + v^\dagger\right)\right\} \cdot \sum_p i\left(\frac{2\pi\hbar\omega_p}{V}\right)^{1/2}\left\{v_p v_p'\left(\xi_p e^{i\boldsymbol{p}\cdot\boldsymbol{r}} - \xi_p^\dagger e^{i\boldsymbol{p}\cdot\boldsymbol{r}}\right)\right\} \quad (8)$$

where $\mu^{\rm el} = \boldsymbol{\mu}^{\rm el}\cdot\boldsymbol{\varepsilon}_p$ and $\mu^{\rm nucl} = \boldsymbol{\mu}^{\rm nucl}\cdot\boldsymbol{\varepsilon}_p$ are the electronic and vibrational dipole moments, respectively, and the creation (annihilation) operators of the electronic and vibrational excitations are denoted as $e^\dagger(e)$ and $v^\dagger(v)$, respectively. Here, we employ exciton polaritons and exciton–phonon polaritons in the corresponding lower branch, taking into consideration incident photon energy. That is why the transformation coefficient from a photon to an exciton polariton v_p and that from an exciton polariton to an exciton–phonon polariton v_p' only appear in (8). The effective interaction between a probe tip and molecule that includes all the effects originating from the macroscopic material-photon system should be employed as a rigorous optical near-field interaction [11] in order to evaluate the transition probability. However, as a first step, we use not such an effective interaction Hamiltonian, but the bare

interaction Hamiltonian given by (8), to easily obtain analytic expressions for the transition probability. The transition probabilities for one-, two-, and three-step excitation (labeled ①, ②, and ③in Fig. 2), $P_{\rm first}(\omega_p)$, $P_{\rm second}(\omega_p)$, and $P_{\rm third}(\omega_p)$, can be written as (9)–(11), shown at the bottom of this page,where γ_m is the linewidth of vibrational levels, and γ'_m is that of electronic levels. The lower polariton frequency is represented as $\omega(p)$. Note that the energy locally transferred to a molecule is conserved, while the momentum is not conserved, as mentioned before. These results clearly show that the transition probability for one-step excitation is linearly proportional to the photon intensity, while the second- and third-step transition probabilities are proportional to the second and third power of the photon intensity, respectively. Moreover, (9) is a unique result for the case using optical near fields because it is zero for the dissociation of DEZn molecules using far-field photons with less energy than that of the electronic excitation of the molecule.

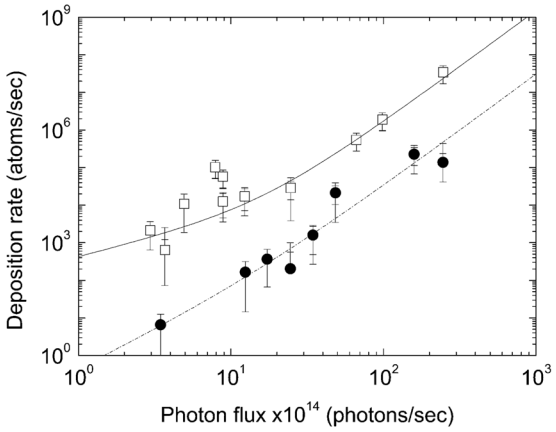

Fig. 3. Zn deposition rate as a function of photon flux. Experimental data for photon energy 2.54 and 1.81 eV are represented by the rectangles and circles, respectively. The solid and dashed curves fit the results using the formula (see the text).

IV. Result

It follows from (9)–(11) that the near-resonant transition probabilities have the following ratio:

$$\frac{P_{\rm second}(\omega_p)/I_0^2(\omega_p)}{P_{\rm first}(\omega_p)/I_0(\omega_p)} = \frac{P_{\rm third}(\omega_p)/I_0^3(\omega_p)}{P_{\rm second}(\omega_p)/I_0^2(\omega_p)} = \frac{\hbar}{2\pi}\frac{P_{\rm first}(\omega_p)}{|\gamma_m|^2 I_0(\omega_p)}\left(\frac{v'_p}{u'_p}\right)^2\left(\frac{\mu^{\rm el}}{\mu^{\rm nucl}}\right)^2 \tag{12}$$

where we simply set $\gamma_m = \gamma'_m$. Using this ratio (12) and experimental deposition data for Zn dots dissociated from DEZn molecules, we analyze the photon energy and intensity dependence of the deposition rate to clarify the origin of the near-field photochemical processes, i.e., the multiple-step transition via an excited state of a molecular vibrational mode. Before the comparison between the theoretical results and experimental data, we briefly summarize experimental results [6], [10] since experimental details of the Zn deposition procedures have already been published [15]. As a test case, we examined two cases where the photodissociation of DEZn and Zn deposition only occurred with an optical near field, not with a propagating far field.

Case 1) The incident photon energy, i.e., 2.54 eV, corresponding to the wavelength of $\lambda = 488$ nm, is larger than the dissociation energy of a DEZn molecule, i.e., 2.26 eV, but much smaller than the energies of the electronic excited states.

Case 2) The incident photon energy, i.e., 1.81 eV, corresponding to the wavelength of $\lambda = 684$ nm, is smaller than both the dissociation and electronic excitation energies required.

Both cases were newly reexamined in [10].

Fig. 3 shows the Zn deposition rate (R) as a function of the photon flux (Φ_0) that is experimentally measured near the probe tip, and the conversion rate between the theoretical and experimental values of Φ_0 is obtained from one of the experimental data. In Fig. 3, experimental data are represented by the rectangles for photon energy 2.54 eV ($\lambda = 488$ nm) and circles for photon energy 1.81 eV ($\lambda = 684$ nm), respectively. For comparison, the experimental deposition rate R is fitted as $R = a_\lambda\Phi_0(\omega_\lambda) + b_\lambda\Phi_0^2(\omega_\lambda) + c_\lambda\Phi_0^3(\omega_\lambda) = R_1(\omega_\lambda) + R_2(\omega_\lambda) + R_3(\omega_\lambda)$ with $a_{488} = 4.1\times10^{-12}, b_{488} = 2.1\times10^{-27}, c_{488} = 1.5\times10^{-42}, a_{684} = 0, b_{684} = 4.2\times10^{-29}$, and $c_{684} = 3.0\times10^{-44}$. The solid and dashed curves show the fitting for Case 1) and Case 2), respectively.

Now let us compare both results. In the first case, all the processes (②and ③), depicted in Fig. 2, are possibly allowed. Fitting $P_{\rm first}(\omega_{488}) = \alpha^{-1}R_1(\omega_{488})$ with a constant α to one experimental value shown in Fig. 3 as $R_1(\omega_{488}) = a_{488}\Phi_0(\omega_{488}) = 2\times10^2$ events/s with reasonable values of

$$P_{\rm first}(\omega_p) = \frac{2\pi}{\hbar}|\langle f_{\rm first}|H_{\rm int}|i\rangle|^2\delta(\hbar\omega_p + E_i - E_f) = \frac{(2\pi)^2}{\hbar d}v_p^2 v_p'^2 u_p'^2(\mu^{\rm nucl})^2 I_0(\omega_p) \tag{9}$$

$$P_{\rm second}(\omega_p) = \frac{2\pi}{\hbar}|\langle f_{\rm second}|H_{\rm int}|i\rangle|^2\delta(\hbar\omega_p + E_i - E_f) = \frac{(2\pi)^3}{\hbar d^2}\frac{v_p^4 v_p'^6 u_p'^2(\mu^{\rm el})^2(\mu^{\rm nucl})^2 I_0^2(\omega_p)}{|\hbar\omega(p) - (E_a - E_i + i\gamma_m)|^2} \tag{10}$$

$$P_{\rm third}(\omega_p) = \frac{2\pi}{\hbar}|\langle f_{\rm third}|H_{\rm int}|i\rangle|^2\delta(\hbar\omega_p + E_i - E_f) = \frac{(2\pi)^4}{\hbar d^3}\frac{v_p^6 v_p'^{10} u_p'^2(\mu^{\rm el})^4(\mu^{\rm nucl})^2 I_0^3(\omega_p)}{|\hbar\omega(p) - (E_a - E_i + i\gamma_m)|^2|\hbar\omega(p) - (E_{\rm ex} - E_g + i\gamma'_m)|^2} \tag{11}$$

$\mu^{\rm nucl} = 1\sqrt{\rm eV(nm)^3}, \mu^{\rm el} = 10^{-3}\mu^{\rm nucl}, \gamma_m = 10^{-1}$ eV, $v_p'^2/u_p'^2 = 0.01$, and $d = 30$ nm, we obtain the following ratio:

$$\frac{b_{488}}{a_{488}} = \frac{P_{\rm second}(\omega_{488})}{P_{\rm first}(\omega_{488})\Phi_0(\omega_{488})} = \frac{\hbar}{2\pi}\frac{P_{\rm first}(\omega_{488})}{|\gamma_m|^2\Phi_0(\omega_{488})}\left(\frac{v_p'}{u_p'}\right)^2\left(\frac{\mu^{\rm el}}{\mu^{\rm nucl}}\right)^2 \simeq 10^{-15} \tag{13a}$$

$$\frac{c_{488}}{b_{488}} = \frac{P_{\rm third}(\omega_{488})}{P_{\rm second}(\omega_{488})\Phi_0(\omega_{488})} = \frac{\hbar}{2\pi}\frac{P_{\rm first}(\omega_{488})}{|\gamma_m|^2\Phi_0(\omega_{488})}\left(\frac{v_p'}{u_p'}\right)^2\left(\frac{\mu^{\rm el}}{\mu^{\rm nucl}}\right)^2 \simeq 10^{-15} \tag{13b}$$

which is in good agreement with the experimental value of 10^{-15}. Here, we use $I_0(\omega_\lambda) = \hbar\omega_\lambda\Phi_0(\omega_\lambda)/d^2$, and each coefficient is assumed to be proportional to the transition probability as $a_\lambda \propto P_{\rm first}(\omega_\lambda), b_\lambda \propto P_{\rm second}(\omega_\lambda)$, and $c_\lambda \propto P_{\rm third}(\omega_\lambda)$. In the second case, the dissociation occurs via either the ②or ③ process shown in Fig. 2. The ratio can be evaluated as

$$\frac{c_{684}}{b_{684}} = \frac{\hbar}{2\pi}\frac{P_{\rm first}\,(\omega_{684})}{|\gamma_m|^2\Phi_0(\omega_{684})}\left(\frac{v_p'}{u_p'}\right)^2\left(\frac{\mu^{\rm el}}{\mu^{\rm nucl}}\right)^2 \simeq 10^{-15} \tag{14}$$

which is also in good agreement with the experimental value of 10^{-15}. For the theoretical estimation, we have used the same experimental value as $P_{\rm first}(\omega_{684}) = \alpha^{-1}R_1(\omega_{488})$ because both transitions are attributed to the coupling between phonons in the probe and molecular vibrations.

In [6], two other possible photodissociation processes have been pointed out as well as a multiple-step transition via an excited molecular vibrational level discussed here. One is the multiple-photon absorption process, and the other is the multiple-step transition via intermediate energy levels induced by the fiber probe. The former possibility is negligibly small because the optical power density used in the experiment was less than 10 kW/cm^2, which is too low for multiple-photon absorption [16]. The latter possibility will not arise because DEZn lacks relevant energy levels for such a broad region as the ultraviolet to near-infrared. The overall agreement between the theory and experimental results supports the transition process discussed here, and suggests that the exciton–phonon polariton model provides a possible way to understand the physical origin of the near-field photodissociation processes; the probe effect or the enhanced coupling between the optical near field and molecular vibration originates from the steep spatial gradient of the optical near field, and it cannot be described by the conventional perturbation method for the propagating light field-matter and the electron-phonon interactions.

V. Conclusion

To clarify the physical origin of the NFO CVD of nanometric Zn dots based on the photodissociation process of gas-phase DEZn under nonresonant conditions, we theoretically investigated incident photon energy and intensity dependence of the deposition rates. We analyzed the dependence using a multiple-step excitation process via the molecular vibrational levels, as well as the exciton–phonon polariton model of an optical near-field probe proposed here. The overall agreement between the theory and experimental results was obtained. The enhanced coupling between the optical near field and molecular vibration originates from the multiple-phonon coupling and the steep spatial gradient of the field. Such a nonadiabatic photochemical process can be applied to other near-field phenomena, and will open up a new way in nanoscale science and technology.

Acknowledgment

The authors gratefully acknowledge valuable comments from H. Hori, Yamanashi University, Kofu, Japan, A. Shojiguchi, S. Sangu, T. Yatsui, all of the Japan Science and Technology Agency, Tokyo, Japan, and H. Ito, and S. Takubo, both of the Tokyo Institute of Technology, Tokyo, Japan.

References

[1] T. Kawazoe, K. Kobayashi, J. Lim, Y. Narita, and M. Ohtsu, "Direct observation of optically forbidden energy transfer between CuCl quantum cubes via near-field optical spectroscopy," *Phys. Rev. Lett.*, vol. 88, pp. 067404-1–067404-4, 2002.

[2] M. Ohtsu, K. Kobayashi, T. Kawazoe, S. Sangu, and T. Yatsui, "Nanophotonics: Design, fabrication, and operation of nanometric devices using optical near fields," *IEEE J. Select. Topics Quantum Electron.*, vol. 8, no. 4, pp. 839–862, Jul./Aug. 2002.

[3] S. Sangu, K. Kobayashi, A. Shojiguchi, T. Kawazoe, and M. Ohtsu, "Excitation energy transfer and population dynamics in a quantum dot system induced by optical near-field interaction," *J. Appl. Phys.*, vol. 93, pp. 2937–2945, 2003.

[4] T. Kawazoe, K. Kobayashi, S. Sangu, and M. Ohtsu, "Demonstration of a nanophotonic switching operation by optical near-field energy transfer," *Appl. Phys. Lett.*, vol. 82, pp. 2957–2959, 2003.

[5] K. Kobayashi, S. Sangu, A. Shojiguchi, T. Kawazoe, K. Kitahara, and M. Ohtsu, "Excitation dynamics in a three-quantum dot system driven by optical near-field interaction: Toward a nanometric photonic device," *J. Microsc.*, vol. 210, pp. 247–251, 2003.

[6] T. Kawazoe, Y. Yamamoto, and M. Ohtsu, "Fabrication of a nanometric Zn dot by nonresonant near-field optical chemical-vapor deposition," *Appl. Phys. Lett.*, vol. 79, pp. 1184–1186, 2001.

[7] T. Yatsui, M. Ueda, Y. Yamamoto, T. Kawazoe, M. Kourogi, and M. Ohtsu, "Fabrication of nanometric single zinc and zinc oxide dots by the selective photodissociation of adsorption-phase diethylzinc using a nonresonant optical near field," *Appl. Phys. Lett.*, vol. 81, pp. 3651–3653, 2002.

[8] R. Jackson, "Vibrational energy of the monoalkyl zinc product formed in the photodissociation of dimethyl zinc, diethyl zinc, and dipropyl zinc," *J. Chem. Phys.*, vol. 96, pp. 5938–5951, 1992.

[9] R. Schinke, *Photodissociation Dynamics*. Cambridge, U.K.: Cambridge Univ. Press, 1993.

[10] T. Kawazoe, K. Kobayashi, S. Takubo, and M. Ohtsu, "Nonadiabatic photodissociation process using an optical near field," *J. Chem. Phys.*, vol. 122, pp. 024715-1–024715-5, 2005.

[11] K. Kobayashi, S. Sangu, H. Ito, and M. Ohtsu, "Near-field optical potential for a neutral atom," *Phys. Rev. A*, vol. 63, pp. 013806-1–013806-9, 2001.

[12] J. J. Hopfield, "Theory of the contribution of excitons to the complex dielectric constant of crystals," *Phys. Rev.*, vol. 112, pp. 1555–1567, 1958.

[13] A. L. Ivanov, H. Haug, and L. V. Keldysh, "Optics of excitonic molecules in semiconductors and semiconductor microstructures," *Phys. Rep.*, vol. 296, pp. 237–336, 1998.

[14] D. P. Craig and T. Thirunamachandran, *Molecular Quantum Electrodynamics*. New York: Dover, 1998.

[15] Y. Yamamoto, M. Kourogi, M. Ohtsu, V. Polonski, and G. H. Lee, "Fabrication of nanometric zinc pattern with photodissociated gas-phase diethylzinc by optical near field," *Appl. Phys. Lett.*, vol. 76, pp. 2173–2175, 2000.

[16] A. Yariv, *Introduction to Optical Electronics*, 3rd ed. New York: Holt, Rinehart and Winston, 1985.

Kiyoshi Kobayashi was born in Okayama, Japan, in 1953. He received the Dr. Sc. degree in physics from the University of Tsukuba, Tsukuba, Japan, in 1982.

Upon graduation, he joined IBM Japan, as a Researcher with the Tokyo Research Laboratory, Tokyo, Japan. In 1998, he became a Theoretical Group Leader of the Localized Photon project for the Exploratory Research for Advanced Technology (ERATO), Japan Science and Technology Agency (JST). Since 2004, he has been a Professor with the 21 Century Center of Excellence Program, Nanometer-Scale Quantum Physics, Department of Physics, Tokyo Institute of Technology, Tokyo, Japan. His main fields of interest are quantum optical near-field theory and its application to nanophotonics/atom photonics.

Prof. Kobayashi is a member of the Physical Society of Japan, the Japan Society of Applied Physics, the American Physical Society, and the Institute of Electrical, Information and Communication Engineering (IEICE), Japan.

Tadashi Kawazoe was born in Kochi, Japan, in 1967. He received the B.S., M.S., and Ph.D. degrees in physics from the University of Tsukuba, Tsukuba, Japan, in 1990, 1993, and 1996, respectively.

He is a Researcher with Solution Oriented Research for Science and Technology (SORST), Japan Science and Technology Agency (JST). In 1996, he joined the faculty of Engineering, Yamagata University, Yonezawa, Japan, as a Research Associate, engaged in research on nonlinear optical materials and devices. Since April 2000, he has been with the JST. His current research interests are in the areas of optical properties of nanomaterials, optical near field, and nanophotonic devices.

Dr. Kawazoe is a member of the Japan Society of Applied Physics and the Physical Society of Japan.

Motoichi Ohtsu (M'88–SM'90) received the B.E., M.E., and Dr. E. degrees in electronics engineering from the Tokyo Institute of Technology, Tokyo, Japan, in 1973, 1975, and 1978, respectively.

In 1978, he became a Research Associate, and in 1982, he an Associate Professor with the Tokyo Institute of Technology. From 1986 to 1987, while on leave from the Tokyo Institute of Technology, he joined the Crawford Hill Laboratory, AT&T Bell Laboratories. In 1991, he became a Professor with the Tokyo Institute of Technology. In 2004, he moved to the University of Tokyo. Since 1993, he has concurrently been the leader of the Photon Control project of the Kanagawa Academy of Science and Technology. Since 1998, he has concurrently been the leader of the Localized Photon project of the Exploratory Research for Advanced Technology (ERATO). Since 2002, he has been a leader of the national project on Ultrahigh density optical storage, which is sponsored by the Ministry of Economy, Trade, and Industry (METI). He has authored or coauthored over 320 papers. He has authored or coauthored 39 books. He holds 87 patents.

Prof. Ohtsu is a Fellow of the Optical Society of America (OSA). He is a member of several academic societies. In 2000, he was the president of the IEEE Lasers and Electro-Optic Society (IEEE LEOS) Japan Chapter. Since 2000, he has been an executive director of the Japan Society of Applied Physics. In 2001, he served as a Technical Program co-chair for the 4th Pacific Rim Conference on Lasers and Electro-Optics (CLEO/PR01). He has been a tutorial lecturer for The International Society for Optical Engineers (SPIE) and the OSA. He is a member of several boards, such as for the Ministry of Education, culture, Sports, Science, and Technology (MEXT) and METI. He was the recipient of ten prizes presented by academic institutions, including the 1984 I. Koga Gold Medal of the International Scientific Radio Union (URSI), the 1988 IBM Japan Science Award, two awards presented by the Japan Society of Applied Physics (JSAP) in 1982 and 1990, and the 1999 Inoue Science Foundation Award. In 2004, he was the recipient of a Purple Ribbon Medal presented by the Japanese Government.

[II] PRESENTATIONS

IN INTERNATIONAL CONFERENCES

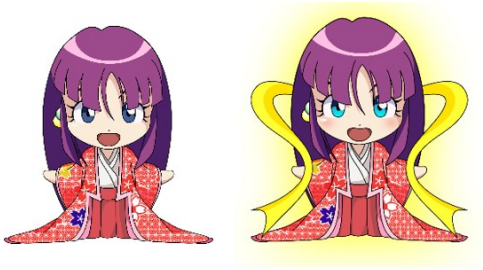

Nanophotonic traceable memory based on energy-localization and hierarchy of optical near-fields

M. Naruse[1,2], T. Yatsui[3], T. Kawazoe[3], Y. Akao[4], and M. Ohtsu[2,3]
[1] New Generation Network Research Center
National Institute of Information and Communications Technology, Tokyo, Japan
[2] School of Engineering, The University of Tokyo, Tokyo, Japan
[3] SORST, Japan Science and Technology Agency, Tokyo, Japan
[4] National Research Institute of Police Science, Chiba, Japan

***Abstract*— Optical near-field interactions allow energy localization at scales smaller than the diffraction limit of light. They also show hierarchical responses, meaning that optical near-fields exhibit different physical behavior at different scales. In this paper, by combining these properties of optical near-fields, that is, energy-localization and hierarchy, we present a novel traceable optical memory that records the event of memory access to each of the bits, which is useful in applications such as high-security information transfer. The basic principle is numerically demonstrated using a metal nanostructure.**

Keywords: optical near-field; nanophotonics; plasmon; metal nanostructure; hierarchy; optical memory; information security

I. INTRODUCTION

Optical near-fields allow localized interactions at scales smaller than the diffraction limit of light [1]. Microscopes and high-density optical memory systems based on optical near-fields have been showing great progress, for instance by engineering nanostructures [2-4]. Furthermore, novel optical signal processing has also been proposed and experimentally demonstrated using quantum dots and optical near-field interactions on the nanometer scale [5, 6].

Such higher integration density, however, is only one of the potential benefits of optical near-fields. For example, the intrinsic hierarchical nature of optical near-fields, meaning that optical near-fields exhibit different physical behavior at different scales, offers another degree-of-freedom for the design of systems [1, 7]. Also, the dissipation process is crucial in utilizing optical near-field interactions. In fact, irreversible signal flow between quantum dots is based on a relaxation process in addition to the near-field interactions [5]. This indicates that certain functionality may be attainable by engineering the energy-dissipating process on a nanometer-scale.

In this paper, by combining these properties of optical near-fields, that is, hierarchy and energy dissipation, we propose a novel traceable optical memory, as schematically shown in Fig. 1. Accesses to this memory will be automatically recorded based on localized energy dissipation, while at the same time, information will be readout based on the hierarchical nature of optical near-fields. These functions will be useful in applications such as high-security information transfer (confidentiality could be ensured) or managing data distribution in content delivery (the distribution of digital content could be physically recorded).

This paper is organized as follows. In Section II, we discuss the basic physical principles of traceable memory. In Section III, we demonstrate an example using a metal nanostructure modeled by finite difference time domain simulations. We conclude the paper in Section IV.

II. PHYSICAL PRINCIPLES

A. Energy localization for recording memory-access events (recording trace)

Localized energy dissipation is applied to recording a memory access. There are several physical principles involved in achieving this function.

The first one is based on the generation of a strong electric-field due to excitation of a plasmon induced in a metal nanostructure [8, 9]. Here, we assume that an electric-field-sensitive material is placed at a position where the strong electric-field will be generated. Now, if a beam of light is irradiated, that optical access excites a plasmon and the induced strong electric-field will cause a physical change in the material. In other words, optical access to the memory is recorded though a plasmon excitation. For example, it is well-known that when we irradiate a bow-tie-shaped metal nanostructure having a small gap between the two wedge-shaped metallic plates, an optical near-field is generated

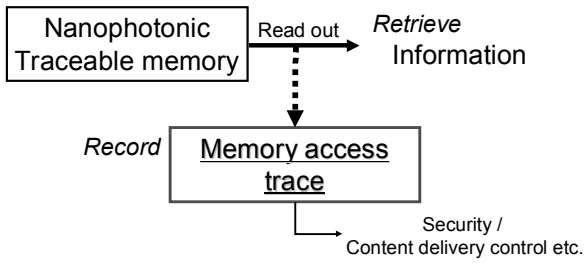

Figure 1. Nanophotonic tracable memory.

between the two apexes due to the interaction of charges concentrated at those points. The intensity of the optical near-field can be enhanced when a plasmon is excited in the metal. This is schematically shown in Fig. 2 (a). Therefore, by placing an electric-field-sensitive material near the gap, an optical access to this structure will be recorded as a physical change in the material.

Another physical principle for localized energy dissipation is based on the irreversible signal flow via optical near-field interactions between quantum dots, which is schematically shown in Fig. 2(b). Here, a larger quantum dot (QD_C) is surrounded by smaller quantum dots, a configuration known as a nanophotonic fountain [10, 11]. Excitons generated in the smaller quantum dots are transferred to the larger one. Its basic operation can be explained by a two-quantum-dot system composed of dots QD_A and QD_C. The ratio of the sizes of QD_A and QD_C is $1:\sqrt{2}$. There is a resonant quantized energy sublevel between those two dots, which are coupled by an optical near-field interaction. This allows the exciton population in the (1,1,1)-level in QD_A to be transferred to the (2,1,1)-level in QD_C [5]. It should be noted that this interaction is forbidden for far-field light. Since the intra-sublevel relaxation via exciton-phonon coupling is fast, the population is quickly transferred to the lower (1,1,1)-level in QD_C, which effectively means that the exciton in QD_A will be transferred to the lower level of QD_C.

What should be noted here is that, if the lower energy level of QD_C is occupied, another exciton cannot be transferred to that level due to the Pauli exclusion principle. This means that the dissipation process at QD_C is crucial to achieve the irreversible signal flow. Therefore, by designing a system so that dissipation in the larger dot may not be blocked, excitons in the smaller dots will be dissipated in the larger dot. Therefore, if we place a material which absorbs the dissipated energy from the QD_C, a certain physical change occurs, and the system thus possesses the capability of recording the energy flow event.

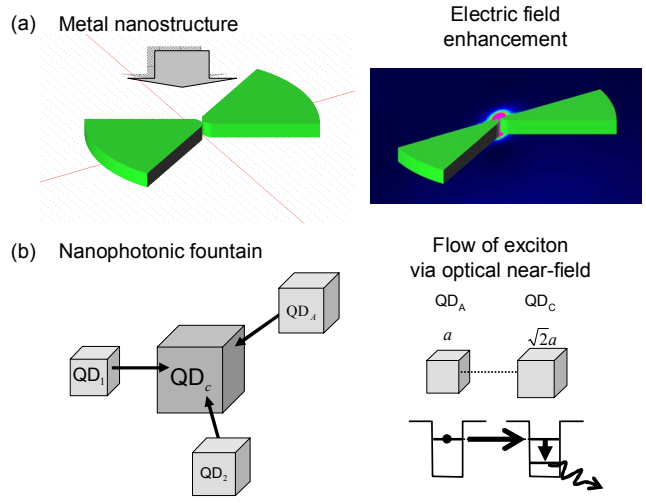

Figure 2. Localized energy dissipation using optical near-field interactions. (a) Excitation of a plasmon in a metal nanostructure. (b) Irreversible flow of exciton via optical neaar-field.

B. *Information hierarchy in optical near-fields*

In addition to the capability of recording the memory-access event described above, the system must store content information, meaning that the system should provide multiple physical states or different output signals, at least two for digital systems. In the following example, we discuss a binary situation, but a multi-valued system is also possible.

To achieve this, we use the hierarchical nature of optical near-fields [7]. As schematically shown in Fig. 3, we can define various kinds of scales in viewing electromagnetic interactions. For example, at a relatively small microscopic scale, which is denoted by "Layer 1" in Fig. 3, local electromagnetic interactions will be observed. On the other hand, by observing the system rather macroscopically, which is denoted by "Layer 2" in Fig. 3, the overall system exhibits behavior that takes account of the structure present in Layer 2. That is, we can observe a kind of hierarchy in optical near-field systems.

In the case of a traceable memory, the issue is to design a system that satisfies the following two conditions simultaneously:

(I) Layer 1 should be capable of indicating a memory trace for each of the physical structures.

(II) Layer 2 should be capable of indicating different digital signals (e.g. bits) of the content information, for example, by different physical structures.

In the case of a bow-tie-shaped metal nanostructure, the local electric field enhancement will occur even if we alter the structure. As numerically demonstrated in detail later in Sec. III, an electric field enhancement on the order of hundreds is maintained even if the structure is altered.

At the same time, the Layer 2 information, which depends on the overall structure of the nanostructure, will be different depending on the alteration made to the nanostructure. Therefore, proper design of the nanostructure can simultaneously satisfy the two conditions (I) and (II).

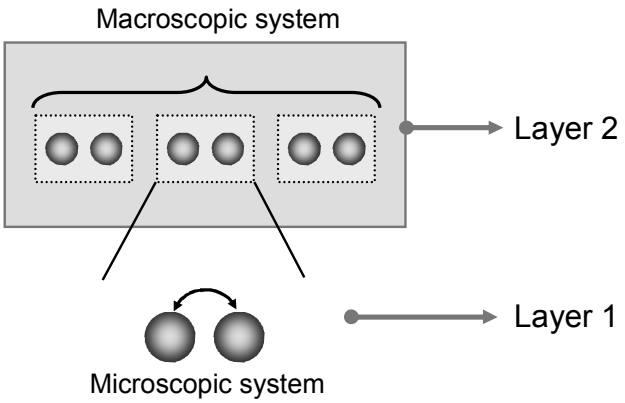

Figure 3. Hierarchy in optical near-field interactions.

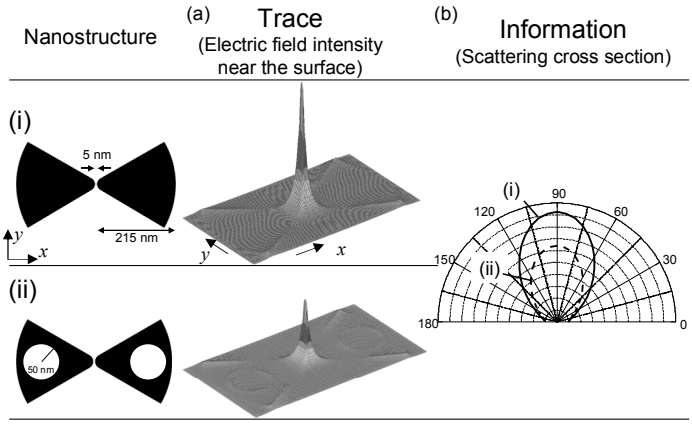

Figure 4. Metal nanostructures for (a) recording memory access traces and (b) information.

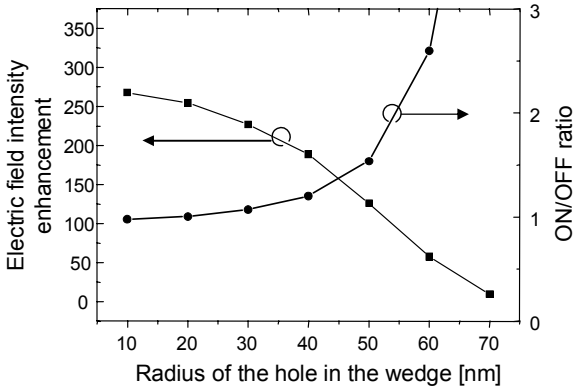

Figure 6. Optimization of the structure: Electric-field intensity enhancment should be high (for trace), and the ON/OFF ratio (for information) should be high by providing circular holes in the metal.

III. EXAMPLES

We demonstrate the principles of the traceable memory shown in Sec. II by using finite-difference time-domain simulations.

Here we assumed a bow-tie-shaped metal nanostructure [9] where two wedge-shaped metal plates are placed facing each other with a small gap between them, as shown in row (i) in Fig. 4. We assumed that the metal was silver, the gap between the two wedges was 5 nm, the horizontal length of one wedge-shaped plate was 215 nm, the radius of curvature of the apex was 20 nm, the angle at the apex was 60 degree, and the thickness was 30 nm. We irradiated a uniform plane wave with a wavelength of 830 nm. The polarization was parallel to the *x* axis in Fig. 4.

Column (a) in Fig. 4 shows the electric field intensity distribution on a plane 5.4 nm away from the metal surface. A strong optical near-field was generated around the gap. The peak intensity was about 250 times larger than that of the incident light. The full-width half-maximum (FWHM) width of the generated strong electric field intensity was about 10 nm in the *x* direction and 23 nm in the *y* direction.

Also, in order to obtain different features in Layer 2, we made two holes in the structure, as shown in row (ii) in Fig. 4, whose radius was 50 nm. The center of each hole was 150 nm away from the center of the gap. A strong optical near-field was still observed, as shown in column (a), where the peak intensity is 122 times as high as the incident light. It was smaller than the case without holes shown in row (i), but it was still the same order of magnitude, namely, hundreds. The FWHM width of the generated strong electric field was nearly equal to that in the case without holes. These results are schematically summarized in Fig. 5, showing that nearly the same characteristics were obtained in terms of the electric field enhancement, or the capability of recording traces.

Equally important, these results show different Layer 2 signals. To analyze this, a scattering cross-section was calculated for each structure, with and without holes. As shown in column (b) in Fig. 4, the scattering cross-section of the structure without holes was nearly twice as large as that with holes. Therefore, it should be possible to easily obtain different signal levels by observing the structures in the far-field or at a scale equivalent to the scale of the entire metal structure.

It is of course possible to obtain the same functional

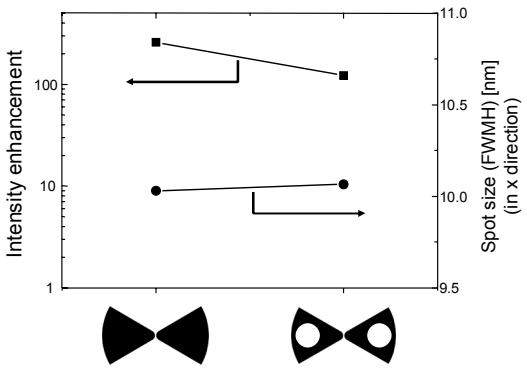

Figure 5. Providing circular-shape holes in the metal wedges does not substantially degrade the localized electric field.

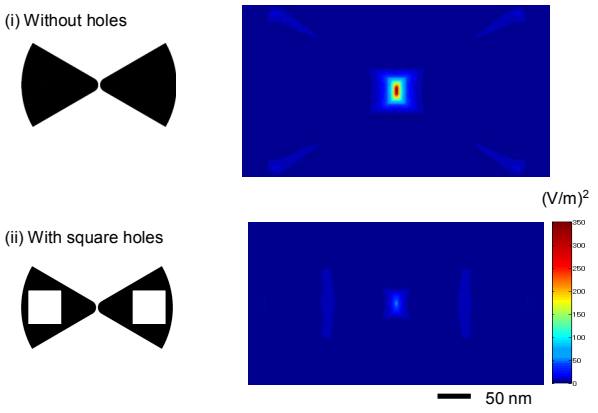

Figure 7. Electric field distribution by a (i) a structure with no holes and (ii) a structure with square-shape holes.

behavior with other shapes and parameters. We tried to optimize the structure to (1) achieve a higher electric enhancement factor, and (2) increase the contrast of the scattering cross-section.

We varied the radius of the holes from 10 nm to 70 nm while maintaining the same center position (150 nm away from the center of the gap.) All other parameters were the same as in the above examples. Fig. 6 shows the results. The electric field enhancement factor increases as the radius of the holes decreases. On the other hand, the scattering cross-section increases as the radius of the holes increases. In Fig. 6, the scattering cross-section is evaluated in terms of an ON/OFF ratio, which is defined as the scattering cross-section without holes divided by that with holes. Therefore, balancing those two conditions determines an optimal structure. A hole radius of 50 nm will satisfy both requirements, that is, increased electric field enhancement and ON/OFF ratio.

The shape of the metal structure is another degree-of-freedom of the traceable memory. As another example, Fig. 7 shows an electric field distribution when we changed the shape of the holes in the wedges from circles to squares of side length 100 nm. In this case, field enhancement was observed around the square-shaped holes in addition to the gap between the wedges. Electric field enhancement at the gap was only as high as 40, which is much smaller than the case of the circles. We believe this is due to the fact that the conditions necessary for exciting the plasmon were substantially destroyed in the case of the square-shaped holes.

IV. CONCLUSION

In summary, we propose a nanophotonic traceable memory. By using localized dissipation of energy based on optical near-field interactions, a memory access event in the memory can be recorded. At the same time, information is read out as a global characteristic of a structure based on the hierarchical nature of optical near-fields. Its principles are verified by finite-element simulations assuming a metal nanostructure. This work offers the possibility of tracing memory accesses, which is potentially useful for security and content delivery applications. We are currently pursuing experimental verification of the fundamental principles described here.

REFERENCES

[1] M. Ohtsu and H. Hori, Near-Field Nano-Optics. Kluwer Academic/Plenum Publishers, New York, 1999.

[2] T. Saiki, S. Mononobe, M. Ohtsu, N. Saito, and J. Kusano, "Tailoring a high-transmission fiber probe for photon scanning tunneling microscope," Appl. Phys. Lett., vol. 68, pp. 2612-2614, May 1996.

[3] T. Yatsui, M. Kourogi, and M. Ohtsu, "Increasing throughput of a near-field optical fiber probe over 1000 times by the use of a triple-tapered structure," Appl. Phys. Lett., vol. 73, pp. 2090-2092, Oct. 1998.

[4] Tineke Thio, K. M. Pellerin, R. A. Linke, H. J. Lezec, and T. W. Ebbesen, "Enhanced light transmission through a single subwavelength aperture," Opt. Lett., vol. 26, pp. 1972-1974, Dec. 2001.

[5] M. Ohtsu, K. Kobayashi, T. Kawazoe, S. Sangu, and T. Yatsui, "Nanophotonics: design, fabrication, and operation of nanometric devices using optical near fields," IEEE J. Sel. Top. Quantum Electron. vol. 8, pp. 839-862, July/Aug. 2002.

[6] M. Naruse, T. Miyazaki, T. Kawazoe, K. Kobayashi, S. Sangu, F. Kubota, and M. Ohtsu, "Nanophotonic computing based on optical near-field interactions between quantum dots," IEICE Trans. Electron., vol. E88-C, pp. 1817-1823, Sep. 2005.

[7] M. Naruse, T. Yatsui, W. Nomura, N. Hirose, and M. Ohtsu, "Hierarchy in optical near-fields and its application to memory retrieval," Optics Express, vol. 13, pp. 9265-9271, Nov. 2005.

[8] R. D. Grober, R. J. Schoelkopf, and D. E. Prober, "Optical antenna: towards a unity efficiency near-field optical probe," Appl. Phys. Lett., vol. 70, Mar. 1997.

[9] T. Matsumoto, T. Shimano, H. Saga, H. Sukeda, and M. Kiguchi, "Highly efficient probe with a wedge-shaped metallic plate for high density near-field optical recording," J. Appl. Phys, vol. 95, pp. 3901-3906, Apr. 2004.

[10] T. Kawazoe, K. Kobayashi, and M. Ohtsu, "Optical nanofountain: A biomimetic device that concentrates optical energy in a nanometric region," Appl. Phys. Lett., vol. 86, pp. 103102-1-3, Mar. 2005.

[11] M. Naruse, T. Miyazaki, F. Kubota, T. Kawazoe, K. Kobayashi, S. Sangu, and M. Ohtsu, "Nanometric summation architecture using optical near-field interaction between quantum dots," Opt. Lett., vol. 30, pp. 201-203, Jan. 2005.

Near-field fabrication of size- and position-controlled ultra-long nanodot chains

T. Yatsui,[*] W. Nomura,[‡] and M. Ohtsu,[*,‡]
** SORST, Japan Science and Technology Agency, 687-1 Tsuruma, Machida, Tokyo, Japan 194-0004*
‡School of Engineering, the University of Tokyo, Tokyo, 7-3-1 Hongo, Bunkyo-ku, Tokyo, Japan 113-8656
yatsui@ohtsu.jst.go.jp

Abstract: We report the self-assembly of a sub-100-nm dot chain, which depends on the photon energy and has a deviation of 5 nm over 100 μm using a novel effect of near-field optical desorption.

OCIS codes: (220.1140) Alignment, (220.4610) Optical fabrication

Future optical transmission systems will require advanced photonic switching device arrays and advanced photonic integrated circuits (ICs) in order to increase data transmission rates and capacity. Consequently, these devices will need to be significantly smaller than conventional diffraction-limited photonic devices. To meet this requirement, we propose a nanometer-scale photonic IC consisting of sub-100-nm scale dots and lines [1]. However, coupling these photonic devices with external conventional diffraction-limited photonic devices requires a nanometer-scale optical waveguide for far/near-field conversion. To realize this, it has been suggested that electromagnetic energy can be guided along a nanodot coupler consisting of chains of closely spaced metallic nanoparticles [2-4]. The energy transfer in the nanodot coupler relies on dipole-dipole coupling between neighboring nanoparticles. To realize a nanodot coupler consisting of 50-nm gold nanoparticles with 50-nm separation, it is estimated that the dispersion of their separation must be as small as 10 nm to obtain an efficiency equivalent to 50% that of an ordered array [2].

To fabricate the nanodot coupler and nanophotonic devices at all scales, we propose a self-assembling method that builds nanodot chains by controlling the desorption with an optical near-field. Our approach is illustrated schematically in Fig. 1(a). A nanodot chain of metallic nanoparticles was fabricated using radio frequency (RF) sputtering under illumination on glass substrate. In order to realize self-assembly, a simple groove 100-nm wide and 30-nm deep was fabricated on the glass substrate. During deposition of the metal, linear polarized light illuminating the groove directly from above (E_{90}) was used to excite a strong optical near-field at the edge of the groove (see Fig. 1(b)), which induced the desorption of the deposited metallic nanoparticles [5]. A metallic dot has strong optical absorption due to plasmon resonance, which strongly depends on particle size. This can induce desorption of the deposited metallic nanodot when it reaches the resonant diameter [5]. As the deposition of metallic dots proceeds, growth is governed by a trade-off between deposition and desorption, which determines dot size, depending on the photon energy of the incident light. Consequently, the metallic nanoparticles should align along the groove (Figs. 1(b) and 1(c)).

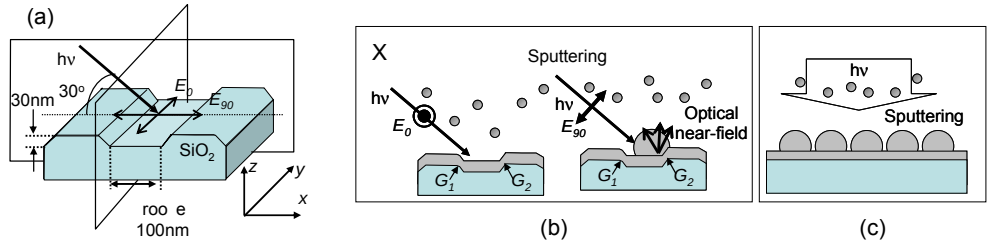

Fig. 1. (a) Size- and position-controlled ultra-long nanodot chain formation. The slanted light had a spot diameter of 1 mm. The groove parallels axis *y*. E_{90} and E_0 are perpendicular and parallel to axis *y*, respectively. (b and c) Cross-sections in planes xz and *yz*, respectively.

Illumination with 2.33-eV light (50 mW) during the deposition of aluminum resulted in the formation of 99.6-nm-diameter aluminum nanodot chains with 27.9-nm separation that were as long as 100 μm in a highly size- and position-controlled manner (Fig. 2(a)). The deviation of both nanodot size and the separation, determined from scanning electron microscopy (SEM) images, was as little as 5 nm. The deviation, which was as small 5%, meets the requirement of the nanodot coupler for an efficiency equivalent to 50% of that of an ordered array. To identify the position of the chain, we compared topographic atomic force microscopy (AFM) images of the surface of the glass

substrate before and after aluminum deposition, at the same position. Curves α and β in Fig. 2(b) show the respective cross-sectional profiles across the groove. Comparison of these profiles showed that the nanodot chain formed around edge G_2. Furthermore, illumination with parallel polarization E_0 along the groove resulted in film growth along the groove structure and no dot structure was obtained. Since the near-field intensity with E_{90} was strongly enhanced at the metallic edge of the groove in comparison with E_0 owing to edge enhancement of the electrical field (see Fig. 1(b)), a strong near-field intensity results in nanodot chain formation. Dot formation at the one-sided edge originates from the asymmetric electric-field intensity distribution, owing to the slanted illumination.

Aluminum-dot chain formation was also observed with RF sputtering of aluminum under illumination with 2.62-eV light (100 mW) with E_{90} using the same grooved (100-nm wide and 30-nm deep) glass substrate, which resulted in the formation of 84.2-nm nanodots with 48.6-nm separation (Fig. 2(c)). Although the deviation of both nanodot size and the separation were as large as 10 nm, the dot size was reduced in proportion to the increase in the photon energy (99.6 nm × (2.33/2.62) = 88.5 nm ~ 84.2 nm). This result indicates that the obtained size is determined by the photon energy and that the size-controlled dot-chain formation originates from photo-desorption of the deposited metallic nanoparticles [5]. The period under 2.62-eV light illumination (132.8 nm) was longer than that (127.5 nm) for fabrication using the 2.33-eV light. However, the ratios of the center-center distance (d) and radius (a) of the nanodots (d/a = 2.56 and 3.15 obtained under 2.33-eV and 2.62-eV light illumination, respectively) are similar to the optimum value, which is in the range of 2.4-3.0, for the efficient transmission of the optical energy along a chain of spherical metal dots calculated using Mie's theory [6]. This is determined by the trade-off between the increase in the transmission loss in the metal and the reduction in the coupling loss between adjacent metallic nanoparticles as the separation increases. Future theoretical analysis, which will include the effect of a continuous metallic film below the nanodot chain, is required to explain the optimum separation of the nanoparticles depending on the photon energy. However, our preliminary results imply that the center-center distance is set at the optimum distance for efficient energy transfer of the optical near-field, given that such a strong optical near-field can induce desorption of the deposited metallic nanoparticles and result in position-controlled dot-chain formation.

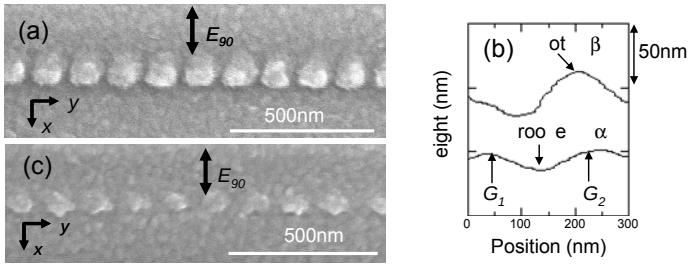

Fig. 2 (a) SEM image of deposited aluminum with perpendicular polarization E_{90} (hυ=2.33 eV). (b) Curves α and β show the respective cross-sectional profiles of AFM images across the groove before and after aluminum deposition, at the same position. (c) SEM image of deposited aluminum with perpendicular polarization E_{90} (hυ=2.62 eV).

Since our deposition method is based on a photo-desorption reaction, illumination at multiple photon energies using a simple lithographically patterned substrate could realize the simultaneous fabrication of size- and position-controlled nanoscale structures with different particle sizes, and with other metals or semiconductors. The use of the self-assembling method with a simple lithographically patterned substrate will dramatically increase the throughput of the production of nanoscale structures, required by future systems.

References

1. M. Ohtsu, K. Kobayashi, T. Kawazoe, S. Sangu, and T. Yatsui, "Nanophotonics: design, fabrication, and operation of nanometric devices using optical near fields," IEEE Journal of Selected Topics in Quantum Electronics **8**, 839-862 (2002).
2. J. R. Krenn et al., "Squeezing the optical near-field zone by plasmon coupling of metallic nanoparticles," Phys. Rev. Lett. **82**, 2590-2593 (1999).
3. S. A. Maier et al., "Local detection of electromagnetic energy transport below the diffraction limit in metal nanoparticle plasmon waveguides," Nat. Mater. **2**, 229-232 (2003).
4. W. Nomura, T. Yatsui, and M. Ohtsu, "Nanodot coupler with a surface plasmon polariton condenser for optical far/near-field conversion," Appl. Phys. Lett. **86**, 181108 (2005).
5. T. Yatsui, S. Takubo, J. Lim, W. Nomura, M. Kourogi, and M. Ohtsu, "Regulating the size and position of deposited Zn nanoparticles by optical near-field desorption using size-dependent resonance," Appl. Phys. Lett. **83**, 1716-1718 (2003).
6. M. Quinten, A. Leitner, J. R. Krenn, and F. R. Aussenegg, "Electromagnetic energy transport via linear chains of silver nanoparticles," Opt. Lett. **23**, 1331-1333 (1998).

Direct observation of optical near-field energy transfer between ZnO nanorod double-quantum-well structures

T. Yatsui,[*] T. Kawazoe,[*] S. Sangu,[†] and M. Ohtsu,[*,‡]
[*] *SORST, Japan Science and Technology Agency, 687-1 Tsuruma, Machida, Tokyo, Japan 194-0004*
+81 42-788-6040, +81 42-788-6031, yatsui@ohtsu.jst.go.jp
[†] *Advanced Technology R&D Center, Ricoh Co., Ltd.,16-1, Shinei-cho, Tsuzuk-kui, Yokohama, Kanagawa, Japan 224-0035*
+81 45-590-1431, +81 45-590-1894
[‡] *School of Engineering, The University of Tokyo, Bunkyo-ku, Tokyo, Japan 113-8656*
+81 3-5841-1189, +81 3-5841-1140

S. J. An, J. Yoo, and G.-C. Yi
National CRI Center for Semiconductor Nanorods and Department of Materials Science and Engineering,
Pohang University of Science and Technology (POSTECH)
San 31 Hyoja-dong, Pohang, Gyeongbuk 790-784, Korea
+82 54-279-2155, +82 54-279-8635

Abstract: We observed nutation in the time-resolved photoluminescence signals from resonantly coupled ZnO double-quantum-well structures via optical near-field energy transfer, in which the period of the nutation was determined to be 550 ps.

OCIS codes: (320.7130) Ultrafast processes in condensed matter, including semiconductors, (260.2160) Energy transfer

Future optical transmission systems will require nanophotonic integrated circuits [1] composed of nanometer-scale dots to increase data transmission rates and capacity. ZnO nanocrystallite is a promising material for realizing room-temperature nanophotonic devices, owing to its large exciton binding energy [2]. Furthermore, the recent demonstration of a semiconductor nanorod quantum-well structure enabled us to fabricate nanometer-scale electronic devices using single nanorods [3]. Recently, ZnO/ZnMgO nanorod single-quantum-well structures (SQWs) were fabricated and the quantum confinement effect was observed successfully [4]. Furthermore, spatially resolved near-field photoluminescence (PL) spectra of individual nanorod ZnO SQWs have been measured using a low-temperature near-field optical microscope (NOM), revealing the valence band anisotropy [5]. To observe the optical interaction between the ZnO quantum structures, we measured the time-resolved near-field PL signals of ZnO double-quantum-well structures (DQWs).

ZnO/ZnMgO DQWs were fabricated on the ends of ZnO nanorods with a mean diameter of 40 nm using catalyst-free metalorganic vapor phase epitaxy [6]. The average concentration of Mg in the ZnMgO layers used in this study was determined to be 20 atm. %. The ZnO well layers, L_w, investigated in this study were 3.5 nm thick and the separation between the ZnO layers was 6 nm, while the thicknesses of the ZnMgO bottom and top barrier

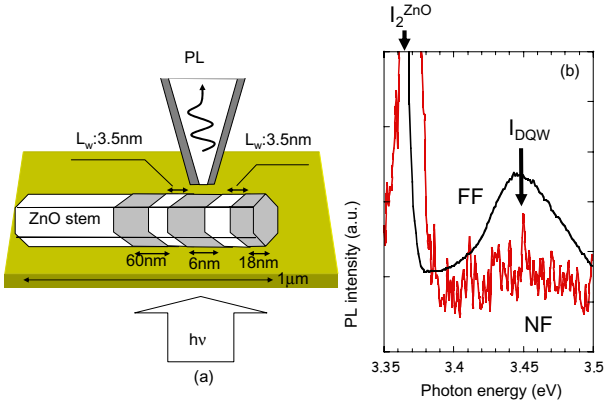

Fig. 1 (a) Schematic of near-field spectroscopy of isolated ZnO DQWs on the ends of ZnO nanorod. (b) Time-integrated far-field (FF) and near-field (NF) PL spectra obtained at 15 K using He-Cd laser (λ=325 nm).

layers in the SQWs were fixed at 60 and 18 nm, respectively. After growing ZnO nanorod DQWs on sapphire (0001) substrate, they were dispersed on the substrate to be isolated. To observe the optical properties of individual ZnO DQWs, we used collection-mode NOM at 15K, using a UV fiber probe with an aperture diameter of 30 nm [Fig. 1(a)]. After determining the position of the DQWs and the emission peak energy of the DQWs using a He-Cd laser (λ=325 nm) [Fig. 1(b)], we obtained time-resolved near-field PL spectra using a 3.450-eV (λ=359.5 nm) second harmonic generation (SHG) of a mode-locked Ti-sapphire laser with a pulse duration of 10 ps for the resonant excitation of the ZnO DQWs.

Figure 2(a) shows the time-resolved near-field PL signals measured at photon energies of 3.365 (I_2^{ZnO}) and 3.450 (I_{DQW}) eV, which correspond to the emission from neutral-donor bound excitons in the ZnO nanorod stem and from excitons confined in the ZnO DQWs, respectively. Both time-resolved near-field PL signals fitted exponential decay curves well. The decay time constants of I_2^{ZnO} and I_{DQW} were found to be 280 and 180 ps, respectively, and are comparable to that of 330 (I_2^{ZnO}) and 170 (I_{SQW}) ps in ZnO nanorod SQWs [4]. Note that an additional peak was observed in the tail of signal of I_{DQW} with a period of 550 ps. We believe that this originated from the nutation between the two resonantly coupled quantum wells via an optical near-field energy transfer [Fig. 2(b)].

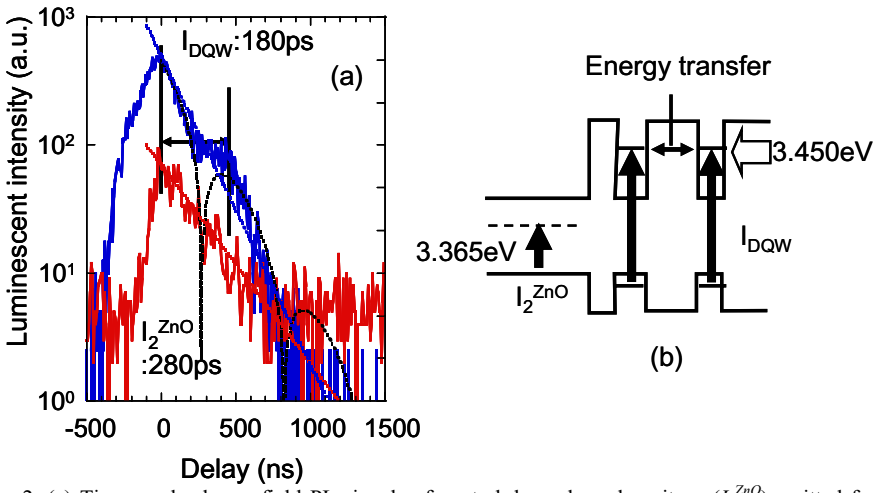

Fig. 2. (a) Time-resolved near-field PL signals of neutral-donor bound excitons (I_2^{ZnO}) emitted form ZnO nanorod stem and excitons emitted from ZnO DQWs (I_{DQW}). (b) Energy diagram of the ZnO nanorod DQWs.

The results shown here provide criteria for designing nanophotonic devices, such as the switching devices confirmed by the authors in CuCl quantum cubes by controlling the dipole forbidden optical energy transfer among resonant energy states in quantum dots [7].

References

1. M. Ohtsu, K. Kobayashi, T. Kawazoe, S. Sangu, and T. Yatsui, "Nanophotonics: design, fabrication, and operation of nanometric devices using optical near fields," IEEE J. Select. Top. Quant. Electron. **8**, 839-862 (2002).
2. A. Ohtomo, K. Tamura, M. Kawasaki, T. Makino, Y. Segawa, Z. K. Tang, G. K. L. Wong, Y. Matsumoto, and H. Koinuma, "Room-temperature stimulated emission of excitons in ZnO/(Mg, Zn)O superlattices," Appl. Phys. Lett. **77**, 2204-2206 (2000).
3. M. S. Gudiksen, L. J. Lauhon, J. Wang, D. C. Smith, and C. M. Lieber, "Growth of nanowire superlattice structures for nanoscale photonics and electronics." Nature **415**, 617-620 (2002).
4. W. I. Park, S. J. An, J. L. Yang, G.-C. Yi, S. Hong, T. Joo, and M. Kim, "Photoluminescent properties of ZnO/$Zn_{0.8}Mg_{0.2}O$ nanorod single-quantum-well structures," J. Phys. Chem. B **108**, 15457-15460 (2004).
5. T. Yatsui et al., "Near-field measurement of spectral anisotropy and optical absorption of isolated ZnO nanorod single-quantum-well structures," Appl. Phys. Lett. **87**, 033101 (2005).
6. W. I. Park, D. H. Kim, S.-W. Jung, and G.-C. Yi, "Metalorganic vapor-phase epitaxial growth of vertically well-aligned ZnO nanorods," Appl. Phys. Lett. **80**, 4232-4234 (2002).
7. T. Kawazoe, K. Kobayashi, S. Sangu, and M. Ohtsu, "Demonstration of a nanophotonic switching operation by optical near-field energy transfer," Appl. Phys. Lett. **82**, 2957-2959 (2003).

Dynamical optical near-field of energy transfers among quantum dots for a nanometric optical buffering

Tadashi Kawazoe[1)], Makoto Naruse[2)], and Motoichi Ohtsu[1,3)]
[1)] *SORST, Japan Science and Technology Agency, Tenkoh building 17-4F, 687-1 Tsuruma, Machida, Tokyo 194-0004, Japan.*
Telephone:+81-42-788-6039, fax:+81-42-788-6031, e-mail: kawazoe@ohtsu.jst.go.jp
[2)] *National Institute of Information and Communications Technology, Koganei, Tokyo 184-8795, Japan.*
[3)] *Department of Electronics Engineering, University of Tokyo, 7-3-1 Hongo, Bunkyo-ku, Tokyo 113-8656, Japan.*

Abstract: We observed energy transfers among quantum dots dynamically. The energy transfer occurs from smaller to larger quantum dots in 150 ps and is applicable to the nanophotonic buffering device.

OCIS codes: (230. 3990) Microstructure devices; (999.9999) Optical Near Field

Energy transfers among quantum dots enable several unique nanophotonic devices, such as an AND-gate [1], NOT-gate [2], an optical nanofountain [3], an optical nano content addressable memory (CAM) [4], and an optical digital to analog converter [5] and so on. Investigations of the energy transfer are essential to construct and optimize these nanophotonic devices. In this paper, we show the experimental results of time-resolved near-field spectroscopy and discuss the energy transfers among quantum dots. The experimental results have indicated the delay time coming from the energy transfer is applicable to the novel optical buffer.

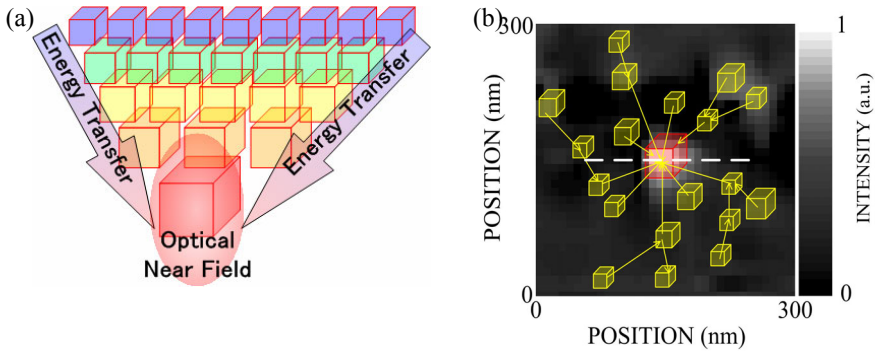

Fig.1. (a) Explanation of the optical nanofountain composing many quantum dots. (b) the two-dimensional near-field scanning image of optical nanofountain.

We have reported energy transfers among quantum dots via an optical near field [6]. The energy transfer occurs from a higher energy level to a lower energy level, *i.e.*, from smaller to larger quantum dots. This unidirectional energy transfer and successive relaxation are applicable to the optical energy concentration. We have called this device an *optical nanofountain*, because its mechanism looks like a fountain, which concentrate and spurt water caught at high potentials. Figure 1 (a) shows a schematic explanation of the optical nanofountain, which is composed of many different-sized quantum dots. When these quantum dots have resonant energy sublevels of carriers, the energy transfer occurs via the optical near field as illustrated by the arrows in Fig. 1(a). Optical energy incident to the optical nanofountain is ultimately concentrated at the largest quantum dot whose size corresponds to the focal spot size of this device. In the experiments, we used CuCl cubic quantum dots embedded in a NaCl matrix. Since this has an inhomogeneous size distribution and a random arrangement of quantum dots, in some areas of the sample, the quantum dots are arranged to act as an optical nanofountain. We maintained the sample temperature at 45 K, as at too low a temperature the resonant condition becomes tight, due to narrowing of the homogeneous linewidth, while at too high a temperature unidirectional energy transfer is obstructed by thermal activation of excitons in the quantum dots. Figure 1 (b) shows the spatial distribution of the output intensity from the optical nanofountain found from the sample with an optical near-field microscope in the collection mode operation. Here, the collected luminescence photon energy was from 3.297 eV to 3.215 eV, which corresponded to the luminescence from 3.1- to 10-nm quantum dots, respectively. The bright spot at the center in the figure

corresponds to the spurt from the optical nanofountain.

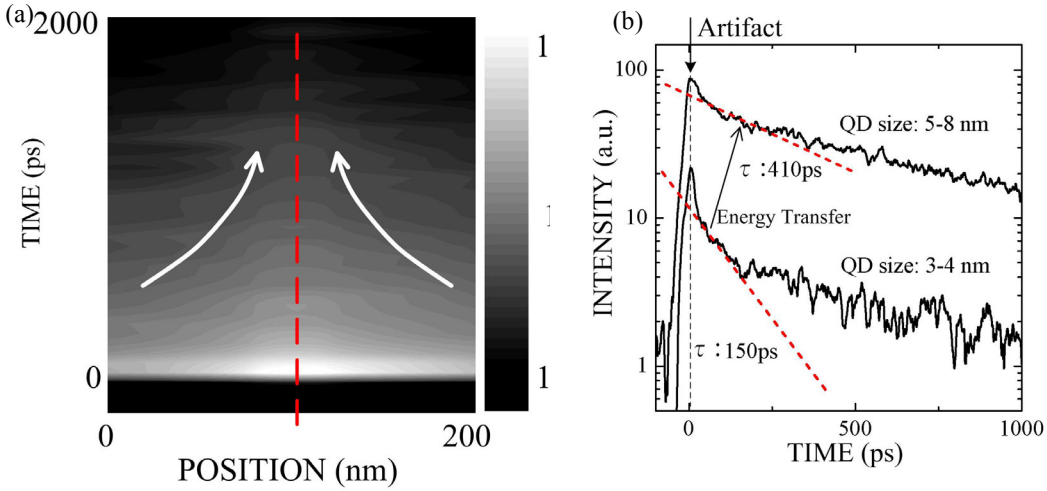

Fig.2. (a)Time evolution of output intensity from the optical nanofountain observed along with the white broken line in Fig.1 (b). (b) Time evolution of output intensity from the optical nanofountain at the spouting spot, *i.e.*, the red broken line.

Figure 2 (a) shows the time evolution of output intensities from the optical nanofountain observed at each position along with the white broken line in Fig.1 (b). Here we used the SHG of mode-locked Ti: sapphire laser (λ=365 nm: pulse duration=2ps: repetition rate=80MHz) as a light source and a micro-channel plate as a photo-detector of the time correlation single photon counting method with a 20-ps time resolution. The signal decay time at the center position (the red broken line) was slower than that of the other positions. This experimental result shows the time-evolution of the energy transfer to the spouting spot of the optical nanofountain, as shown by the two arrows.

Figure 2 (b) shows the time evolution of output intensity from the optical nanofountain at the spouting spot. AT the time origin, the small artifact of the pump pulse was observed and the signal quickly decayed. The radiative life time of quantum dots was proportional to their volume (for example τ=2ns for 3.5-nm quantum dots)[7]. However, the intensity of the smaller quantum dots (QD size: 3-4 nm) decayed faster than the larger quantum dots (QD size: 5-8 nm) and their decay time was 150 ps and 410 ps, respectively, because the excitation energy in the smaller quantum dot transfers to the larger neighboring quantum dot. After 300 ps, both signal decayed with the relaxation time of 700 ps. This relaxation time agrees with the radiative lifetime of the 7-nm CuCl quantum dot [7], which was larger than mean quantum-dot size of the used sample (mean size: 4-nm). Namely, the energy transfers to larger quantum dots accelerate radiative recombination.

These time-resolved experimental results are reasonable to previous works [1-6]. Additionally, we can propose a new nanophotonic device, which is the nanometric optical buffer by using the long recombination lifetime of smaller quantum dot. For example, when 2-nm CuCl quantum dots are used as excitation energy buffers, we preserve the signal for 10 ns. Such long time optical buffering function in nanometric region is only realized by the nanophotonic device using energy transfer and is very important for the nanophotonic system.

[1] T. Kawazoe, K. Kobayashi, S. Sangu, and M. Ohtsu, Appl. Phys. Lett., **82**, 2957 (2003).
[2] T. Kawazoe, K. Kobayashi, and M. Ohtsu, CLEO 2005, CTuF4, May 24 - 26, 2005 in Baltimore, USA.
[3] T. Kawazoe, K. Kobayashi, and M. Ohtsu, Appl. Phys. Lett., **86**(10), 103102 (2005).
[4] M. Naruse, T. Miyazaki, F. Kubota, T. Kawazoe, K. Kobayashi, S. Sangu, M. Ohtsu, Optics Letters, **30**, 201 (2005).
[5] M. Naruse, T. Miyazaki, T. Kawazoe, K. Kobayashi, S. Sangu, F. Kubota, M. Ohtsu, IEICE Trans. on Electron., Vol. E88-C, 1817 (2005).
[6] T. Kawazoe, K. Kobayashi, J. Lim, Y. Narita, and M. Ohtsu, Phys. Rev. Lett. **88**, 067404 (2002).
[7] T. Itoh, T. Ikehara, and Y. Iwabuchi, J. Lumin. **45**, 29 (1990).

Energy transfer in a near-field photochemical process via localized photons dressed by polarons

Kiyoshi Kobayashi,[1] Tadashi Kawazoe,[2] and Motoichi Ohtsu [2,3]
[1] Department of Physics, Tokyo Institute of Technology,
2-12-1-H79 O-okayama, Meguro-ku, Tokyo 152-8551, Japan
[2] SORST, Japan Science and Technology Agency, 687-1 Tsuruma, Machida, Tokyo 194-0004, Japan
[3] Department of Electronics Engineering, University of Tokyo, 7-3-1 Hongo, Bunkyo-ku, Tokyo 113-8656, Japan

Optical near fields and their inherent phenomena have opened a door to imaging and characterization, manipulation and fabrication, photonic functional devices and systems on a nanometer scale. Nanofabrication with a precise control of size and position, however, has been one of the key issues for future device and system applications. Here we propose a new model to clarify a fundamental and important process involved in a near-field photochemical reaction, which leads to a future manipulation and fabrication method of nanostructure.

Localized phonon modes are well known in a one-dimensional (1D) system with open ends, such as 1D glass, nanowire, and nanotube etc., and tend to couple to other localized phonon modes [1]. Due to a large local static lattice distortion, an electron (hole)-phonon interacting system forms a small-polaron state, which is basically a multiphonon state and characterized by strong on-site electron (hole)-phonon correlations [2,3]. Based on such an understanding, we use localized photons dressed by polarons, as quasiparticles, for near-field photochemical reactions. In our model, localized photons dressed by polarons are transferred to a dissociating molecule whose vibrational excitation due to the polaronic nature of the quasiparticle as well as electronic excitation due to the photonic character can be performed.

On the basis of the model, we analyzed anomalous experimental results found that vapor molecules of both diethylzinc (DEZn) and bis(acetylacetonato)-zinc can be dissociated by incident photons with less energy than the dissociation energies of the corresponding molecules only if an optical near field is used. We have obtained a good agreement between the theoretical and experimental results [4,5]. It indicates that the polaronic nature of the quasiparticle plays an important role in a near-field photodissociation process, and that the couplings between the optical near field and molecular vibrations are enhanced to permit a non-resonant photodissociation. This is the unique and suitable property for nanostructure fabrication that cannot be accomplished with a propagating far field.

This work was supported in part by a 21st Century COE program at Tokyo Institute of Technology "Nanometer-Scale Quantum Physics" and by a Grant-in-Aid for Scientific Research from the Ministry of Education, Culture, Sports, Science and Technology, Japan.

References

[1] D. N. Payton, III and W. Visscher, *Phys. Rev.* **156**, 1032 (1967).
[2] T. Itoh, M. Nishijima, A. I. Ekimov, C. Gourdon, Al. L. Efros, and M. Rosen, *Phys. Rev. Lett.* **74**, 1645 (1995).
[3] G. Wellein and H. Fehske, *Phys. Rev. B* **58**, 6208 (1998).
[4] T. Kawazoe, K. Kobayashi, S. Takubo, and M. Ohtsu, *J. Chem. Phys.* **122**, 024715 (2005).
[5] K. Kobayashi, T. Kawazoe, and M. Ohtsu, *IEEE Trans. Nanotechnology*. (2005) in press.

Near-field optical energy transfer of a nanodot coupler with resonant light scattering of Au nanoparticles

W. Nomura,[1] T. Yatsui,[2] and M. Ohtsu[1, 2]

[1] School of Engineering, The University of Tokyo / 7-3-1 Hongo, Bunkyo-ku, Tokyo 113-8656, Japan

[2] "Nanophotonics" team, SORST, Japan Science and Technology Agency

687-1 Tsuruma, Machida, Tokyo 194-0004, Japan

For future optical transmission systems, nanophotonic integrate circuits [1], which are composed of sub-100 nm scale dots, are necessary to increase data transmission rates and capacity. To operate this, coupling them with external conventional diffraction-limited photonic devices is required by using a nanometer-scale optical waveguide for far/near-field conversion. To meet this requirement, we proposed a nanodot copuler with a surface plasmon polariton condenser as the far/near-field conversion device. The nanodot copuler consists of closely spaced metallic nanoparticles, which results in high transmission efficiency owing to the plasmon resonance in the metallic nanoparticles [2]. Furthermore, as a preliminary near-field measurement of nanodot coupler, it was found that the propagation length of the nanodot coupler of 230 nm in diameter was three times longer than that of the metallic core waveguide with a same width [3].

In order to optimize the efficiency in the nanodot coupler, first we checked whether the Au nanoparticles led to efficient scattering. For this purpose, we observed the spatial distribution of the optical near-field intensity for the 50-nm thick Au nanoparticles on the glass in diameter D range from 100 to 300 nm using the collection mode near-field optical microscope (NOM) at λ = 785 nm. The optical near-field intensity takes the maximum for the Au nanoparticle with 200 nm in diameter (open circles in Fig.1 (a)), which was in good agreement with the theoretical resonant diameter 190nm (solid curve in Fig.1 (a)), in which a calculation was performed. Mie's theory of scattering by an Au prolate spheroid and only the first TM mode was considered [4].

Next, we checked the optical near-field energy transfer along the Au nanodot coupler. We observed the optical near-field intensity distribution of linear array of Au nanoparticles in diameter D range from 150 to 300 nm with their separation of 2.4D by the collection mode NOM at λ = 785nm. As shown in Fig. 1(b), the output energy was efficiently obtained only for the nanodot coupler with D = 200 nm (Fig.1 (c)), which is consistent with the experimental results of resonant size for the isolated Au nanoparticles as shown in Fig.1 (a).

These results confirm that it will be possible to create the optical far/near-field conversion devices required by future systems.

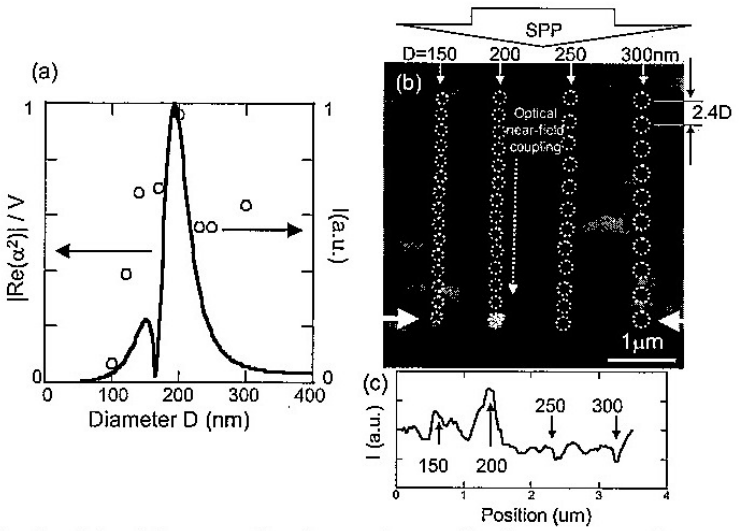

Fig.1 (a) The peak intensity of the respective Au nanoparticles (open circles). The normalized polarizability of Au prolate spheroid (solid curve). (b) Spatial distribution of optical-near field intensity of nanodot coupler. (c) Cross-sectional profile between the solid white arrows in (b).

References

[1] M. Ohtsu, K. Kobayashi, T. Kawazoe, S. Sangu, and T. Yatsui, IEEE Journal of Selected Topics in Quantum Electronics **8**, 839 (2002).

[2] M. L. Brongersma, J. W. Hartmanm and H. A. Atwater, Phys. Rev. B **62**, R16356 (2000).

[3] W. Nomura, M. Ohtsu and T. Yatsui, Appl. Phys. Lett. **86**, 181108 (2005)

[4] H. Kuwata, H. Tamaru, K. Miyano, Appl. Phys. Lett. **83**, 4625 (2003).

Near-field measurement of spectral anisotropy and optical absorption of isolated ZnO nanorod single-quantum-well structures

T. Yatsui,[1] S. Sangu,[2] T. Kawazoe,[1] M. Ohtsu,[1,3] J. Yoo,[4] S. J. An,[4] and G.-C. Yi[4]
[1] SORST, Japan Science and Technology Agency, Machida, Tokyo, Japan.
[2]Advanced Technology R&D Center, Ricoh Co., Ltd., Yokohama, Kanagawa, Japan
[3] School of Engineering, the University of Tokyo, Bunkyo-ku, Tokyo, Japan
[4] National CRI Center for Semiconductor Nanorods and
Department of Materials Science and Engineering, POSTECH, Pohang, Kyungbuk, Korea

ZnO nanocrystallites are promising material for realizing nano-scale photonic devices [1] at room temperature, owing to their large exciton binding energy [2]. Furthermore, ZnO/ZnMgO nanorod heterostructures were fabricated and the quantum confinement effect even from the single-quantum-well structures (SQWs) was successfully observed [3]. Here we report low-temperature near-field spectroscopy of isolated ZnO SQWs.

ZnO/$Zn_{0.8}Mg_{0.2}O$ SQWs (well width of 3.75 nm) were fabricated on the ends of ZnO nanorods with a mean diameter of 40 nm. They were grown vertically from the sapphire (0001) substrate using catalyst-free metalorganic vapor phase epitaxy, in which the ZnO nanorod was grown in the *c* orientation. After growing the ZnO/ZnMgO nanorod SQWs, they were dispersed so that they were laid down on a sapphire substrate to isolate them from each other. We used a collection-mode near-field optical microscope using a He-Cd laser (λ = 325 nm) for excitation, and an apertured (diameter of 30 nm) UV fiber probe. In addition to the PL measurements, absorption spectra were obtained using a halogen lamp.

First, we obtained near-field PL spectra with polarization perpendicular to the *c*-axis. At the ZnO nanorod, the single emission peak was observed at 3.365 eV which correspond to the neutral-donor bound exciton (DOX). However, at the well layer, the emission from DOX was suppressed, while blue-shifted PL emission peak was emerged at 3.444 eV (I_{1a}^{QW}). The value of the blue shift was consistent with the theoretical prediction using finite square-well potential of the quantum confinement effect in the ZnO well layer. The spectral width (3 meV) of peak from the SQWs was much narrower than those of the far-field PL spectra (40 meV). Furthermore, the Stokes shift of 3 meV was much smaller than the reported value (50 meV) in ZnO/ZnMgO superlattices. The small Stokes shift may result from the decreased piezoelectric polarization effect by the fully relaxed strain for the ZnO/ZnMgO nanorod quantum structures in contrast to ZnO/ZnMgO heteroepitaxial multiple layers.

Second, we obtained polarization-dependent near-field PL spectra of isolated ZnO SQWs. In contrast to the near-field PL spectra obtained with perpendicular polarization, a new peak at 3.483 eV (I_{1b}^{QW}) was observed in the PL spectrum with parallel polarization. By considering the valence band anisotropy of ZnO owing to the wurtzite crystal structure and the energy difference between Γ_5 and Γ_1 in the center of the zone around 40 meV for bulk material, emission peaks I_{1a}^{QW} and I_{1b}^{QW} are allowed for the exciton from Γ_5 and Γ_1, respectively. This successful observation of a Γ_1 exciton in PL spectra originates from the enhancement of the exciton binding energy owing to the quantum confinement effect.

The results shown here provide criteria for realizing nano-scale photonic devices, such as the switching devices using near-field energy transfer via resonant energy states among quantum dots [4].

References

[1] M. Ohtsu, et al., *IEEE J. Sel. Top. Quant. Electron.* **8**, 839 (2002).
[2] A. Ohtomo, et al., *Appl. Phys. Lett.* **77**, 2204 (2000).
[3] W. I. Park, et al., *J. Phys. Chem. B* **108**, 15457 (2004).
[4] T. Kawazoe, et al., *Appl. Phys. Lett.* **82**, 2957 (2003).

Fabrication of GaN whiskers using photochemical etching for realizing nanophotonic device

K. Kitamura[1], T. Yatsui[2] and M. Ohtsu[1,2]
[1] School of Engineering, The University of Tokyo
7-3-1, Hongo,Bunkyo-ku, Tokyo 113-8656, Japan,
[2] SORST, Japan Science and Technology Agency
687-1, Tsuruma, Matida-shi, Tokyo 194-0004, Japan

For future optical transmission system, size reduction of the optical devices beyond the diffraction limit is required. As a representative device, nanophotonic switch has been developed, which consists of nano-scale quantum dots with nano-scale separation [1]. To realize this, nano-scale controllability in position and size are required. GaN is a promising material for nanophotonic switch at room temperature because of is large exciton binding energy. To realize position- and size-controlled alignment of GaN nanoparticle, we propose here near-field optical chemical etching of GaN. The controllability in size and position is expected using size selective excitation due to the quantum size effect in GaN nanocrystallite, and using nano-scale template and the subsequent optical near-field distribution, respectively. In order to confirm the promising optical properties of GaN nanostructures, we used a collection-mode near-field optical microscope using a He-Cd laser (λ = 325 nm) for excitation, and a UV fiber probe

First, we performed photochemical etching of GaN film in the solution [HF(50%):H_2O_2(30%)=1:1] under He-Cd laser(λ=325nm) illumination for 30 minutes. Note that the conjugated whiskers of GaN were aligned perpendicular to the incident light polarization (Figs. 1(a) and 1(b)), in which the smallest diameters of whiskers are found to be less than 10nm (Fig. 1(d)). Curve FF_1 in Fig. 2 shows the far-field PL spectra of whiskers. In comparison to the far-field PL from the unetched GaN (FF_0) blue shifted peak due to quantum size effect was observed at 3.62 eV. Next, we obtained near-field PL at several points in conjugated GaN whiskers (curves NF_1~NF_4 in Fig. 2). The high spatial resolution of near-field microscope resulted in the small (10 meV) spectral width, much narrower than those of the far-field PL spectra (100 meV), revealed the diameter distribution from 4 to 10 nm. We will also discuss possibilities of the size selection in the individual GaN whisker depending on the photon energy used for photochemical etching at the session.

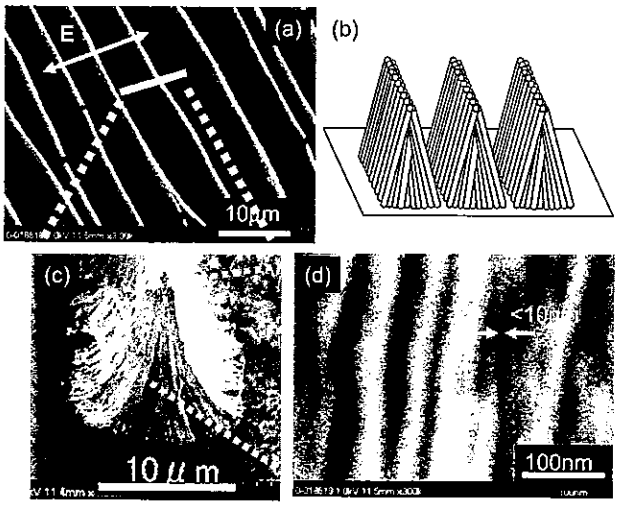

Fig. 1 (a) (b) SEM image and schematic of obtained whiskers. (c) (d) Magnified SEM image of whiskers.

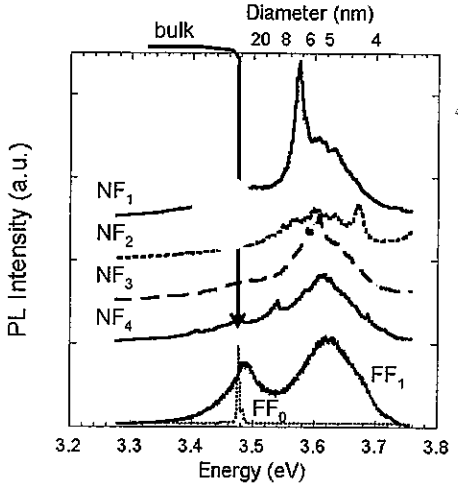

Fig. 2 Far-field (FF_0:unetched substrate, FF_1:etched sub.) and near-field (NF) PL spectra.

References

[1] M. Ohtsu, K. Kobayashi, T. Kawazoe, S. Sangu, and T. Yatsui, *IEEE Journal of Selected Topics in Quantum Electronics* **8**, 839 (2002).

Electroless Nickel Plating under Ultrasonic Irradiation to Fabricate a Scanning Near-Field Optical Microscopy Probe

Yuichi SAITO[1,2], Shuji MONONOBE[4], Ikuhiro KATO[2], Motoichi OHTSU[5], Hideo HONMA[3]
[1]Kanto Gakuin University Surface Engineering Research Institute
4-4-1 Ikeda-cho, Yokosuka-shi, Kanagawa 239-0806, Japan
[2]Graduate School of Engineering, Kanto Gakuin University,
[3]Faculty of Engineering, Kanto Gakuin University
Mutsuurahigashi, Kanazawa-ku, Yokohama 236-8501, Japan
[4]Kunitake "Organization and Function" Research Area, PRESTO, Japan Science and Technology Agency / Kanagawa Academy of Science and Technolog
KSP East 408, 3-2-1 Sakado, Takatsu-ku, Kawasaki 213-0012, Japan
[5] School of Electronics Engineering, University of Tokyo
7-3-1 Hongo, Bunkyo-ku, Tokyo 113-8656, Japan

Generally, a scanning near-field optical microscope (SNOM) probe is fabricated by formation of metal film and removal of metal film from the apex. However, it is difficult to mass-produce SNOM probes by this methods due to the low reproducibility of the metal removal. And this probe with large tip diameter cannot obtain high resolution topography by shear-force feedback technique. To achieve high resolution topography, the metal film thickness of probe gradually decreases to a few tens of nanometers toward the apex.

We have proposed a new method to achieve mass production and high resolution topography. This method applied electroless nickel plating under ultrasonic irradiation for mass production and high resolution topography.[1]

Fig. 1 shows scanning electron micrographs of magnified top regions of the fabricated probe plated with ultrasonic irradiation and entirely coated probe plated without ultrasonic irradiation, respectively. The white lines represent the cross-sectional profiles of the tapered fibers. In Fig. 1(a), the thickness of metal film gradually decreases toward the apex. This result indicates effectiveness of electroless nickel plating under ultrasonic irradiation as a probe fabrication. In summary, we succeeded in fabricating a nickel-coated probe that have high resolution SNOM / shear-force microscopy.

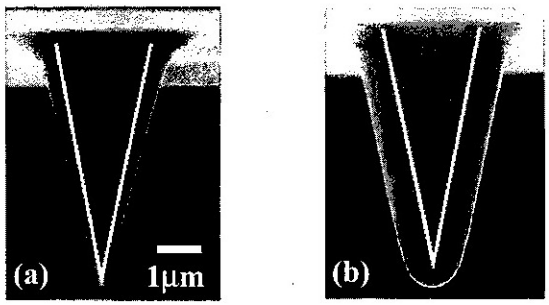

Fig.1 Scanning electron micrographs of magnified top views of the fabricated probes by electroless plating under ultrasonic irradiation.
(a) 1MHz ultrasonic irradiation, (b) without ultrasonic irradiation

Acknowledgement

This work was supported by "High-Tech Research Center" project for Private Universities; matching fund subsidy from MEXT(Ministry of Education, Culture, Sports, Science and Technology),2005-2010

Reference

[1] S. Mononobe, Y. Saito, M. Ohtsu, and H. Honma, Jpn. J. Appl. Phys. 43, 2862(2004).

Nanofabrication using Nonadiabatic Near-field Photolithography

Tadashi Kawazoe1, Hiroki Yonemitsu[2], and Motoichi Ohtsu[1, 2]
[1]Japan Science and Technology Agency, Machida, Tokyo 194-0004, Japan
[2]Department of Electronics Engineering, University of Tokyo, Bunkyo-ku, Tokyo 113-8656, Japan

We have studied the application of optical near field to nanostructure fabrication using its novel properties, *e.g.*, higher resolution than diffraction limit and unique photochemical reaction [1]. This unique photochemical reaction is called a nonadiabatic photochemical reaction [1], and can be explained by the exciton-phonon polariton (EPP) model [2, 3]. In the previous work of Chemical Vapor Deposition, we demonstrated the unique photodissociation involving multiple-step excitation via molecular vibration modes based on EPP model. In this paper, we have applied this nonadiabatic photochemical reaction to photolithography. Here, we call this novel method of photolithography "*Nonadiabatic Near-Field Photolithography*".

Recently, to satisfy the demand for mass production of photonic and electronic devices, various methods of nanofabrication are contrived. Among all, nonadiabatic photolithography is widely useful because it enables conventional photolithographic components and systems for nanofabrication beyond the diffraction limit of light. The wave properties of light can cause problems for nanometric photolithography, including not only the diffraction limit, but also coherency and polarization dependence. In photolithography of high-density nanometric arrays, the optical coherent length is longer than their separation between adjacent corrugations, even when an Hg lamp is used, and there is not enough photoresist absorption to suppress fringe interference of scattered light. The transmission intensity of light passing through a photo-mask strongly depends on its polarization, so the design of photo-mask structures must include such effects. The largest advantage of nonadiabatic photolithography is free from these problems coming from wave properties of light.

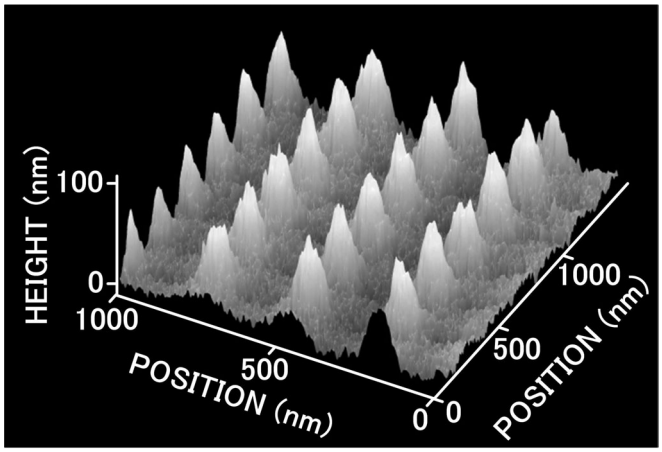

Fig.1. AFM images of photoresist (TDMR-AR87) exposed by g-line after development.

By using the nonadiabatic near-field photolithography, we obtained the nano-structures as shown in Fig.1, which is AFM image of photoresist (TDMR-AR87) after the development. This photoresist was optimized for the light of i-line (365 nm) and its photosensitivity for a g-line light of Hg (436 nm) was very low. However, two dimensional arrays of nano-dots appeared clearly. Their height and width (FWHM) were 100 nm and 70 nm, respectively. The sizes of fabricated structures were smaller than the diffraction limit, since the photoresist was exposed by the optical near-field. In a presentation, we will show the experimental results, which indicate the advantages of the nonadiabatic near-field photolithography.

A part of this work was supported by "Nanotechnology Support Project" of the Ministry of Education, Culture, Sports, Science and Technology (MEXT), Japan.

References

[1] T.Kawazoe, Y. Yamamoto, and M. Ohtsu, Appl. Phys. Lett., **79**, 1184, (2001).
[2] T.Kawazoe and M. Ohtsu, Proceeding of Spie, **5339**, 624, (2004).
[3] T. Kawazoe, K. Kobayashi, S. Takubo, and M. Ohtsu J. Chem. Phys., **122**, 024715, (2005).

From optical near-field interaction to nanophotonic information systems

Makoto Naruse*[a], Tetsuya Miyazaki[a], Tadashi Kawazoe[b], Takashi Yatsui[b], Suguru Sangu[c], Kiyoshi Kobayashi[d], and Motoichi Ohtsu[b,e]
[a]National Institute of Information and Communications Technology
[b]Japan Science and Technology Agency
[c]Ricoh Co. Ltd.
[d]Tokyo Institute of Technology
[e]The University of Tokyo

ABSTRACT

Here we show our architectural approaches to nanophotonics to benefit from unique physical properties obtained by local interactions between nanometric elements, such as quantum dots, via optical near fields, that provide ultra high-density integration capability beyond the diffraction limit of light. We discuss a memory-based architecture and a simple hierarchical architecture. By using resonant energy levels between quantum dots and inter-dot interactions, nanometric data summation and broadcast architectures are demonstrated including their proof-of-principle experimental verifications using CuCl quantum dots. Through such architectural and physical insights, we are seeking nanophotonic information systems for solving the integration density limited by diffraction limit of light and providing ultra low-power operations as well as unique functionalities which are only achievable using optical near-field interactions.

Keywords: nanophotonics, optical near-field, quantum dot, information and communications systems, hierarchical system

1. INTRODUCTION

To accommodate the continuously growing amount of digital data handled in information and communications systems[1], optics is expected play a wider role in enhancing the overall system performance by performing certain functional behavior[2] in addition to merely serving as the communication medium. In this regard, for example, so-called all-optical packet switching has been thoroughly investigated. Also, the application of inherent optical features, such as parallelism, in computing systems has been investigated[3, 4]. However, many technological difficulties remain to be overcome in order to adopt optical technologies in critical information and communication systems: one problem is the poor integrability of optical hardware due to the diffraction limit of light, which is much larger than the gate width in VLSI circuits, resulting in relatively bulky hardware configurations.

Nanophotonics, on the other hand, which is based on local interactions between nanometer-scale elements, such as quantum dots, via optical near fields, provides ultrahigh-density integration since it is not constrained by the diffraction limit[5]. From an architectural perspective, this drastically changes the fundamental design rules of functional optical systems. Consequently, suitable architectures may be built to exploit this capability of the physical layer. In this paper, we approach nanophotonics from a system architecture perspective, considering the unique physical principles provided by optical near-field interactions and the functionality required for practical applications.

This paper deals with two architectures utilizing several physical properties provided by nanophotonics. First in Sec. 2, we discuss a memory-based architecture in which a large lookup table is recorded by configuring the size and positions of quantum dots, as well as individually implementing the required logical operation mechanisms for each table entry. Two basic functions are derived from this architecture. One is a data gathering, or summation, mechanism suitable for similarity evaluation, which is discussed in Sec. 3. As an extension of this summation architecture, Sec. 3 also discusses digital-to-analog conversion by configuring the coupling strength between QDs. The other basic function is broadcasting where query data is distributed to multiple table entries, as described in Sec. 4. We will present enabling architectures by appropriate use of resonant energy levels between quantum dots and inter-dot interactions via optical

* naruse@nict.go.jp; phone 81 42 327 6794; fax 81 42 327 7035

Nanophotonics for ommunication: Materials and e ices II, edited by Nibir . har, Achyut . utta, iyoshi Asaka a,
Proc. of SPIE Vol. 6017, 601701, (2005) · 0277-786X/05/$15 · doi: 10.1117/12.632748

near-fields that are forbidden for far-field light. Experimental results are also shown using CuCl quantum dots. In Sec. 5, we will discuss hierarchical systems that use the different natures of light exhibited in optical near fields and far fields. The overall structure of this paper is outlined in Fig. 1. Through such architectural and physical insights, we seek nanophotonic information and communications systems that can overcome the integration-density limit imposed by the diffraction limit of light with ultralow-power operation as well as unique, or silicon-complement, functionalities which are only achievable using optical near-field interactions.

2. NANOPHOTONIC COMPUTING ARCHITECTURE BASED ON HIGH-DENSITY TABLE LOOKUP

This section discusses the overall processing architecture. We begin with a concrete example of a packet forwarding application, which is an important function in routers. In this application, the output port for an incoming packet is determined based on a routing table. For such functions, a content addressable memory (CAM)[6] or its equivalent is used; in a CAM, an input signal (content) serves as a query to a lookup table, and the output is the address of data matching the input. All optical means for implementing such functions have been proposed, for instance, by using planar lightwave circuits[7]. However, since we need separate optical hardware for each table entry if based on today's known methods, if the number of entries in the routing table is on the order of 10,000 or more, the overall physical size of the system becomes unfeasibly large. On the other hand, by using diffraction-limit-free nanophotonic principles, huge lookup tables can be configured compactly.

First, we begin by relating the table lookup problem to an inner product operation. We assume an N-bit input signal $\boldsymbol{S} = (s_1,...,s_N)$ and reference data $\boldsymbol{D} = (d_1,...,d_N)$. Here, the inner product $\boldsymbol{S} \bullet \boldsymbol{D} = \sum_{i=1}^{N} s_i \bullet d_i$ will provide a maximum value when the input perfectly matches the reference data. However, the inner product alone is, in fact, not sufficient to

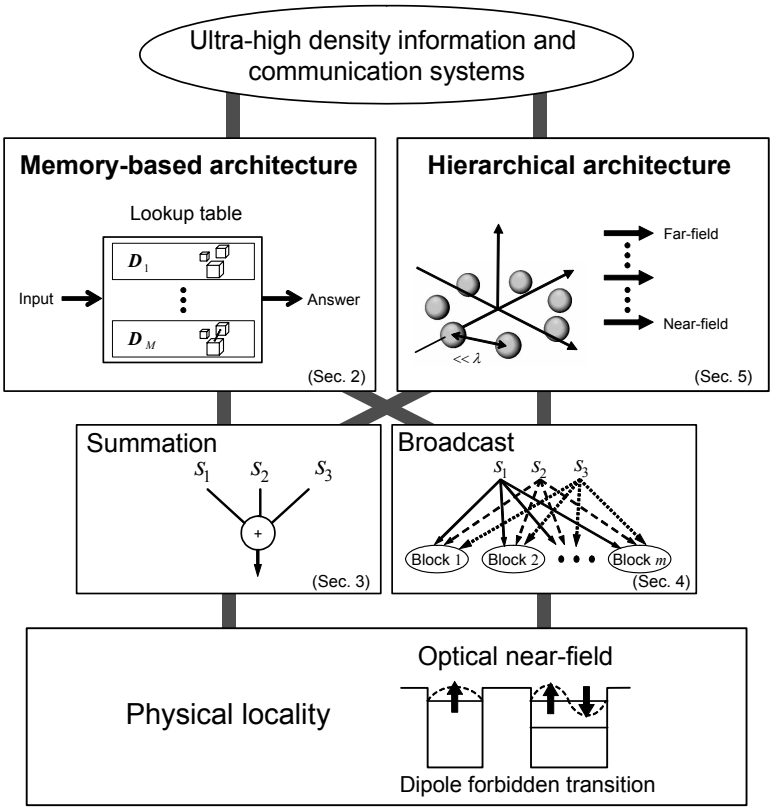

Fig. 1 Examples of system architectures utilizing the physics of nanophotonics, showing a memory-based architecture and a hierarchical architecture.

determine correct matching of the input and reference. This can be demonstrated as follows. Assume, for example, a 4-bit input $\boldsymbol{S} = (1010)$ and two items of reference data $\boldsymbol{D}_1 = (1010)$ and $\boldsymbol{D}_2 = (1110)$. Both inner products result in a value of 2, but the correctly matching data is only $\boldsymbol{D}_1$. Thus, the exclusiveness of the matching operations must also be considered. Correct matching can be achieved by also calculating the inner product of the *inverted* input signal and reference data. However, inversion is a difficult function to implement optically. One possible option is to properly design the modulation format[8], for instance, by representing a logical level by two digits, such as Logic 1="10" and Logic 0="01". Then, an N-bit logical input is physically represented by 2N bits, which makes the inner product equivalent to the matching operation.

For packet data transfer, an operation known as longest prefix matching is important[9]. In this operation, a "don't care" state is required. In the format described above, it can be simply coded by "11". Then, the resultant multiplication of a don't-care bit with an input bit will be 1 for either Logic 0 or 1.

Suppose that the reference data in the memory $\boldsymbol{D}_j$ $(j = 1,...,M)$ and the input $\boldsymbol{S}$ are represented in the above format. Then, the function of the CAM will be to derive j that maximizes $\boldsymbol{S} \bullet \boldsymbol{D}_j$. A nanophotonic implementation of such a function can be implemented in a highly dense form, as shown in Sec. 3. In addition, a large array of such inner product operations will allow a massively parallel processing system to be constructed.

Consequently, multiple inner products are equivalent to a matrix-vector multiplication, which is capable of implementing a wide range of parallel computations[4]. As a simple example, digital-to-analog conversion will be demonstrated by tuning the near-field interaction strength, as discussed in Sec. 3.2.

Furthermore, arbitrary combinational logic can be reformulated as a table lookup operation; more specifically, any computation is equivalent to performing a lookup in a table where all possible input/answer combinations are pre-recorded. For example, consider a two-input, two-bit ADD operation, $\boldsymbol{A}$+$\boldsymbol{B}$. In the ADD operation, the third-bit of the output (the carry bit) should be logical 1 when the second bits (that is, the 2^1 bit positions) of both inputs are 1, regardless of their first bits, that is, when ($\boldsymbol{A}$, $\boldsymbol{B}$) = (1*, 1*). Therefore, following the data representation format introduced above (Logic 1 = 10, Logic 0 = 01, and don't care = 11), the table lookup entry $\boldsymbol{D}$ should be (10111011), so that any input combination satisfying ($\boldsymbol{A}$, $\boldsymbol{B}$) = (1*, 1*) will provide a maximum inner product $\boldsymbol{S} \bullet \boldsymbol{D}$. This procedure is summarized in Fig. 2(a).

3. DATA SUMMATION USING NEAR-FIELD INTERACTIONS

3.1 Data gathering mechanism

As discussed in Sec. 2, the inner product operations are the key functionality of the present architecture. The multiplication of two bits, namely $x_i = s_i \bullet d_i$, has already been demonstrated by a combination of three quantum dots[10, 11]. Therefore, one of the key operations remaining is the summation, or data gathering scheme, denoted by Σx_i, where all data bits should be taken into account.

In known optical methods, wave propagation in free-space or in waveguides, using focusing lenses or fiber couplers, for example, well matches such a data gathering scheme because the physical nature of propagating light is inherently suitable for global functionality such as global summation. However, the level of integration of these methods is restricted due to the diffraction limit of light. In nanophotonics, on the other hand, the near-field interaction is inherently physically local, although functionally global behavior is required.

Here we implement a global data gathering mechanism, or summation, based on the uni-directional energy flow via an optical near field, as schematically shown in Fig. 2(b), where surrounding excitations are transferred towards a quantum dot QD_C located at the center[12, 13]. As a fundamental case, we assume two quantum dots QD_A and QD_B, as shown in Fig. 2(c). The ratio of the sizes of QD_A and QD_B is $1:\sqrt{2}$. There is a resonant quantized energy sublevel between those two dots, which are coupled by an optical near-field interaction[10, 11, 14], which allows the exciton population in the (1,1,1)-level in QD_A to be transferred to the (2,1,1)-level in QD_B[10, 14]. It should be noted that this interaction is forbidden for far-field light[15]. Since the intra-sublevel relaxation via exciton-phonon coupling is fast, the population is quickly transferred to the lower (1,1,1)-level in QD_B. Similar energy transfers may take place among the resonant energy levels in the dots surrounding QD_C so that energy flow can occur. One may worry that if the lower energy level of QD_B is occupied, another exciton cannot be transferred to that level due to the Pauli exclusion principle. Here, thanks again to the nature of the optical near-field interaction, the exciton population goes back and forth in the resonant energy level between QD_A and QD_B, a phenomenon which is known as optical nutation[10, 11, 14]. Finally, both excitons can be transferred to

QD_B. The lowest energy level in each quantum dot is coupled to a free photon bath to sweep out the excitation radiatively. The output signal is proportional to the (1,1,1)-level population in QD_B.

Numerical calculations were performed based on quantum master equations in the density matrix formalism. The model Hamiltonian of the two dots is given by

$$H = \hbar \begin{pmatrix} \Omega_A & U \\ U & \Omega_B \end{pmatrix} \tag{1}$$

where $\hbar U$ is the optical near field interaction, and $\hbar\Omega_A$ and $\hbar\Omega_B$ respectively refer to the eigenenergies of QD_A and QD_B. For a two-exciton system, we can prepare seven states, as summarized in Fig. 2(d), where one or two excitons occupy either one or two levels among the (1,1,1)-level in QD_A (denoted by A), the (2,1,1)-level in QD_B (denoted by B2), and the (1,1,1)-level in QD_B (denoted by B1). These seven states are interconnected either by inter-dot near-field coupling (U), exciton-phonon coupling (Γ), or relaxation to the radiation photon bath (γ_A for QD_A and γ_B for QD_B). Within the Born-Markov approximation of the Liouville equation[14-16], we can derive multiple differential equations. In the following we assume $U^{-1} = 50$ ps, $\Gamma^{-1} = 10$ ps, $\gamma_A^{-1} = 2\sqrt{2}$ ns, and $\gamma_B^{-1} = 1$ ns as a typical parameter set.

First we consider an initial condition where there are two excitons in the system: one in QD_A and the other in QD_B (two-exciton system). The population of the (1,1,1)-level in QD_B corresponds to the output signal, which is composed of three states indicated by (i), (ii), and (iii) in Fig. 2(d). The populations for those three bases, which are diagonal elements of the density matrix, are respectively denoted by $\rho_{A,B1}(t)$, $\rho_{B1,B2}(t)$, and $\rho_{B1}(t)$, the first two of which, $\rho_{A,B1}(t)$ and $\rho_{B1,B2}(t)$, are related to the two-exciton dynamics of the system. They respectively show the time evolution of the one-exciton population in QD_A or in the upper level of QD_B, in addition to an exciton in the lower level of QD_B. The time evolution of $\rho_{A,B1}(t) + \rho_{B1,B2}(t)$ is shown by the solid curve in Fig. 2(e). The other population, $\rho_{B1}(t)$, has just one exciton in B1, and so it represents the output evolution of the one-exciton system, which is shown by the dashed curve in Fig. 2(e). Incidentally, the population when QD_A has an exciton, namely the sum of the populations related to bases (i), (iv), and (v) in Fig. 2(d), is denoted by the dotted curve in Fig. 2(e). Nutation is observed as expected since the lower level of QD_B is likely to be busy and the inter-dot near-field interaction is faster than the relaxation bath coupling at each dot.

We then compare the population dynamics between one- and two-exciton systems. The dotted curve in Fig. 2(f) shows

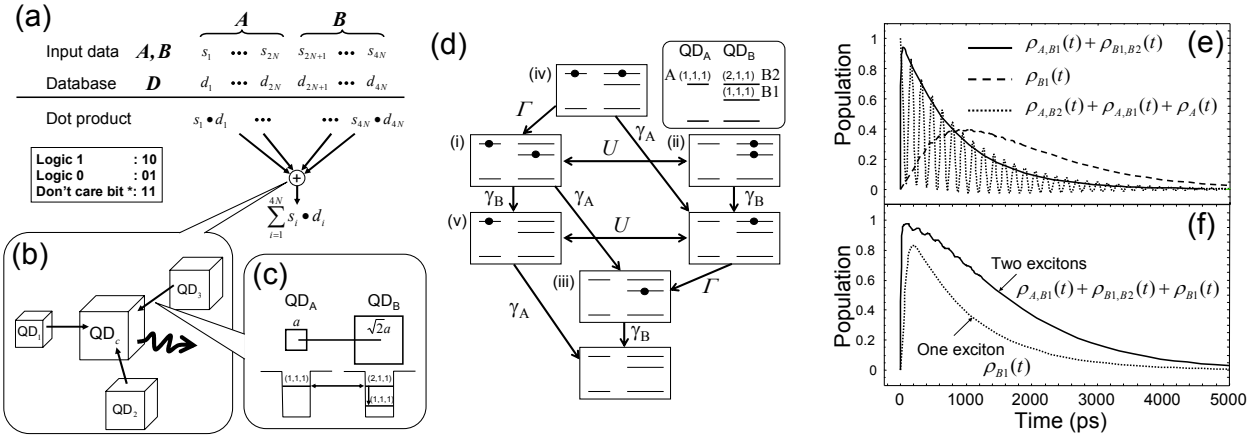

Fig. 2 (a) Inner product operation as a table lookup. (b) Summation mechanism in quantum dots. (c) Inter-dot interaction via an optical near-field. (d) Bases of two-exciton system in two quantum dots coupled by optical near fields. (e) Time evolution of the population in a two-exciton system. (f) Population comparison between one- and two-exciton systems.

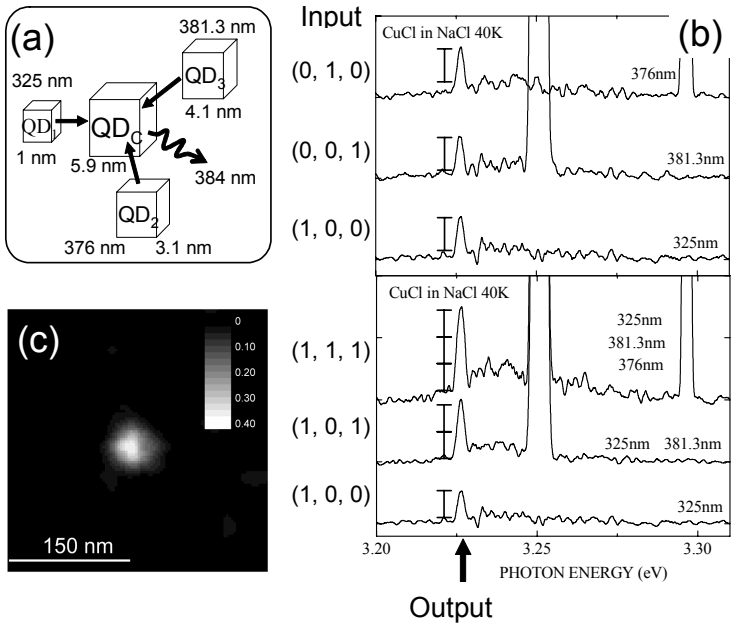

Fig. 3 Experimental results of the nanometric summation. (a) A quantum dot arrangement. (b) Luminescence intensity for three different numbers of excited QDs. (c) Spatial intensity distribution of the output photon energy.

the time evolution of the population in the lower level of QD_B, where, as initial conditions, one exciton exists only in QD_A. The solid curve in Fig. 2(f) is that for the two-exciton system. Physically the output signal is related to the integration of the population in the lower level of QD_B. Numerically integrating the population between 0 and 5 ns, we can obtain the ratio of the output signals between the two- and one-exciton systems as 1.86:1, which reflects the number of initial excitons. This is the summation mechanism.

A proof-of-principle experiment was performed to verify the nanoscale summation using CuCl quantum dots in a NaCl matrix, which has also been employed for demonstrating nanophotonic switches[10] and optical nano-fountains[13]. We selected a quantum dot arrangement where small QDs (QD_1 to QD_3) surrounded a "large" QD at the center (QD_C), as schematically shown in Fig. 3(a). Here, we irradiate at most three light beams with different wavelengths, 325 nm, 376 nm, and 381.3 nm, which respectively excite the quantum dots QD_1 to QD_3 having sizes of 1 nm, 3.1 nm, and 4.1 nm, respectively. The excited excitons are transferred to QD_C, and their radiation is observed by a near-field fiber probe. Notice the output signal intensity at a photon energy level of 3.225 eV in Fig. 3(b), which corresponds to a wavelength of 384 nm or a QD_C size of 5.9 nm. The intensity varies approximately as 1:2:3 depending on the number of excited QDs in the vicinity, as observed in Fig. 3(b). The spatial intensity distribution was measured by scanning the fiber probe, as shown in Fig. 3(c), where the energy is converged at the center. Hence, this architecture works as a summation mechanism, counting the number of input channels, based on exciton energy transfer via optical near-field interactions.

Such a quantum-dot-based data-gathering mechanism is also extremely energy efficient compared to other optical methods such as focusing lenses or optical couplers. For example, the transmittance between two materials with refractive indexes n_1 and n_2 is given by $4n_1n_2/(n_1+n_2)^2$; this gives a 4% loss if n_1 and n_2 are 1 and 1.5, respectively. The transmittance of an N-channel guided wave coupler is 1/N from the input to the output if the coupling loss at each coupler is 3 dB. In nanophotonic summation, the loss is attributed to the

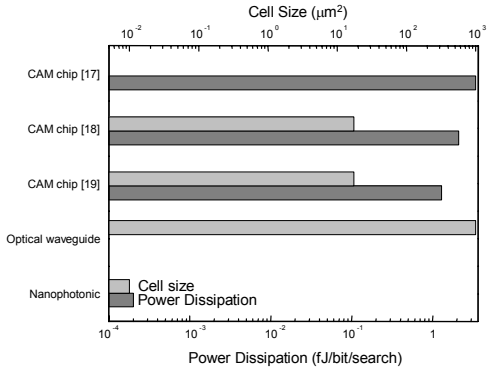

Fig. 4 Power dissipation and cell size comparison with electrical CAM VLSI chips and optical waveguides.

dissipation between energy sublevels, which is significantly smaller. Incidentally, it is energy- and space-efficient compared to electrical CAM VLSI chips[17-19], as shown in Fig. 4.

We should also note, in terms of interconnections, that the input data should be commonly applied to all lookup table entries, which allows another possible interconnection mechanism. Since the internal functionality is based on energy transfer via optical near-field interactions and it is forbidden for far-field light, global input data irradiation, that is, broadcast interconnects, via far-field light may be possible; this is discussed in Sec. 4.

3.2 Digital-to-analog conversion using near-field interactions

In the summation mechanism shown in Sec. 3.1, the coupling strengths between the input QDs and the output QD are uniform. However, these coupling strengths can be independently configured, for instance, by modifying the relative distances. Theoretically, this corresponds to configuring U of the Hamiltonian in eq. (1). For instance, consider three input QDs, QD_0 to QD_2, as schematically shown in Fig. 5(a). By choosing U^{-1} of 410 ps, 240 ps, and 50 ps between QD_0 to QD_2 and the output QD, respectively, the simulated time evolution of the output population is as shown in Fig. 5(b). The time integrals of the output populations originating from QD_0 to QD_2 between 0 and 5 ns are approximately in a ratio of 1:2:4. This leads to a digital-to-analog conversion formula given by

$$d = 2^0 s_0 + 2^1 s_1 + 2^2 s_2 \tag{2}$$

where d is the output, and s_0, s_1, and s_2 represent the presence/absence of excitations in QD_0 to QD_2, respectively. Here each of the inputs s_i is optically applied to the system, whose frequency is resonant with the (1,1,1)-level in QD_i. It should be noted that they are not coupled to the other QDs (i.e., input QD_j $(j \neq i)$ and the output QD) since the corresponding energy levels are optically forbidden for the other QDs. Also, the initial state of the system is considered to be one in which an exciton is excited at each dot.

In the experiment, CuCl QDs in a NaCl matrix were used, as in Sec. 3.1, and three different input light frequencies were assigned to the three-bit input. Here, the output signal is considered to be the radiative relaxation from the lowest energy level of the output QD, which is observed with a near-field fiber probe at a wavelength of 384 nm. One remark here is that not every excited exciton produces the output signal; for instance there will be loss due to relaxation at each of the input QDs when the output energy level is occupied. However, such effects may not be serious since, as discussed in Sec. 3.1, nutation occurs among resonant energy levels and the relaxation rate at the output QD, which is the largest

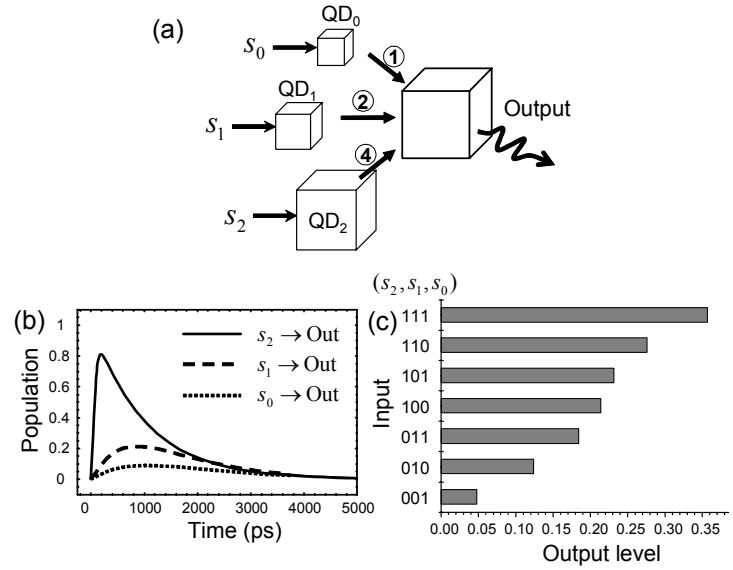

Fig. 5 (a) Digital-to-analog (DA) conversion. The near-field coupling is tuned so as to satisfy the relation for DA conversion. (b) Time evolution from each of the input bits to the output. (c) Experimental results of the output intensity level as a function of 3-bit input combinations.

in the system in terms of size, is smaller than that at the input QDs. Fig. 5(c) shows output signal intensity as a function of the presence (1) or absence (0) of the input excitation, as specified by (s_2, s_1, s_0), which were respectively 381.3 nm, 376 nm, and 325 nm. The output intensity is approximately linearly correlated to the input bit set combination, which indicates the validity of the digital-to-analog conversion mechanism. Compared to known optical approaches, such as those based on space-domain filtering and focusing lenses[3, 4], or optical waveguides and intensity filters[20], the nanophotonic approach achieves a significantly higher spatial density.

4. BROADCAST INTERCONNECTS

Nanophotonics allows subwavelength scale device integration, but it imposes stringent interconnection requirements to couple external signals to nanophotonic devices. To fulfill such requirements, far- and near-field conversion has been pursued based on, for instance, plasmon waveguides[21, 22]. In this section, we show another interconnection scheme based on both far- and near-field interactions for data broadcasting purposes[23].

As discussed in Sec. 2, data broadcasting is a fundamental operation found in memory-based architectures in which multiple functional blocks require the same input data. Example of such architecture include matrix-vector product[3, 4] and switching operations, such as in a broadcast-and-select architecture[24]. For example, consider a matrix-vector multiplication given by $\boldsymbol{v} = A\boldsymbol{s}$, where $\boldsymbol{v} = (v_1,...,v_m)$ and $\boldsymbol{s} = (s_1,...,s_n)$, and A is an $m \times n$ matrix. Here, to compute every v_j from the input data $\boldsymbol{s}$, broadcast interconnects are required if every v_j is calculated at distinct processing hardware. Optics is in fact well suited to such broadcast operations in the form of simple imaging optics[3, 24] or in optical waveguide couplers thanks to the nature of wave propagation. However, its integration density is physically limited by the diffraction limit, which leads to bulky system configurations.

The overall physical operation principle of broadcasting is as follows. In nanophotonics, uni-directional energy transfer is possible between neighboring QDs via local optical near-field interactions and intrasublevel relaxation, as discussed in Sec. 3.

Suppose that arrays of nanophotonic circuit blocks, such as the nanophotonic switches described later, are distributed within an area whose size is comparable to the wavelength. Here, for broadcasting, multiple input QDs simultaneously accept identical input data carried by diffraction-limited far-field light by tuning their optical frequency so that the light is coupled to dipole-allowed energy sublevels, and described in more detail below. In a frequency multiplexing sense, this interconnection method is similar to multi-wavelength chip-scale interconnects[25]. Known methods, however, require a physical space comparable to the number of diffraction-limited input channels due to wavelength demultiplexing, whereas in our proposed scheme, the device arrays are integrated on the sub-wavelength scale, and multiple frequencies are multiplexed in the far-field light supplied to the device.

Here we explain the far- and near-field coupling mentioned above based on a model assuming CuCl QDs, which are employed in experiments described below. The potential barrier of CuCl QDs in a NaCl crystal can be regarded as infinitely high, and the energy eigenvalues for the quantized Z_3 exciton energy level (n_x, n_y, n_z) in a CuCl QD with side of length L are given by

$$E_{(n_x,n_y,n_z)} = E_B + \frac{\hbar^2\pi^2}{2M(L-a_B)^2}(n_x^2 + n_y^2 + n_z^2) \tag{3}$$

where E_B is the energy of the bulk Z_3 exciton, M is the mass of the exciton for the center-of-mass (C. M.) motion, a_B is its Bohr radius, n_x, n_y, and n_z are quantum numbers for the C. M. motion ($n_x, n_y, n_z = 1,2,3,...$), and $a = L - a_B$ corresponds to an effective side length, taking into account the dead layer correction[26]. The exciton energy levels with even quantum numbers are dipole-forbidden states[15]. According to (1) there exists a resonance between the quantized exciton energy sublevel of quantum number (1,1,1) for the QD with effective side length *a* and that of quantum number (2,1,1) for the QD with effective side length $\sqrt{2}a$. (For simplicity, we refer to the QDs with effective side lengths *a* and $\sqrt{2}a$ as "QD *a*" and "QD$\sqrt{2}a$", respectively.) Energy transfer between QD *a* and QD$\sqrt{2}a$ occurs via optical near fields, which is forbidden for far-field light[10, 11, 14].

We note that the input energy level for the QDs, that is, the (1,1,1)-level, can also couple to the far-field excitation. We utilized this fact for data broadcasting. One of the design restrictions is that energy-sublevels for input channels do not overlap with those for output channels. Also, if there are QDs internally used for near-field coupling, dipole-allowed

energy sublevels for those QDs cannot be used for input channels since the inputs are provided by far-field light, which may lead to misbehavior of internal near-field interactions if resonant levels exist. Therefore, frequency partitioning among the input, internal, and output channels is important. The frequencies used for broadcasting, denoted by $\Omega_i = \{\varpi_{i,1}, \varpi_{i,2}, ..., \varpi_{i,A}\}$, should be distinct values and should not overlap with the output channel frequencies $\Omega_o = \{\varpi_{o,1}, \varpi_{o,2}, ..., \varpi_{o,B}\}$. A and B indicate the number of frequencies used for input and output channels, respectively. Also, there will be frequencies needed for internal device operations that are not used for either input or output (discussed later in the sum of product examples), denoted by $\Omega_n = \{\varpi_{n,1}, \varpi_{n,2}, ..., \varpi_{n,C}\}$ where C is the number of those frequencies. Therefore the design criteria for global data broadcasting is to exclusively assign input, output, and internal frequencies, Ω_i, Ω_o, and Ω_n, respectively.

Fig. 6(a) illustrates an example of frequency partitioning, where the horizontal axis shows QD size and the vertical axis shows energy sublevels. The 3-digit sets in the diagram are the quantum numbers of the QDs. In an example shown in Fig. 6(a), we used a nanophotonic switch (2-input AND gate) composed of three QDs with a size ratio of $1:\sqrt{2}:2$. The details of the switching principle are shown in reference[10]. The two input channels are assigned to QD *a* and QD 2*a*, and the output appears from QD $\sqrt{2}a$. Here, multiple input dots QD *a* and QD *2a* can accept identical input data via far-field light for broadcasting purposes. Adding more optical switches for different channels means adding different size dots, for instance, by multiplying the scale of the QDs by a constant while maintaining the ratio $1:\sqrt{2}:2$, such as a QD trio of $2\sqrt{2}a$, $4a$, and $4\sqrt{2}a$, so that the corresponding far-field resonant frequencies do not overlap with the other channels. More dense integration is also possible by appropriately configuring the size of the QDs. As an example, consider a QD whose size is $\sqrt{4/3}a$. The (1,1,1)-level in this QD $\sqrt{4/3}a$ can couple to the far-field excitation. It should be noted that this particular energy level is equal to the (2,2,1)-level in QD 2*a*, which is an already-used input QD; however, the far-field excitation in this particular energy level cannot couple to QD 2*a* since the (2,2,1)-level in QD 2*a* is a dipole-forbidden energy sublevel. Therefore, a QD trio composed of QDs of size $\sqrt{4/3}a$, $\sqrt{8/3}a$, and $\sqrt{16/3}a$ can make up another optical switch, while not interfering with other channels, even though all of the input light

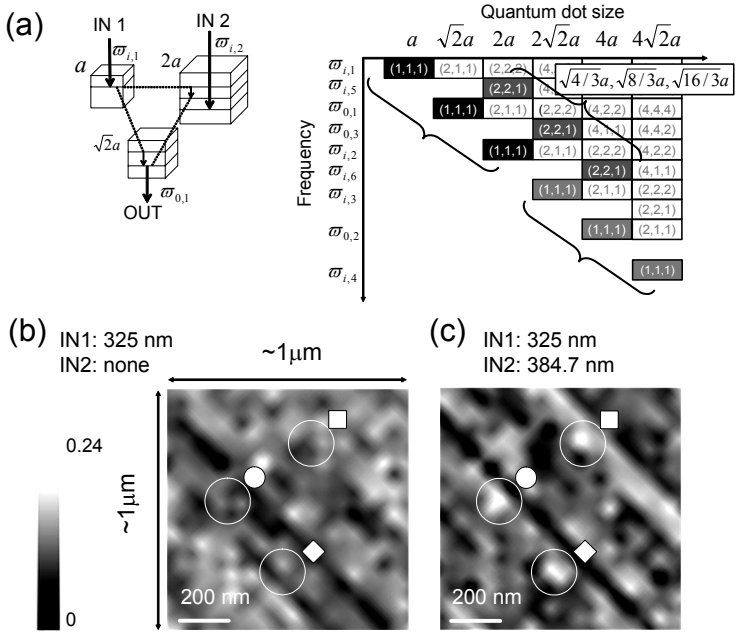

Fig. 6 Broadcast interconnects. (a) Frequency-and-QD-size-diagram. (b,c) Experimental results. Spatial intensity distribution of the output of 3-dot AND gates. (b) Output level: low (1 AND 0 = 0), and (c) output level: high (1 AND 1 = 1)

is irradiated in the same area.

To verify the broadcasting method, we performed the following experiments using CuCl QDs inhomogeneously distributed in an NaCl matrix at a temperature of 22 K. To operate a 3-dot nanophotonic switch (2-input AND gate) in the device, we irradiated at most two input light beams (IN1 and IN2). When both inputs exist, an output signal is obtained from the positions where the switches exist, as described above. In the experiment, IN1 and IN2 were assigned to 325 nm and 384.7 nm, respectively. They were irradiated over the entire sample (global irradiation) via far-field light. The spatial intensity distribution of the output, at 382.6 nm, was measured by scanning a near-field fiber probe within an area of approximately 1 μm × 1 μm. In Fig. 6(b), only IN1 was applied to the sample where the output of the AND gate is ZERO (low-level), whereas in Fig. 6(c) both inputs were irradiated, which means the output is ONE (high-level). Note the regions marked by ■, ●, and ◆. In those regions, the output signal levels were respectively low and high in Figs. 6(b) and (c), which indicates that multiple AND gates were integrated at densities beyond the scale of the globally irradiated input beam area. That is to say, broadcast interconnects to nanophotonic switch arrays are accomplished by diffraction-limited far-field light.

Combining this broadcasting mechanism with the summation mechanism discussed in Sec. 3 will allow the development of nano-scale integration of optical parallel processing devices, which have conventionally resulted in bulky systems.

5. HIERARCHICAL NANOPHOTONIC SYSTEMS

5.1 Hierarchy and nanophotonics

One of the problems for ultra high-density nanophotonic systems is interconnection bottlenecks, which have been addressed previously in Sec. 4 in terms of broadcast interconnects. Hierarchy is another perspective for solving interconnection issues in systems. One of the fundamental points differentiating nanophotnics from electronics is that nanophotonics is physically based on the flow of excitation, not electron transfer. This can be demonstrated simply by the fact that a certain nanostructure can be observed differently depending on how we see it. For instance, an object that has a structure with sub-wavelength precision cannot be resolved by far-field light due to the diffraction limit of light, but can be resolved by a near-field optical microscope (NOM), as schematically shown in Fig. 7(a) and (b). From a system perspective, therefore, we should deal with such hierarchical structures in nanophotonic systems in a systematic manner in future, but this section discusses a simple approach regarding a hierarchical optical memory system.

To achieve ultrahigh-capacity optical data storage, various methods to increase the storage density have been pursued, such as shortening the operating wavelength[27]. With such methods, the storage density is still bound by the diffraction limit of light. One technique to overcome this limitation is to use optical near-fields[28]. These high-density optical memories, however, need certain seeking or scanning mechanisms, which might be a problem, for instance, when searching entire terabyte- or petabyte-scale memories. In dealing with this problem, we first note that information has hierarchy in terms of its meaning or quality, such as "*abstract*" and "*detailed*" information, "*low*" and "*high*" resolution information, and so forth. Similarly, as discussed below, we can find physical hierarchy in the different modes of light propagation. For example, in a near-field, a spatial distribution of the individual dipole moments is obtained, whereas in a far-field, the macroscopic features of the dipole moments are obtained. We associate these hierarchies in the system demonstrated in this section, that is, a hierarchical optical memory system having both near- and far-field readout functions with a simple digital coding scheme. As schematically shown in Fig. 7, in the far-field mode, low-density, rough information is read-out, whereas in the near-field mode, high-density, detailed information is read-out.

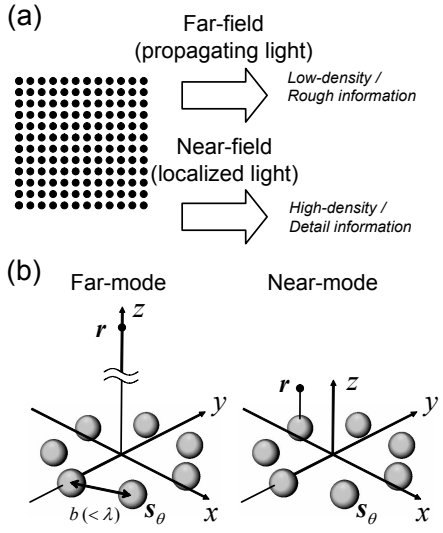

Fig. 7 A simple example of inherent hierarchy in nanophotonics.

5.2 Physical and logical hierarchy using nanophotonics

The two-layer hierarchical memory in this section is explained using the notations *far-code* and *near-code*. The *far-code* depends on the array of bits distributed within a certain area and is determined logically to be either ZERO or ONE. Each *far-code* is comprised of multiple smaller-scale elements, whose existence is determined by the *near-code*. To obtain such information hierarchically, we introduce the following simple logical model.

Consider an (N+1)-bit digital code, where N is an even number. Now, let the far-code be defined depending on the number of ONEs (or ZEROs) contained in the (N+1)-bit digital code:

$$\text{far}-\text{code} = \begin{cases} 1 & \text{If the number of ONEs} > \text{N/2} \\ 0 & \text{otherwise} \end{cases} \tag{4}$$

The (N+1) digits provide a total of 2^{N+1} possible different permutations, or codes. Here, we note that half of them, namely 2^N permutations, have less than N/2+1 ONEs among the (N+1) digits (i.e., far-code = 1), and the other half, also 2^N permutations, have more than N/2+1 ZEROs (i.e., far-code = 0). In other words, 2^N different codes could be assigned to two (N+1)-bit digital sequences so that their corresponding far-codes are ZERO and ONE, respectively. We call this (N+1)-bit code a near-code.

In Fig. 8, example near-codes are listed when N = 8. The correspondence between 2^N original codes and the (N+1)-bit near-codes is arbitrary. Therefore, we need a table-lookup when decoding an (N+1)-bit near-code to the original code. The example near-codes shown in Fig. 8(a) are listed in ascending order, but other lookup-tables or mappings are also possible.

Fig. 8(b) schematically demonstrates example codes in which a 9-bit near-code is represented in a 3 × 3 array of circles, where black and white mean ONE and ZERO, respectively. Here, (1) if the number of ONEs in the near-code is larger than five, then the far-code is ONE; and (2) if the number of ONEs in the near-code is four or less, then the far-code is ZERO.

Suppose, for example, that the far-code stores text data and the near-code stores 256-level (8-bit) image data. Consider a situation where the far-code should represent an ASCII code for "A", whose binary sequence is "0100001". Here, we assume that the gray levels of the first two pixels, which will be coded in the near-code, are the same value. (Here, they are at a level of "92".) However, the first two far-codes are different (ZERO followed by ONE). Referring to the rule shown in Fig. 8(a), and noticing that the first far-code is ZERO and the near-code should represent "92", the first near-code should be "001101010". In the same way, the second near-code is "110001011", so that it represents the level "92", while its corresponding far-code is ONE.

The far-code is determined based on the rule given by eq. (4), which depends on the number of ONEs coded in the near-code. Here, we employ a simple physical model where the near-code is represented by an array of dipole moments. As schematically shown in Fig. 7(b), dipole moments are distributed in an xy plane, where an (N+1)-bit code is assigned in an equally spaced grid. (In Fig. 7(b), each of the dipole moments is assumed to be induced in a small particle which is placed on a circle, and the distance between adjacent particles is b.) The electrical field at position $\boldsymbol{r}$ in Fig. 7(b) is

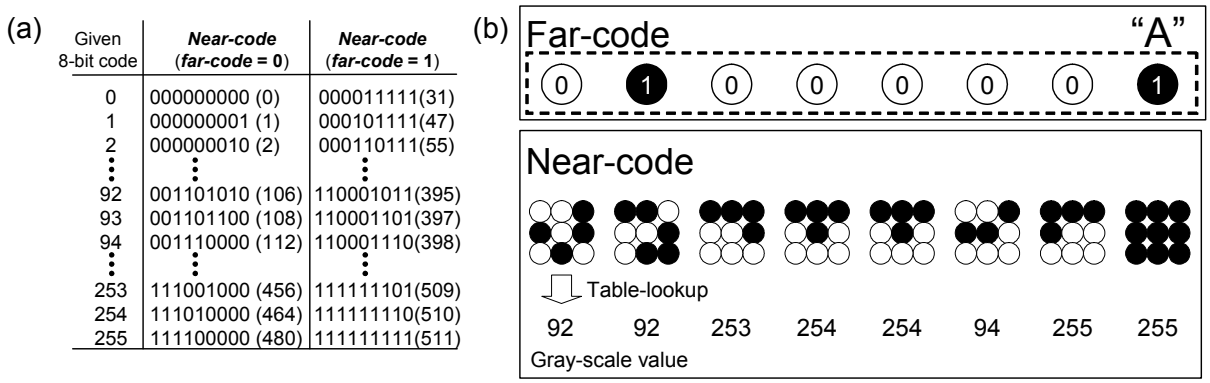

Fig. 8 Example of logical model for the near-code and far-code. Here, the original 8-bit information is coded differently in the near-code depending on its corresponding far-code, which is either ZERO or ONE.

given by

$$E(\mathbf{r}) = \sum_{\theta} E_{\theta} e^{-i\omega t + ik|\mathbf{r}-\mathbf{s}_{\theta}|} \frac{1}{|\mathbf{r}-\mathbf{s}_{\theta}|} \tag{5}$$

where ϖ is the operating frequency, k is the wave number, and $\boldsymbol{s}_{\theta}$ represents the position of a dipole specified by index θ[29]. The existence of the dipole at the position $\boldsymbol{s}_{\theta}$ is given by the near-code as

$$E_{\theta} = \begin{cases} 0 & \text{nearcode}(\theta) = 0 \\ E_0 & \text{nearcode}(\theta) = 1 \end{cases} \tag{6}$$

Suppose that the pitch of adjacent dipoles is b. Here, if we assume that b<<1<<r, then eq. (5) is simplified to

$$E(\boldsymbol{r}) = E_0 \frac{e^{-i\omega t + ikr}}{r} \sum_{\theta} \text{nearcode}(\theta) \tag{7}$$

which means that the electrical field intensity at position r is proportional to the number of ONEs given by the near-code in that area.

Simulations were performed assuming ideal isotropic metal particles to see how the scattering light varies depending on the number of particles for the far-code using a Finite Difference Time Domain-based simulator (*Poynting for Optics*, a product of Fujitsu, Japan). Here we assume that 80-nm-diameter particles are distributed over a 200-nm-radius circular grid with a constant interval, as shown in Fig. 9(a). The solid circles in Fig. 9(b) show calculated scattering cross-sections as a function of the number of particles. The assignment of particle(s) in the grid is also shown. A linear correspondence to the number of particles was observed. This result supports the simple physical model described above.

In order to experimentally demonstrate such principles, we obtained far-field intensity distributions of an array of Au particles, each with a diameter around 80 nm, was distributed over a SiO_2 substrate in a 200-nm-radius circle. These particles were fabricated by a liftoff technique using electron-beam (EB) lithography with a Cr buffer layer. Each group of Au particles was spaced by 2 μm. An SEM image is shown in Fig. 9(c) in which the values indicate the number of particles within each group. In order to illuminate all Au particles in each group and collect the scattered light from them, we used a near-field optical microscope (NOM) with a large-diameter-aperture (500 nm) metallized fiber probe, as shown in Fig. 9(d), in an illumination collection setup. The light source used was a laser diode with an operating wavelength of 680 nm. The distance between the substrate and the probe was maintained at 750 nm. Fig. 9 (e) is an

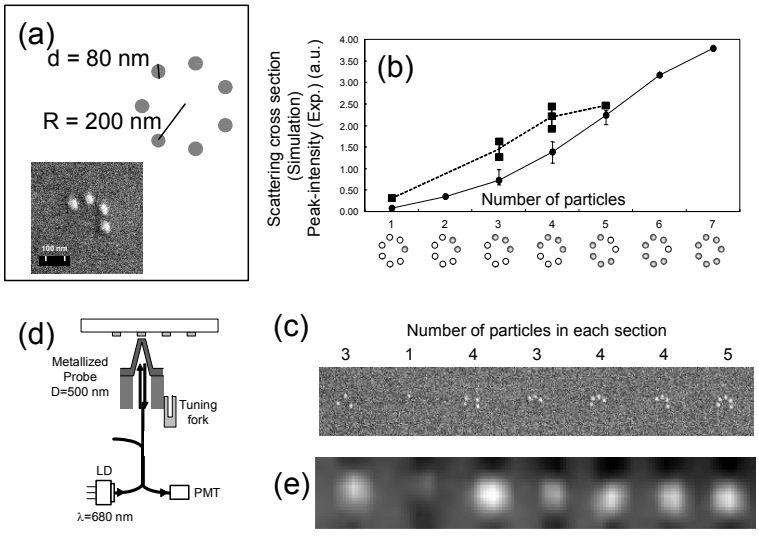

Fig. 9 (a) Each section consists of small particles. (b, circular marks) Scattering cross-sections are calculated depending on the number of particles in each section. (c) SEM picture of an Au particle array. (d) Experimental setup. (e) Intensity profile captured for the *far-code*. (b, square marks) Peak-intensity of each section.

intensity profile captured by the probe, by which the information in the far-mode is retrieved. The solid squares in Fig. 9(b) indicate the peak intensity of each section, which increased linearly. Since the signal level difference in the far-mode is small when the difference in the number of particles is small, a better way of resolving signals in the far-mode will be required. However, the experimental results shown here represent one fundamental architecture that we can exploit the physical hierarchy achievable by nanophotonics.

To summarize this section, a hierarchical optical memory system is presented in which near-fields are used to read detailed dipole distributions, whereas far-fields are used to detect features within a region-of-interest. Simulations and experimental results were also shown. With hierarchical coding, near- and far-field accesses are associated with different hierarchical information, which should help overcome problems involved in searching huge memory spaces. General analysis and design issues for hierarchical nanophotonic systems are presently under investigation.

6. SUMMARY AND DISCUSSION

Two architectural approaches to nanophotonic information and communication systems are discussed. One is a memory-based architecture which is based on table lookup using near-field interactions between QDs. In addition, content addressable memories, digital logic, and matrix-vector multiplication can be implemented in this architecture. As fundamental functional elements, a data summation mechanism, digital-to-analog conversion, and broadcast interconnects are presented, and their proof-of-principle experiments are demonstrated using CuCl QDs. Owing to its high spatial density and low power dissipation, a massive array of such functional components will be useful in applications such as massive table lookup operations in networking and information processing systems. Another approach is one focusing on hierarchy. As an example, a hierarchical memory system is presented with simulations and experimental results using Au particles distributed on a sub-wavelength scale.

Generality of processing remains an open issue since it requires random access memories; other design strategies, such as binary decision diagrams[29], are other possible candidates. Delay-line buffers are also extremely important for optical networks to replace the bulky optical fiber loops used for buffering[30]; the possibility of using nanophotonic devices in these applications is now being pursued[11]. The extremely high spatial density will also lead to novel system design concepts, for instance, in redundancy or fault tolerance[31]. In addition, further investigation of system application issues is indispensable, such as interconnections, hierarchical architectures, the fabrication limitations of nanostructures[32], and new applications unachievable by other technologies.

REFERENCES

1. For example, 2004 WHITE PAPER, Information and Communications in Japan, Ministry of Internal Affairs and Communications, Japan.
2. S. Yao, B. Mukherjee, and S. Dixit, “Advances in photonic packet switching: an overview,” IEEE Commun. Mag., vol. 38, pp. 84-94, 2000.
3. J. W. Goodman, A. R. Dias, and L. M. Woody, “Fully parallel, high-speed incoherent optical method for performing discrete Fourier transforms,” Opt. Lett., vol. 2, pp 1-3, 1978.
4. P. S. Guilfoyle and D. S. McCallum, “High-speed low-energy digital optical processors,” Opt. Eng., vol. 35, pp. 436-442, 1996.
5. M. Ohtsu, K. Kobayashi, T. Kawazoe, S. Sangu, and T. Yatsui, “Nanophotonics: design, fabrication, and operation of nanometric devices using optical near fields,” IEEE J. Select. Topics Quantum Electron., vol. 8, pp. 839-862, 2002.
6. H. Liu, “Routing table compaction in ternary CAM,” IEEE Micro, vol. 22, pp. 58-64, 2002.
7. A. Grunnet-Jepsen, A. E. Johnson, E. S. Maniloff, T. W. Mossberg, M. J. Munroe, and J. N. Sweetser, “Fibre Bragg grating based spectral encoder/decoder for lightwave CDMA,” Electron. Lett., vol. 35, pp. 1096-1097, 1999.
8. M. Naruse, H. Mitsu, M. Furuki, I. Izumi, Y. Sato, S. Tatsuura, M. Tian, and F. Kubota, “Terabit all-optical logic based on ultrafast two-dimensional transmission gating,” Opt. Lett., vol. 29, pp. 608-610, 2004.
9. K. Kitayama and M. Murata, “Versatile optical code-based MPLS for circuit, burst, and packet switchings,” IEEE J. Lightwave Technol., vol. 21, pp. 2753-2764, 2003.
10. T. Kawazoe, K. Kobayashi, S. Sangu, and M. Ohtsu, “Demonstration of a nanophotonic switching operation by optical near-field energy transfer,” Appl. Phys. Lett., vol. 82, pp. 2957-2959, 2003.

11. S. Sangu, K. Kobayashi, A. Shojiguchi, and M. Ohtsu, "Logic and functional operations using a near-field optically coupled quantum-dot system," Phys. Rev. B, vol. 69, pp. 115334-1-13, 2004.
12. M. Naruse, T. Miyazaki, F. Kubota, T. Kawazoe, K. Kobayashi, S. Sangu, and M. Ohtsu, "Nanometric summation architecture using optical near-field interaction between quantum dots," Opt. Lett., vol. 30, pp. 201-203, 2005.
13. T. Kawazoe, K. Kobayashi, and M. Ohtsu, "The optical nano-fountain: a biomimetic device that concentrates optical energy in a nanometric region," Appl. Phys. Lett., vol. 86, pp. 103102, 2005.
14. T. Kawazoe, K. Kobayashi, J. Lim, Y. Narita, and M. Ohtsu, "Direct Observation of Optically Forbidden Energy Transfer between CuCl Quantum Cubes via Near-Field Optical Spectroscopy", Phys. Rev. Lett., vol. 88, pp. 067404-1-4, 2002.
15. Z. K. Tang, A. Yanase, T. Yasui, Y. Segawa, and K. Cho, "Optical selection rule and oscillator strength of confined exciton system in CuCl thin films," Phys. Rev. Lett., vol. 71, pp. 1431-1434, 1993.
16. H. J. Carmichael, Statistical Methods in Quantum Optics I, Springer-Verlag, Berlin, 1999.
17. I. Arsovski and A. Sheikholeslami, "A current-saving match-line sensing scheme for content-addressable memories," 2003 IEEE International Solid-State Circuits Conference, Digest of Technical Papers, vol. 1, pp. 304-494, 2003.
18. I. Arsovski, T. Chandler, and A. Sheikholeslami, "A ternary content-addressable memory (TCAM) based on 4T static storage and including a current-race sensing scheme," IEEE Journal of Solid-State Circuits, vol. 38, pp. 155-158, 2003.
19. P.-F. Lin and J. B. Kuo, "A 1-V 128-kb four-way set-associative CMOS cache memory using wordline-oriented tag-compare (WLOTC) structure with the content-addressable-memory (CAM) 10-transistor tag cell," IEEE Journal of Solid-State Circuits, vol. 36, pp. 666-675, 2001.
20. T. Saida, K. Okamamoto, K. Uchiyama, K. Takiguchi, T. Shibata, and A. Sugita, "Integrated optical digital-to-analogue converter and its application to pulse pattern recognition," Electron. Lett., vol. 37, pp. 1237-1238, 2001.
21. T. Yatsui, M. Kourogi, and M. Ohtsu, "Plasmon waveguide for optical far/near-field conversion," Appl. Phys. Lett., vol. 79, pp. 4583-4585, 2001.
22. J. Takahara, Y. Suguru, T. Hiroaki, A. Morimoto, and T. Kobayashi, "Guiding of a one-dimensional optical beam with nanometer diameter," Opt. Lett., vol. 22, pp. 475-477, 1997.
23. M. Naruse, F. Kubota, T. Kawazoe, S. Sangu, K. Kobayashi, and M. Ohtsu, "Optical interconnects using optical far- and near-field interactions for high-density data broadcasting," Conference on Lasers and Electro-Optics (CLEO) 2005, paper CWF6.
24. B. Li, Y.Qin, X. Cao, and K. M. Sivalingam, "Photonic packet switching: Architecture and performance," Optical Networks Magazine, vol. 2, pp. 27-39, 2001.
25. E. A. De Souza, M. C. Nuss, W. H. Knox, and D. A. B. Miller, "Wavelength-division multiplexing with femtosecond pulses," Opt. Lett., vol. 20, pp. 1166-1168, 1995.
26. N. Sakakura and Y. Masumoto, "Persistent spectral-hole-burning spectroscopy of CuCl quantum cubes", Phys. Rev. B, vol. 56, pp. 4051-4055, 1997.
27. For example, http://www.blu-ray.com/
28. M. Ohtsu and K. Kobayashi, Optical Near Fields (Springer, 2004), Chap. 4.
29. S. B. Akers, "Binary decision diagram," IEEE Trans. Comput., vol. C-27, pp. 509-516, 1978.
30. D. K. Hunter, M. C. Chia, and I. Andonovic, "Buffering in optical packet switches," IEEE J. Lightwave Technol., vol. 16, pp. 2081-2094, 1998.
31. K. Nikolic, A. Sadek, and M. Forshaw, "Fault-tolerant techniques for nanocomputers," Nanotechnology, vol. 13, pp. 357-362, 2002.
32. T. Yatsui, S. Takubo, J. Lim, W. Nomura, M. Kourogi, and M. Ohtsu, "Regulating the size and position of deposited Zn nanoparticles by optical near-field desorption using size-dependent resonance," Appl. Phys. Lett., vol. 83, pp. 1716-1718, 2003.

Photoluminescent characteristics of ZnO nanorods and ZnO/ZnMgO nanorod heterostructures

Gyu-Chul Yi[*a], Won Il Park[a], Jinkyoung Yoo[a] , Dong-Wook Kim[a], Taiha Joo[b], T. Yatsui[c], J. Lim[d] and M. Ohtsu[c,d,e]

[a]National CRI center for Semiconductor Nanorods and Dept. of Materials Science and Engineering, Pohang University of Science and Technology (POSTECH), Pohang 790-784, Korea;
[b]Division of Molecular and Life Sciences, Dept. of Chemistry, POSTECH, Pohang 790-784, Korea
[c]SORST, Japan Science and Technology Agency, 687-1 Tsuruma, Machida, Tokyo, Japan 194
[d]Interdisciplinary Graduate School of Science and Engineering, Tokyo Institute of Technology 4259 Nagatsuta, Midori-ku, Yokohama 226-8502, Japan
[e]Faculty of Engineering, the University of Tokyo, Tokyo, Japan

[*]E-mail: gcyi@postech.ac.kr

ABSTRACT

We report on photoluminescent properties of ultrafine ZnO nanorods and ZnO/$Zn_{0.8}Mg_{0.2}O$ nanorod quantum-well structures. The catalyst-free metalorganic chemical vapor deposition (MOCVD) technique enables control of ZnO nanorod diameters in the range of 5 to 150 nm. From the PL spectra of ultrafine ZnO nanorods with a mean diameter smaller than 10 nm, a systematic blue-shift in their PL peak position was observed by decreasing their diameter, presumably due to the quantum confinement effect along the radial direction in ZnO nanorods. In addition, we obtained time-integrated and time-resolved PL spectra of ZnO/$Zn_{0.8}Mg_{0.2}O$ nanorod single-quantum-well structures (SQWs) in the temperature range of 10 K to 300 K. The nanorod SQWs also showed a PL blue-shift and the energy shift was dependent on ZnO well layer width. The PL peak position shift originates from the quantum confinement effect of carriers in nanorod quantum structures. Furthermore, we investigated spatially-resolved PL spectra of individual nanorod SQWs using scanning near-field optical microscopy.

Keywords: ZnO, nanorods, quantum structures, photoluminescence

1. INTRODUCTION

One-dimensional (1D) semiconductor nanostructures can be used for the efficient transport of electrons and optical excitations, and are thus potentially ideal functional components for nanometer-scale electronic and optoelectronic device fabrication.[1-3] Among numerous semiconductors, ZnO has attracted increasing interest due to its unique electrical and optical properties: ZnO has a direct band-gap (E_g = 3.37 eV) with a large exciton binding energy (60 meV)[4-8]. Recent demonstration of room-temperature ultraviolet lasing in ZnO nanowires stimulated extensive research activities on these nanostructures[5]. Furthermore, heteroepitaxial nanorod quantum structures may greatly enhance versatility and improve performance of the nanoscale devices, as various heterojunction planar devices have been proposed, including nanoscale resonant tunneling devices, field effect transistors, and light-emitting devices[9,10]. Nevertheless, difficulties in fabricating nanorod heterostructures have not allowed careful characterization of their intriguing properties.

Optical characterization methods such as photoluminescence (PL) spectroscopy requiring no physical contacts are useful for defect characterization of the nanomaterials since it is difficult to make reliable metal contacts on nano-scale materials. In particular, low temperature PL spectroscopy is a very sensitive tool for characterizing radiative defects.[11,12] Nevertheless, low temperature PL spectroscopy of semiconductor nanorods has not been extensively investigated. In addition, time-resolved PL (TRPL) is a non-destructive and powerful technique for the optical characterization of

Optoelectronic e ices: Physics, abrication, and Application II, edited by oachim Piprek,
Proc. of SPIE Vol. 6013 (SPIE, Bellingham, WA, 2005) · 0277-786X/05/$15 · doi: 10.1117/12.631517

semiconductor thin films. Recently, TRPL measurements of ZnO nanorods have shown that the radiative recombination rates of ZnO nanorods, depending on their size, are different from those of ZnO bulk material epilayers.[13] In addition, time-resolved second-harmonic generation and transient PL spectroscopy for ZnO nanowires and nanoribbons have been studied.[14] Recently, we fabricated high quality ZnO nanorods and ZnO/$Zn_{0.8}Mg_{0.2}O$ nanorod heterostructures using the catalyst-free metalorganic chemical vapor deposition (MOCVD) method: the monolayer control capability enables us to grow ZnO nanorods with diameters smaller than 10 nm, and single quantum well heterostructures with atomically sharp interfaces.[9] Here, we report on time-integrated and time-resolved PL properties of ultrafine ZnO nanorods and ZnO/$Zn_{0.8}Mg_{0.2}O$ nanorod SQWs.

2. EXPERIMENTAL

For ZnO nanorod growth, we used the metalorganic chemical vapor deposition (MOCVD) method without the aid of any catalyst.[9] This non-catalytic approach can avoid unintentional impurity doping from metal catalysts which have been used for metal-catalyst vapor-liquid-solid nanowire growth and may be a source of defect centers.[5] In our MOCVD technique, variation of growth temperature controlled the nanorod diameter. Ultrafine ZnO nanorods with diameters smaller than 10 nm were prepared at high temperatures of 800−1000°C while low growth temperatures of 400−600°C yielded thick nanorods with diameters larger than 20 nm. During nanorod growth, oxygen and diethylzinc (DEZn) flow rates, used as the reactants, were in the range of 20 sccm and 1.0–3.0 sccm at DEZn bubbler temperatures of –15 °C, respectively. Typical growth time was in the range of 0.5−2 hour.

An arbitrary $Zn_{1-x}Mg_xO$/ZnO quantum well structure, one of the most sophisticated heteroepitaxial structures, can be fabricated in nanorods by controlling layer thickness down to a few Å. Here we employed a $Zn_{1-x}Mg_xO$ ($x < 0.3$) alloy layer as a barrier layer because it has a lattice mismatch less than 1 % as well as a larger fundamental band gap energy than that of ZnO.[16] ZnO well layer thickness (L_w) ranged from 1.1 to 9 nm, while the thicknesses of $Zn_{0.8}Mg_{0.2}O$ bottom and top barrier layers in nanorod SQWs were fixed to be 30 and 6 nm, respectively. For $Zn_{1-x}Mg_xO$ layer growth, bis-cyclopentadienyl-Mg (cp2Mg) was used as the Mg precursor and the Mg concentration was controlled by changing the Mg precursor partial pressure.[16] Energy dispersive X-ray spectroscopy in a transmission electron microscopy chamber was used to determine the average Mg concentration in the (Zn,Mg)O layers to be about 20 at.%.

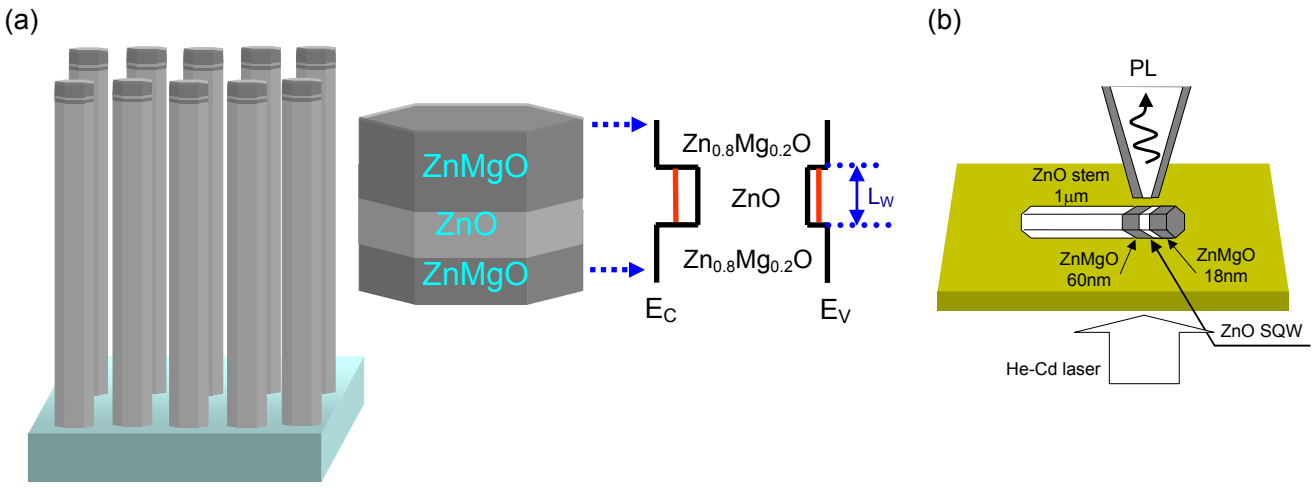

Fig.1. Schematic diagrams of (a) single-quantum-well nanorod structures consisting of $Zn_{0.8}Mg_{0.2}O$/ZnO/$Zn_{0.8}Mg_{0.2}O$ on the tips of ZnO nanorods and (b) near-field spectroscopy of the isolated ZnO SQWs on the ends of ZnO nanorod.

For optical characterizations of the materials, both the time-integrated PL (TIPL) and TRPL of the ZnO films and nanorods were measured. TIPL measurements were performed using a continuous wave He-Cd laser (λ=325 nm) as the excitation source. Details on the TIPL measurements have previously been reported.[17] A TRPL measurement system consists of a femtosecond Ti:sapphire oscillator, a home-built multi-pass Ti:sapphire amplifier operating at 5 kHz, a

frequency tripler, and a time correlated single photon counting system employing a microchannel plate photomultiplier tube. The fundamental output of the Ti:sapphire amplifier at 800 nm was frequency tripled to 267 nm (4.65 eV), and used as an excitation light. The instrumental response of the entire system was 39 ps (FWHM), providing ~8 ps time-resolution with deconvolution. To confirm the promising optical properties of individual ZnO SQWs, we used collection-mode scanning near-field optical microscopy (SNOM) at 15K, in which a He-Cd laser was used for the excitation. We used a UV fiber probe with an aperture diameter of 30 nm [Fig. 1(b)].

3. RESULTS AND DICUSSION

3.1. Photoluminescent properties of ZnO nanorods

Figures 2(a) and (b) show typical field-emission SEM (FE-SEM) images of thick and ultrafine ZnO nanorods, respectively. Ultrafine ZnO nanorods grown at 800 ºC exhibited a very thin diameter of 9 nm and a long length above 3 μm while thick ZnO nanorods grown at 500 ºC showed a mean diameter of 30–45 nm. Thick ZnO nanorods are vertically well aligned but ultrafine nanorods are randomly oriented, as shown in Fig. 2.

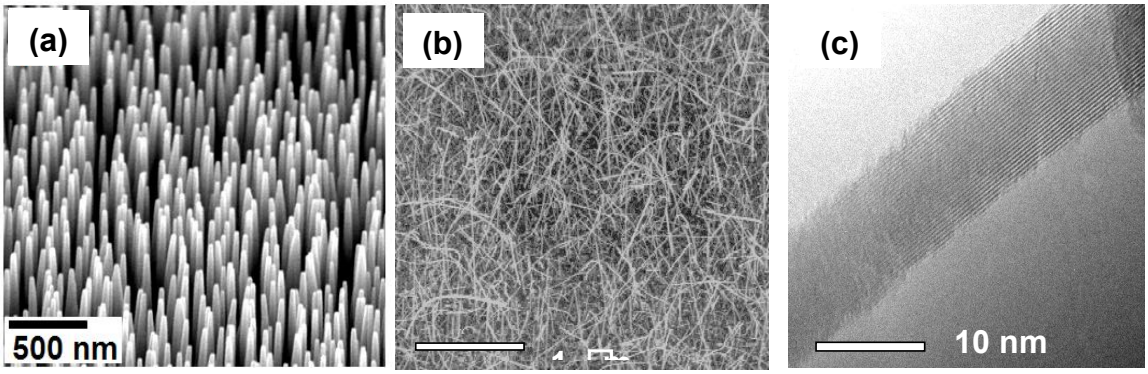

Fig. 2. FE-SEM images of thick ZnO nanorods with a mean diameter of 35 nm (a) and ultrafine ZnO nanorods with a mean diameter of 9 nm (b) and a TEM image of an ultrafine ZnO nanorod (c).

More detail in the crystal structure of ultrafine ZnO nanorods was investigated using high-resolution TEM (HR-TEM). The HR-TEM image in Fig. 2(c) shows that the diameter of an ultrafine ZnO nanorod is as small as 7 nm with a normalized standard deviation value (a standard deviation divided by a mean) of 0.2–0.3. Furthermore, the TEM images displayed a highly ordered lattice image of the ultrafine ZnO nanorod, indicating that ZnO nanorods are almost defect-free and single crystalline.

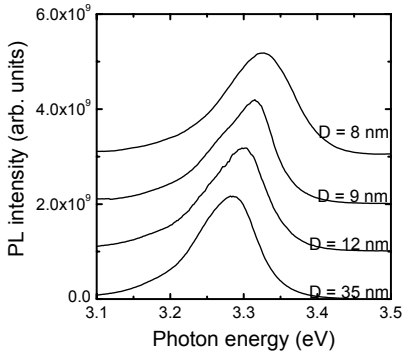

Fig. 3. Room temperature PL spectra of both ultrafine and thick ZnO nanorods with different mean diameters of 8±3.2 nm, 9±3.1 nm, 12±2.9 nm, and 35±4.1 nm.

Figure 3 shows room temperature PL spectra of ZnO nanorods with various mean diameters of 8±3.2 nm, 9±3.1 nm, 12±2.9 nm, and 35±4.1 nm. A dominant PL peak emission for the 35 nm-thick ZnO nanorods is located at 3.285 eV, and the peak position is almost the same of that for bulk ZnO[15, 16]. For ultrafine ZnO nanorods with diameters of 12, 9, and 8 nm, dominant peak energies are 3.301, 3.316, and 3.327 eV with corresponding peak shifts of 16, 31, and 42 meV, respectively. A larger blue-shift in the PL peak position for smaller nanorod diameter strongly suggests the 1D quantum confinement effect in ZnO nanorods. It is also noted that the energy shifts (ΔE) in our nanorods are much smaller than the reported value of 14-nm (120 meV) in PL spectra from 6-nm-thick ZnO nanobelts.[18] For quantitative understanding of this quantum size effect, we calculated the energy shift (ΔE) for a cylindrical potential based on an effective mass model with a simple finite potential barrier. In these calculations, we employed the previously reported values for effective masses of electrons and holes of ZnO: 0.28 m_0 and 1.8 m_0, respectively[19]. The calculated values of ΔE were 24, 44, and 55 meV for their diameters of 12, 9, and 8 nm, respectively. In this simplified model, Coulomb interaction between electrons and holes, which reduces ΔE, was not considered but this may cause a larger energy shift in calculation than the experimental values. Nevertheless, these simple calculations strongly support the possibility that a blue-shift in the PL spectra of ultrafine ZnO nanorods results from the diameter-dependent quantum confinement effect.

3.2. Photoluminescent properties of ZnO/ZnMgO nanorod heterostructures

A schematic of $ZnO/Zn_{0.8}Mg_{0.2}O$ nanorod QWs is shown in Fig. 1. ZnO well layer thickness (L_w) investigated in this study ranged from 11 to 90 Å while the thicknesses of $Zn_{0.8}Mg_{0.2}O$ bottom and top barrier layers in nanorod single-quantum-well (SQW)s were fixed to 300 and 60 Å, respectively. Electron microscopy images reveal the general morphology of $ZnO/Zn_{0.8}Mg_{0.2}O$ nanorod SQW arrays. The nanorod SQWs with a mean diameter of 40 nm were well-aligned vertically over $Al_2O_3(0001)$ substrates. Typical mean lengths of $ZnO/Zn_{0.8}Mg_{0.2}O$ nanorod SQWs were ascertained to be 970±20 nm. The normalized standard deviation value in length distributions was as small as 0.02, indicating that the nanorod SQWs exhibit uniform length distribution, which also implies uniform ZnO well width distribution.

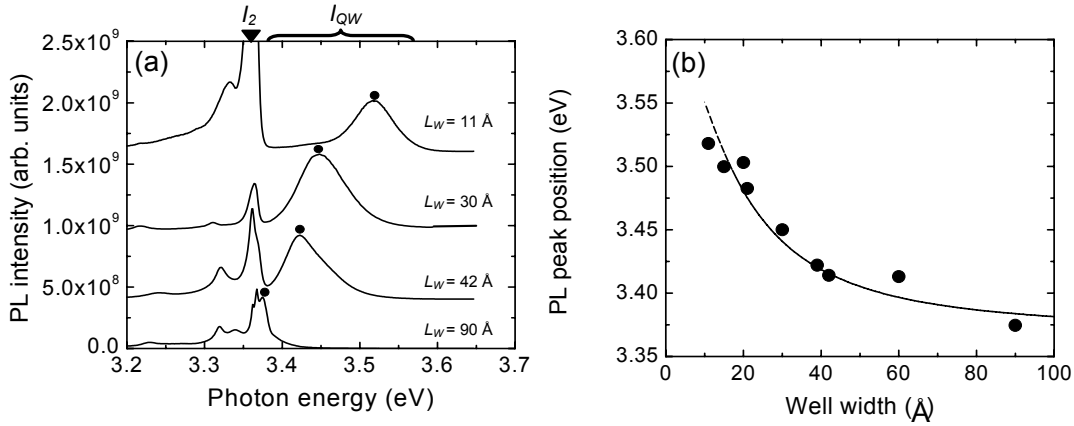

Fig. 4. (a) 10 K PL spectra of $ZnO/Zn_{0.8}Mg_{0.2}O$ nanorod heterostructure and SQWs with different ZnO well layer widths. (b) ZnO well layer width vs PL peak energy position in $ZnO/Zn_{0.8}Mg_{0.2}O$ nanorod SQWs (closed circles) and theoretically calculated values (dashed curves).

Figure 4(a) shows low temperature PL spectra of $ZnO/Zn_{0.8}Mg_{0.2}O$ nanorod heterostructure (with $Zn_{0.8}Mg_{0.2}O$ layer thickness of ~200 nm) and SQWs with different ZnO well layer widths. As shown in Fig. 4(a), the nanorod heterostructure exhibited PL peaks only at 3.360 eV (I^{ZnO}) and 3.58 eV (I^{ZnMgO}) from ZnO nanorod stems and ZnMgO layers, respectively. No peak was observed between the ZnO and ZnMgO peaks. However, the nanorod SQWs

exhibited PL peaks at 3.360–3.366 eV and 3.375–3.518 eV, and the PL peak energy blue-shifted from 10 to 160 meV as the well layer width decreased from 90 to 11 Å. Furthermore electroreflectance spectra of the nanorod quantum structures clearly exhibited the existence of the quantized state. Variation in the I^{QW} peak energy depending on the ZnO well layer width, as well as theoretical predictions in finite square-well potential, are depicted in Fig. 4(b). In this calculation, we employed the following parameters;[20] $0.28m_0$ and $1.8m_0$ for the effective masses of electrons and holes in ZnO, respectively, the ratio of conduction and valance band offsets ($\Delta E_c/\Delta E_v$) of 9, and the band gap offset (ΔE_g) of 250 meV. The experimental data agrees well with the results from theoretical calculations, indicating that the systematic increase in the PL emission peak by reducing the well layer width results from the quantum confinement effect.

Further experiments on temperature-dependent evolution of the PL peaks in $ZnO/Zn_{0.8}Mg_{0.2}O$ nanorod SQWs confirms the origin of the PL peaks. Figure 5 exhibits the typical PL spectra of $ZnO/Zn_{0.8}Mg_{0.2}O$ nanorod SQWs with L_w of 30 Å measured in the temperature range from 10 to 300 K. At 10 K, the strong and sharp peak (I^2) due to bound exciton recombination in ZnO nanorod stems was observed at 3.361 eV, while the broad peak (I^{QW}) with a FWHM of 70 meV appeared at 3.45 eV. The IQW peak originated from the recombination of excitons at the thin ZnO well layers in the nanorod SQWs. As the temperature increased, the peak intensity drastically decreased and almost disappeared at temperatures above 90 K, whereas the IQW peak quenched rather slowly and survived even at RT.

It is remarkable that the nanorod SQWs showed excellent PL properties including strong RT luminescence, even though the nanorod SQWs were grown on Si substrates with a large lattice mismatch with ZnO. Since the PL thermal quenching rate is generally dependent on interface quality, the low thermal quenching and strong PL at RT implies a high structural quality of SQWs with clean ZnO/ZnMgO interfaces. High resolution TEM also confirmed that most defects due to large lattice mismatches were formed at the interface of ZnO/substrate rather than inside the nanorod SQWs,[1] which leads to improved interface quality of the ZnO/ZnMgO quantum well layer on nanorods.

The PL spectra clearly show temperature-dependent behavior of I_{ex}^{ZnO}, I_2^{ZnO} and I^{QW} peak positions. The free exciton peak (I_{ex}^{ZnO}) and I_2^{ZnO} energies decreased with band gap energy shrinkage according to Varshni's formula as generally observed from ZnO bulk crystals and films.[21] However, the I^{QW} emission peak position exhibits so-called "S-shaped" behavior, i.e., a red–blue–redshift of the peak position with increasing temperature.[23] As traced by the solid curve in Fig. 5, the I^{QW} peak shows a blueshift of 7 meV in the range of 50–180 K. The blue-shift in the temperature-dependent PL emission is frequently observed from diverse semiconductor thin films with quantum structures, and has been explained in terms of localized states or a piezoelectric field (PEF) effect.[22,23]

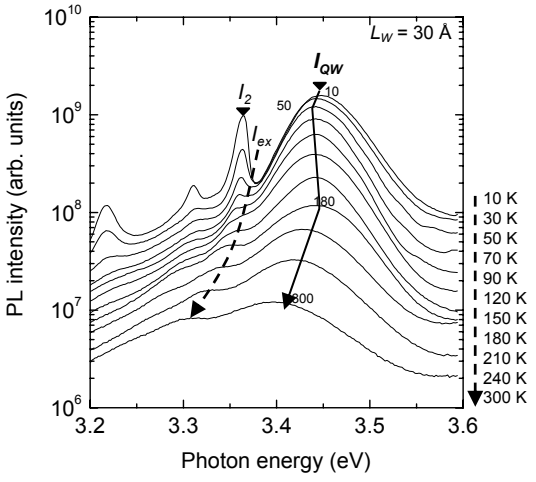

Fig. 5. Temperature-dependent PL spectra of $ZnO/Zn_{0.8}Mg_{0.2}O$ SQW nanorods with a well layer width of 30 Å at 10-300 K.

In addition to the TIPL, TRPL spectra of $ZnO/Zn_{0.8}Mg_{0.2}O$ nanorod SQWs were measured in order to investigate exciton dynamics in nanorod SQWs. Figure 6 shows TRPL signals measured at photon energies of 3.36 and 3.43 eV,

which correspond to I_2^{ZnO} emitted from ZnO nanorod stems and I^{QW} emitted from thin ZnO single quantum wells in the nanorods, respectively. Both I_2^{ZnO} and I^{QW} peak positions from TRPL data fit well with a double exponential decay curve function with a 25–30 ps rise component. Double-exponential decay behavior was observed from epitaxial ZnO thin films,[16] which strongly suggests that two different decay and/or capture processes are involved in the emission.

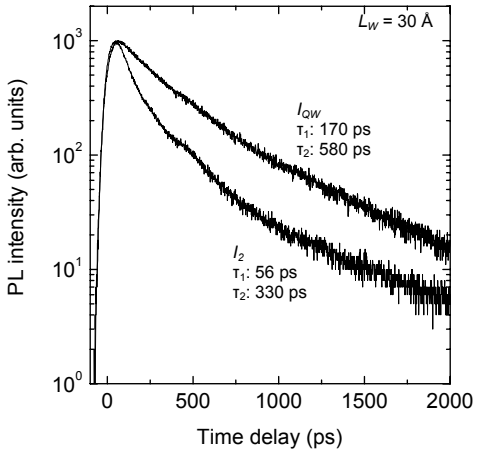

Fig. 6. TRPL data of bound exciton (I_2^{ZnO}) emitted from ZnO nanorod stems and I^{QW} emitted from thin ZnO quantum well layers obtained from ZnO/$Zn_{0.8}Mg_{0.2}O$ nanorod SQWs with a well layer width of 30 Å.

The TRPL of I^{QW} shows a slower decay than that of I_2^{ZnO}. From the curve fittings, the decay time constants of I^{QW} are estimated to be 170 and 580 ps, much longer than those of I_2^{ZnO}, 56 and 330 ps. The different PL lifetimes of I^{QW} and I_2^{ZnO} can be explained in terms of size-dependent light-matter interaction in low dimensional nanostructures.[14] In particular, light-matter interaction based on exciton-polariton pictures predicted that radiative recombination time increases as size decreases in cases where particle size is small enough to be comparable to the exciton Bohr diameter.[17] Additionally, the thermal release effect of excitons from localized to delocalized states at the wells might also increase the PL life time.[15,18,19]

Even though giant exciton-polariton coupling has been predicted in low dimensional quantum structures,[24] recent experiments have shown strongly quenched excitonic emission of nanoparticles.[25] This discrepancy may result from nonradiative processes, such as surface state trapping and defect-mediated deep level traps, and multi-phonon scattering. In addition, in quantum wells or dots buried in barriers with wider band gaps, carrier leakage through poor hetero-interfaces leads to an increase of a nonradiative recombination rate, and thus decreases of PL lifetimes.[26] From this point of view, it is remarkably noted that the decay time constants (170 and 580 ps) of I^{QW} in nanorod SQWs is comparable to or even longer than those of localized excitons (88–190 ps) measured in a series of ZnO/ZnMgO MQW thin films by Chia et al.[25]

In the near-field spectra, the emission peaks at 3.365 and 3.52 eV originate from the neutral-donor bound exciton (D_OX) in the ZnO stem, and the free exciton in ZnMgO layers, respectively, which correspond to those of far-field spectra [dashed curves in Fig. 7(a)]. However, at the well layer, the emission from D_OX was suppressed, while the blue-shifted PL emission peak emerged at 3.499 (L_w = 2.5 nm), 3.444 (L_w = 3.75 nm), and 3.410 eV (L_w = 5.0 nm), respectively. The value of the blue shift was consistent with the theoretical prediction using the finite square-well potential of the quantum confinement effect in the ZnO well layer. Spatial distributions of the optical near-field intensity for ZnO SQWs of L_w = 3.75 nm [Figs. 7(b) and 7(c)] also supported the theory that the blue-shifted emission peaks were confined to the end of the ZnO stem. Furthermore, their spectral width (3 meV) for ZnO SQWs of L_w = 2.5 nm and L_w = 3.75 nm were much narrower than those of far-field spectra (40 meV).

In order to estimate the linewidth of the isolated ZnO SQWs, we observed the power-dependent PL spectra of Lw = 3.75 nm [Fig. 8(a)] at various excitation densities ranging from 0.6 to 4.8 W/cm^2. The line shape of each spectrum can

be reproduced by the Lorentzian function indicated by the solid line. As shown in Figs. 8(b) and 8(c), the integrated PL intensity (I_{PL}) linearly increases and the homogeneous width (Δ) is maintained constant around 3 meV. These results indicate that the emission line at 3.444 eV can be identified as emission from a single-exciton state in ZnO SQWs, and the linewidth of the PL spectra is governed by homogeneous broadening, owing to the internal electric field effect in ZnO[27] or large stem width (40 nm).

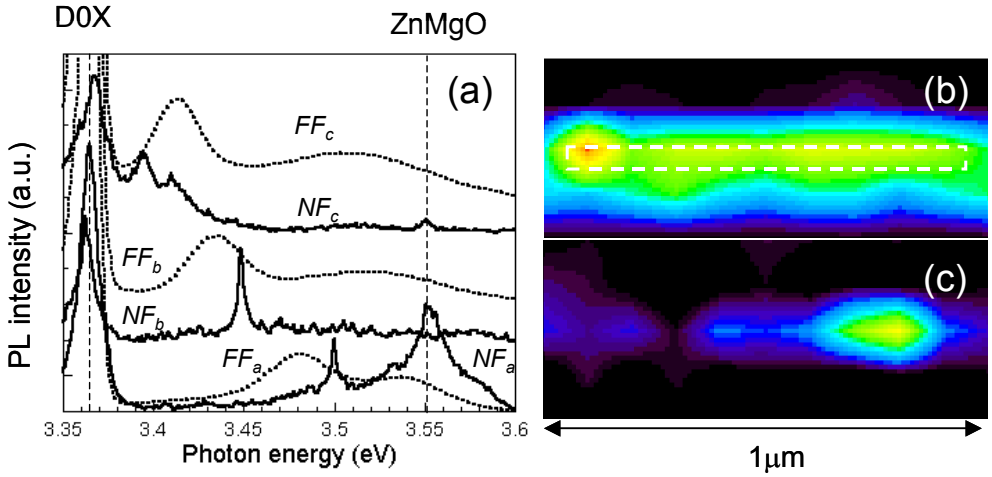

Fig. 7. (a) Size-dependent PL spectra of isolated ZnO nanorod SQWs with L_W = 2.5 nm (FF_a, NF_a), 3.75 nm (FF_b, NF_b), and 5.0 nm (FF_c, NF_c), respectively, obtained at 15 K. FF: far-field spectrum of vertically aligned ZnO nanorod SQWs. NF: near-field PL spectrum of the isolated ZnO SQWs obtained at the well layer. Near-field intensity distributions of the isolated ZnO SQWs (L_W = 3.75 nm) obtained at (b) 3.365 and (c) 3.444 eV, respectively.

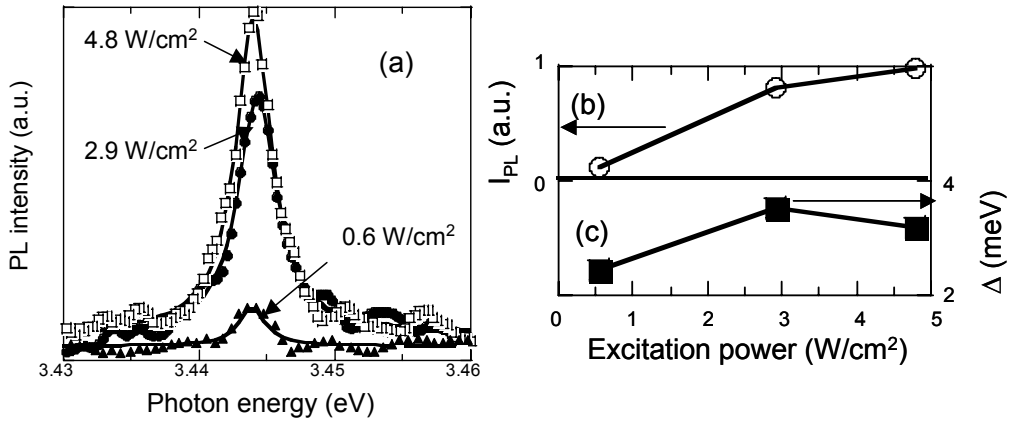

Fig. 8. (a) Low-temperature (15 K) near-field PL spectrum of the isolated ZnO SQWs (L_W=3.75 nm) at various excitation densities ranging from 0.6 to 4.8 W/cm^2. Power dependence of (b) integrated PL intensity I_{PL} and (c) linewidth (Δ).

4. CONCLUSIONS

In summary, we investigated the photoluminescent properties of ZnO single-crystal nanorods and $ZnO/Zn_{0.8}Mg_{0.2}O$ SQW nanorods grown by catalyst-free MOCVD. Both materials exhibited free exciton peaks at 10 K with an extremely weak deep level emission, indicating high optical quality of materials. The excitonic emission peaks of the ultrafine ZnO nanorods were blue-shifted, presumably because of the quantum confinement effect along the radial direction in ZnO nanorods. The PL spectra of $ZnO/Zn_{0.8}Mg_{0.2}O$ SQW nanorods showed strong ZnO well layer width dependence and a blue-shift of the near-bandedge emission peak. Temperature-dependent PL spectra of $ZnO/Zn_{0.8}Mg_{0.2}O$ SQWs exhibited slow thermal quenching and a red-blue-redshift of the peak position of I^{QW} with increasing temperature. In addition, TRPL showed that PL decay time constants of I^{QW} (170 and 580 ps) were larger than those of ZnO nanorods (56 and 330 ps). Furthermore, spatially-resolved PL spectra of the isolated nanorod QWS were measured using SNOM, which exhibited a very narrow PL peak from the quantum well embedded in the nanorod.

REFERENCES

1. C. Dekker, *Phys. Today* **52**, 22 (1999).
2. J. Hu, T. W. Odom, and C. M. Lieber, *Acc. Chem. Res.* **32**, 435 (1999)
3. J. T. Hu, L. Li, W. Yang, L. Manna, L. Wang, and A. P. Alivisatos, *Science* **292**, 2060 (2001)
4. G.-C. Yi, C. Wang, and W. I. Park, *Semicond. Sci. Technol.* **20**, S22 (2005).
5. M. H. Huang, S. Mao, H. Feick, H. Yan, Y. Wu, H. Kind, E. Weber, R. Russo, and P. Yang, *Science* **292**, 1897 (2001).
6. Z. L. Wang, *Mater. Today* **7**, 26 (2004).
7. Y. W. Heo, D. P. Norton, L. C. Tien, Y. Kwon, B. S. Kang, F. Ren, S. J. Pearton, and J. R. LaRoche, *Mater. Sci. Eng. R* **47**, 1 (2004).
8. S. F. Yu, C. Yuen, S. P. Lau, W. I. Park, and G.-C. Yi, *Appl. Phys. Lett.* **84**, 3241 (2004).
9. W. I. Park, G.-C. Yi, M. Kim, and S. J. Pennycook, *Adv. Mat.* **15**, 526 (2003).
10. M. T. Björk, B. J. Ohlsson, C. Thelander, A. I. Persson, K. Deppert, L. R. Wallenberg, and L. Samuelson, *Appl. Phys. Lett.* **81**, 4458 (2002).
11. H. B. Bebb and E. W. Willams, *Semiconductor and Semimetals* (Academic, New York, 1972), Vol. 8, pp. 181-320.
12. G. D. Gilliland, *Mater. Sci. Eng., R.* **18**, 99 (1997).
13. J. Johnson, K. P. Knutsen, H. Yan, M. Law, P. Yang, and R. Saykally, *Nano. Lett.* **4**, 197 (2004).
14. S. Hong, T. Joo, W. I. Park, and G.-C. Yi, *Appl. Phys. Lett.* **83**, 4157 (2003).
15. W. I. Park, D. H. Kim, S.-W. Jung, and G.-C. Yi, *Appl. Phys. Lett.* **80**, 4232 (2000).
16. W. I. Park, G.-C. Yi, and H. M. Jang, *Appl. Phys. Lett*. **79**, 2022 (2001).
17. S. W. Jung, W. I. Park, H. D. Cheong, G.-C. Yi, H. M. Jang, S. Hong, and T. Joo, *Appl. Phys. Lett.* **80**, 1924 (2002).
18. X. Wang, Y. Ding, C. J. Summers, and Z. L. Wang, *J. Phys. Chem. B* **108**, 8773 (2004).
19. L. E. Brus, *J. Chem. Phys*. **80**, 4403 (1984).
20. A. Ohtomo, M. Kawasaki, I. Ohkubo, H. Koinuma, T. Yasuda, and Y. Segawa, *Appl. Phys. Lett.* **75**, 980 (1999).
21. Y. P. Varshni, *Physica*, **34**, 149 (1967).
22. Y.-H. Cho, G. H. Gainer, A. J. Fischer, J. J. Song, S. Keller, U. K. Mishra, and S. P. DenBaars, *Appl. Phys. Lett.* **73**, 1370 (1998).
23. A. Bell, J. Christen, F. Bertram, F. A. Ponce, H. Marui, and S. Tanaka, *Appl. Phys. Lett.* **84**, 58 (2004).
24. B. Gil and A. V. Kavokin, *Appl. Phys. Lett.* **81**, 748 (2002).
25. (a) C. H. Chia, T. Makino, Y. Segawa, M. Kawasaki, A. Ohtomo, K. Tamura, and H. Koinuma, *J. Appl. Phys.* **90**, 3650 (2001). (b) T. Makino, N. T. Tuan, H. D. Sun, C. H. Chia, Y. Segawa, M. Kawasaki, A. Ohtomo, K. Tamura, T. Suemoto, H. Akiyama, M. Baba, S. Saito, T. Tomita, and H. Koinuma, *Appl. Phys. Lett.* **78**, 1979 (2001).
26. K. C. Zeng, J. Li, J. Y. Lin, and H. X. Jiang, *Appl. Phys. Lett.* **76**, 3040 (2000).
27. T. Makino, A. Ohtomo, C. H. Chia, Y. Segawa, H. Koinuma, and M. Kawasaki, *Physica E* **21**, 671 (2004).

Nanophotonics: Devices, Fabrication and Systems

Motoichi Ohtsu

Department of Electronics Engineering, University of Tokyo, Bunkyo-ku, Tokyo 113-8656, Japan

ohtsu@ee.t.u-tokyo.ac.jp

***Abstract* — This paper introduces resent successes in nanophotonics utilizing local electromagnetic interactions between a few nanometric elements (*i.e.*, an optical near-field interaction). Each section of this paper reviews nanophotonic devices, nanofabrications, and systems to operate nanophotonic devices efficiently. Using CuCl quantum dots, the operations of an optical switch with 20-nm in size (*i.e.*, a nanophotonic switch) and nanometric optical condenser, which attract optical energy into a 10-nm spot (*i.e.*, an optical nano-fountain) were experimentally verified. Power consumption of these devices is only 1/100,000 as high as that of the conventional electronic devices. A nonadiabatic photochemical reaction using optical near field enables secure and low-cost nanofabrication by its applications to an optical chemical vapor deposition (CVD) and a photolithography. The novel photochemical reaction dissociate a stable (optically inactive) molecule ($Zn(AcAc)_2$), and expose even UV photoresist using a visible light source. Novel nanophotonic systems, a nanophotonic computing architecture based on high-density table lookup are also discussed for a telecommunication and a date processing in nanophotonics. A high-density packaging of nanophotonic devices enables a nanometric optical content addressable memory and a digital-to-analog converter.**

***Keywords* — Nanophotonics, Optical near field, Energy transfer, nanofabrication, nanophotonic system**

I. INTRODUCTION

We first present possible technical problems that are faced by the future optical technology in order to explain the motivation [1].

Optical fiber transmission systems require increased integration of photonic devices if data transmission rates are to reach as high as 10 Tb/s by the year 2015. To support this increase, it is estimated that the size of photonic matrix switching devices should be reduced to a 100-nm scale, to integrate more than 10000×10000 input and output channels on a substrate. Since conventional photonic devices, *e.g.*, diode lasers and optical waveguides including photonic crystals, have to confine the lightwave within their cavities and core layers, respectively, their minimum sizes are limited by the diffraction of light. Therefore, they cannot meet this requirement, because the required size is beyond this diffraction limit.

Progress in electronic device technology, *e.g.*, CPU and DRAM, has been supported by progresses in photolithography. It is anticipated that it should be possible to fabricate patterns narrower than 50 nm by the year 2010. Although several methods using special light sources, *e.g.*, an extreme ultraviolet (UV) light source and a synchrotron radiation light source, have been developed, they require linewidth that far exceeds the diffraction limit of visible light.

From these points, it can be readily understood that a novel optical nanotechnology that goes beyond the diffraction limit is required in order to support the optical science and technology of the 21st century. To meet this requirement, M. Ohtsu has proposed a novel technology, called nanophotonics [2]. Nanophotonics is defined as a technology that utilizes local electromagnetic interactions between a small nanometric element and an optical near field (ONF). Since ONF is free from the diffraction of light due to its size-dependent localization and resonance features, nanophotonics enables the fabrication, operation, and integration of nanometric devices. The primary advantage of nanophotonics is its capacity to realize novel functions based on local electromagnetic interactions. It should be noted that some of the conventional concepts of wave optics, such as interference, are no longer essential in nanophotonics. Instead, concepts of surface elementary excitation and nanofabrication technology are essential.

Section II outlines of the nanophotonic devices which we proposed. Its function is based on a unique ONF energy transfer, which is allowed between nanometric elements by the exchange of near-field photons. Operations of a nanophotonic switch and an optical nano-fountain are described. Section III reviews the chemical vapor deposition (CVD) process and photolithography using ONF. An essential feature of ONF interactions allows a nonadiabatic photochemical reaction which is applicable to these fabrication methods. Section IV reviews novel approach of a nanophotonics from a system architecture perspective, considering the unique physical principles provided by ONF interactions and the functionality required for practical applications. Section VIII summarizes the main points discussed in this paper.

II. NANOPHOTONIC DEVICES

The energy transfer from smaller to larger quantum dots (QDs) have been studied by the spectrally, spatially, and time resolved experiment [3]. We proposed the model for the unidirectional resonant energy transfer between QDs via ONF interaction and observed the energy transfer

among randomly dispersed CuCl QDs using the ONF spectrometer [4]. The theoretical analysis and time evolution of the energy transfer via ONF interaction were also discussed [5, 6]. Crooker et al. also studied the dynamics of exciton energy transfer in close-packed assemblies of monodisperse and mixed-size CdSe nanocrystal QDs, and reported the energy-dependent transfer rate of excitons from smaller to larger dots [7]. Nanophotonic devices which we proposed are realized by controlling this energy transfer [8-11].

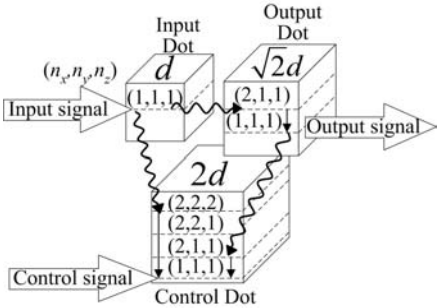

Fig. 1. Schematic mechanism of the proposed nanophotonic switch using cubic QDs. The arrows input, output, and control refer to the switching system interface.

Energy eigenvalues for the quantized exciton energy level in a cubic QD with the side length of L are given by

$$E_{n_x,n_y,n_z} = E_B + \frac{\hbar^2\pi^2}{2M(L-a_B)^2}(n_x^2+n_y^2+n_z^2) \quad , \qquad (1)$$

where E_B is the bulk exciton energy, M is the translational mass of exciton, a_B is exciton Bohr radius and (n_x, n_y, n_z) are quantum numbers (=1, 2, 3,...), and d = (L-a_B) corresponds to an effective side length given by consideration of the dead layer correction. When three cubic QDs with effective side lengths of d, $\sqrt{2}d$, and $2d$ are closely spaced, as shown in Fig.1, the switching operation is expected. The quantized energy sublevels (2,2,2) in Control Dot, (2,1,1) in Output Dot, and (1,1,1) in Input Dot resonates with each other. Under such resonant conditions, the coupling energy of near-field interaction between two resonant energy states is given by the following Yukawa-type function;

$$V(r) = A\frac{\exp(-\mu \cdot r)}{r} \quad . \qquad (2)$$

Here, r is a separation between two QDs, A is a coupling coefficient. The values A should be determined from the experiment essentially, however, we estimated it from the result of the previous work on the interaction between a Rb atom and the near-field probe. Assuming that the separation r between two QDs is equal to 10 nm, the transition time is about 100 ps which is much shorter than the few ns carrier lifetime. In addition, inter sub-level transition is generally less than few ps and is much shorter than the transition time due to near-field coupling. Thus, the switching operation is permitted by the following mechanisms.

In the OFF state, *i.e.*, without the control signal, almost all of the exciton energy in Input Dot is transferred to the (1,1,1) level in Control Dot, and finally, the input energy is dissipated from Control Dot by a recombination radiation, and consequently no optical output signals are generated from Output Dot. In the ON state, *i.e.*, with the control signal, by contrast, the escape routes to Control Dot are blocked by the excitation of Control Dots, due to state filling in Control Dot by applying the control signal. Thus, the input energy is transferred to Output dot and an optical output signal is generated.

We used cubic CuCl QDs in a NaCl matrix as a device material. For CuCl QDs, any other possible energy transfer except for the ONF interaction, such as carrier tunneling, Coulomb coupling, and so on, can be neglected because a carrier wave function is localized in cubes due to deep potential depth of more than 4 eV and the Coulomb interaction is weak due to small exciton Bohr radius of 0.68 nm. The conventional optical energy transfer is also negligible, since the transition to the energy levels with an even principal quantum number in the cubic CuCl QDs are optically-forbidden, due to the long-wave and point-dipole approximations. However, the ONF interaction, which is incommensurate to such approximations, becomes a finite value, as mentioned above. Namely, this nanophotonic switching operation is ensured by the one of the essential features of ONF.

To realize the switching operation, the fiber probe was carefully scanned to search for a trio of QDs that satisfied an effective size ratio of $1:\sqrt{2}:2$ for the switching operation. Since the homogeneous linewidth of a CuCl QD increases with temperature, the allowance in the resonatable size ratio is 10 % at 15 K. The separation of the QDs must be less than 30 nm for the proposed switching operation, because the energy transfer time increases with separation; however, it must be shorter than the exciton lifetime. It is estimated that at least one trio of QDs exists in a $2\,\mu m \times 2\,\mu m$ scan area that satisfies these conditions. To demonstrate the switching operation, we found a QDs trio in the sample whose sizes, L, were 3.5, 4.6, and 6.3 nm. Since their effective sizes d were 2.8, 3.9, and 5.6 nm, the size ratio was close to $1:\sqrt{2}:2$ and they could be used as Input Dot, Output Dot, and Control Dot, respectively. In the experiment, SHG of Ti:sapphire lasers (λ = 379.5 nm and λ =385 nm), which were tuned to the (1,1,1) exciton energy levels in Input Dot and Control Dot, respectively, were used as the input and the control light sources. The output signal was collected by the fiber probe, and its intensity was measured by a cooled micro-channel plate after passing through three interference filters of 1-nm bandwidth tuned to the (1,1,1) exciton energy level in Output Dots at λ =383 nm.

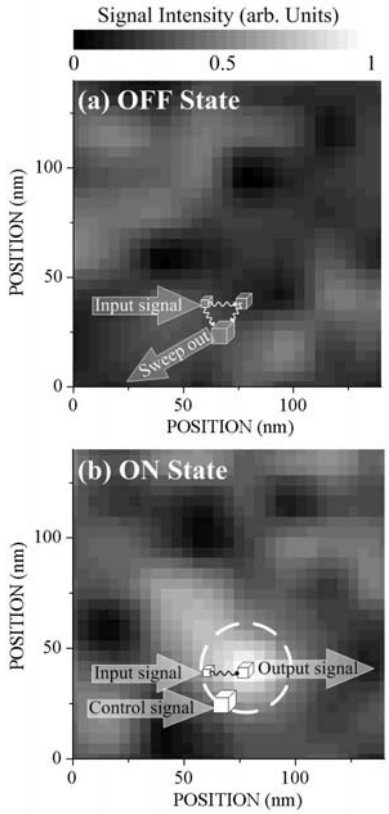

Fig. 2. Spatial distribution of the output signal from the nanophotonic switch measured by a near-field microscope, in the OFF (a) and ON (b) states.

Figures 2 (a) and (b) show the spatial distribution of the output signal intensity in the OFF state and the ON state, using near-field spectroscopy at 15 K. The insets in Fig. 2 are schematic drawings of the existing QD trio used for the switching, which was confirmed by the near-field luminescence spectrum. Here the separation of the QDs by less than 20 nm was theoretically estimated from time-resolved measurements, as explained in the next paragraph. In the OFF state, no output signal was observed, because the energy of the input signal was transferred to Control Dot and swept out as luminescence at 385 nm. To quench the output signal in the OFF state, which is generated by exciton accumulation in Control Dot, the input signal density in Control Dot was regulated to less than 0.1 excitons. In the ON state, we obtained a clear output signal in the broken circle. The output signal was proportional to the intensity of the control signal, where its density in Control Dot was 0.01 ~ 0.1 excitons. The internal quantum efficiency was close to 1.

Next, the dynamic behavior of the nanophotonic switch was evaluated by using the time correlation single photon counting method. As a pulse-control light source, the 385-nm SHG of a mode-locked Ti-sapphire laser was used. The repetition rate of the laser was 80 MHz. To avoid cross talk of the input and control signals, which originates from spectral broadening for the pulse duration, the pulse duration of the mode-locked laser was set to be 10 ps. The time resolution of the experiment was 15 ps. Figure 3 shows the time evolution of the control pulse signal (upper part) applicable to Control Dot and the output signal (lower part) from Output Dot. The output signal rises synchronously within less than 100 ps, with the control pulse. As this signal rise time is determined by the energy transfer time, the separation between the QDs can be estimated from the rise time as being less than 20 nm. The rise time can be shortened to a few ps by decreasing the separation of the QDs. Since the decay time of the output signal is limited by the exciton lifetime, this nanophotonic switch is able to operate at a few hundred MHz, and it is anticipated that the operation frequency can be increased to several GHz by means of exciton quenching using a plasmon coupling. The ON-OFF ratio was about 10, which is sufficient for use as an all-optical switch, and can be increased by a saturable absorber and electric field enhancement of the surface plasmon.

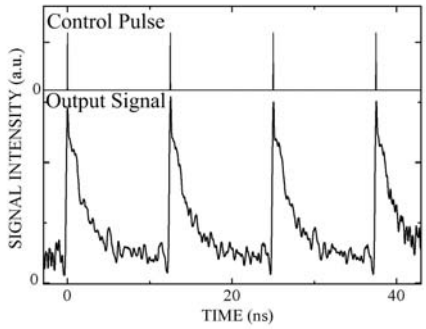

Fig. 3. Time evolution of the control pulse signal (upper part) and the output signal (lower part) from the nanophotonic switch at the broken circle in Fig. 2 (b). The duration and repetition rate of the control pulse were 10 ps and 80 MHz, respectively.

The advantages of this nanophotonic switch are its small size and high-density integration capability based on the locality of ONF. The figure of merit (FOM) of an optical switch should be more important than the switching speed. Here, we have defined the FOM as $F=C/(V \bullet t_{sw} \bullet P_{sw})$, where C, V, t_{sw}, and P_{sw} are the ON-OFF ratio, the volume of the switch, the switching time, and the switching energy, respectively. The FOM of our demonstrated switch is more than 10 times higher than that of a conventional photonic switch, because its volume and switching energy are 10^{-5} times and 10^{-3} times smaller, respectively. Power consumption of these devices, which generates heat is only 1/100,000 as high as that of the conventional electronic devices, because only the sublevel transition generates heat which is less than 30 meV/cycle at room temperature operation. We consider this ultra low heat generation is most important advantage of the nanophotonic device.

As we and other research groups mentioned, the principle of the energy transfer among QDs is equivalent to that of the light-harvesting photosynthetic system, which skillfully concentrates and harvests optical energy

in nanometric photosynthetic systems. The photosynthetic purple bacteria Rhodopseudomonas acidophila has two light-harvesting antennae: LH1 and LH2. LH1 contains a 32-bacteriochlorophyll (BChl) ring, and LH2 contains a B800 ring with 9 BChls and a B850 ring with 18 BChls. They harvest photons and efficiently transfer the excitation energy from B800 to LH1, where the excitonic energy of B800 is higher than that of LH1. This unidirectional energy transfer is due to the nanometric dipole-dipole interaction, i.e., an ONF interaction, among BChl rings with low energy dissipation. The optical energy concentrator "optical nano-fountain", which we propose, operates in the same manner as the light harvesting system in the photosynthetic bacteria [10].

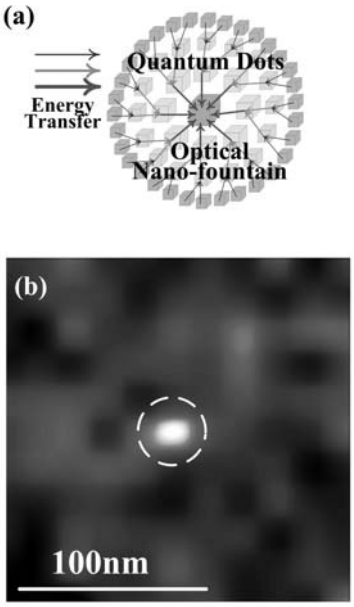

Fig. 4. (a) Schematic explanation of the optical nano-fountain and unidirectional energy transfer. (b) Spatial distribution of the luminescence intensity in an optical nano-fountain. The bright spot surrounded by a broken circle is the focal spot.

When different sized QDs with resonant energy sublevels are distributed as shown in Fig. 4(a), energy transfer occurs via ONF, as illustrated by the arrows. Light incident to the QD array is ultimately concentrated in the largest QD. The size of the area of light concentration corresponds to that of the QD. Therefore, this device realizes nanometric optical concentration. Since the mechanism of the optical nano-fountain is similar to that of the light-trapping system in photosynthetic bacteria, the operation of the optical nano-fountain is a biomimetic action. The device proposed here is called an "*optical nano-fountain*" because light spurts from the largest QD after it is concentrated by stepwise energy transfer from smaller neighboring QDs. In action, the device looks like a fountain in a basin.

For the operation, we maintained a sample at the optimum temperature T (40 K). At T<40 K, the resonant condition becomes tight due to narrowing of the homogeneous linewidth of the quantized energy sublevels, while at T>40 K, the unidirectional energy transfer is obstructed by the thermal activation of excitons in the QDs. A 325-nm He-Cd laser was used as the excitation light source. A double-tapered UV fiber probe with an aperture 20 nm in diameter was fabricated using chemical etching and coated with a 150-nm-thick Al film to ensure sufficiently high detection sensitivity. We have never observed luminescence of the exciton molecules due to the low excitation density of less than 1 W/cm^2. At 40 K, it is not so difficult to find the QD array acting as optical nano-fountain. We found about one optical nano-fountain in 5x5 μm^2 region on the sample surface experimentally.

Figure 4 (b) shows the typically spatial distribution of the luminescence emitted from QDs that operates well as an optical nano-fountain. Here, the collected luminescence photon energy, Ep, was 3.215 eV≤Ep≤3.350 eV, which corresponded to the luminescence from QDs of size 2.5nm≤L≤10nm. The bright spot inside the broken circle corresponds to a spurt from an optical nano-fountain, *i.e.*, the focal spot of the nanometric optical condensing device. The diameter of the focal spot was less than 20 nm, which was limited by the spatial resolution of the near-field spectrometer. From the Rayleigh criterion (*i.e.*, resolution=0.61•λ/NA), we obtained its numerical aperture (NA) of 12 for λ=385nm.

By conventional fabrication method, it is difficult to fabricate the nanophotonic devices, such as the QDs trio functioning as the optical switch, because it is required that the designed sized QDs are placed at designed positions which are closely spaced. Therefore, we are now researching materials, fabrication methods, and systems, such as ZnO dots [12], near-field optical chemical vapor deposition, and a plasmon wave-guide [13], respectively, for the realization of actual nanophotonic devices. Based on these results, we hope that these nanophotonic-device systems will have applications in the future data transmission systems.

II. NANOFABRICATION USING OPTICAL NEAR FIELD

First, the near-field optical chemical vapor deposition (NFO-CVD) is reviewed here [14-16]. In NFO-CVD, ultra-high purity argon (Ar) was used as a buffer gas and diethylzinc (DEZn) as a reacting molecular gas source. A He-Cd laser (λ=325 nm) was used as the light source, which had a photon energy $\hbar\omega$ (=3.81 eV) that was nearly resonant to the absorption band edge E_{abs} of DEZn (4.13eV). The Ar^+ (λ= 488 nm:2.54 eV) and diode (λ=684 nm:1.81 eV) lasers were used as nonresonant light sources. The fiber probe used for NFO-CVD was a high throughput single tapered fiber probe, which was fabricated by pulling and etching a pure silica core fiber.

The cone angle of the fabricated fiber probe was 30 degrees and its apex diameter was 30 nm. Here we used a bare fiber probe for the deposition. Therefore, ONF was generated by light leaking through the circumference of the fiber probe, while ONF was generated at the apex. The separation between the fiber probe and the sapphire substrate was controlled to within several nanometers by using a shear-force technique. The sizes of the deposited Zn dots were measured using a shear-force microscope. During deposition, the partial pressure of DEZn was 100 mTorr and the total pressure in the chamber was 3 Torr.

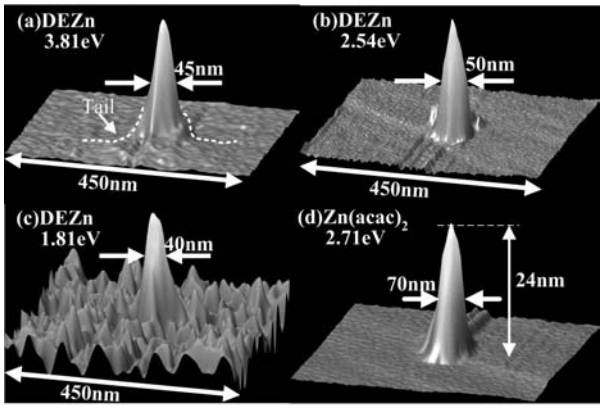

Fig. 5. Shear-force topographical images after NFO-CVD at photon energy of $\hbar\omega$ = 3.81 eV (a), 2.54 eV (b), and 1.81 eV (c) for DEZn. (d) A topographical image after NFO-CVD at photon energy of $\hbar\omega$ = 2.71 eV for $Zn(acac)_2$.

Figure 5 shows the shear-force topographical images of the sapphire substrate after NFO-CVD using ONF with photon energies of 3.81 eV (a), 2.54 eV (b), and 1.81 eV (c), respectively. The laser power and the irradiation time were (a) 2.3 μW and 60 s, (b) 360 μW and 180 s, and (c) 1 mW and 180 s, respectively. The high purity quality of the deposited Zn was confirmed by X-ray photoelectron spectroscopy, and we observed luminescence from ZnO dots prepared by oxidizing the Zn dots fabricated by NFO-CVD. In Fig. 5 (a), the photon energy, is higher than the dissociation energy, E_d, of DEZn, and is close to the absorption band edge, E_{abs}, of DEZn. The diameter (FWHM) and height of the topographical image were 45 and 26 nm, respectively. This image has a small tail, as shown by dotted curves. This tail is a Zn layer, less than 2 nm thick, which is deposited by far-filed light leaking from the bare fiber probe. This deposition is possible because DEZn absorbs a small amount of light with $\hbar\omega$ = 3.81 eV. The very high peak in the image suggests that the ONF enhances the photodissociation rate at this photon energy, because the ONF intensity rapidly increases near the apex of the fiber probe. In Fig.5 (b), the photon energy still exceeds the dissociation energy of DEZn, but it is lower than the absorption band of DEZn. The diameter and height of the image were 50 nm and 24 nm, respectively. While some high intensity far-field light leaked from the bare fiber probe, it did not deposit a Zn layer, so there is no foot at the base of the peak. This confirmed that the photodissociation of DEZn and Zn deposition only occurred with an ONF. In Fig.5 (c), even with such low photon energy ($\hbar\omega$ =1.81 eV), we succeeded in depositing of Zn dots. The topographical image showed a diameter and height of 40 nm and 2.5 nm, respectively.

The photochemical reactions using the ONF with low photon energy have been explained by the excitation of molecular vibration modes. For an optical far field, the adiabatic approximation describes a reaction of molecules well. Since the field intensity is uniform in a neutral molecule smaller than the wavelength, only the electrons in the molecule respond to the electric field with the same phase and intensity. Thus, an optical far field cannot excite the molecular vibration. By contrast, the field intensity is not uniform in a molecule for an ONF with a steep spatial gradient and the electrons respond non-uniformly. As a result of this non-uniform response of the electrons changes the molecular orbital. Thus, the adiabatic approximation becomes unsuitable and the molecular vibration modes are directly excited by photons, as shown in Fig. 6 (a). To evaluate these contributions, we propose an exciton-phonon polariton (EPP) model. The exciton-phonon polariton is a quasi-particle, which is an exciton polariton trailing the phonon (lattice vibration) generated by the steep spatial gradient of its optical filed, as shown in Fig. 6 (b).

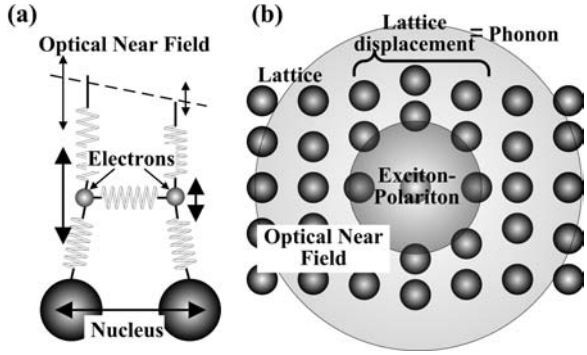

Fig. 6. Schematic explanations of the excitation of molecular vibration mode by the optical near field (a) and the exciton phonon polariton (b).

Such unique transition enables optically inactive molecules to be materials for the optical CVD. We show the deposition of nanometric Zn dots by NFO-CVD using the metal-organic gas zinc-bis(acetylacetonate) ($Zn(acac)_2$), which is not usually used for conventional optical CVD due to its low optical activity, as shown in Fig. 5 (d). In the experiment, ONFs of $\hbar\omega$=2.71 eV (Ar^+ laser) was used. During deposition, the partial pressure of $Zn(acac)_2$ was maintained at 70 mTorr. The laser power and the irradiation time were 1 mW and 15 s, respectively. The diameter and height of the Zn dot were 70 nm and 24 nm, respectively. In spite of the low optical activity of $Zn(acac)_2$, the optical near field can activate the molecule

and its deposition rate was almost the same as that of deposition in which DEZn gas was used, although for the conventional optical CVD, we carried out that DEZn has a deposition rate of more than 1000 times higher that of $Zn(acac)_2$. We consider that the physical origin of this photodissociation of $Zn(acac)_2$ is also the nonadiabatic photochemical process by ONF.

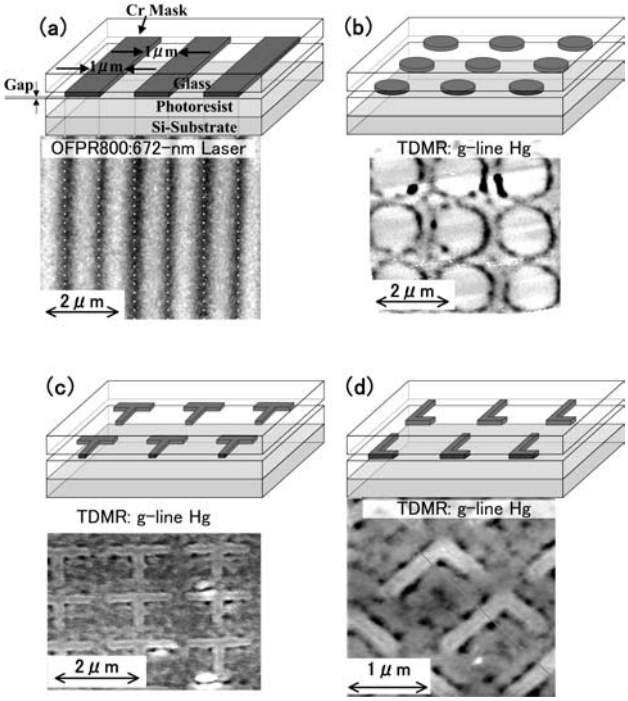

Fig. 7. A schematic of the photo-mask used and the Si-substrate spin-coated with photoresist (OFPR-800 or TDMR-AR87) during the exposure process. AFM images of photoresist after developments for L&S (a), solid circle- (b), T- (c), and L- (d) shaped arrays.

According to EPP model, the nonadiabatic photochemical reaction, that seems to violate the Franck-Condon principle, is a universal phenomenon and is applicable to many other photochemical processes. We applied the nonadiabatic photochemical reaction to photolithography [17]. Figure 7 shows the schematic configuration of the used photo-mask and the Si-substrate spin-coated with two kinds of photoresists (OFPR800 or TDMR-AR87: Tokyo Ohka Kogyo Co., LTD.) at the exposure process in contact mode and the atomic force microscope (AFM) images of the photoresists surface after development, exposed by 672-nm laser for OFPR800 and g-line of Hg lamp for TDMR-AR87, respectively. The 672-nm laser developed the corrugation pattern on the photoresist though this photoresist must be inactive to the 672-nm light. The width and depth of the groove in the corrugation pattern were 200nm and 25nm, respectively. The grooves on the photoresist appeared along the edges of the Cr mask pattern. The exposure process cannot occur by direct irradiation of 672-nm light. However, a steeply spatial gradient of optical energy, which indicates the existence of ONF, is at the edges of the Cr mask pattern. Therefore, these exposed results indicate that the nonadiabatic process originates from the ONF effect.

In demonstrations of nano-photolithography, the photomask with the lines and spaces structure are popularly used, because the problems comes from the interference fringes and the negative effect of light polarization can be reduced by selecting the polarization. However, for more general patterns, *e.g.*, circle-, T-, and L-shaped array, it is impossible to reduce the problem even if the polarization is controlled. Figs 7 (b), (c), and (d) show the AFM images of photoresist after the development. We used photomasks with solid-circle (Fig.7(b)), T- (Fig.7(c)), and L- (Fig.7(d)) Cr mask-arrays. At the exposure, we used the linear polarized light with g-line ($\hbar\omega$ = 2.71 eV) of Hg for i-line ($\hbar\omega$ = 3.40 eV) photoresist of TDMR-AR87. We succeeded in forming arrays of expected shape in a reproducible manner. For comparison, we exposed the photoresist using i-line of a Hg lamp, which has been used for conventional photolithography. We did not obtain the expected shape but obtained only the pattern exposed by the interference fringes of light. This successful development of the arrays of complex structure means that the nonadiabatic near-field photolithography is useful for the practical use. This novel process for photolithography is one of the promising techniques for nanofabrication, because it does not require the expensive vacuum UV light source and optics for the nano-photolithography.

IV. NANOPHOTONIC SYSTEM

This section reviews the overall processing architecture for nanophotonic integrated devices based on high density table lookup. The output port for an incoming packet is determined based on a routing table. For such functions, a content addressable memory (CAM) [18] is used. In a CAM, an input signal serves as a query to a lookup table, and the output is the address of data matching the input. All optical means for implementing such functions have been proposed, for instance, by using planar lightwave circuits. However, since we need separate diffraction-limited optical hardware for each table entry if based on conventional lightwave technology, the overall physical size of the system becomes unfeasibly large, when the number of entries in the routing table is on the order of 10, 000 or more. On the other hand, by using diffraction-limit-free nanophotonic principles, huge lookup tables can be configured compactly.

Suppose that the reference data in the memory $\boldsymbol{D}_j$ (j = 1, · · · , M) and the input $\boldsymbol{S}$ = (s_1, · · · , s_n) are represented in the above format. Then, the function of the CAM will be to derive j that maximizes

$$\boldsymbol{S}\bullet\boldsymbol{D}_j = \left(\sum_{i=1}^{n} s_i \bullet d_i\right)_j . \qquad (3)$$

A nanophotonic implementation of such a function can be implemented in a highly dense form. In addition, a large array of such inner product operations will allow a massively parallel processing system to be constructed [19].

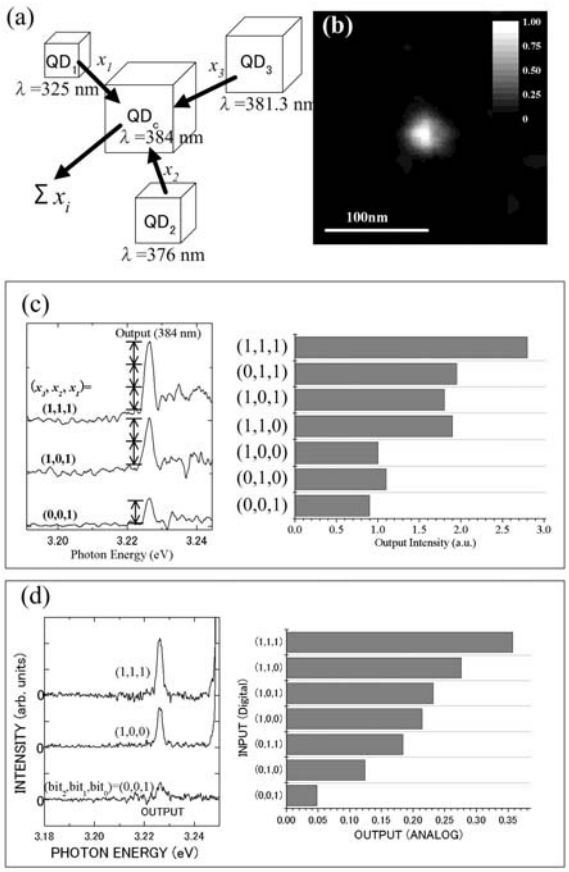

Fig. 8. A schematic explanation of the nanometric summation and experimental result. (b) A scanning image of the output signal from the adder. (c) Experimental results of summation (spectrum and linearity). (d) Experimental result of the digital-to-analog conversion.

The multiplication of two bits, namely $x_i = s_1 \bullet d_i$, has already been demonstrated by a combination of three QDs, *i.e.*, a nanophotonic switch, as shown in Sect. II. Therefore, one of the key operations remaining is the summation, or data gathering scheme, denoted by Σx_i, where all data bits should be taken into account. Here we implement a global data gathering mechanism, or summation, based on the unidirectional energy flow via ONF, as schematically shown in Fig. 8 (a), where surrounding excitations are transferred towards a quantum dot QD_C located at the center.

A proof-of-principle experiment was performed to verify the nanoscale summation using CuCl QDs in a NaCl matrix, which has also been employed for demonstrating nanophotonic switches [9] and optical nano-fountains[10]. We selected a QD arrangement where small QDs (QD_1 to QD_3) surrounded a "large" QD at the center (QD_C), as schematically shown in Fig. 8 (a). Here, these QDs are coupled by ONF. When the energy transfer time between QDs is much faster than the exciton lifetime in QDs, the output signal intensity at a photon energy level form a QD_C with size of 5.9 nm varies approximately as 1:2:3 depending on the number of excited QDs in the vicinity. Hence, this architecture works as a summation mechanism, counting the number of input channels, based on exciton energy transfer via ONF interactions.

In the experiment, three different input light frequencies were assigned to the three-bit input. Here, the output signal is considered to be the radiative relaxation from the lowest energy level of the output QD, which is observed with a near-field fiber probe at a wavelength of 384 nm. The spatial intensity distribution was measured by scanning the fiber probe, as shown in Fig. 8 (b), where the energy is converged at the center. One remark here is that not every excited exciton produces the output signal; for instance there will be loss due to relaxation at each of the input QDs when the output energy level is occupied. However, such effects may not be serious since nutation occurs among resonant energy levels and the relaxation rate at the output QD, which is the largest in the system in terms of size, is smaller than that at the input QDs. Fig. 8(c) shows output signal intensity as a function of the presence (1) or absence (0) of the input excitation, as specified by (x_3, x_2, x_1), which were respectively $\lambda =$ 381.3 nm, 376 nm, and 325 nm. The experimental result shows the output intensity is approximately linearly correlated to the input bit set combination, as shown in Fig. 8 (c) and the set of coupled QDs makes the function of summation. The validity of the digital-to-analog conversion mechanism also obtained using this device. Namely, the output signal intensity at a photon energy level from a QD_C with size of 5.9 nm varies approximately as 1:2:4 depending on the number of excited QDs in the vicinity, as shown in Fig. 8 (d) [20]. Compared to known optical approaches, such as those based on space-domain filtering and focusing lenses or optical waveguides, and intensity filters, the nanophotonic approach achieves a significantly higher spatial density.

V. Conclusion

This paper reviewed nanophotonics, a novel optical nanotechnology utilizing local electromagnetic interactions between nanometric elements via ONF. Its potential for high integration beyond the diffraction limit of light can solve the technical problems of the future optical industry. In the nanophotonic device, ONF is used as a carrier to transmit the signal. As key devices, we reviewed a nanophotonic switch and an optical nano-fountain based on ONF energy transfer between QDs.

We demonstrated NFO-CVD of nanometric Zn dots based on the photodissociation of gas-phase diethylzinc using ONF under nonresonant conditions. We explain the

photodissociation mechanism using multiple-step excitation process via the molecular vibration mode. In this process, the enhanced coupling between the optical field and molecular vibration originates from the steep spatial gradient of the optical power of ONF. Such a nonadiabatic photochemical process violates the Franck-Condon principle, and it can be applied to other photochemical phenomena. The process involved in the photochemical reaction based on ONF reported here will open new method in nanotechnology. As applicable examples of this nonadiabatic photochemical reaction, we demonstrated the patterning by the near-field photolithography using a visible light for UV photoresist. The experimental results of the near-field photolithography also strongly support the nonadiabatic photochemical process.

An architectural approach to nanophotonic information and communication systems is also discussed. One is a memory-based architecture which is based on table lookup using an ONF interaction between QDs. In addition, content addressable memories, digital logic, and matrix-vector multiplication can be implemented in this architecture. As fundamental functional elements, a data summation mechanism and digital-to-analog conversion are presented, and their proof-of-principle experiments are demonstrated using CuCl QDs. Owing to its high spatial density and low power dissipation, a massive array of such functional components will be useful in applications such as massive table lookup operations in networking and information processing systems.

REFERENCES

[1] M. Ohtsu, K. Kobayashi, T. Kawazoe, S. Sangu, and T.Yatsui, “Nanophotonics: design, fabrication, and operation of nanometric devices using optical near fields”, IEEE J. Sel. Top. Quant. Electron, vol. 8, p839-862, Jul./Aug. 2002.

[2] M. Ohtsu, ”Near-field nano-optics toward nano/atom deposition”, in Tech. Dig. 18th Congr. Int. Commission for Optics, 1999, SPIE, pp. 478–479, vol. 3749, 1999.

[3] C. R. Kagan, C. B. Murray, M. Nirmal, and M. G. Bawendi, “Electronic energy transfer in CdSe quantum dot solids”, Phys. Rev. Lett. Vol. 76, p1517-1520, Feb. 1996.

[4] T. Kawazoe, K. Kobayashi, J. Lim, Y. Narita, and M. Ohtsu, "Direct Observation of Optically Forbidden Energy Transfer between CuCl Quantum Cubes via Near-Field Optical Spectroscopy", Phys. Rev. Lett., vol.88, no.6, pp.067404-1 - 067404-4, Feb. 2002,

[5] S. Sangu, K. Kobayashi, A. Shojiguchi, T. Kawazoe, and M. Ohtsu, "Excitation energy transfer and population dynamics in a quantum dot system induced by optical near-field interaction", J. Appl. Phys., Vol.93, No.5, pp.2937-2945, Mar. 2003.

[6] K. Kobayashi, S. Sangu, T. Kawazoe, and M. Ohtsu, “Exciton dynamics and logic operations in a near-field optically coupled quantum-dot system”, J. of Lumin., Vol.112, No. 1-4, pp. 117-121, Apr. 2005.

[7] S. A. Crooker, J. A. Hollingsworth, S. Tretiak, and V. I. Klimov, “Spectrally resolved dynamics of energy transfer in quantum-dot assemblies: Towards engineered energy flows in artificial materials,” Phys. Rev. Lett., vol. 89, p. 186802-1 - 186802-4, Oct. 2002.

[8] T. Kawazoe, K. Kobayashi, S. Sangu, and M. Ohtsu, "Demonstrating nanophotonic switching using near-field pump-probe photoluminescence spectroscopy of CuCl quantum cubes", J. Microscopy, Vol.209, Pt 3, pp.261-266, Mar. 2003.

[9] T. Kawazoe, K. Kobayashi, S. Sangu, and M. Ohtsu, "Demonstration of a nanophotonic switching operation by optical near-field energy transfer", Appl. Phys. Lett., Vol.82, No.18, p.2957-2959, May 2003.

[10] T. Kawazoe, K. Kobayashi, and M. Ohtsu, “Optical nanofountain: A biomimetic device that concentrates optical energy in a nanometric region”, Appl. Phys. Lett., Vol.86, No.10, pp.103102-1 - 103102-3, Mar. 2005.

[11] W. Nomura, M. Ohtsu, and T. Yatsui, “Nanodot coupler with a surface plasmon polariton condenser for optical far/near-field conversion,” Appl. Phys. Lett. Vol. 86, No.18, p.181108-1 – 181108-3, May 2005.

[12] T. Yatsui, T. Kawazoe, T. Shimizu, Y. Yamamoto, M. Ueda, M. Kourogi, M. Ohtsu, and G.H. Lee, "Observation of size-dependent features in the photoluminescence of zinc oxide nanocrystallites by near-field ultraviolet spectroscopy", Appl. Phys. Lett., vol.80, no.8, p1444-1446, Feb. 2002.

[13] T. Yatsui, M. Kourogi, and M. Ohtsu, "Plasmon waveguide for optical far/near-field conversion", Appl. Phys. Lett., vol.79, no.27, p 4583-4585, Dec. 2001.

[14] Y. Yamamoto, M. Kourogi, M. Ohtsu, V. Polonski and G.H. Lee, "Fabrication of nanometric zinc pattern with photodissociated gas-phase diethylzinc by optical near field", Appl. Phys. Lett., vol.76, no.16, p2173-2175, Apr. 2000.

[15] T. Kawazoe, Y. Yamamoto, and M. Ohtsu, "Fabrication of nanometric Zn dots by nonresonant near-field optical chemical-vapor deposition", Appl. Phys. Lett., vol.79, no.8, pp.1184-1186, Aug. 2001.

[16] T. Kawazoe, K. Kobayashi, S. Takubo, and M. Ohtsu, “Nonadiabatic photodissociation process using an optical near field”, J. Chem. Phys., Vol.122, No.2, pp.024715-1 – 024715-5, Jan. 2005.

[17] T. Kawazoe and M. Ohtsu, "Adiabatic and nonadiabatic nanofabricatin by localized optical near fields", Proceedings of SPIE Vol. 5339, p619-631, Jan. 2004.

[18] H. Liu, "Routing Table Compaction in Ternary CAM", IEEE Micro, vol. 22, no. 1, pp. 58-64, Jan.-Feb. 2002.

[19] M. Naruse, T. Miyazaki, F. Kubota, T. Kawazoe, K. Kobayashi, S. Sangu, M. Ohtsu, “Nanometric summation architecture using optical near-field interaction between quantum dots”, Optics Letters, Vol. 30, No. 2, p201-203, Jan. 2005.

[20] M. Naruse, T. Miyazaki, T. Kawazoe, K. Kobayashi, S. Sangu, F. Kubota, M. Ohtsu “Nanophotonic computing based on optical near-field interactions between quantum dots”, IEICE Transaction on Electronics Special Section on Nanophotonics, to be published, 2005.

[IS19]

Nanophotonics using optical near fields

T. Kawazoe[1]*, T. Yatsui[1] and M. Ohtsu[1,2]
[1]Japan Science and Technology Agency, Japan; [2]University of Tokyo, Japan
kawazoe@ohtsu.jst.go.jp

Optical data transmission systems require increased integration of photonic devices for higher data transmission rates. It is estimated that the size of photonic switching devices should be reduced to a sub-wavelength scale, as in the near future it will be necessary to integrate more than 10000×10000 input and output channels on a module. Since conventional photonic devices, *e.g.*, diode lasers and optical waveguides, have to confine light waves within their cavities and core layers, respectively, their minimum sizes are limited by the diffraction of light. Therefore, they cannot meet the size requirement, which is beyond this diffraction limit. It can be readily understood that a novel optical nanotechnology, i.e., nanophotonics, is required in order to go beyond the diffraction limit [1].

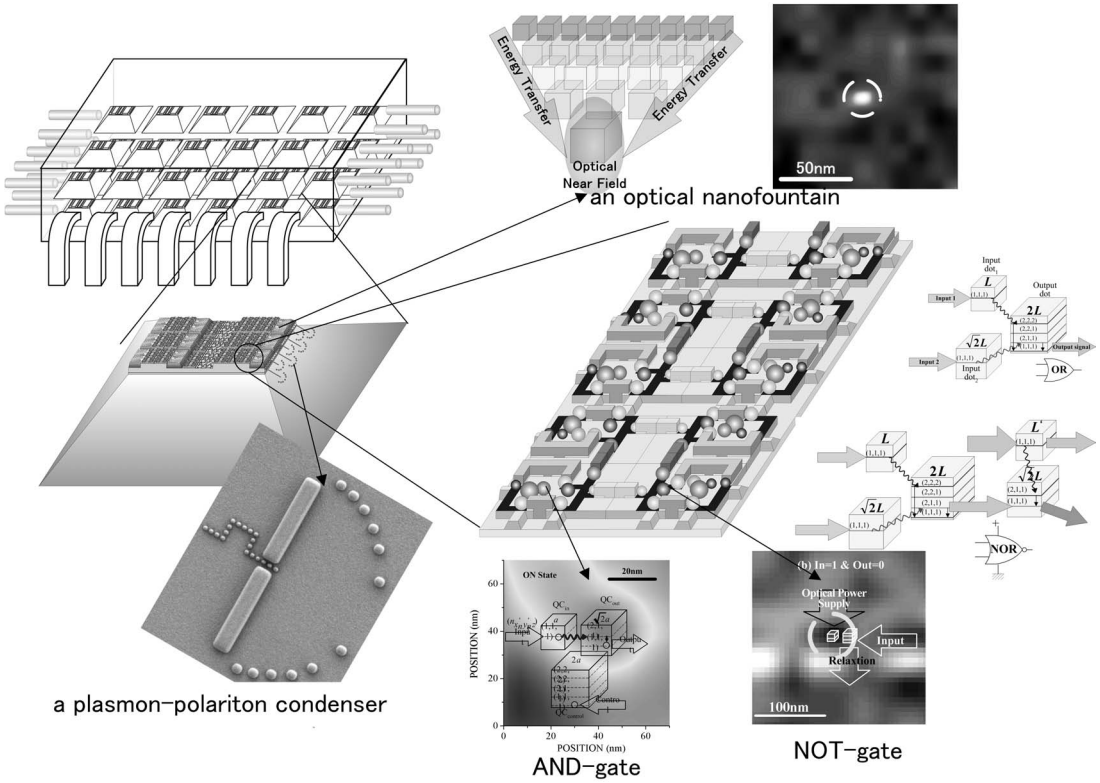

An optical near field, which is generated on the nanometric element, is free from the diffraction of light and enables the operation and integration of nanometric optical devices. Namely, by using the localized optical near field as the signal carrier, which is transmitted from one nanometric element to another, the nanoscale photonic device going beyond the diffraction limit can be realized. The primary advantage of nanophotonics is the capacity to achieve novel functions that are based on local electromagnetic interactions, while realizing nanometer-sized photonic devices. Based on this idea, we observed an optically forbidden energy transfer between neighboring QDs via an optical near-field [2] and proposed the several kinds of nanometric optical device [3-6]. They are a nanometric AND- [3], NOT-, XOR- [4] logic gates, a surface plasmon-polariton condenser [5], and an optical nanofountain (*i.e.*, a nanometric optical condenser) [6], as shown in the figure. So far, we have succeeded in the demonstration of the operations of the AND gate, the surface plasmon-polariton condenser and the optical nanofountain. We introduce and demonstrate these unique devices using optical near field.

[1] M. Ohtsu, et al., IEEE J. Sel. Top. Quant. Electron **8**, 839 (2002).
[2] T. Kawazoe, K. Kobayashi, J. Lim, Y. Narita, and M. Ohtsu, Phys. Rev. Lett. **88**, 067404 (2002).
[3]T. Kawazoe, K. Kobayashi, S. Sangu, and M. Ohtsu, Appl. Phys. Lett., **82**, 2957 (2003).
[4] S. Sangu, K. Kobayashi, A. Shojiguchi, and M. Ohtsu, Phys. Rev. B, **69**, 115334.
[5] W. Nomura, T. Yatsui, and M. Ohtsu, submitted to Appl. Phys. Lett.
[6] T. Kawazoe, K. Kobayashi, and M. Ohtsu, to be published Appl. Phys. Lett., **86**, (2005).

Keywords: Nanophotonics, Nanophotonic Device, Optical near field, Energy transfer,

Development of optical far-/near-field conversion device

Motoichi Ohtsu [a,b], Wataru Nomura [a] and Takashi Yatsui[b]

[a] School of Engineering, The University of Tokyo, 7-3-1 Hongo, Bunkyo-ku, Tokyo 113-8656, Japan
[b] "Nanophotonics" team SORST, Japan Science and Technology Agency, 687-1 Tsuruma, Machida, Tokyo 194-0004, Japan

ohtsu@ee.t.u-tokyo.ac.jp

Abstract — **To transmit an optical signal to a nanophotonic device, a nanodot coupler was fabricated from a linear array of closely spaced metallic nanoparticles. To increase the optical far- to near-field conversion efficiency, a surface plasmon polariton (SPP) condenser was also fabricated so that it worked as a "phased array". The SPP was focused with a spot size as small as 400 nm at λ = 785 nm. When the focused SPP was incident into the nanodot coupler, its transmission length through the nanodot coupler was confirmed to be three times longer than that of a metallic core waveguide and this efficient energy transmission was also observed in a zigzag-shaped nanodot coupler. Furthermore, we confirmed that the nanodot coupler transfers optical energy more efficiently with the resonant light scattering of Au nanoparticle.**

Keywords — **nanophotonics, optical near-field coupling, surface plasmon polariton, localized surface plasmon**

I. Introduction

Future optical transmission and data processing systems will require advanced photonic devices, and their integration, in order to increase data processing rates and capacity. Consequently, these devices will have to be significantly smaller than conventional diffraction-limited photonic devices. To meet this requirement, we have proposed nanometer-scale photonic integrated circuits (nanophotonic ICs) that are composed of nanometer-sized elemental devices (nanophotonic devices).[1] As a representative device, a nanophotonic switch was proposed and its operation was demonstrated by controlling the dipole forbidden optical energy transfer among resonant energy states in CuCl quantum cubes via an optical near field.[2] To fabricate nanophotonic devices, we also developed a near-field optical chemical-vapor deposition technique with nanometer-scale resolution and accuracy in size, position, and separation.[3-5]

II. Optical Far/Near-Field Conversion Device

For use in future photonic systems, the nanophotonic devices and ICs must be connected to conventional diffraction-limited photonic devices. This connection requires a far/near-field conversion device, such as a nanometer-scale optical waveguide. The performance parameters required of this device include:

A) High conversion efficiency
B) A guided beam width of less than 100 nm for efficient coupling of the converted optical near-field to sub-100 nanometer-sized dots.
C) A transmission length that is longer than the optical wavelength to avoid direct coupling of the propagating far-field light to the nanophotonic device consisted of nanometer-scale dots. (The transmission length l_t is defined as $I(z) = I(0)\ exp(-z/l_t)$, where $I(z)$ is the optical intensity and z is the longitudinal position measured from the input terminal ($z = 0$)).

One candidate device that meets these performance requirements is a plasmon waveguide using a metallized silicon wedge structure that converts propagating far-field light to an optical near-field.[6] In this device, a one-dimensional TM plasmon mode is excited efficiently via a metallic core waveguide along the plateau. However, the l_t of the TM plasmon mode is still in the order of 700 nm (at λ = 830 nm) for a metallic core waveguide with a gold core (diameter D = 10 nm) insulated using air.[7] To increase l_t, a more promising candidate is a nanodot coupler consisting of an array of closely spaced metallic nanoparticles, because higher transmission efficiency is expected owing to the plasmon resonance in the closely spaced metallic nanoparticles.[8] Energy transfer along the nanodot coupler relies on the near-field coupling between the plasmon-polariton mode of the neighboring nanoparticles.

To increase in the efficiency of exciting localized surface plasmon in the nanodot coupler than that excited by propagating far-field light, we equipped the nanodot coupler with a surface plasmon polariton (SPP) condenser for efficient far/near-field conversion. Figure 1(a) shows the proposed optical far/near-field conversion device. Incoming far-field light is first transformed into the two-dimensional SPP mode on the gold film [see Fig. 1(b)]. Then, the SPP mode is scattered and focused by the SPP condenser, which consists of several hemispherical metallic submicron particles that are arranged in an arc and work as a "phased array" [Fig.

1(c)].[9] The input terminal of the nanodot coupler is fixed at the focal point of the SPP. Finally, after the localized surface plasmon transmits through the nanodot coupler, it is converted into an optical near-field so that it couples to the nanophotonic device.

The advantages of this device are that it has

(1) A high conversion efficiency, from the SPP mode to the localized surface plasmon in the nanodot coupler, owing to coupling the scattering at the inlet metallic nanoparticle.[10]
(2) No cut-off diameter of the metallic nanoparticle array, *i.e.*, the beam width decreases with the diameter because the electric field vector, which is dominant in the nanodot coupler, involves only a Förster field.[8]
(3) Long-distance propagation of the TM-plasmon mode. For example, the calculation using the finite-difference time domain (FDTD) method estimated a transmission length of l_t = 2 μm (at an optical wavelength λ = 785 nm) for a plasmon-polariton mode with linearly aligned 50-nm dots with 10-nm separation.[11,12]

Advantages (1) to (3) are compatible with meeting requirements (A) to (C), respectively.

III. Surface Plasmon Polariton Condenser

To fabricate the nanodot coupler and SPP condenser using a focused ion beam (FIB), we used a silicon-on-insulator (SOI) wafer to avoid ion beam drift. The fabrication process was as follows:

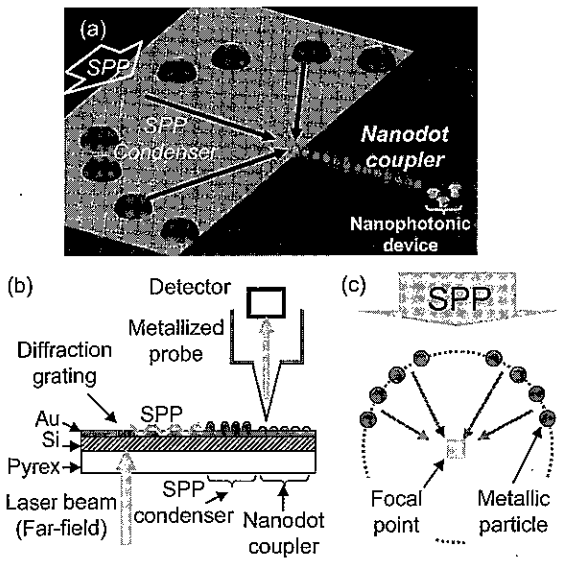

Fig. 1 (a) Bird's eye view of a nanodot coupler with a surface plasmon-polariton (SPP) condenser. (b) Experimental system. (c) Schematic illustration of the SPP condenser.

(i) A (100)-oriented SOI wafer was bonded to a glass substrate by anodic bonding (300 V, 350 °C, 10 min.) [Fig. 2(a)].[13] Maintaining the silicon wafer thickness at less than 10 μm kept the optical propagation loss sufficiently low.
(ii) After removing the silicon substrate and SiO_2 layer from the SOI wafer by wet etching, carbon hemispheres were deposited using FIB [Fig. 2(b)].
(iii) To excite SPP mode and enhance the optical near-field energy, a 120-nm-thick gold film was applied using sputtering [Fig. 2(c)]. The number of hemispheres, their positions, and their sizes were optimized using the FDTD method in order to minimize the focused spot size.[12]
(iv) Finally, a diffraction grating was fabricated using a FIB milling technique 50 μm below the condenser in order to excite the SPP by the incident optical far-field (a laser beam).

Figures 2(d) and 2(e) show scanning electron microscopic (SEM) images of the SPP condenser and nanodot coupler. Two banks were fabricated, in order to avoid illumination of the nanodot coupler by the satellite spots (originating from higher-order diffraction) [Fig. 2(d)]. The nanodot coupler consisted of a linear array of nanoparticles with diameters of 230 nm separated by 70 nm. The SPP condenser consisted of twelve scatterers 350 nm in diameter, aligned on an arc with a diameter of 10 μm.

The spatial distribution of the optical near-field energy was observed using a collection mode near-field optical microscope (NOM) [see Fig.1 (b)]. A light source with a wavelength of λ = 785-nm light was used to transmit the far-field light through the 10-μm-thick Si substrate. A

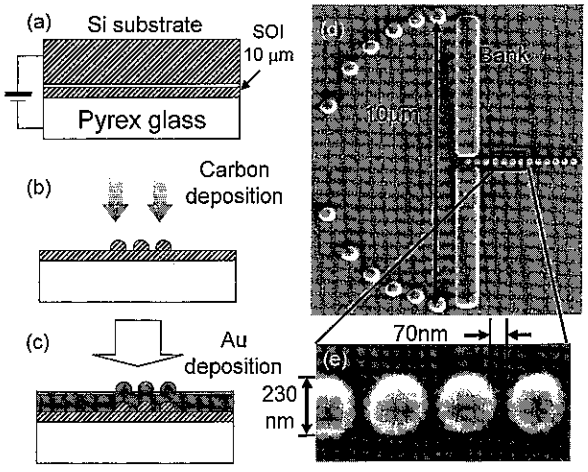

Fig. 2 Fabrication of the nanodot coupler and SPP condenser: (a) anodic bonding [step (i)], (b) carbon hemisphere deposition using FIB [step (ii)], (c) 120-nm gold film deposition using sputtering [step (iii)], (e) and (d) SEM images of the fabricated nanodot coupler and SPP condenser.

sharpened fiber probe with 20-nm-thick gold film was used to enhance the collection efficiency.[14]

First, we checked whether the SPP condenser led to efficient scattering and resultant focusing of the SPP by exciting the SPP mode through the grating coupler. Figures 3(a) and 3(b) show a shear-force image of the SPP condenser and the spatial distribution of the optical near-field energy, respectively. As shown in the cross-sectional profile [dashed curve in Fig. 3(d)] through the focal point of the SPP [white dotted line in Fig. 3(b)], the full width at half maximum (FWHM) of the spatial distribution of the SPP was as narrow as 400 nm. Figure 3(c) shows the spatial distribution of the optical near-field energy in the SPP condenser calculated using the FDTD method, where each cell was 50 × 50 × 25 nm and the model consisted of 240 × 240 × 80 cells. Considering the tip diameter (50 nm) of the metallized fiber probe used for collection mode, the observed distribution [Fig. 3(b) and dashed curve in Fig. 3(d)] was in good agreement with the calculated results [FWHM = 380 nm, solid curve in Fig. 3(d)]. These results imply that our device works as an efficient phased array.

IV. NANODOT COUPLER VS METALLIC CORE WAVEGUIDE

Next, we measured the spatial distribution of the optical near-field energy on a linear nanodot coupler, the input terminal of which was fixed at the focal point of the SPP. Figures 4(a) and (b) show an SEM image and the spatial distribution of the optical near-field energy on the nanodot coupler, respectively. The black dots in Fig. 4(c) show cross-sectional profiles along the white broken line in Figure 4(b). Position $x = 0$ corresponds to the focal point of the SPP condenser. Although not all of the energy couples to the nanodot coupler owing to mode mismatch, the optical near-field intensity has a maximum at each edge of the nanoparticles. This is due to artifact resulting from the fiber probe at constant height mode. The dips indicated by arrows *A* and *B* originate from interference of the localized surface plasmon in the nanodot coupler that arises from reflection at the output terminal. However, the exponential envelope [solid curve of Fig. 4(c)] fitted by neglecting these influences indicates that the transmission length l_t was 4.0 μm. l_t was five times longer than the wavelength, which meets requirement (C). The beam width was 250 nm, which is comparable to the nanoparticle size. As the size of the nanoparticles was determined by the resolution of FIB for carbon hemisphere deposition, the beam width can be decreased to sub-50 nm scale using electron beam lithography, which will meet requirement (B).

Then we checked whether near-field coupling between the neighboring nanoparticles resulted in lower propagation loss by comparing our device with a metallic core waveguide. For this purpose, we fabricated a gold core waveguide the same width as the diameter of the nanoparticles in the nanodot coupler, with its input terminal also fixed at the focal point of the SPP. The open circles in Fig. 4(d) show the cross-sectional profile of the metallic core waveguide and the exponential envelope [solid curve in 4(d)] indicates that the transmission length l_t was 1.2 μm. To evaluate the observed transmission length, we calculated the theoretical value of our metallic core waveguide. Since the Au core waveguide is placed on a Si substrate, we calculated one-dimensional TM plasmon mode[15] in the cylindrical Au core waveguide with an diameter of 250 nm ($\varepsilon_{Au} = (0.174 + i\ 4.86)^2 = -23.59 + i\ 1.69$)[16] surrounded by the medium with an average dielectric constant of Si and air,[17] $\varepsilon_{cl} = \{(3.705 + i\ 0.007)^2 + 1\}/2 = 7.36 + i\ 0.03$.[16] Based on these assumptions, the calculated transmission length of our Au core waveguide is 1.4 μm. Since this is in good agreement with the

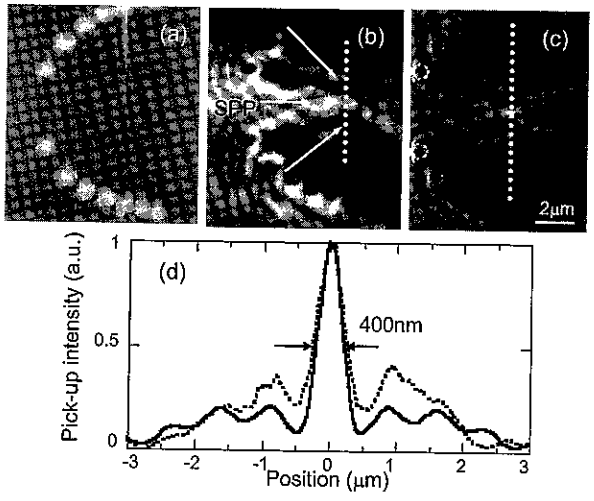

Fig. 3 (a) Shear-force image of the SPP condenser. (b) The near-field energy distribution of (a) taken at λ = 785 nm. (c) Calculated spatial distribution of the electric-field energy using the FDTD method. The dashed and solid curves in (d) are cross-sectional profiles along the dashed white lines in (b) and (c), respectively.

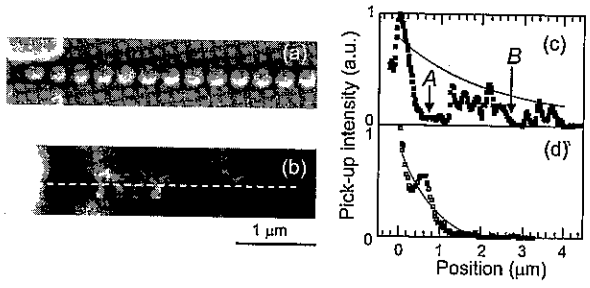

Fig. 4 SEM image (a) and the near-field energy distribution (b) of a linearly chained nanodot coupler. (c) Solid circles show the cross-sectional profiles along the white dashed line in (b). The solid curve shows the fitted exponential envelope. A and B indicate dips resulting from the length of the nanodot coupler. (d) Open circles show the cross-sectional profiles along metallic core waveguide and the solid curve shows the fitted exponential envelope.

observed value (1.2 μm), the comparison confirmed that more efficient energy transfer was realized by the nanodot coupler.

Furthermore, we also observed the spatial distribution of the optical near-field energy for a zigzag-shaped nanodot coupler [see Fig. 5(a) and 5(b)]. Corners A to D in Fig. 5(c) represent the profiles at locations A to D in Fig. 5(d), respectively. Comparing adjacent curves, we found that the energy loss at corners A-D was negligible. This is attributed to efficient coupling of the TM and TE localized surface plasmon at the corners. As a result, the transmission length through this zigzag-shaped nanodot coupler was equivalent to that through a linear one.[18] Although efficient coupling was predicted using the point-dipole approximation,[8] this is the first experimental confirmation of it. Such high flexibility in the arrangement of nanoparticles is an outstanding advantage for optical far/near-field conversion for driving nanophotonic devices.

V. Resonant Light Scattering

It is known that the metallic nanoparticle that is component of nanodot coupler has resonant light scattering. Therefore, it can be thought that the nanodot coupler also has the particle size dependence in optical energy transmission efficiency. To clear this matter, we confirmed the relationship between the nanodot coupler and the resonant light scattering.

We checked whether the Au nanoparticles led to efficient scattering. Au nanoparticles were fabricated on the glass substrate using FIB milling technique. The fabrication process was as follows:

(i) A 50nm thick Au film was deposited using sputtering on the glass substrate [Fig.6 (a)].
(ii) Carbon hemispheres were deposited using FIB [Fig.6 (b)].
(iii) Using carbon hemisphere as a mask, Au nanoparticles were obtained by FIB milling [Fig.6 (c)].

Fig.6 (d) shows the SEM image of Au nanoparticles. They were arranged with longer separation than each diameter, resulting in no near-field interaction each other.

The spatial distribution of the optical near-field intensity for the Au nanoparticles in diameter D range from 100 to 300 nm were observed by the collection mode NOM at λ = 785 nm. Figures 7(a) and 7(b) show the topographical and NOM images of the Au nanoparticles. As shown in the cross sectional profile [see Fig. 7(c)], the optical near-field intensity I takes the maximum for the Au nanoparticle with 200 nm in diameter (labeled w). In order to find the origin of this resonance, a calculation was performed. Mie's theory of scattering by an Au prolate spheroid (see Fig. 7(d)) was employed, and only the first TM mode was considered.[17] The solid curve in Fig. 7(e) represents the normalized polarizability $|\mathrm{Re}(\alpha^2/V)|$ (α:polarizability, V : volume) as a function of the diameter D of the Au prolate spheroid whose short axis was fixed as 50 nm. The calculated resonant diameter (190 nm) is in good agreement with the experimentally confirmed particle size (D = 200 nm).

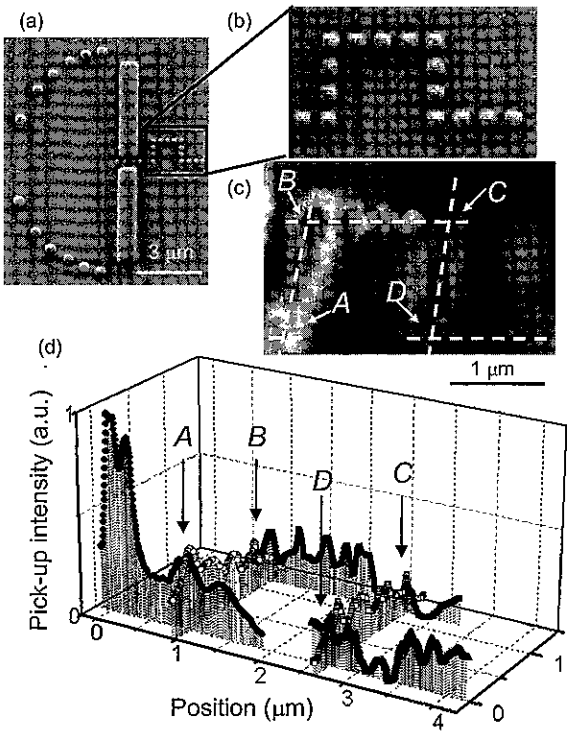

Fig. 5 SEM (a) (b) images and the near-field intensity distribution (c) of a zigzag-shaped nanodot coupler. (d) The cross-sectional profiles along the dashed white lines in (c). The arrows A to D indicate the corners.

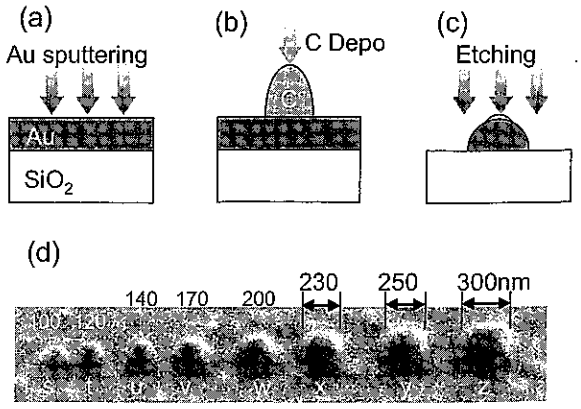

Fig. 6 Fabrication of Au nanoparticles on the glass substrate: (a) Au film sputtering [step(i)] (b) Carbon hemisphere deposition using FIB [step(ii)] (c) FIB milling [step(iii)] (d) The SEM image of Au nanoparticles with respective diameter D=100 nm *(s)*, 120 nm *(t)*, 140 nm *(u)*, 170 nm *(v)*,

Next, we checked the optical near-field energy transfer along the Au nanodot coupler. As a nanodot coupler, a linear array of Au nanoparticles in diameter D range from 150 to 300 nm with their center to center separations of 1.2 D were fabricated using FIB milling technique (Fig. 6(a)~(c)). The spatial distributions of optical near-field energy were observed by the collection mode NOM taken at arrangement for 2D SPP mode excitation by Attenuated Total Reflection method. Figure 8(a) and 8(b) show the topographical and NOM images of the nanodot couplers, respectively. Figure 8(c) shows the cross-sectional profile through the outlet of the nanodot couplers. Note that the output energy was efficiently obtained only for the nanodot coupler with D = 200 nm, which is consistent with the experimental results shown in Fig.7. These results confirm that such an efficient energy transfer along the Au nanoparticles is due to the near-field coupling between resonant plasmon-polariton modes of neighboring particles.

VI. Conclusion

In summary, we proposed and fabricated an optical far/near-field conversion device that consisted of a nanodot coupler and an SPP condenser. The FWHM of the spatial distribution of the optical near-field energy at the focal point of the SPP was as small as 400 nm at λ = 785 nm. Furthermore, installing a linear nanodot coupler at the focal point of the SPP realized efficient excitation of plasmon-polariton mode with a transmission length of 4.0 μm. Equivalent energy transfer was observed in zigzag-shaped nanodot couplers.

Furthermore, we directly observed resonant light scattering of Au metallic nanoparticle in diameter of

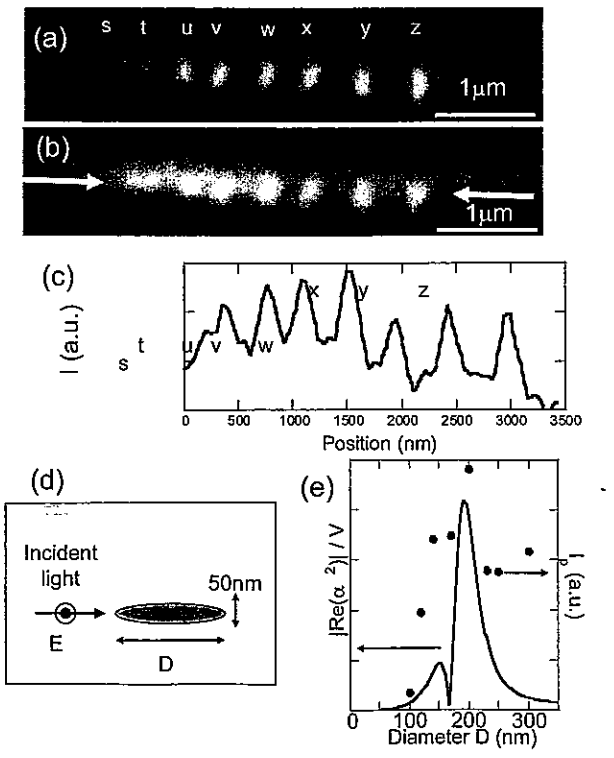

Fig.7 (a) Shear-force image of Au nanoparticles. Each label indicates the same nanoparticle with Fig6 (d). (b) Intensity I distribution of optical near-field of (a). (c) Cross-sectional profiles between the white arrows in (b). (d) Calculation model of prolate spheroid. (e) Solid circles show the peak intensity I_P of the respective Au nanoparticles. Solid curve shows the calculated normalized polarizability of Au prolate spheroid.

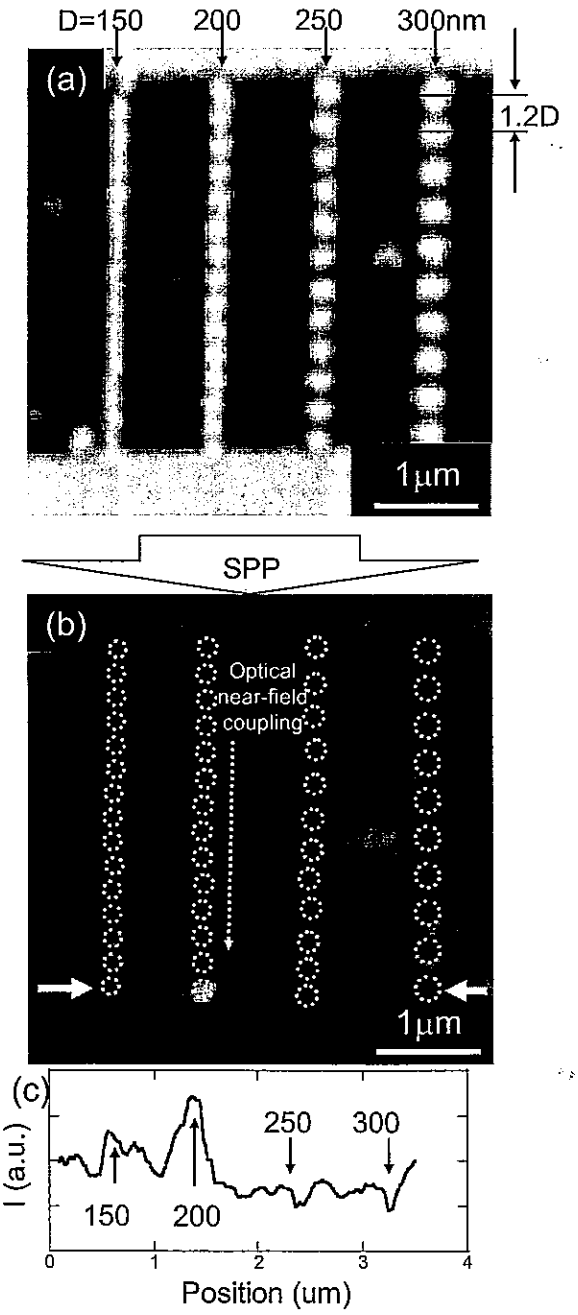

Fig.8 (a) Shear-force and (b) NOM image of Au nanodot couplers of D=150, 200, 250, 300nm. (c) Cross-sectional profiles between the white arrows in (b).

200nm at the wavelength λ = 785nm. And we confirmed that the nanodot coupler transfers optical energy more efficiently with nanoparticles in the resonant size.

These results confirm that a nanodot coupler with an SPP condenser can be used as the optical far/near-field conversion device required by future systems.

REFERENCES

[1] M. Ohtsu, K. Kobayashi, T. Kawazoe, S. Sangu, and T. Yatsui, *IEEE Journal of Selected Topics in Quantum Electronics*, vol. 8, pp. 839 (2002).

[2] T. Kawazoe, K. Kobayashi, S. Sangu, and M. Ohtsu, *Appl. Phys. Lett.*, vol. 82, pp. 2957 (2003).

[3] Y. Yamamoto, M. Kourogi, M. Ohtsu, V. Polonski, and G.H. Lee, *Appl. Phys. Lett.*, vol. 76, pp. 2173 (2000).

[4] Y. Yamamoto, M. Kourogi, M. Ohtsu, and T. Kawazoe, *IEICE Trans. Electron.*, vol. E85-C, pp. 2081 (2002).

[5] T. Yatsui, T. Kawazoe, M. Ueda, Y. Yamamoto, M. Kourogi, and M. Ohtsu, *Appl. Phys. Lett.*, vol. 81, pp. 3651 (2002).

[6] T. Yatsui, M. Kourogi, and M. Ohtsu, *Appl. Phys. Lett.*, vol. 79, pp. 4583 (2001).

[7] J. Takahara, S. Yamagishi, H. Taki, A. Morimoto, and T. Kobayashi, *Opt. Lett.*, vol. 22, pp. 475 (1997).

[8] M. L. Brongersma, J. W. Hartmanm and H. A. Atwater, *Phys. Rev. B*, vol. 62, pp. R16356 (2000).

[9] I. I. Smolyaninov, D. L. Mazzoni, J. Mait, and C. C. Davis, *Phys. Rev. B*, vol. 56, pp. 1601 (1997).

[10] T. Yatsui, M. Kourogi, and M. Ohtsu, *Appl. Phys. Lett.*, vol. 71, pp. 1756 (1997).

[11] M. Quinten, A. Leitner, J. R. Krenn, and F. R. Aussenegg, *Opt. Lett.*, vol. 23, pp. 1331 (1998).

[12] The computer simulations in this paper are performed by a FDTD-based program, *Poynting for Optics*, a product of Fujitsu, Japan.

[13] T. R. Anthony, *J. Appl. Phys.*, vol. 58, pp. 1240 (1998).

[14] T. Yatsui, K. Itsumi, M. Kourogi, and M. Ohtsu, *Appl. Phys. Lett.*, vol. 80, pp. 2257 (2002).

[15] L. Novotny and C. Hafner, *Phys. Rev.*, vol. E 50, pp. 4094 (1994).

[16] Edited by E. D. Palik, *Handbook of Optical Constants of Solids*, (Academic, New York, 1985).

[17] H. Kuwata, H. Tamaru, K. Esumi, and K. Miyano, *Appl. Phys. Lett.*, vol. 83, pp. 4625 (2003).

[18] W. Nomura, M. Ohtsu and T. Yatsui, *Appl. Phys. Lett.*, vol. 86, pp. 181108 1-3 (2005)

4C-059-P

Fabrication of a Near-Field Optical Probe by Electroless Nickel Plating

Ikuhiro Kato, Shuji Mononobe,***, Motoichi Ohtsu****, Hideo Honma***

Graduate School of Engineering, Kanto Gakuin University
**Faculty of Eng., Kanto Gakuin Univ., 1-50-1, Mutsuurahigashi, Yokohama 236-8501, Japan*
*** PRESTO, Japan Sci. & Technol. Agency,*
****Kanagawa Acad. of Sci. & Technol.*
KSP East 409, 3-2-1, Sakado, Takatsu, Kawasaki 213-0012 Japan
***** Electron. Eng., Univ. of Tokyo, Tokyo 113-8656, Japan*
surfeng@kanto-gakuin.ac.jp

Scanning near field optical microscopy (SNOM) employing a probe is widely applied for nanometric optical imaging, spectroscopic investigation, molecular sensing, and so on. To fabricate high resolution probes, tapering an optical fiber that metallizing and protruding its apex from metal film has been used as an effective method. However, it is difficult to mass-produce SNOM probes by the methods due to the low reproducibility of the protruding. We proposed a new method to produce SNOM probes based on the electroless plating. This method involves four wet processes: etching, surface sensitization, palladium nucleation, and electroless plating. However, reproducibility for preparation of micro aperture on a probe apex is low due to the lack of stability of sensitization and palladium nucleation solution. Therefore we developed new catalyst method using palladium spattering and followed plating. We have been investigated that influence of addition of lead and ammonium ion for aperture size on a probe apex. As a result, we are able to prepare the aperture size under 100 nm on a probe apex.

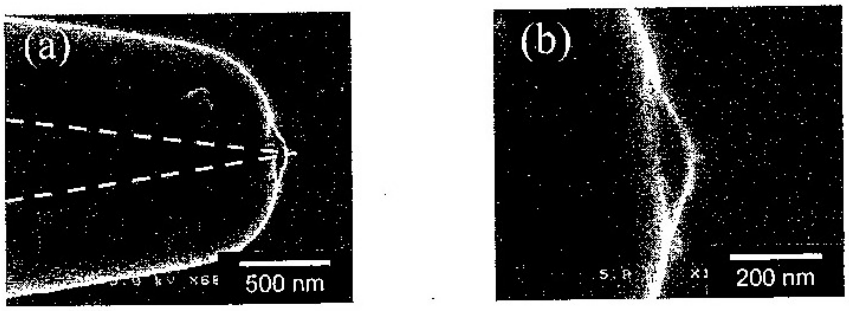

Figure 1. Scanning electron microscope (SEM) images of SNOM probe fabricated by electroless plating.
(b): expansion image of (a). Aperture size of the probe is 30 nm

Size- and position-controlled nano-scale fabrication for nanophotonic devices

Takashi Yatsui[*a], Wataru Nomura[b], and Motoichi Ohtsu[a,b]

[a] SORST, Japan Science and Technology Agency, 687-1 Tsuruma, Machida, Tokyo 194-0004 Japan

[b] School of Engineering, the University of Tokyo, 7-3-1 Hongo, Bunkyo-ku, Tokyo 113-8656 Japan

*yatsui@ohtsu.jst.go.jp; phone 81 42 788 6030; fax 81 42 788 6031

ABSTRACT

Particles several tens of nanometers in size were aligned in the desired positions in a controlled manner by using capillary force interaction and suspension flow. Latex beads 40-nm in diameter were aligned linearly around a 10-μm-hole template fabricated by lithography. Further control of their position and separation was realized using colloidal gold nanoparticles by controlling the particle-substrate and particle-particle interactions using an optical near field generated on the edge of a Si wedge, in which the separation of the colloidal gold nanoparticles was controlled by the direction of polarization.

Keywords: near-field, size-regulation, desorption, nanophotonics

1. INTRODUCTION

For future optical transmission and signal processing systems with high data transmission rates and capacity, we have proposed nanometer-sized photonic integrated circuits (*i.e.*, nanophotonics ICs) [1]. As a representative device, the operation of a nanophotonic switch was demonstrated by controlling the dipole forbidden optical energy transfer among resonant energy states in CuCl quantum cubes via an optical near field [2]. The switch is made of three CuCl quantum cubes with a size ratio of $1:\sqrt{2}:2$ on a sub-10-nm scale, and the size and position of the cubes on the substrate must be controlled with nanometer-scale accuracy.

Coupling these nanophotonic devices and ICs with external conventional diffraction-limited photonic devices requires a nanometer-sized optical waveguide for far-/near- field conversion. To realize this, we reported a plasmon waveguide that uses a metallized Si wedge structure that converts far-field light into an optical near-field via a metallic core waveguide [3]. Furthermore, it has been suggested that electromagnetic energy can be guided along a nano-dot coupler, which consists of chains of closely spaced metallic nanoparticles [4]. Energy transfer in the nano-dot coupler relies on dipole-dipole coupling between neighboring nanoparticles. To realize a nano-dot coupler consisting of 50-nm gold nanoparticles with 50-nm separation, the dispersion of their separation is estimated to be as small as 10 nm to obtain an efficiency equivalent 50 % that of an ordered array [4].

Promising components for integrating these nanometer-sized photonic devices include chemically synthesized nanocrystals, such as metallic nanocrystals [5], semiconductor quantum dots [6], and nanorods [7], because they have

Plasmonics: Metallic Nanostructures and Their Optical Properties III, edited by Mark I. Stockman,
Proceedings of SPIE Vol. 5927 (SPIE, Bellingham, WA, 2005) · 0277-786X/05/$15 · doi: 10.1117/12.614259

uniform size, controlled shape, defined chemical composition, and tunable surface chemical functionality. However, position- and size-controlled deposition methods have not yet been developed. Since several methods have been developed to prepare nanometer-sized templates reproducibly [8], it is expected that the self-assembly of colloidal nanostructures into a lithographically patterned substrate will enable precise control at all scales [9]. Capillary forces play an important role, because colloidal nanostructures are synthesized in solution. Recently, successful integration of polymer or silica spheres [10,11] and complex nanostructures such as nanotetrapods [11] into templates by controlling the capillary force using appropriate template structures has been reported, although their size and separation are typically uniform.

To fabricate nanophotonic devices, we propose a novel method of assembling nanoparticles by controlling the capillary force interaction and suspension flow. Further control of the positioning and separation of the nanoparticles is realized by controlling the particle-particle and particle-substrate interactions using an optical near field.

2. ONE-DIMENSIONAL ALIGNMENT OF LATEX BEADS

To control position and separation very accurately, preliminary experiment was performed on a patterned Si substrate, where an array of 10-μm holes in 100-nm-thick SiO_2 was fabricated using photolithography [Fig. 1(a)]. Subsequently, a suspension containing latex beads with a mean diameter of 40 nm were dispersed on the substrate and the latex beads were aligned after solvent evaporation. The deposited latex beads were not subjected to any surface treatment and were dispersed in pure water at 0.001 wt%. Although the 10-μm-sized template resulted in low selectivity in the position of the latex beads [Figs. 1(b) and 1(c)], the beads were deposited only on the SiO_2 surface owing to its higher capillarity.

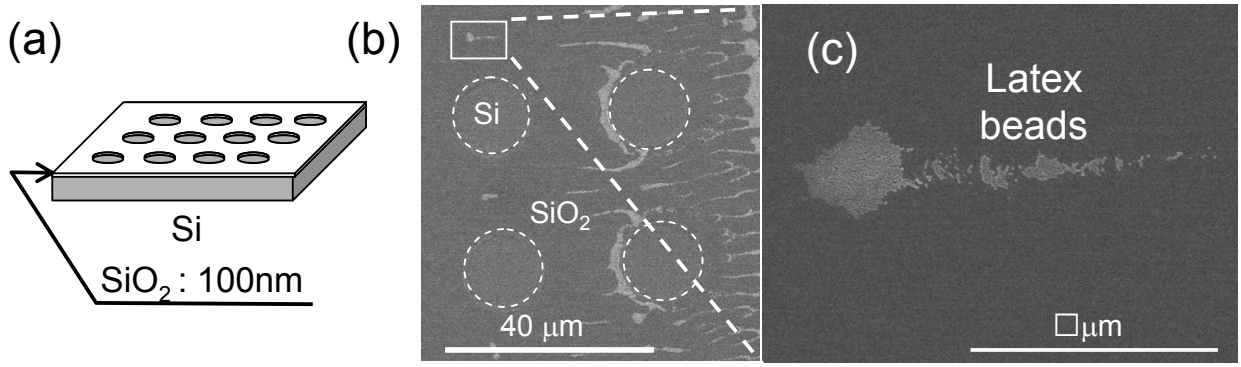

Fig. 1 (a) Schematic of lithographically patterned Si substrate. (b and c) SEM images of latex beads dispersed on the lithographically patterned Si substrate.

For higher positional selectivity, the suspension containing latex beads was dropped onto a lithographically patterned Si substrate that were spinning at 3,000 revolutions per minute (rpm). As shown in Fig. 2(a), the suspension flow split into two branches at the SiO_2 hole. Scanning electron microscope (SEM) images [Figs. 2(b)-(d)] show that the chain of colloidal beads were aligned at the Si/SiO_2 interface. Note that the number of rows of latex beads decreased [Figs. 2(b) and 2(c)] and only the smallest beads, which were 20 nm in diameter, reached the end of the suspension flow

[Fig. 2(d)]. Assuming the same particle-suspension contact angle [denoted ψ in Fig. 2(e)] for various particles diameters, the flow speed of the larger latex beads had greater deceleration since the magnitude of the force pushing the particles on the SiO_2 [denoted F in Fig. 2(e)] owing to evaporation of the solvent is proportional to the particle diameter [11]. In other ward, the size selection was realized.

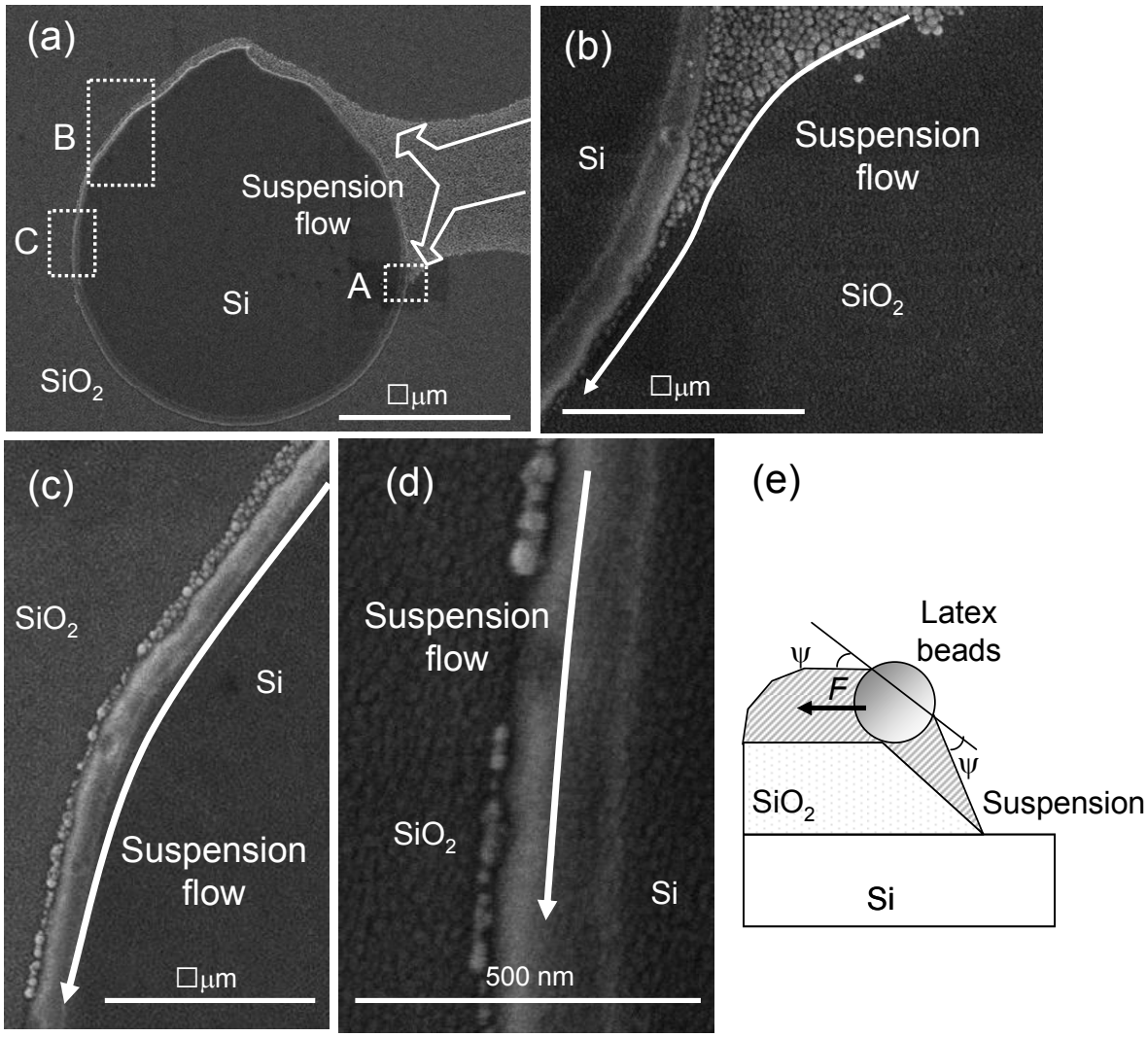

Fig. 2 (a) SEM image of latex beads dispersed on the lithographically patterned Si substrate rotated at 3,000 rpm. Higher magnification SEM images of white squares A (b), B (c), and C (d) in (a). (e) Schematic illustrating of the particle-assembly process driven by the capillary force and suspension flow.

3. SELF-ASSEMBLY OF AU NANOPARTICLES USING AN OPTICAL NEAR FIELD

Based on the results of preliminary deposition, we tried assembling metallic nanoparticles because they are the material used to construct nano-dot couplers [4]. In this trial, we investigated the assembly of colloidal gold

nanoparticles with a mean diameter of 20 nm dispersed in citrate solution at 0.001%. The nanoparticles were prepared by the citric acid reduction of gold ions and terminated by a carboxyl group (approximate length is 0.2 nm) with a negative charge [12]. However, they could not be aggregated using the same deposition process as for the latex beads. To aggregate these particles, we fabricated a SiO_2 line structure with a plateau width of 50 nm on the Si substrate using photolithography [Fig. 3(a)]. The solvent containing the colloidal gold nanoparticles was dropped onto this substrate at 3,000 rpm. Then, the colloidal gold nanoparticles aggregated along the plateau of the SiO_2 line [Figs. 3(b) and 3(c)]. This indicates that the capillary force induced by the lithographically patterned substrate, which is caused by the higher wettability of SiO_2 than that of the Si, was larger than the repulsive force owing to the negative charge of the carboxyl group on the colloidal gold nanoparticles. Furthermore, the gold nanoparticles were aligned along the plateau of the SiO_2. Such aggregation is caused by its wedge structure. This is because the suspension at the edge is thinner than that on the slope of the SiO_2 owing to its low capillarity, and this causes the convective transport of particles toward the edge [13], which resulted in the aggregation and alignment of the colloidal gold nanoparticles at high density.

For further control of size, separation, and positioning, we examined the aggregation of colloidal gold

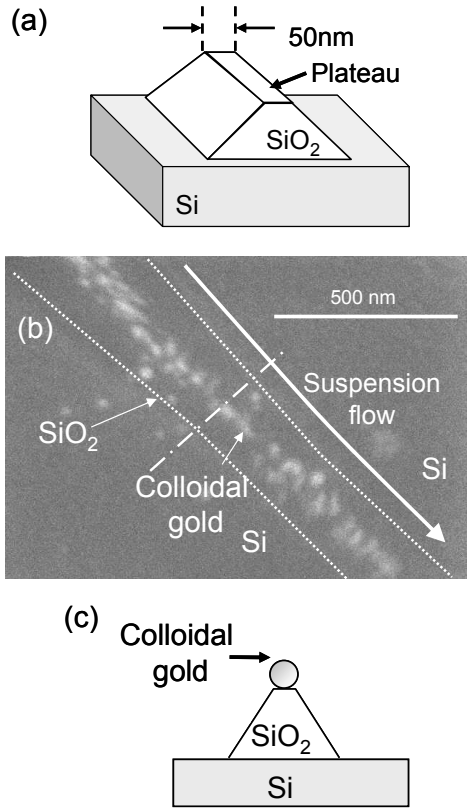

Fig. 3 (a) Schematic of the SiO_2 line structure fabricated on the Si substrate. (b) SEM images of colloidal gold nanoparticles dispersed on the SiO_2 line rotated at 3,000 rpm. (c) Cross-section of the substrate along the white line (dashes and dots) in (b).

nanoparticles under illumination, because the colloidal gold nanoparticles have strong optical absorption. Strong absorption should desorb the carboxyl group from the colloidal gold nanoparticles and result in their aggregation. Such an aggregation of colloidal gold nanoparticles were confirmed by the illumination of light. Figure 4(a) shows the aggregated gold nanoparticles over the pyramidal Si substrate under the 690-nm-light illumination for 60 seconds. However, since the light was illuminated through the droplet of the colloidal gold nanoparticles, aggregated colloidal gold nanoparticles were spread outside the beam spot. In order to realize selective aggregation of the gold nanoparticles at the desired position, the suspension was illuminated from behind [Fig. 4(b)]. Furthermore, we used a Si wedge, because this is a suitable structure for a far-/near-field conversion device [3]. The Si wedge structure was fabricated by three steps:

(i) A (100)-oriented silicon-on-insulator (SOI) wafer was bonded to the glass substrate using anodic bonding.

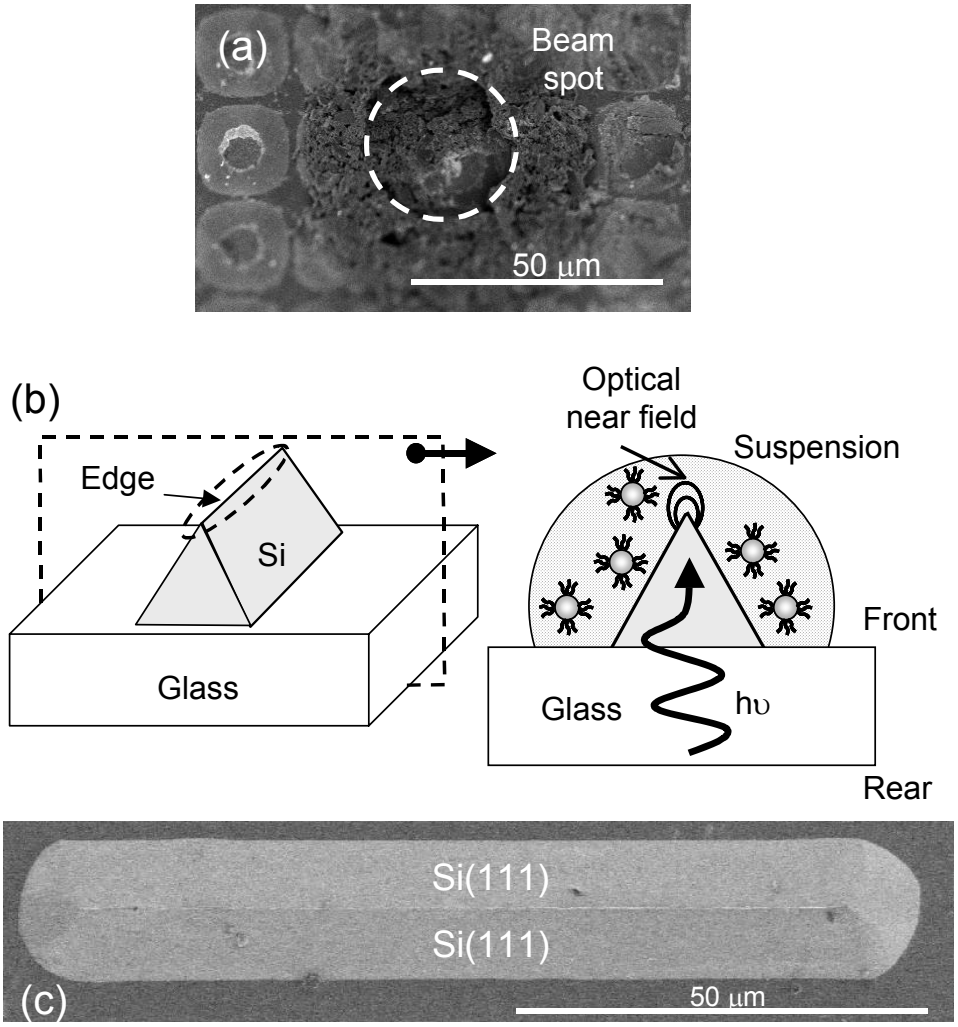

Fig. 4 (a) Aggregated colloidal gold nanoparticles with frontal illumination under 690-nm light (25 mW/mm^2) for 60 seconds. (b) Schematic of the experimental setup. (c) SEM image of the fabricated Si wedge structure.

(ii) After removing the Si substrate from the SOI wafer by wet etching, the SiO_2 layer was patterned using photolithography.

(iii) The Si wedge was fabricated by anisotropic etching (40 g KOH + 60 g H_2O + 40 g isopropyl alcohol, 80 ºC). Maintaining the Si wedge height at less than 10 μm also kept its propagation loss sufficiently low.

Figure 4(c) shows an SEM image of the fabricated Si wedge structure after removing the SiO_2 layer.

For this structure, colloidal gold nanoparticles were deposited around the edge after evaporating the suspension without illumination [Figs. 5(a) and 5(b)]. Such aggregation is caused by its wedge structure, as observed for the SiO_2 wedge structure [Fig. 3(c)] [13]. Further selective alignment along the edge of the Si wedge was realized using rear

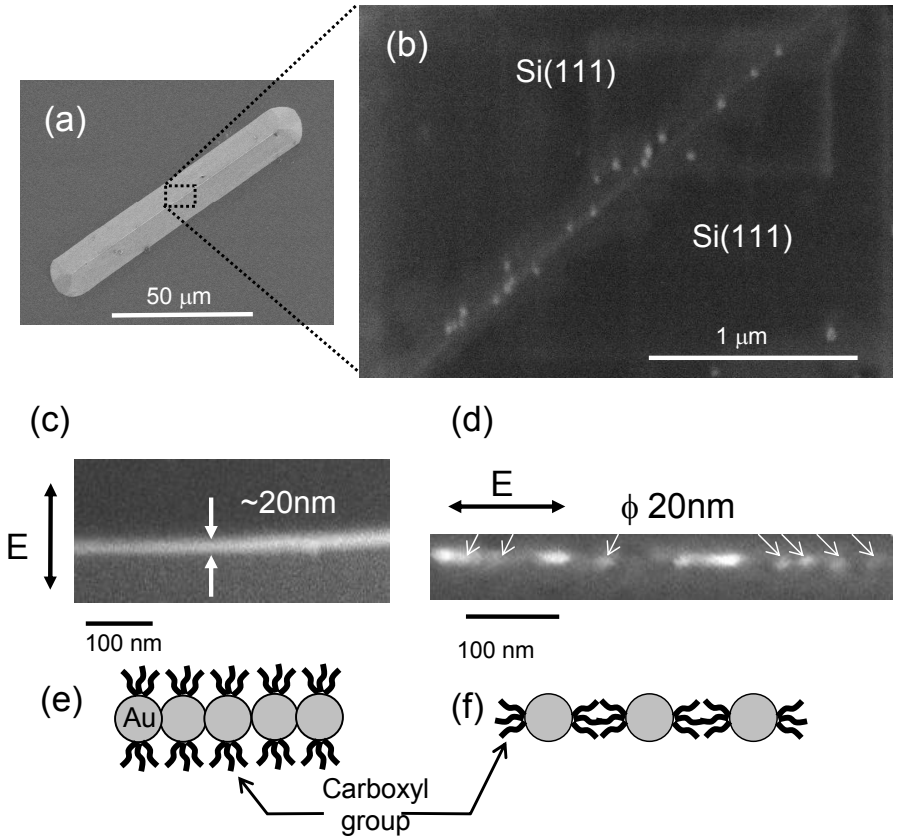

Fig. 5 (a) Overview of the Si wedge structure. (b) SEM image of colloidal gold nanoparticles deposited on the edge of the Si wedge structure without illumination. SEM images of colloidal gold nanoparticles on the Si wedge structure under illumination with polarization perpendicular (c) and parallel (d) to the edge. Schematic diagrams of the aggregation of colloidal gold nanoparticles along the edge of the Si wedge with polarization perpendicular (e) and parallel (f) to the edge.

illumination. Figures 5(c) and 5(d) show the deposited colloidal gold nanoparticles with illumination under 690-nm light (25 mW/mm^2) for 60 seconds. Since the optical near-field energy is enhanced at the edge owing to the high refractive index of Si [see Fig. 4(b)] [14], selective aggregation along the edge with higher density is seen in these figures. This is due to the desorption of the carboxyl group by the absorption of light by the colloidal gold nanoparticles.

Note that the colloidal gold nanoparticles were closely aggregated and aligned linearly to form a wire shape when the polarization was perpendicular to the edge axis [Fig. 5(c)], while they were aligned with separation of several tens of nanometers in the parallel polarization [Fig. 5(d)]. As the optical near-field energy for parallel polarization is higher than that for perpendicular polarization [3], greater aggregation is expected for parallel polarization. Nevertheless, the parallel polarization resulted in less aggregation. The low resolution of SEM images does not determine the distribution of the carboxyl molecules. However, such a repulsive force for disaggregation is caused by the carboxyl molecules which remained on the colloidal gold nanoaprticles. Thus, we believe that the difference in the degree of aggregation originated from differences in the charge distribution induced inside the gold nanoparticles. Based on the polarization dependence of the aggregation, it is reasonable to consider that the aggregation along the edge with perpendicular polarization is owing to partially adsorbed carboxyl groups [Fig. 5(e)], while the disaggregation with the parallel polarization resulted from the repulsive force induced by the partially attached carboxyl group on the colloidal gold nanoparticles [Fig. 5(f)].

4. CONCLUSION

We present experimental results that demonstrate the controlled assembly of 40-nm latex particles in desired positions using capillary force interaction. Further controllability in separation and positioning was demonstrated using colloidal gold nanoparticles by introducing the Si wedge structure and controlling the direction of polarization. The experimental results and suggested mechanisms described here show the potential advantages of this technique in improving the regulation of the separation and positioning of nanoparticles, and possible application to realize a nano-dot coupler for far-/near-field conversion.

5. ACKNOWLEDGEMENT

The authors thank Prof. H. Hori, University of Yamanashi, for valuable discussions.

REFERENCES

[1] M. Ohtsu, K. Kobayashi, T. Kawazoe, S. Sangu, and T. Yatsui, “Nanophotonics: Design, fabrication, and operation of nanometric devices using optical near fields,” IEEE J. of Sel. Top. Quantum Electron., vol..8, no.4, pp.839-862, 2002.

[2] T. Kawazoe, K. Kobayashi, S. Sangu, and M. Ohtsu, “Demonstration of nanophotonic switching by optical near-field energy transfer,” Appl. Phys. Lett., vol.82, no.18, pp.2957-2959, 2003.

[3] T. Yatsui, M. Kourogi, and M. Ohtsu, “Plasmon waveguide for optical far/near-field conversion,” Appl. Phys. Lett., vol.79, no.27, pp.4583-4585, 2001.

[4] S. A. Maier, P. G. Kik, H. A. Atwater, S. Meltzer, E. Harel, B. E. Koel, and A. G. Requicha, “Local detection of electromagnetic energy transport below the diffraction limit in metal nanoparticle plasmon waveguides,” Nature Materials, vol.2, pp.229-232, 2003.

[5] M. Brust, C. J. Kiely, “Some recent advances in nanostructure preparation from gold and silver particles: short topical review,” Colloids Surf. A, vol.202, pp.175-186, 2002.

(□) P. Alivisatos, “Semiconductor clusters, nanocrystals, and quantum dots,” Science, vol.271, pp.933-937, 1996.

[6] P. Yang, “Wires on water,” Nature, vol.425, pp.243-244, 2003.

[7] M. D. Austin, H. Ge, W. Wu, M. Li, Z. Yu, D. Wasserman, S. A. Lyon, and S. Y. Chou, “Fabrication of 5 nm linewidth and 14 nm pitch features by nanoimprint lithography,” Appl. Phys. Lett., vol.84, no.26, pp.5299-5301, 2004.

[8] G. M. Whitesides, B. Grzybowski, “Self-assembly at all scales,” Science, vol.295, pp.2418-2421, 2002.

[9] Y. Yin, Y. Lu, Y. Xia, “Assembly of monodispersed spherical colloids into one-dimensional aggregates characterized by well-controlled structures and length,” J. Mater. Chem., vol.11, pp.987-989, 2001.

[10] Y. Cui, M. T. Björk, J. A. Liddle, C. Sönnichsen, B. Boussert, and A. P. Alivisatos, “Integration of colloidal nanocrystals into lithographically patterned devices,” Nano Lett. vol.4, no.6, pp.1093-1098, 2004.

[11] G. Frens, Nature Phys. Sci., “Controlled nucleation for the regulation of the particle size in monodisperse gold suspensions,” vol.241, 20-22, 1973.

[12] N. D. Denkov, O. D. Velev, P. A. Kralchevsky, I. B. Ivanov, H. Yoshimura, L. Nagayama, “Two-dimensional crystallization”, Nature, vol.361, pp.26, 1993.

[13] T. Yatsui, K. Itsumi, M. Kourogi, and M. Ohtsu, “Metallized pyramidal silicon probe with extremely high throughput and resolution capability for optical near-field technology,” Appl. Phys. Lett., vol.80, no.13, pp.2257-5529, 2002.

Efficient energy transfer of a nanodot coupler with resonant light scattering of metallic nanoparticles

Wataru Nomura,*[1] Takashi Yatsui,[2] and Motoichi Ohtsu[1, 2]

[1] School of Engineering, The University of Tokyo,
7-3-1 Hongo, Bunkyo-ku, Tokyo 113-8656, Japan
[2] "Nanophotonics" team, SORST, Japan Science and Technology Agency
687-1 Tsuruma, Machida Tokyo 194-0004, Japan

ABSTRACT

To realize a nanometer-scale optical waveguide for far-/near-field conversion, we proposed a nanodot coupler which is the linear array of closely spaced metallic nanoprticles in order to transmit the optical signal to a nanophotonic device. In comparison with metallic core waveguide, the use of nano-dot coupler is expected to realize lower energy loss due to the resonant in the metallic nanoparticles.

First, to optimize the efficiency in the nanodot coupler, we checked whether the single Au nanoparticles led to efficient scattering. The Au nanoparticles on the glass substrate were fabricated by the focused ion beam milling technique. The optical near-field intensity for the Au nanoparticles in diameter range from 100 to 300nm with constant height of 50nm were observed by the collection mode near-field optical microscope (NOM) at λ = 785nm. Near-field intensity took the maximum for the Au nanoparticle with 200nm in diameter, and this result is in good agreement with the calculated value of plasmon resonance by Mie's theory for an Au prolate spheroid.

Next, we examined the plasmon-polariton transfer of nanodot couplers whose diameter range from 150 to 300nm by the collection mode NOM. The efficient energy transfer was observed only in the nanodot coupler with 200nm in diameter. This result agreed well with that of single Au nanoparticles.

From these results, efficient energy transfer along nanodot coupler was confirmed by the near-field coupling between plasmon-polariton in the nanoparticles.

Keywords: nanophotonics, near-field coupling, localized surface plasmon, resonant light scattering

Plasmonics: Metallic Nanostructures and Their Optical Properties III, edited by Mark I. Stockman,
Proceedings of SPIE Vol. 5927 (SPIE, Bellingham, WA, 2005) · 0277-786X/05/$15 · doi: 10.1117/12.614308

1. INTRODUCTION

Future optical transmission and data processing systems will require advanced photonic devices, and their integration, in order to increase data processing rates and capacity. Consequently, these devices will have to be significantly smaller than conventional diffraction-limited photonic devices. To meet this requirement, we have proposed nanometer-scale photonic integrated circuits (nanophotonic ICs) that are composed of nanometer-sized elemental devices (nanophotonic devices) [1]. As a representative device, a nanophotonic switch was proposed and its operation was demonstrated by controlling the dipole forbidden optical energy transfer among resonant energy states in CuCl quantum cubes via an optical near field [2]. To fabricate nanophotonic devices, we also developed a near-field optical chemical-vapor deposition technique with nanometer-scale resolution and accuracy in size, position, and separation [3-5].

For use in future photonic systems, the nanophotonic devices and ICs must be connected to conventional diffraction-limited photonic devices. This connection requires a far/near-field conversion device, such as a nanometer-scale optical waveguide. The required performance parameters are:

A) High conversion efficiency

B) A guided beam width of less than 100 nm for efficient coupling of the converted optical near-field to sub-100 nanometer-sized dots.

C) A transmission length that is longer than the optical wavelength to avoid direct coupling of the propagating far-field light to the nanophotonic device consisted of nanometer-scale dots. (The transmission length l_t is defined as $I(z) = I(0) \exp(-z/l_t)$, where $I(z)$ is the optical intensity and z is the longitudinal position measured from the input terminal ($z = 0$)).

One candidate device that meets these performance requirements is a plasmon waveguide using a metallized silicon wedge structure that converts propagating far-field light to an optical near-field [6]. In this device, a one-dimensional TM plasmon mode is excited efficiently via a metallic core waveguide along the plateau. However, the l_t of the TM plasmon mode is still in the order of 700 nm (at $\lambda = 830$ nm) for a metallic core waveguide with a gold core (diameter D = 10 nm) insulated using air [7]. To increase l_t, a more promising candidate is a nanodot coupler consisting of an

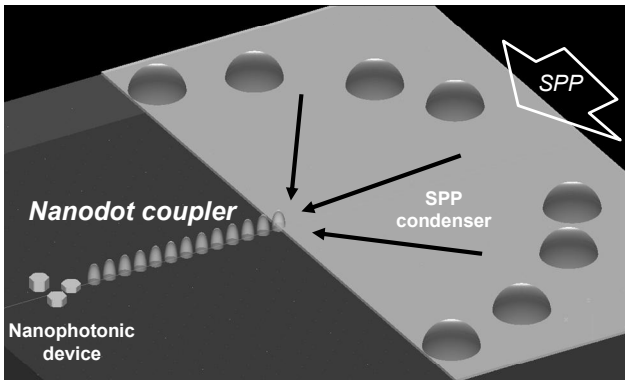

Fig.1 Bird's eye view of a nanodot coupler with a surface plasmon polariton condenser for optical far/near-field conversion devices.

array of closely spaced metallic nanoparticles, because higher transmission efficiency is expected owing to the plasmon resonance in the closely spaced metallic nanoparticles [8]. Energy transfer along the nanodot coupler relies on the near-field coupling between the plasmon-polariton mode of the neighboring nanoparticles.

2. OPTICAL FAR/NEAR-FIELD CONVERSION DEVICE

To increase in the efficiency of exciting localized surface plasmon in the nanodot coupler than that excited by propagating far-field light, we equipped the nanodot coupler with a surface plasmon polariton (SPP) condenser for efficient far/near-field conversion. Figure 1 shows the proposed optical far/near-field conversion device. Incoming far-field light is first transformed into the two-dimensional SPP mode on the gold film. Then, the SPP mode is scattered and focused by the SPP condenser, which consists of several hemispherical metallic submicron particles that are arranged in an arc and work as a "phased array" [9]. The input terminal of the nanodot coupler is fixed at the focal point of the SPP. Finally, after the localized surface plasmon transmits through the nanodot coupler, it is converted into an optical near-field so that it couples to the nanophotonic device.

The advantages of this device are that it has

(1) A high conversion efficiency, from the SPP mode to the localized surface plasmon in the nanodot coupler, owing to coupling the scattering at the inlet metallic nanoparticle [10].

(2) No cut-off diameter of the metallic nanoparticle array, i.e., the beam width decreases with the diameter because the electric field vector, which is dominant in the nanodot coupler, involves only a Förster field [8].

(3) Long-distance propagation of the TM-plasmon mode. For example, the calculation using the finite-difference time domain (FDTD) method estimated a transmission length of l_t = 2 μm (at an optical wavelength λ = 785 nm) for a plasmon-polariton mode with linearly aligned 50-nm dots with 10-nm separation [11,12]. Furthermore, as a preliminary near-field measurement of nanodot coupler, it was found that the transmission length of the nanodot coupler width 230 nm in diameter was three times longer than that of the metallic core waveguide with a same width [13].

Advantages (1) to (3) are compatible with meeting requirements (A) to (C), respectively.

3. EXPERIMENT

In order to optimize the efficiency in the nanodot coupler, first we checked whether the Au nanoparticles led to efficient scattering. Au nanoparticles were fabricated using focused ion beam (FIB) milling technique. The fabrication process was as follows:

(i) A 50nm thick Au film was deposited using sputtering on the glass substrate [Fig.2 (a)].

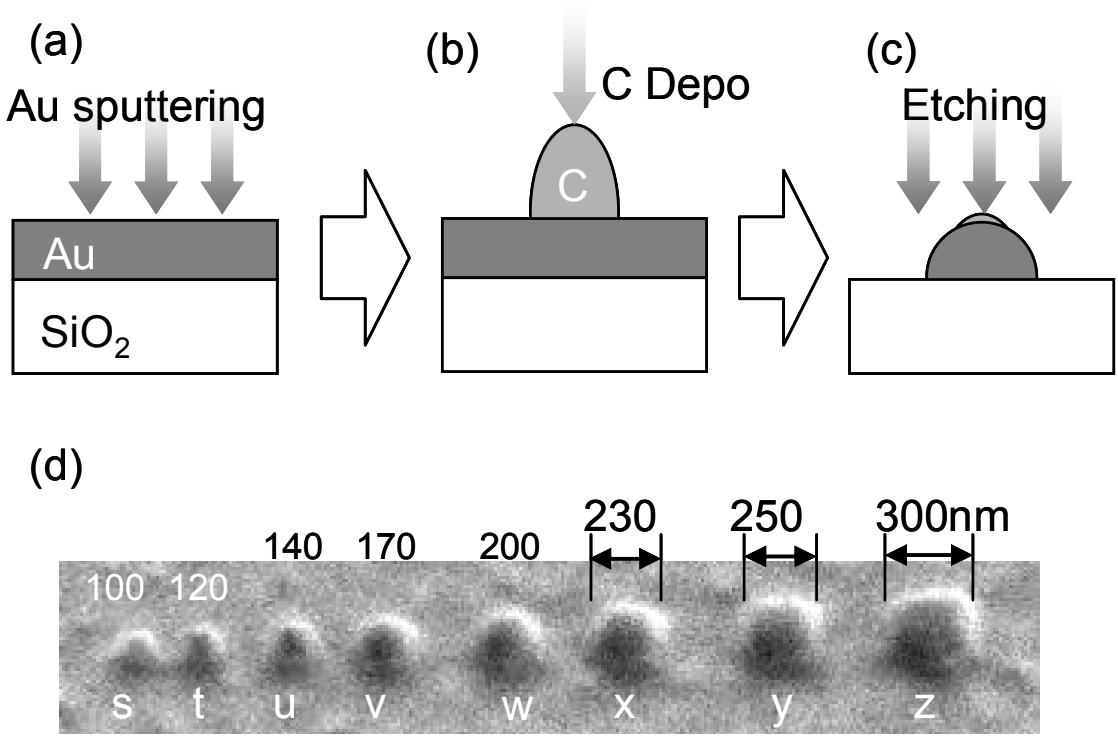

Fig.2 Fabrication of Au nanoparticles: (a) Au sputtering [step(i)]. (b) Carbon hemisphere deposition using FIB [step (ii)]. (c) Au film etching by FIB [step (iii)]. (d) SEM image of the fabricated Au nanoparticles

(ii) Carbon hemispheres were deposited using FIB [Fig.2 (b)].

(iii) Using carbon hemisphere as a mask, Au nanoparticles were obtained by FIB milling [Fig.2 (c)].

Fig.2 (d) shows the SEM image of Au nanoparticles. They were arranged with longer separation than each diameter, resulting in no near-field interaction each other.

The spatial distribution of the optical near-field intensity for the Au nanoparticles in diameter *D* range from 100 to 300 nm were observed by the collection mode near-field optical microscope (NOM) at λ = 785 nm. Figures 3(a) and 3(b) show the topographical and NOM images of the Au nanoparticles. As shown in the cross sectional profile [see Fig. 3(c)], the optical near-field intensity *I* takes the maximum for the Au nanoparticle with 200 nm in diameter (labeled *w*). In order to find the origin of this resonance, a calculation was performed. Mie's theory of scattering by an Au prolate spheroid (see Fig. 3(d)) was employed, and only the first TM mode was considered [14]. The solid curve in Fig. 3(e) represents the normalized polarizability $\mathrm{Re}(|\alpha|^2/V)$ (α : polarizability, V : volume) as a function of the diameter *D* of the Au prolate spheroid whose short axis was fixed as 50 nm. The calculated resonant diameter (190 nm) is in good agreement with the experimentally confirmed particle size (*D* = 200 nm).

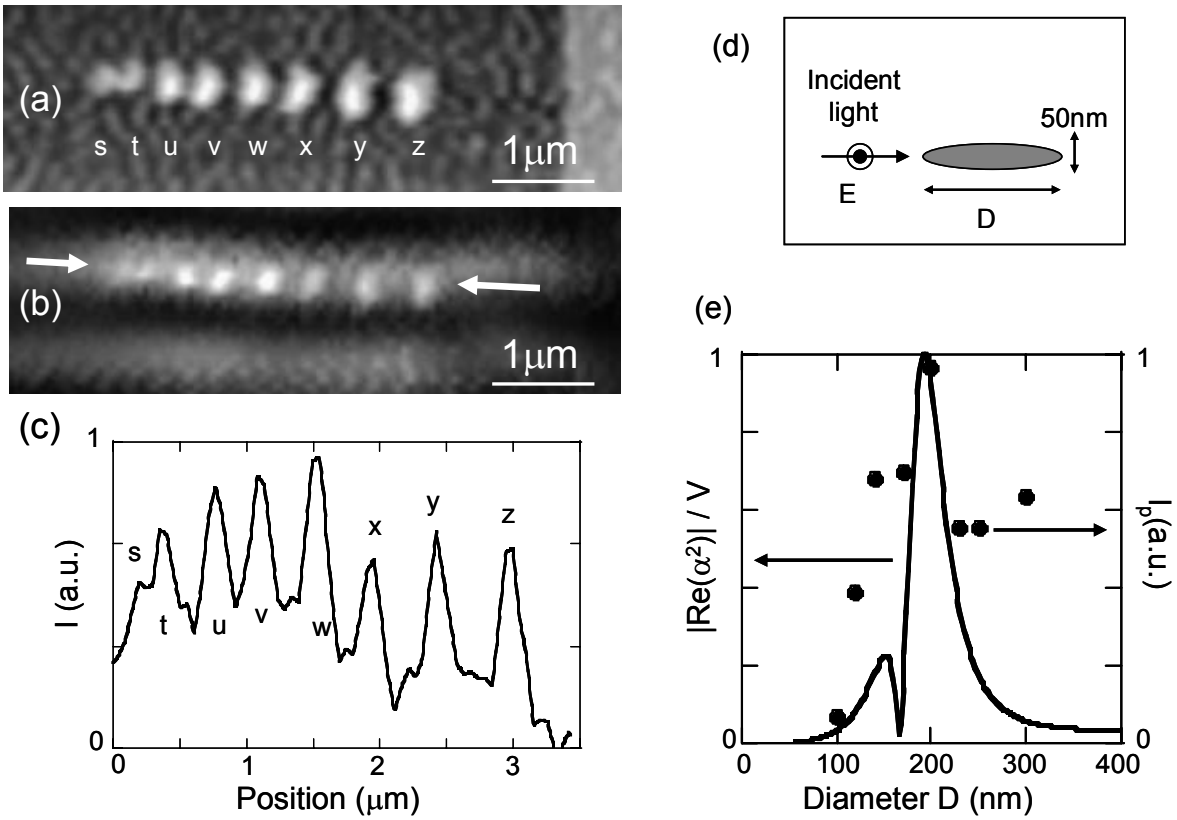

Fig.3 (a) Shear-force image of Au nanoparticles with respective diameter shown in Fig.2 (d). (b) Intensity *I* distribution of optical near-field of (a). (c) Cross-sectional profiles between white arrows in (b). (d) Calculation model of prolate spheroid. (e) Solid circles show the peak intensity I_P of the respective Au nanoparticles. Solid curve shows the normalized polarizability ($|\mathrm{Re}(\alpha^2)|$ / V) of Au prolate spheroid.

Next, we checked the optical near-field energy transfer along the Au nanodot coupler. As a nanodot coupler, a linear array of Au nanoparticles in diameter *D* range from 150 to 300 nm with their center to center separations of 1.2 *D* were fabricated using FIB milling technique (Fig. 2(a)~(c)). The spatial distributions of optical near-field energy were observed by the collection mode NOM taken at arrangement for 2D SPP mode excitation by ATR method(Fig.4). Figure 5(a) and 5(b) show the topographical and NOM images of the nanodot couplers, respectively. Figure 5(c) shows the cross-sectional profile through the outlet of the nanodot couplers. Note that the output energy was efficiently obtained only for the nanodot coupler with D = 200 nm, which is consistent with the experimental results shown in Fig.3. These results confirm that such an efficient energy transfer along the Au nanoparticles is due to the near-field coupling between resonant plasmon-polariton modes of neighboring particles.

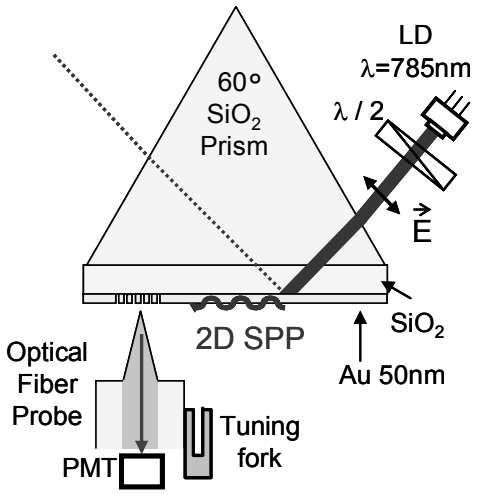

Fig.4 Schematic illustration of the NOM measurement system

4. CONCLUSIONS

We fabricated a nanodot coupler as far-field and near-field convertion device. Highly efficient energy transport was observed in the nanodot coupler via near-field coupling between localized surface plasmon of neighboring particles. These results confirm that it will be possible to create the optical far/near-field conversion devices required by future systems.

REFERENCES

[1] M. Ohtsu, K. Kobayashi, T. Kawazoe, S. Sangu, and T. Yatsui, "Nanophotonics: Design, Fabrication, and Operation of Nanometric Devices Using Optical Near Fields", IEEE Journal of Selected Topics in Quantum Electronics **8**, 839 (2002).

[2] T. Kawazoe, K. Kobayashi, S. Sangu, and M. Ohtsu, "Demonstration of a nanophotonic switching operation by optical near-field energy transfer", Appl. Phys. Lett. **82**, 2957 (2003).

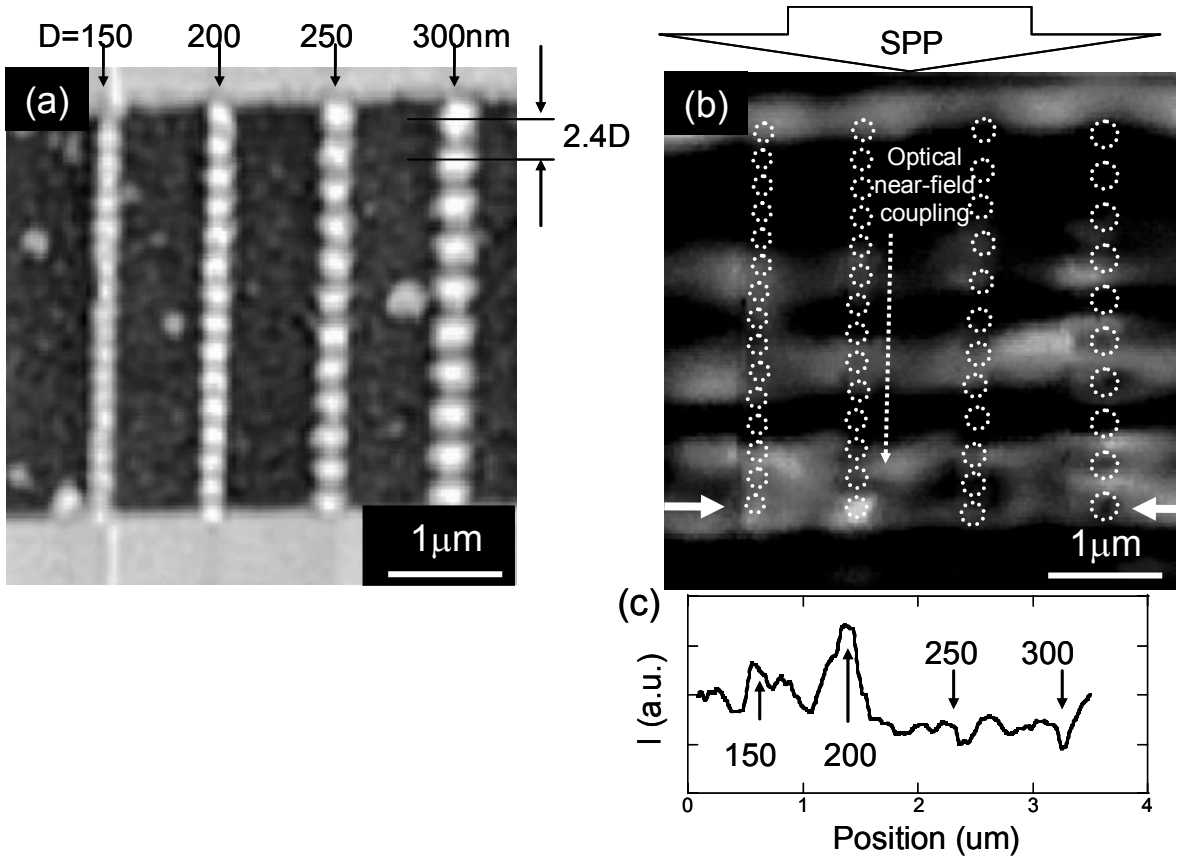

Fig. 5 (a) Shear-force image of Au nano-dot coupler with D = 150, 200, 250, and 300 nm. (b) Spatial distribution of optical-near field intensity of (a). (c) Intensity *I* distribution of optical near field between the solid white arrows in (b).

[3] Y. Yamamoto, M. Kourogi, M. Ohtsu, V. Polonski, and G.H. Lee, "Fabrication of nanometric zinc pattern with photodissociated gas-phase diethylzinc by optical near field", Appl. Phys. Lett. **76**, 2173 (2000).

[4] Y. Yamamoto, M. Kourogi, M. Ohtsu, and T. Kawazoe, "Lateral Integration of Zn and Al Dots with Nanometer-Scale Precision by Near Field Optical Chemical Vapor Deposition Using a Sharpened Optical Fiber Probe", IEICE Trans. Electron. E85-C, 2081 (2002).

[5] T. Yatsui, T. Kawazoe, M. Ueda, Y. Yamamoto, M. Kourogi, and M. Ohtsu, "Fabrication of nanometric single zinc and zinc oxide dots by the selective photodissociation of adsorption-phase diethylzinc using a nonresonant optical near field", Appl. Phys. Lett. **81**, 3651 (2002).

[6] T. Yatsui, M. Kourogi, and M. Ohtsu, "Plasmon waveguide for optical far/near-field conversion", Appl. Phys. Lett. **79**, 4583 (2001).

[7] J. Takahara, S. Yamagishi, H. Taki, A. Morimoto, and T. Kobayashi, "Guiding of a one-dimensional optical beam with nanometer diameter", Opt. Lett. **22**, 475 (1997).

[8] M. L. Brongersma, J. W. Hartmanm and H. A. Atwater, "Electromagnetic energy transfer and switching in nanoparticle chain arrays below the diffraction limit", Phys. Rev. B **62**, R16356 (2000).

[9] I. I. Smolyaninov, D. L. Mazzoni, J. Mait, and C. C. Davis, "Experimental study of surface-plasmon scattering by individual surface defects", Phys. Rev. B **56**, 1601 (1997).

[10] T. Yatsui, M. Kourogi, and M. Ohtsu, "Highly efficient excitation of optical near-field on an apertured fiber probe with an asymmetric structure", Appl. Phys. Lett. **71**, 1756 (1997).

[11] M. Quinten, A. Leitner, J. R. Krenn, and F. R. Aussenegg, "Electromagnetic energytransport via linear chains of silver nanoparticles", Opt. Lett. **23**, 1331 (1998).

[12] The computer simulations in this paper are performed by a FDTD-based program, Poynting for Optics, a product of Fujitsu, Japan.

[13] W. Nomura, M. Ohtsu and T. Yatsui, "Nanodot coupler with a surface plasmon polariton condenser for optical far/near-field conversion", Appl. Phys. Lett. **86**, 181108 1-3 (2005)

[14] H. Kuwata, H. Tamaru, K. Miyano, "Resonant light scattering from metal nanoparticles: Practical analysis beyond Rayleigh approximation", Appl. Phys. Lett. **83**, 4625 (2003).

[III] REVIEW PAPERS

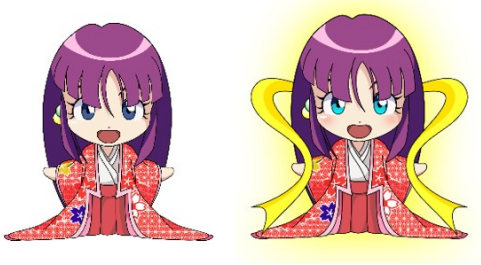

ナノフォトニクスによる質的変革の年がスタート

Starting a new year realizing qualitative innovation by nanophotonics

東京大学　大津元一
The University of Tokyo　***Motoichi Ohtsu***

日本人は外圧に弱いと言われていることを切り口に，まず米国発の情報をご紹介しよう：光情報処理などの高速化・大容量化のためには光集積回路の高集積化が必要であるが，それを構成する光デバイス（レーザー，光変調器，光スイッチなど）の小型化・低消費電力化に限界が見えてきており，光デバイス動作の基本的概念の変革が必要とのことである[1]。

小型化のためには最近流行しているナノテクノロジー，すなわち微小物質を扱う技術が有望とされている。しかし物質を微小化しても光デバイスは小さくならず，全く別の概念が必要である。一方，本年度策定された第3期科学技術基本計画ではナノテクノロジーがどのような出口（たとえば材料からデバイスへ，デバイスからシステムへ，システムから社会貢献へ，など）を持つか否かが問われており，その意味ではこれまでのナノテクノロジーは上記の問題を解決するための解答と出口を与えているとはいえない。解答を与える技術として生まれたのが光の小さな粒である近接場光を用いるナノフォトニクスであるが，この新技術が重要なのは，単に小型化・低消費電力化という大→小，高→低といった量的な改良や変革をもたらすことではない。重要かつ本質的なことは，この新しい技術によって従来技術では不可能であったことが可能になること，すなわち無から有を生むという「質的変革」である。ナノフォトニクスが注目されている理由はこれを実現する技術だからである。現在までに大容量光ストレージ，リソグラフィ装置などの開発のための産学連携事業が優れた成果を上げている。また，質的変革をもたらす光デバイス，システムの開発も本格的になってきた。これらに呼応して，欧米，さらには東アジア諸国もナノフォトニクスに大きな興味をもつようになり，日本への共同研究提案が増えた。さらにナノフォトニクスの名前を冠した学会講演会，講演会内セッション，研究センターなどの数が急増している。

従来の光技術では物質と光，あるいは光源と光と光検出器は明瞭に区別されていたが，ナノフォトニクスでは物質と光とを明確に切り分けることは適当ではなく，いわば物質と光（光は「場」とも呼ばれている）が融合された新概念，すなわち「物質と場の融合学」に立脚している。

従来の光技術の大半の分野をナノフォトニクスによって置き換えることができると考えられており，従ってそのカバーする範囲は，材料，加工，デバイス，システムと多岐にわたる。これらを開発するためにはナノフォトニクスを推進する人材育成の要求が多く寄せられているので，ここで人材とその能力について考えてみよう。従来は「結晶成長は得意だが光学は不得意」，「マクスウェル方程式を解く光学は好きだが物質にはタッチしない」というように，光技術では分野ごとの垣根が高かったように思われる。今後はこの垣根を取り払い，物質と光の両方が得意な人材が必要とされる。また，ナノテクノロジーに見られるように微小物質→材料→デバイスといったボトムアップ的な手法のみでなく，社会のニーズ→システム→デバイス→材料といったトップダウン的な戦略がとれる能力も必要となる。

最後に主張したいことは上述の「出口論」に振り回されるのではなく，「物質と場の融合学」のような革新概念の基礎を確立する基礎研究が以前にもまして重要になるということである。ナノフォトニクスの研究開発は，すでに萌芽的研究の時代を過ぎ，実用化にむかって進んでいるので，今年こそいよいよ「質的変革」が実を結ぶ年になりそうだ。

参考文献

1）R.A. Athale, “Optical Interconnections: How far will it go?”, Conference on Lasers and Electro-Optics, May 16 - 21, 2004, San Francisco, USA, paper number CThE5

□おおつ　もといち
□東京大学　大学院工学系研究科　電子工学専攻　教授
〒113-8656　東京都文京区本郷7-3-1
Tel. 03-5841-1189　Fax. 03-5841-1140
E-mail : ohtsu@ee.t.u-tokyo.ac.jp

□1973年東京工業大学工学部電子工学科卒業，1978年同大学大学院博士課程電子物理工学専攻修了。同年同大学助手，助教授を経て1991年同大学大学院総合理工学研究科教授。2004年4月から東京大学大学院工学系研究科電子工学専攻教授。この間，1986年～1987年米国AT&Tベル研究所研究員。ナノフォトニクスの研究に従事している。OSAフェロー。電波科学国際連合I.KOGA Gold Medal，日本IBM科学賞，応用物理学会賞，井上学術賞，井上春成賞など受賞。2004年紫綬褒章。

特集：進化するナノテクノロジー

超音波照射を用いた無電解ニッケルめっきによる近接場光学プローブの作製

齋藤 裕一[*1,*2]，物部 秀二[*4,*5]，大津 元一[*6]，本間 英夫[*2,*3]

[*1]関東学院大学 大学院工学研究科(〒236-8501 神奈川県横浜市金沢区六浦東 1-50-1)
[*2]関東学院大学 表面工学研究所(〒239-0806 神奈川県横須賀市池田町 4-4-1)
[*3]関東学院大学 工学部(〒236-8501 神奈川県横浜市金沢区六浦東 1-50-1)
[*4]神奈川科学技術アカデミー(〒213-0012 神奈川県川崎市高津区坂戸 3-2-1 KSP 東棟 409)
[*5]科学技術振興機構 さきがけ 国武「組織化と機能」領域
(〒213-0012 神奈川県川崎市高津区坂戸 3-2-1 KSP 東棟 409)
[*6]東京大学 工学部(〒113-0033 東京都文京区本郷 7-3-1)

Fabrication of a Scanning Near-Field Optical Microscopy Probe Using Electroless NiP Plating Under Ultrasonic Irradiation

Yuichi SAITO[*1,*2], Shuji MONONOBE[*4,*5], Motoichi OHTSU[*6] and Hideo HONMA[*2,*3]

[*1]Graduate School of Engineering, Kanto Gakuin University(1-50-1, Mutsuurahigashi, Kanazawa-ku, Yokohama-shi, Kanagawa 236-8501)
[*2]Kanto Gakuin University Surface Engineering Research Institute(4-4-1, Ikeda-cho, Yokosuka-shi, Kanagawa 239-0806)
[*3]Faculty of Engineering, Kanto Gakuin University(1-50-1, Mutsuurahigashi, Kanazawa-ku, Yokohama-shi, Kanagawa 236-8501)
[*4]Kanagawa Academy of Science and Technology(KSP East 409, 3-2-1, Sakado, Takatsu-ku, Kawasaki 213-0012)
[*5]Kunitake "Organization and Function" Research Area, PRESTO, Japan Science and Technology Agency(KSP East 409, 3-2-1, Sakado, Takatsu-ku, Kawasaki 213-0012)
[*6]Faculty of Engineering, University of Tokyo(7-3-1, Hongo, Bunkyo-ku, Tokyo 113-8656)

Key Words: Electroless NiP Plating, Ultrasonic, Optical Fiber

1. はじめに

ファイバープローブを用いる近接場光学顕微鏡は，ナノメートル分解能を達成する超高分解能光学顕微鏡であり，ナノ光計測，局所的分光分析，ナノ光加工などへの応用が期待されている[1)-4)]。この顕微鏡の光学的な空間分解能は，コアを円錐状に先鋭化した光ファイバープローブの先端径，および試料－プローブ間距離により決定され，プローブが微小光源，または散乱集光体として働くかによって，illumination モード(以下 i-mode)，collection モード(以下 c-mode)の二つの顕微鏡方式に分けられる。また，プローブ－試料間距離の制御や試料の凹凸形状を同時に測定するために，シアフォース顕微鏡など非接触原子間力顕微鏡システムが導入される。プローブ先端が試料上に局在する近接場光を散乱し，ファイバー導波路によって近接場光を光検出器まで導く c-mode において，近接場光信号を高効率検出するためには，測定点以外で散乱したノイズ光を遮断しなければならない[5)-7)]。一方，i-mode 用微小光源プローブとして考案された開口型プローブは，プローブの先端を除いてサブミクロンオーダーの膜厚で金属被覆された構造を持ち，c-mode 動作においても，その金属膜によってノイズ光成分を遮断する空間フィルターとして働くため，c-mode プローブとして優れた光学的特性を示すことが知られている。しかし，開口型プローブの先端径は 10 nm 以下の先端径サイズの無コートプローブに比べて非常に大きい値(200 nm 以上)となるため，開口型プローブを用いて高分解シアフォース顕微鏡像を得ることはできない。我々は，近接場光学顕微鏡とシアフォース顕微鏡の双方において，高分解能を達成するプローブを実現するため，コア先鋭部根元から先端に向かって金属遮光膜の膜厚が徐々に減少し，かつ先端径がサブミクロン以下であるプローブを提案しており，超音波を用いた無電解めっきによって，先端に向かって膜厚が徐々に減少するプロファイルのニッケル膜を持つプローブの作製に成功した[8)-10)]。本論文では，プローブへのめっきの再現性実証実験など，超音波照射下無電解めっきの最近の研究成果について紹介する。

2. 光ファイバープローブの作製方法

試料にはクラッド径 125 μm，コア径 2 μm，屈折率 2.5% の分散補償光ファイバー(三菱電線工業製)を，NH_4F を含んだ緩衝フッ化水素酸溶液で化学エッチングしたコア先鋭角

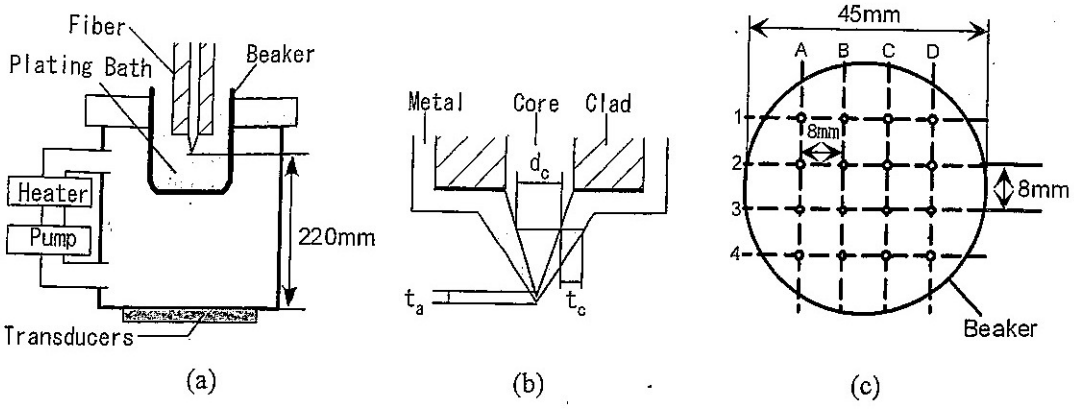

図1　実験装置およびプローブ形状
(a) 超音波照射無電解めっき装置
(b) プローブ形状(d_c=コア直径，t_c=コア部ニッケル膜厚，t_a=先端部ニッケル膜厚)
(c) ビーカー内のファイバーの配置図

20°，クラッド径25μmの光ファイバーを用いた。化学エッチングは，コアとクラッドの組成により生じる溶解速度の差を利用し，コア部の先鋭化を行う方法である[11),12)]。エッチング処理は二工程で構成され，40 wt%NH_4F：50 wt%HF：H_2Oの組成のエッチング液で，体積比が1.7：1：1のエッチング液に25°Cで70分，10：1：1のエッチング液に25°Cで90分間浸漬した。

次に，先鋭化した光ファイバーを塩化スズ溶液および塩化パラジウム溶液の二液に交互に2回づつ浸漬して触媒を付与し[8)]，窒素で脱気した無電解ニッケルめっき浴に浸漬した後，図1(a)に示す装置を用いて超音波照射下で15分間めっきした。超音波照射装置は本多電子製W-357HPを使用した。振動子の周波数は1 MHz，振動子は圧電セラミックス型，振動子の出力は最大4.3 W/cm² であり，振動板の大きさは126 mm×110 mmである。

3．超音波照射照射と機械かく拌

超音波未照射および周波数1 MHzの超音波を照射した場合の光ファイバーコア先鋭部のSEM像を図2に示す。図中の白線はコア部の断面の位置を表す。図2(a)の超音波未照射のコア部のニッケル膜厚はコア根元付近，コア先端付近ともにほとんど変化していない。一方，図2(b)に示す超音波照射の場合はコア根元からコア先端に向かって膜厚が徐々に減少することが確認された。

次に，図1(b)に示すように，コア先鋭部先端の膜厚(t_a)とファイバー断面直径1.0μmのコア部の膜厚(t_c)の比(t_c/t_a)から，プローブ形状を評価した。c-modeにおいては，コア先鋭部先端は光の検出を行い，それ以外の部分は遮光する機能が必要とされ，この膜厚の比が大きいほど，より遮光機能に優れたプローブであることを示す。超音波未照射の場合のニッケル膜厚比(t_c/t_a)は1.2であり超音波照射の場合の膜厚比は7.4であった。これは超音波照射によって先端部と断面直径1 μmの部分のニッケル膜厚比が6倍以上に増大したことを意味する。以上の結果から，近接場光学顕微鏡用プローブとして有効な形状の金属遮光膜が，無電解めっき時の超音波照射により成膜可能であることが分かった。

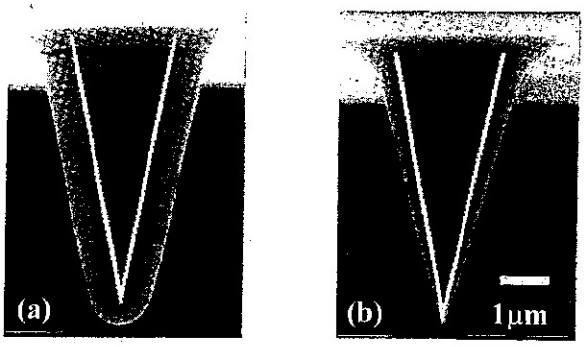

図2　無電解めっき後のコア部のSEM像
(a) 超音波照射なし　(b) 無電解めっき中超音波照射

次に，本手法の量産化への対応について評価するため，超音波の面内分布によるニッケル膜の形状再現性について調査した。図1(c)のように光ファイバーを8 mm間隔で格子状に配置し，めっきを施した。その結果を図3に示す。図中の記号は図1(c)の記号に対応している。試料として用いた16本すべてのプローブはコア先鋭部根本より先端部に向かって薄膜化していた。特に，中心部分に配置されたファイバーB2，B3，C2，C3では先端のニッケル膜厚が30 nm以下であり皮膜形状は酷似していた。一方，外側に配置されたファイバーは，中心付近に配置されたファイバーと比較し，先端部のニッケル膜厚が若干厚くなっている。この原因としては，外側に配置されたファイバーはビーカーの側壁に近接しており，図1(a)に示す装置のように超音波は下側から照射されるため，ビーカー底部の曲面の部分で反射，減衰し，外側に設置されたファイバーに対する超音波出力が中心付近より低下しめっき浴のかく拌効果が低減したと考える。

このようにコア先鋭部根本より先端部に向かって薄膜化するニッケル膜の形成には，超音波のかく拌効果が理由として考えられる[13)]。静置した条件での無電解めっき時におけるプローブの反応界面では，還元剤の酸化反応により水素が発生する。この水素の発生により，無電解めっき反応界面近傍の溶存酸素濃度は水素濃度の上昇にともない，めっき浴の沖合いより減少する。一方，かく拌状態ではプローブの反応界面

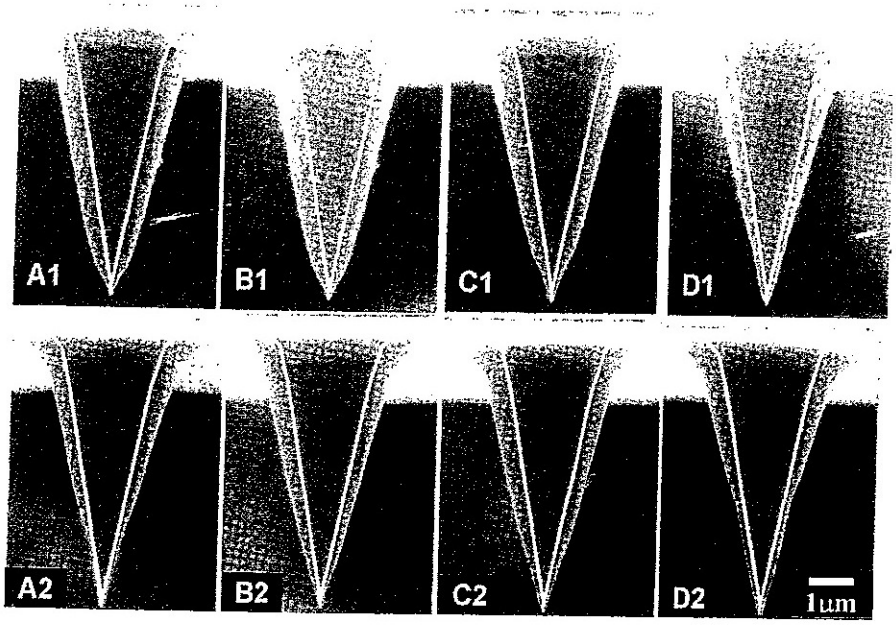

図3　超音波照射下の無電解めっきにより複数同時作製したプローブ

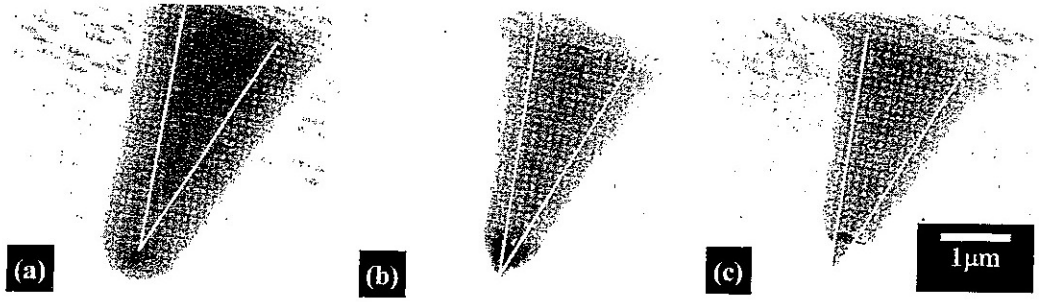

図4　めっき浴の機械かく拌の影響
(a) 0 rpm　(b) 100 rpm　(c) 300 rpm

近傍に沖合いから液が供給されるため，溶存酸素濃度は沖合いの値近くまで増加する。また，溶存酸素を飽和させためっき浴では，光ファイバークラッドのような断面直径100 μm以下の部分の無電解めっき反応が開始しない[14]。本研究で用いた基板は，コア先鋭部が突出した構造をしているため，先端部はよりかく拌の影響を受けやすい。したがって，超音波のかく拌効果によりめっき反応界面近傍の溶存酸素濃度が高くなることが，コア先鋭部先端からの選択的なめっき反応の抑制を起こすと考える。

さらに，超音波かく拌と通常かく拌の効果を比較するため，めっき浴にかく拌子を投入し，スターラーによって連続回転させながら，めっきを行った。その結果を図4に示す。かく拌速度の増大にともなって，コア先鋭部先端でのめっきの析出が抑制された。しかしながら，このような機械かく拌では，めっき浴の流速がビーカー中心部から側壁部まで場所により異なるため，めっき浴中のファイバープローブの位置がめっき析出の形態に大きく影響する。このことからも，超音波かく拌がプローブ作製のために非常に効果的であることが分かる。また，1 MHzセラミック振動子から超音波照射を行った図3の結果は，ビーカー中心部にて複数のプローブを浸漬することで量産が可能であることを示すものである。このような量産化は，従来の開口型プローブ作製法，すなわち，まず先鋭化光ファイバープローブにスパッタリングによって金属膜を堆積し，次にプローブをシアフォース帰還制御のもと[17),18)]，先端を覆う金属を機械的にはく離する方法では困難な[15),16)]，無電解めっき法に固有の発展性である[8)~10)]。

4．おわりに

近接場光学顕微鏡およびシアフォース顕微鏡の双方において，高分解能を達成するプローブとして，光ファイバーコア先鋭部根元から先端に向かって金属遮光膜の膜厚が徐々に減少し，かつ先端径がサブミクロン以下となる金属膜の形成を目指し，超音波照射を用いた無電解ニッケルめっきによるコア先鋭部の選択析出性制御を試みた。その結果，無電解めっき時に周波数1 MHzの超音波を連続照射することにより，コア部根元から先端に向かって膜厚が徐々に減少するプローブが得られた。このプローブはコア先端部の金属膜厚が平均30 nm以下のため試料表面の近接場光の検出が可能であり，コア部の断面直径1.0 μm部分は遮光に有効な200 nm以上の膜厚であった。また，このプローブを複数同時に作製可能であることを確認した。

(2005-8-26　受理)

文　献

1) S. Kawata, M. Ohtsu and M. Irie eds. ; *Nano-Optics*, p. 1 (Springer, 2002)
2) 大津元一, 河田　聡, 堀　裕和　編；ナノ光工学ハンドブック, p. 3 (朝倉書店, 2002)
3) ナノテクノロジーハンドブック編集委員会編；ナノテクノロジーハンドブック, p. 42 (朝倉書店, 東京, 2002)
4) S. Mononobe and M. Ohtsu ed. ; *Progress in Nano-Electro Optics III*, Chap. 1., p. 1 (Springer-verlag, 2005)
5) E. Betzig and J. K. Trautmann ; *Science*, 257, 189 (1992).
6) Z. -Y. Shi and R. Kopelman ; *Anal. Chem.*, 64, 2985 (1992)
7) R. Uma Maheswari, H. Tatsumi, Y. Katayama and M. Ohtsu ; *Opt. Commun.*, 120, 325 (1995)
8) T. Kobayashi, J. Ishibashi, S. Mononobe, M. Ohtsu and H. Honma ; *J. Electrochem. Soc.*, 147, 1046 (2000)
9) 石川　薫, 阿部　治, 三浦修平, 物部秀二, 大津元一, 本間英夫；エレクトロニクス実装学会, 5, 171 (2002)
10) S. Mononobe, Y. Saito, M. Ohtsu and H. Honma ; *Jpn. J. Appl. Phys.*, 43 (5 B), 2862 (2004)
11) S. Jiang et al. ; *Jpn. J. Appl. Phys.*, 31, 2282 (1992)
12) S. Mononobe and M. Ohtsu ed. ; *Near-Field Nano/Atom Optics and Technology*, Springer-Verlag, Tokyo, Chap. 3., p. 31 (1998)
13) 超音波便覧編集委員会編；超音波便覧, p. 305 (丸善, 1999)
14) Jan W. M. Jacobs and Jan M. G. Rikken ; *J. Electrochem. Soc.*, 135, 2822 (1988)
15) 酒井　優, 穂坂紀子, 斎木敏治；*New Glass*, 19, 11 (2004)
16) 穂坂紀子, 斎木敏治；*Jasco Report*, 42, 59 (2000)
17) 物部秀二, 石橋純一, 阿部真二, 本間英夫, 大津元一；第57回応用物理学会学術講演会講演予稿集, p. 778 (1996)

連載

最終回 ナノフォトニック加工

ナノフォトニクスの将来展望

大津 元一*
東京大学大学院

まえがき

本連載の第1回(6月号)では光の小さな粒である近接場光について、さらにそれを用いた新しい光技術であるナノフォトニクスについて概説した。ナノフォトニクスの定義は、「近接場光により媒介されるナノ物質間の局所相互作用に基づく加工、デバイス動作、システム構築の技術」であることを述べ、その例として微細加工、すなわち「ナノフォトニック加工」を取り上げたが、これが従来の光加工の限界を打破する技術の急先鋒として注目されている理由は、加工の微小化という「量的変革」のみでなく、本質的なこととして、「伝搬光では実現し得ない機能、現象を引き出して使うこと、これにより光技術の『質的変革』を実現すること」であることを指摘した。第2回～第5回はナノフォトニック加工の詳細を説明し、質的変革の例を多数示した。

連載の最終回である本稿では、ナノフォトニック加工はナノフォトニクス全体から見るとまだ入り口にすぎず、その後にはデバイス、システムなどの広範な分野があることを指摘したい。

*おおつ もといち：工学系研究科 教授
㈱科学技術振興機構 SORST ナノフォトニクスチーム リーダー
〒113-8656 東京都文京区本郷7-3-1
☎03-5841-1189 E-mail：ohtsu@ee.t.u-tokyo.ac.jp

デバイスへ、システムへ

ナノフォトニック加工は、すでに実用的な加工装置開発の段階へと進んでいる。例えば、近接場光リソグラフィについては、加工寸法50nmの実用機の試作が始まっている。これらの実用機における近接場光発生には、ファイバプローブのように加工速度を制限する要素はすでに駆逐され、大面積一括加工可能なフォトマスクが使われている。さらには、フォトマスクの不要な方法(8月号の第3回の記事参照)も検討されている。

ナノフォトニック加工は、新しい光デバイスを作るための手段としてすでに使われている。特に、冒頭のナノフォトニクスの定義に従って動作するナノフォトニックデバイスを作ることが第一目標とされている。このデバイスは、図1に示すように寸法が光の回折限界を超えて微小化され量的変革をもたらしているだけでなく、ナノフォトニクスでなくては実現しない新規機能を示し、質的変革がなされている。その例として、ナノ寸法の光スイッチ、順序論理ゲート、光バッファメモリ、ナノ集光器、光加算器、デジタル-アナログ変換器、ナノ光導波路、などが開発されている[1]。

さらに、これらのナノフォトニックデバイスを用いた新しいシステム開発が進んでいる。我が国では世界に先駆け、すでに記録密度1Tb/inch^{2}の

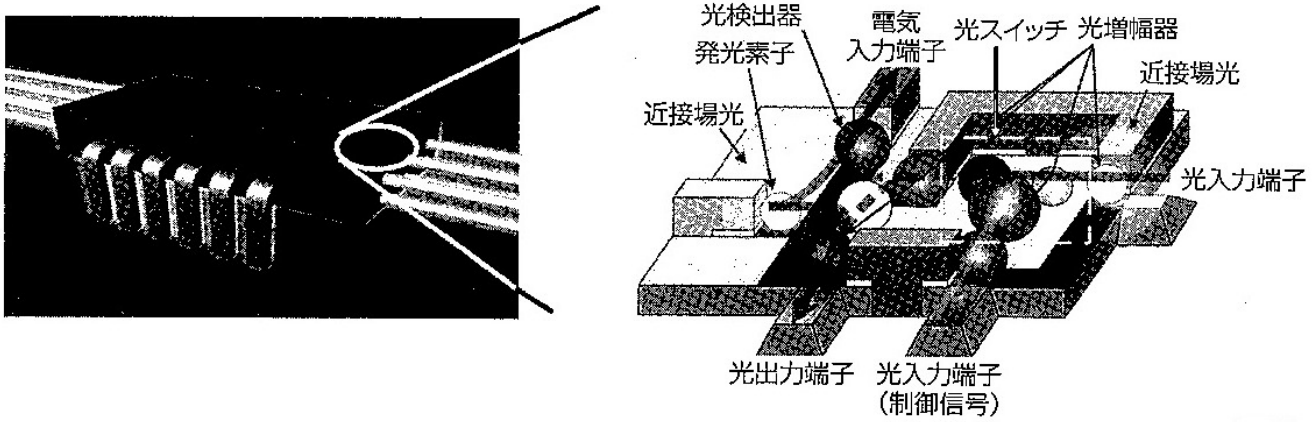

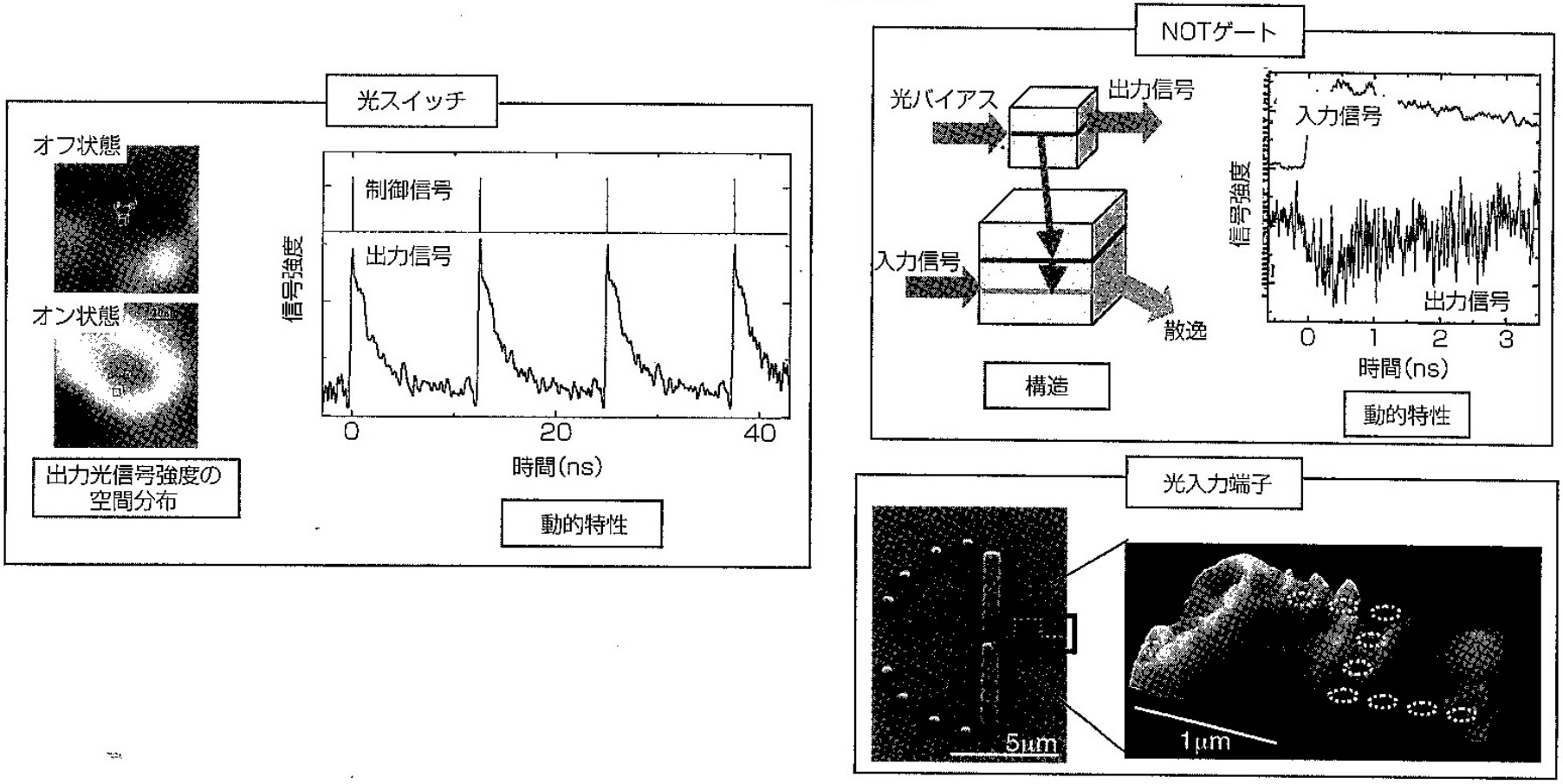

図1　ナノフォトニックデバイスとその集積化。デバイスの例として、光スイッチ、NOTゲート（順序論理ゲートの一例）、ナノ光導波路の構造、動作特性などを示す）

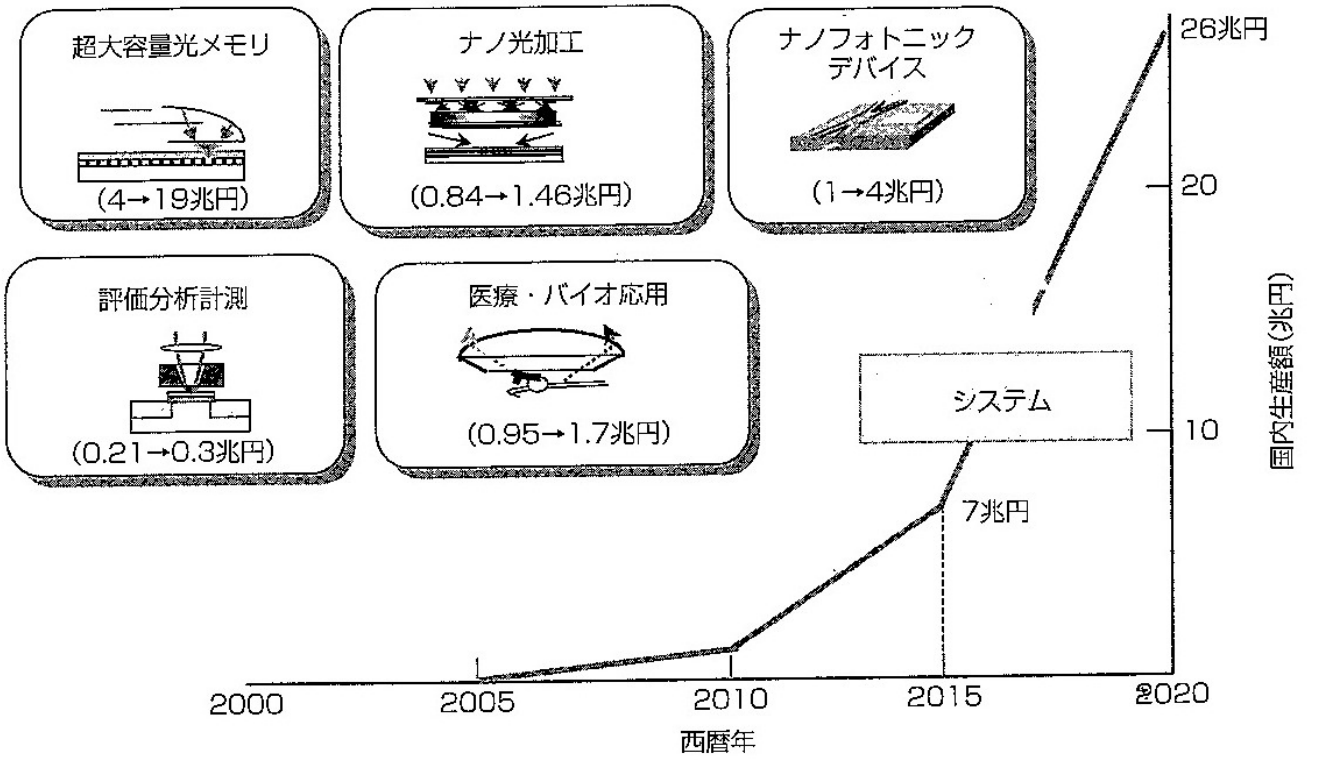

図2　ナノフォトニクスの産業と市場規模。現在～西暦2020年の新規国内生産額(波及効果も含めて)

大容量光メモリの実用化開発が最終段階に達しており[2]、また、情報通信用の光ルーターなどの開発も進み、フォトンコンピュータも提案されている[3]。これらの技術開発は、経済産業省の大型プロジェクト、文部科学省や総務省の産学連携プロジェクトで推進されている。

一方、諸外国でもナノフォトニクスの研究開発が加速されている。すなわち、従来の光情報通信システムでは超高速性を追求してきたが、電子デバイスが高速化されたことから方向転換され、ナノフォトニクスの方向に進んでいる。ただし、諸外国におけるこれらの研究開発はまだ上記のナノフォトニクスの定義に沿って進展するには至っておらず、単にフォトニック結晶と呼ばれる波動光学を利用したフィルタ技術であったり、金属内の自由電子の振動を利用した波動デバイス(この技術はプラズモニクスと呼ばれている)に留まっている。もちろん、質的変革はまだ現れていない。しかし近い将来、諸外国でも上記の定義に沿った真のナノフォトニクスの技術が進展し、我が国の技術水準に迫ることが予想される。

このように、ナノフォトニクスについての関心は国際的に高まっており、最近、欧米では関連する研究センターなどが10件以上新設されている。また、先導している日本の研究への興味が高く、米国、ドイツ、台湾などが日本と2国間ワークショップなどを幾つか開催している。

将来展望

最近の市場規模予測によると、ナノフォトニクスの主要市場は大容量光メモリ、加工、デバイス、評価分析計測、医療・バイオ応用などとされており、図2に示すように、西暦2010年から本格的市場が成長を始め、市場規模の著しい増大が見込まれている。なお、これに上記のシステム市場が加わると、その規模は更に増大する。ナノフォトニクスの技術ロードマップも既に策定されており、安心を安価に得、価値あるものに投資できる社会(生活の質の向上)、療養にお金をかけない社会(健康年齢と寿命の一致)、地球を保護する社会(環境保護)、多様な文化を尊重する社会(多国籍化)の実現に貢献するために必要な開発項目が抽出されている[4]。また、開発が進んでいる記録密度1Tb/inch^{2}大容量光メモリの次世代技術として、

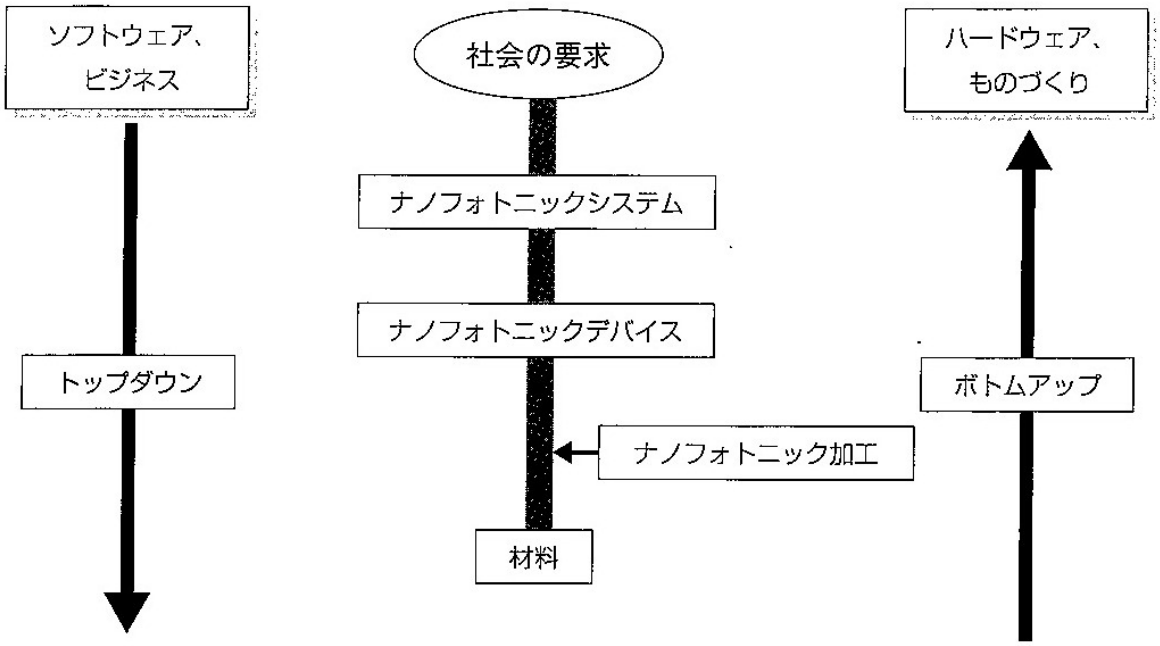

図3　ナノフォトニクスによる加工、デバイス、システムの階層とトップダウン、ボトムアップ的考え方

最近では記録密度1Pb/inch^{2}の実現に向けたロードマップの策定作業も、諸外国に先駆けて我が国で進んでいる。

21世紀の社会を支える基盤技術としてのナノフォトニクスを成熟させるために、ナノフォトニック加工、それを用いて作られるナノフォトニックデバイス、それを用いて構成するナノフォトニックシステムは、互いに連携していることを意識すべきであろう。これらを開発する際、従来のナノテクノロジーの技術のように微小な材料を積み上げ、組み立てて大きな材料を作っていくというボトムアップ的な考え方のみでなく、図3に示すように、システムの要求からデバイス、加工を考える、「トップダウン」的な考え方も両立させることが重要である。

ナノテクノロジーは、微細な材料から大きなものを作っていくというボトムアップ的な技術と呼ばれ、他方、従来の加工技術は大きな材料を加工して微細な構造を作るので、トップダウン的な技術と呼ばれている。これに対し、上記の「トップダウン」的な考え方とは取り扱う材料の大小ではなく、システム→デバイス→材料という技術の階層を意味している。すなわち、単に材料を扱い、それを加工するだけでなく、将来の社会の要請を満たすシステムを考案し、それを実現するためのデバイス、それを作るための加工について大局的に考えることが重要である。

以上、6回にわたって連載したように、日本で生まれたナノフォトニクスによってもたらされた光技術のパラダイムシフトを契機として、新技術・新市場の成長拡大を加速するために、国内の先進研究者集団、先進技術者集団の連携、情報交換、さらには技術動向調査の場としてNPOナノフォトニクス工学推進機構が本年4月に発足した。ご興味のある方はそのホームページを参照していただければ幸いである[5]。

参考文献

1）T. Kawazoe, K. Kobayashi, S. Sangu, and M. Ohtsu, Appl. Phys. Lett., 82, 2957 (2003)
2）(独)新エネルギー・産業技術総合開発機構、成果レポート最前線2005、3(2005)
3）M. Ohtsu, Technical Digest of 2004 ICO International Conference on Optics & Photonics in Technology Frontier, 13C4-2 (2005)
4）(財)光産業技術振興協会、近接場光ナノ加工技術に関する調査研究報告書、10(2004)
5）ホームページのURLはhttp://www.nanophotonics.info/

ナノ光デバイスとその製作
―近接場光特有の動作と加工技術

科学技術振興機構戦略的創造研究推進事業　八井　崇
東京大学大学院工学系研究科電子工学専攻　大津　元一

1. はじめに

情報通信の高速化・大容量化により，光通信における光集積回路は微小化が必要不可欠であり，光産業技術振興協会により取りまとめられた光通信ロードマップ（http://www.oitda.or.jp/index.html）によると2015年にはこれらを構成する光機能素子の寸法は100nm以下になると予想される。しかしながら，伝搬光を用いた素子では光の回折限界により波長以下の微小化は不可能である。この問題を解決する有効な手段として，筆者らは量子ドットによって構成され近接場光によって動作するナノフォトニックスイッチを提案している[1]。この集積回路を実現するためには，外部の光素子の情報伝送媒体である伝搬光をナノフォトニックスイッチに用いられる近接場光に変換するデバイスが必要となる。さらには，これらのデバイスを作製する技術開発も大きな課題となっている。

本稿では，まず伝搬光を近接場光に変換する素子として必要となるナノメートル寸法の光伝送路の一例を紹介する。この微小な光伝送路としては，遮断径の存在しない（光の回折限界以下まで絞れる）金属コア導波路[2]が提案されており，筆者らは金属薄膜が成膜された楔型シリコン構造によるプラズモン導波路[3]を開発した。さらに近年，より高い近接場光エネルギーの伝送効率をめざしナノ微粒子列によって構成されるナノドットカプラーの開発を行っている。

上記デバイスを実用化するためには，デバイスとして動作する構造を一括で大面積にわたり加工する必要がある。これを実現する手法として，露光装置とエッチングを用いる加工法(トップダウン)と原子・分子を積み上げる加工法（ボトムアップ）が挙げられる。トップダウンは，近年X線などを用いたリソグラフィーにより20nm以下の精度の加工が可能であるが[4]，「削る」ことによる加工が主となるため基板などの損傷が問題となる。これに対してボトムアップは「積み上げる」加工のため損傷は回避できる。近年，著者らは近接場光を用いた化学気相堆積法を開発し，20nm程度の金属および半導体ナノ寸法微粒子を20nm程度の間隔で高密度かつ，ナノ寸法の位置設定誤差で堆積が可能であることを示した[5),6),7)]。さらには，物質寸法に依存する光脱離法を用いた手法により特定の寸法で近接場光誘起の脱離効果により成長を止めることで，自己組織的に寸法を制御可能な技術を開発した[8]。この技術を応用することで，均一粒径ナノ微粒子を一括で作製可能であることも明らかにした[9]。この手法は，いわば寸法がゼロのものから堆積を行い，特定の寸法で成長を止め，均一粒径微粒子を一括で作製する手法である。その一方で，近年の化学合成技術の発展により，粒径の揃った誘電体[10]や金属[11]，さらには半導体微小球[12]の作製が容易に可能となっている。この様な微粒子の配列についても，近接場光の技術を用いることで，位置を制御して配列させることが可能となる[13]。

2. ナノドットカプラー

筆者らは**図1**に示す伝搬光・近接場光素子を提案している[14]。この構造は，入力される表面プラズモン・ポラリトン（Surface Plasmon Polariton：SPP）を複数の散乱体により集光する集光器部分と，集光されたエネルギーをナノメートル寸法の光デバイスに導くナノドッ

やつい　たかし，おおつ　もといち

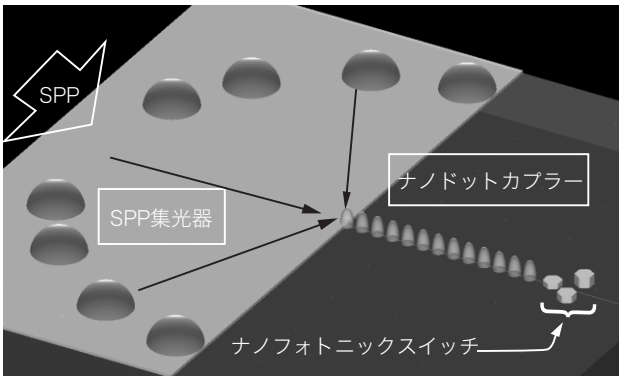

図1　伝搬光・近接場光変換器の概念図

トカプラーから構成されている。プラズモン集光器は，複数の金属突起によって構成され，各突起からのSPPの干渉によりSPPを集光させる。ナノドットカプラーは，同一寸法の金属微粒子が等間隔で配列することにより，各微粒子間を近接場光の相互作用によりプラズモン・ポラリトンが伝送するものである[15), 16)]。この構造はコア材を金属とする導波路（金属コア導波路）と比較して，金属中での伝送部が短い為，伝送損失が小さいと期待される[17)]。

ナノドットカプラーは，プラズモン集光器の焦点を入力点として，集束イオンビーム（Focused Ion Beam: FIB）によるカーボン突起（直径230nm，間隔70nm）の堆積とスパッタリングによる金（膜厚120nm）の堆積により作製した。また比較として，同様のプロセスにより同じ幅を持つ金属コア導波路も作製した。集光器及び作製した試料の電子顕微鏡像を**図2**(a)，2(b)に示す。波長785nmの光を光源として評価した伝送路部分の各近接場光学像を図2(c)，2(d)に，伝送路の中心を通る白破線部分の断面図を図2(e)に示す。この結果から，金属コア導波路の場合〔図2(e)における破線〕はSPPの焦点である入力部分より1μm程度伝搬すると光強度が1/10に減衰するのに対し，ナノドットカプラーの場合〔図2(e)における実線〕は4μm先までプラズモン・ポラリトンが伝送しており，ナノドットカプラーの優位性が実験的に初めて観測された。

また，突起列伝送路の近接場光分布幅は250nmとナノドットカプラーを構成するドット径とほぼ同等であった。これは現状の作製プロセスにおいて，突起物の寸法が作製に用いたFIBの分解能に制限されているためであり，電子ビーム描画装置等を用いることで数10nmの伝送路が実現可能である。

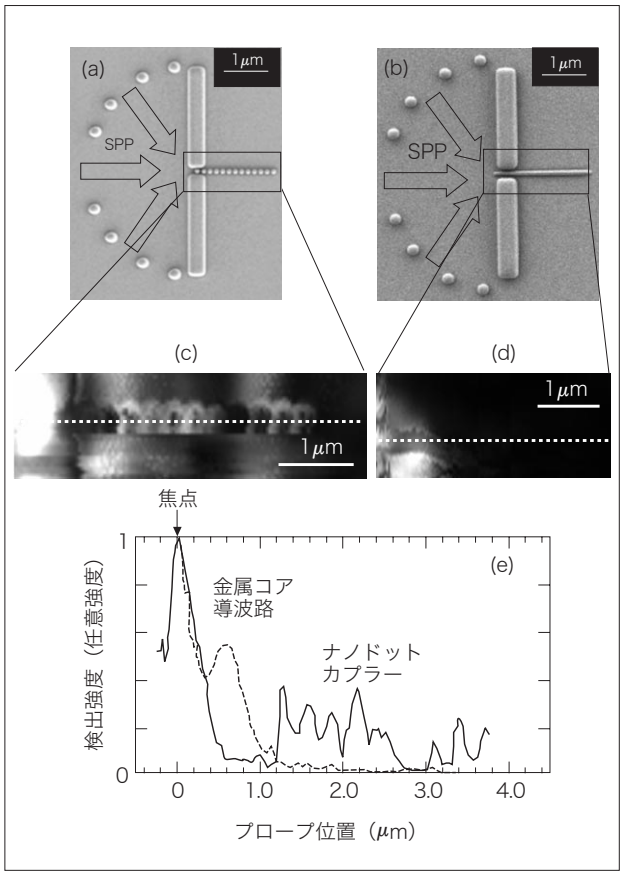

図2　電子顕微鏡像　(a)プラズモン集光器及びナノドットカプラー，(b)プラズモン集光器及び金属コア導波路，(c)近接場光学像ナノドットカプラー〔図(a)黒四角部〕，(d)金属コア導波路〔図(b)黒四角部〕，(e)図(c)及び(d)における白破線上の断面図

さらに，本デバイスの特長として，配置の高い自由度が挙げられる。金属細線導波路などでは，曲げ部での損失が非常に大きいために，単独のデバイスとしても用いる場合には良いが，集積化の点において問題となる。これに対して，ナノドットカプラーは，直角に曲げた場合でも損失がほぼゼロになるということが理論的に予測されているので[18)]，自由なデバイス設計が可能となる。

この予測を実験により確かめた結果を**図3**に示す。直線形状のナノドットカプラー同様に，プラズモン集光器の焦点を入力点とし，FIBにより直角な曲げ部を有するナノドットカプラーを作製した〔図3(a)〕。この形状に対する近接場光学像〔図3(b)，波長785nm〕より，曲げ部においても伝送損失がほとんど見られず，直線状に配列されたナノドットカプラー同様の伝送距離が得られていることが分かる〔図3(c)〕。

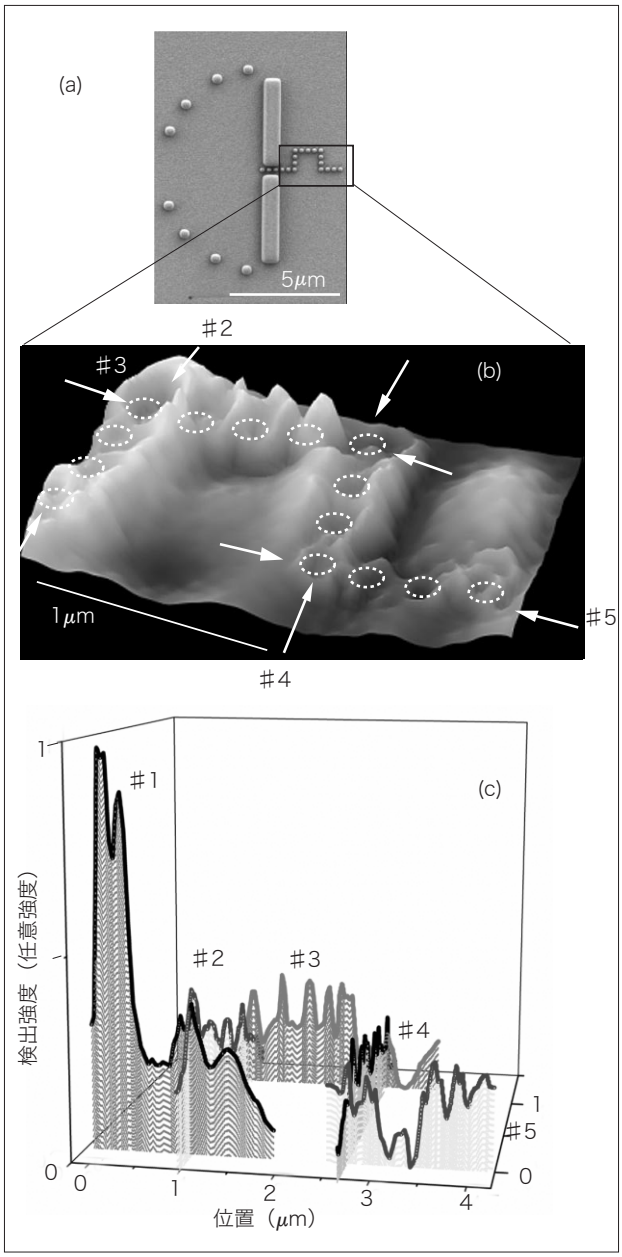

図 3　(a) プラズモン集積路及び曲げ部を有するナノドットカプラーの電子顕微鏡，(b) ナノドットカプラー〔図(a)黒四角部〕上における近接場光学像用，(c) 図(b)におけるナノドットカプラー上の断面図

また，金属微粒子間は近接場光により結合されるため，ナノドットカプラーを並列化した際の干渉は小さいと考えられ，プラズモン集光器を用いた周波数多重による超並列化が期待される。

3. 近接場光を用いた金微粒子配列

前節で紹介した金ナノ微粒子によるナノドットカプラーへの応用を考慮して，ナノ微粒子として塩化金酸の還元により合成した平均直径 20nm の金コロイド粒子を用いて配列実験を行った。この際，金コロイド表面にはカルボキシル基が付着しているため，微粒子同士の反発が発生し，高濃度に配列させることは困難である。そこで，この金微粒子の凝集を発生させるために，金微粒子に発生する近接場光による脱離現象を利用する。金ナノ微粒子は可視光に対して強い吸収を有するため，このエネルギーにより金コロイド表面のカルボキシル基の脱離が誘起され，金コロイドの凝集が発生すると期待される。さらに，コロイドの凝集位置を選択的に行うために，基板として高さ 10μm のシリコン楔型構造〔**図 4**(a)〕を用いた。ここで，シリコン楔型構造は，屈折率が非常に高いことから光は強く閉じ込められる。さらにはテーパ形状となっているために根本から照射すると楔型先端のみに近接場光が発生し，金コロイドの選択的な凝集が期待される。この際，溶液側から光を照射すると，溶液中における凝集により制御性が低くなるため，基板側から光を照射した〔λ=690nm, 25mW/mm^2，図 4(b)〕。ここでは，シリコン基板中での光吸収を低減させるために，シリコン楔型をガラス基板に陽極接合した基板〔図 4(c)〕を用いた。

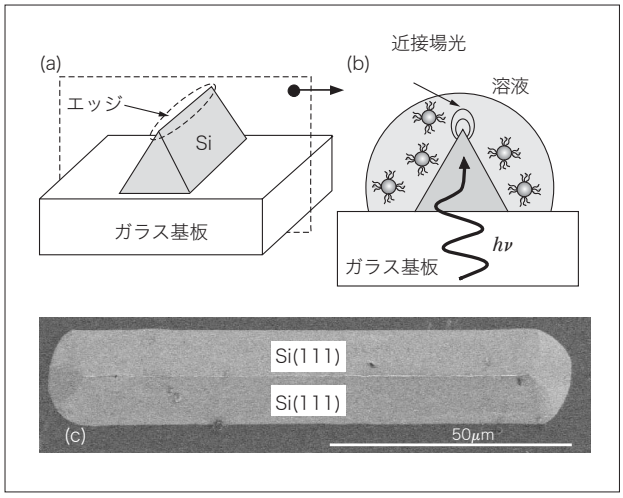

図 4　(a), (b) 近接場光を用いた金微粒子配列手法 (c) 使用したシリコン楔型の電子顕微鏡写真

この基板に対して，まず 0.001 % に希釈した金微粒子溶液を光を照射せずに塗布した結果を**図 5**(a)，(b)に示す。この場合，基板の凹凸構造に対して選択性が低いことが分かる。これに対して，金微粒子溶液を塗布する際に，楔型に対して垂直及び平行偏光の光を導入して塗

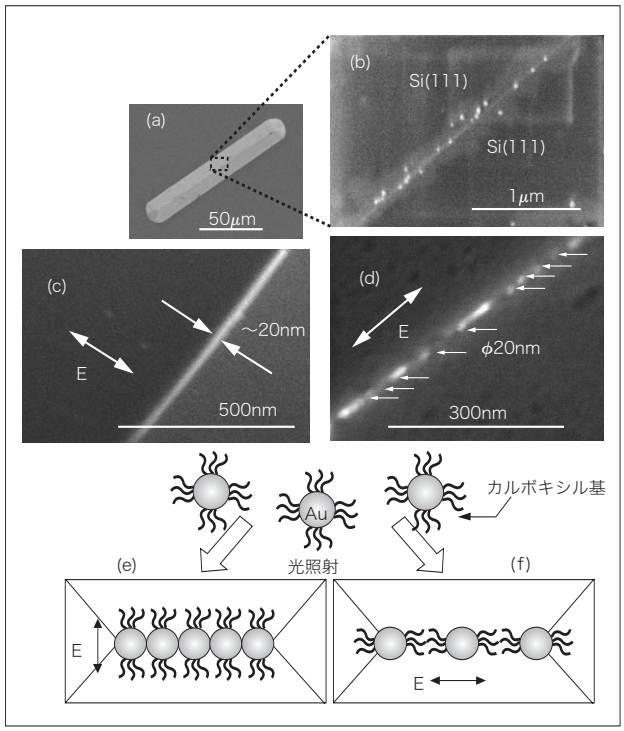

図 5　シリコン楔型の電子顕微鏡写真　(a) 無照射，(b) 無照射〔(a) の拡大図〕，(c) 垂直偏光，(d) 平行偏光。近接場光誘起による金微粒子配列の原理図：(e) 垂直偏光，(f) 平行偏光

布した結果を図 5(c)及び図 5(d)に示す。これらの結果に示されるように，光を照射することで，楔型のエッジに近接場光が誘起され，ここに微粒子が選択的に凝集し配列している様子が分かる。さらには，偏光方向によって凝集の様子が変化していることが分かる。このような差異は，金微粒子における残留カルボキシル基の影響であると考えられる。つまり，垂直偏光の場合には，凝集する方向に対してカルボキシル基が脱離しているために凝集が発生した〔図 5(e)〕のに対して，平行偏光ではカルボキシル基の残存により凝集が妨げられた〔図 5(f)〕のであろう。

4. あとがき

本稿ではナノフォトニクスを用いてのみ実現可能なナノ光デバイスと，そのような構造を実現するためのナノ寸法精度かつマクロな構造が作製可能な近接場光加工について解説した。本方法は，光化学反応を利用したものであるため，ここで示した金以外の金属微粒子（Ag, Pt 等）や半導体微結晶（CdSe，GaN，ZnO 等）の配列にも応用可能であり，より高効率なナノドットカプラーの実現や，量子サイズ効果を用いたナノフォトニックスイッチ[1]などの高機能素子の実現が期待される。

また，従来のナノ微細加工技術としては，半導体微細加工などに用いられている電子ビームリソグラフィーなどが一般であるが，これらの技術においても「加工する」ことと，デバイスとして「動作させる」こととは別の技術であり，ナノ寸法のデバイスを実現させるためには大きな技術的・機能的限界が存在する。これに対し，近接場光による加工は単にナノ寸法の微細加工が可能ということではなく，近接場光で動作するナノフォトニックデバイスを作製する手法としては，作製後デバイスとしての動作を保証する自己完結的手法であると期待される。

参考文献

1) M. Ohtsu, K. Kobayashi, T. Kawazoe, S. Sangu, and T. Yatsui: IEEE J. Sel. Top. Quantum Electron., Vol. 8, No. 4, pp. 839～862 (2002)
2) J. Takahara, S. Yamagishi, H. Taki, A. Morimoto, and T. Kobayashi: Opt. Lett., Vol. 22 No. 7, pp. 475～477 (1997).
3) T. Yatsui, M. Kourogi, and M. Ohtsu: Appl. Phys. Lett., Vol. 79, No. 27, pp. 4583～4585 (2001)
4) M. D. Austin, H. Ge, W. Wu, M. Li, Z. Yu, D. Wasserman, S. A. Lyon, and S. Y. Chou: Appl. Phys. Lett., Vol.84, No.26, pp. 5299～5301 (2004)
5) Y. Yamamoto, M. Kourogi, M. Ohtsu, V. Polonski, and G. H. Lee: Appl. Phys. Lett. Vol. 76, No. 16, pp. 2173～2175 (2000)
6) T. Yatsui, T. Kawazoe, M. Ueda, Y. Yamamoto, M. Kourogi, and M. Ohtsu: Appl. Phys. Lett.,Vol. 81, No. 19, pp. 3651～3653 (2002)
7) J. Lim, T. Yatsui, and M. Ohtsu: IEICE Transactions on Electronics, Vol. E88–C, No. 9, pp. 1832～1835 (2005)
8) T. Yatsui, S. Takubo, J. Lim, W. Nomura, M. Kourogi, and M. Ohtsu: Appl. Phys. Lett., Vol. 83, No. 9, pp. 1716～1718 (2003)
9) 大津元一，川添忠，八井崇：O plus E, Vol. 25, No. 12, pp. 1369～1373 (2003)
10) R. Micheletto, H. Fukuda, and M. Ohtsu: Langmuir, Vol. 11, No. 9, pp. 3333～3336 (1995)
11) Y. Sun and Y. Xia: Science, Vol. 298, pp. 2176～2179 (2002)
12) A. P. Alivisatos: Science, Vol. 271, pp. 933～937 (1996)
13) T. Yatsui, W. Nomura, and M. Ohtsu: IEICE Transactions on Electronics, Vol. E88–C, No. 9, pp. 1798～1802 (2005).
14) W. Nomura, T. Yatsui, and M. Ohtsu: Appl. Phys. Lett., Vol.

86, No.18, 181108 (2005)
15) S. A. Maier, P. G. Kik, H. A. Atwater, S. Meltzer, E. Harel, B. E. Koel, and A. A. G. Requicha: Nature Materials, Vol. 2, pp. 229～232, (2003)
16) J. R. Krenn, A. Dereux, J. C. Weeber, E. Bourillot, Y. Lacroute, J. P. Goudonnet, G. Schider, W. Gotschy, A. Leitner, F. R. Aussenegg, and G. Girard: Phys. Rev. Lett., Vol. 82 , No. 12, pp. 2590～2593 (1999)
17) M. Quinten, A. Letner, J. R. Krenn, and F. R. Aussenegg: Opt. Lett., Vol. 23, No. 17, pp.1331～1333 (1998)
18) M. L. Brongersma, J. W. Hartman, and H. A. Atwater: Phys. Rev. B, Vol. 62, No. 24, R16356 (2000)

[Ⅳ] PUBLISHED BOOKS

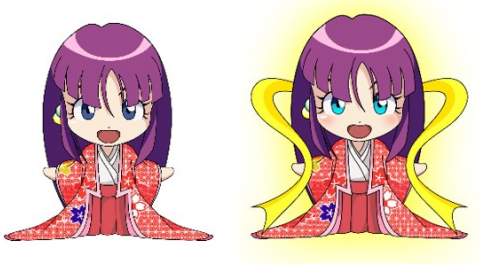

Motoichi Ohtsu (Ed.)

Progress in Nano-Electro-Optics V

Nanophotonic Fabrications, Devices, Systems, and Their Theoretical Bases

With 122 Figures

Springer

Professor Dr. Motoichi Ohtsu
Department of Electronics Engineering
School of Engineering
The University of Tokyo
7-3-1 Hongo, Bunkyo-ku, Tokyo 113-8656, Japan
E-mail: ohtsu@ee.t.u-tokyo.ac.jp

ISSN 0342-4111

ISBN-10 3-540-28665-9 Springer Berlin Heidelberg New York

ISBN-13 978-3-540-28665-3 Springer Berlin Heidelberg New York

Library of Congress Cataloging-in-Publication Data

Progress in nano-electro-optics V : nanophotonic fabrications, devices, systems, and their theoretical bases / Motoichi Ohtsu (ed.). p.cm. – (Springer series in optical sciences ; v. 117)
Includes bibliographical references and index.
ISBN 3-540-28665-9 (alk. paper)
1. Electrooptics. 2. Nanotechnology. 3. Near-field microscopy. I. Ohtsu, Motoichi. II. Series.
TA1750 .P75 2002 621.381'045–dc21 2002030321

Springer is a part of Springer Science+Business Media.

springer.com

Printed in The Netherlands

Typesetting: SPI, Pondicherry, India
Cover concept by eStudio Calamar Steinen using a background picture from The Optics Project. Courtesy of John T. Foley, Professor, Department of Physics and Astronomy, Mississippi State University, USA.
Cover production: *design & production* GmbH, Heidelberg

Printed on acid-free paper SPIN: 11540205 57/3100/SPI 5 4 3 2 1 0

Contents

ナノオプティクス

ナノフォトニクスの基礎

大津 元一・小林 潔◎共著

Ohmsha

目　　次